ENVIRONMENTALLY FRIENDLY TECHNOLOGY:

THE BEHAVIOUR OF NATURAL AND SYNTHETIC BINDER SYSTEMS WITHIN

PAPER COATINGS

by

GIULIANO MAURIZIO LAUDONE

A thesis submitted to the University of Plymouth
in partial fulfilment for the degree of

DOCTOR OF PHILOSOPHY

School of Earth, Ocean and Environmental Sciences
Faculty of Science

In collaboration with
Omya AG, Oftringen, Switzerland

February 2005

ii

Abstract

by Giuliano Maurizio Laudone

Environmentally friendly technology: The behaviour of natural and synthetic binder systems within paper coatings.

Coating shrinkage upon drying is a phenomenon well known to the paper coating industry, where it often causes changes in the final structure of the coating layer leading to poor results in terms of gloss, light scattering, surface strength, coverage, uniformity and printability. Such shrinkage has in previous studies been wrongly associated with shrinkage of the polymeric binders used in the coating formulation, by making erroneous comparison with solvent-based paint systems. Natural binders, as starch or proteins, which come from renewable resources and are therefore environmentally friendly, suffer more from this shrinkage phenomenon than synthetic binders. The aim of this research project was to improve the understanding of the processes involved in the drying of a coating layer and to create a model able to describe them.

Shrinkage while the coating layer dries has been successfully measured by observing the deflection of coated strips of a synthetic elastically-deformable substrate. Ground calcium carbonate was used as the coating pigment, together with latex binders of both low and high glass transition temperature, T_g, respectively, and also with starch which is a natural film-forming water soluble binder. The final dry coatings were studied with mercury porosimetry and by scanning electron microscopy in order to characterise their porous structure. The flow and rheological properties of the coating colour formulations were measured in order to probe the particle-particle interaction between the different species in the wet coating colour.

 The void space of the dry coating layers was modelled using Pore-Cor, a software which generates simulated porous networks. A new algorithm was developed to model, within the simulated void space, the effective particles or "skeletal elements" representative of the solid phase of the dried porous system. The water-filled porous structures at the beginning of the shrinkage process (first critical concentration, FCC) were subsequently modelled by creating Pore-Cor structures with the same solid skeletal elements distribution as at the second critical concentration (at which the particles lock their positions), but with higher given porosity to account for the water present. The capillary forces acting on the surface of the simulated coating were calculated, and found to be several orders of magnitude larger than the measured shrinkage forces. The shrinkage process was thus described as resulting from the effect of capillary forces in the plane of the coating layer resisted by a stick-slip process, where the capillary forces yield shrinkage only if a resistance force within the drying coating layer holds the structure in place and allows the menisci to form. The stick-slip theory was strongly supported by quantitative comparisons between the experimental forces required to intrude mercury, and the capillary forces within the simulated void structure.

List of contents

List of figures

vii

List of tables

List of equations

Acknowledgements

Author's declaration

At no time during the registration for the degree of Doctor of Philosophy has the Author been registered for any other University award.

This project was funded by the University of Plymouth-Faculty of Science and by Omya AG, Oftringen, Switzerland.

Relevant scientific seminars and conferences were regularly attended at which work was often presented; external institutions were visited for consultation purposes and several papers were prepared for publication.

44 133 words.

Signed...

Date......25.08.05...........................

Conferences, publications and training

Conferences:

Department of Environmental Science - Research seminar - Natural and synthetic binder systems in paper coating, University of Plymouth. January 2002. Oral presentation.

Third international Symposium on Contact Angle, Wettability and Adhesion, Providence, Rhode Island (USA); 20-22 May 2002. Oral presentation.

Department of Environmental Science- Research seminar – Measurement of shrinkage upon drying in paper coating, University of Plymouth. February 2003. Oral presentation.

Tappi Advanced Coating Fundamentals Symposium, Chicago (USA); 8-10 May 2003. Oral presentation. Award for Best Student Presentation.

Publications:

Laudone G.M., Matthews G.P. and Gane P.A.C (2002), Indirect measurement of the shrinkage forces acting during the drying of a paper coating layer, Contact Angle, Wettability and Adhesion Vol. 3 (Mittal, K.L. ed.), VSP.

Laudone G.M., Matthews G.P. and Gane P.A.C (2003) Coating shrinkage during evaporation: observation, measurement and modelling within a network structure, *2003 Tappi Advanced Coating Fundamentals Symposium*, Atlanta, Tappi Press.

Laudone G.M., Matthews G.P. and Gane P.A.C. (2004), Observation of shrinkage during evaporative drying of water-based paper coatings, *Industrial and Engineering Chemistry Research* **43**: pp 712-719.

Laudone G.M, Matthews G.P., Gane P.A.C., Matthews A.G., Ridgway C.J., Schoelkopf J. and Huggett S. (2005), Estimation of representative particle sizes in sand and compacted blocks of ground calcium carbonate using a void network model, *Powder Technology*, submitted for publication.

Training:

External training on numerous analytical instruments relevant to the paper coating industry was performed at Omya AG, Oftringen, Switzerland. All other training was performed at the Environmental and Fluid Modelling Group, University of Plymouth.

1 INTRODUCTION

1.1 Structure of the thesis

This thesis is divided into two main sections: experimental and modelling. In the experimental section of this work, both existing and novel experimental techniques are described and their results presented. In the modelling section, a full description of an existing computer modelling software is given, the development of novel algorithms is presented and the results, obtained by application of the existing modelling software and the novel algorithms, are shown.

The Introduction will describe the industrial, environmental and scientific background of this research project, with a review of relevant scientific literature. This should enable the reader of the thesis to gain a general understanding of this work. The hypotheses and the objectives of the thesis will also be stated in the Introduction. In Chapter 2, the existing experimental techniques and their use will be presented. A novel experimental technique for the measurement of shrinkage forces acting upon drying of a paper coating layer, and its results, are presented in Chapter 3. Chapter 4 will describe the results of rheological measurements on paper coating formulations. Chapter 5 will describe the software "Pore Cor" for the simulation of porous network and its use to model paper coating. In Chapters 6 and 7, a novel algorithm for the calculation of the effective sizes of particles constituting the skeletal solid material in a porous structure is described and its results presented. Chapter 8 will describe the modelling of the phenomena occurring while a paper coating layer dries, and how these phenomena cause the shrinkage of the coating layer. Finally it will compare the results of this modelling of the shrinkage forces with the experimental results. In Chapter 9, a final overview of this thesis will be presented and conclusions will be drawn.

1

1.2 Collaborative basis of this research project

In this thesis, we have investigated the shrinkage forces acting upon drying of a paper coating layer, with the aim of improving the understanding of the phenomena causing such shrinkage and of reducing their detrimental effect on the final properties of the coated paper.

This research project has been developed in collaboration between Omya AG, a Swiss-based world-leading supplier of mineral pigments for paper coating, and the Environmental and Fluid Modelling Group at the University of Plymouth. The modelling expertise of the Environmental and Fluid Modelling Group has led to the development of the Pore-Cor Research Suite, a highly sophisticated void network model. The R & D department of Omya AG has knowledge and expertise in the study of pigmented coating layers, solid-liquid interactions, microscopy and rheology. The collaboration has given rise to several prior and concurrent research projects, involving the development of an inertial absorption algorithm, the modelling of throats with converging-diverging geometry, and the study of anisotropic structures and ink-pigment interaction.

1.3 Environmental issues in paper coating industry

The environmental issues faced by the paper coating industry are mainly related to the component materials and their origin.

The mining of the different types of pigments used in paper coating production has different environmental impacts. Traditionally, the mineral most commonly used in Europe has been primary kaolin, which is usually extracted from rocks with only 15-20 % of kaolinite in the ore, thus requiring a process of refinement with high waste. Higher yields are possible from

secondary deposits, such as the kaolins used in the US and the Far East, but these lack the particle shape characteristics so prized for coverage.

Ground calcium carbonate (GCC), on the other hand, is produced via a low-waste mining process, as about 80 % of the ore is calcite, $CaCO_3$. In this respect, the use of calcium carbonate is more environmentally friendly.

After extraction of the ore, both kaolin and GCC are processed and ground, for purification and to create the desired particle size distribution. The energy costs of these processing steps vary depending on particle size. For the finest grades of GCC and primary kaolins, they are comparable for the two minerals.

Precipitated calcium carbonate (PCC), which is $CaCO_3$ chemically synthesised under highly controlled conditions (section 1.6.2), requires for its production an overall higher amount of energy, due to the requirement to burn limestone, creating carbon dioxide, CO_2, both from waste flue gas and from the calcite itself, only part of which is re-captured in the precipitation process, and is therefore less environmentally friendly and ultimately more expensive.

Coatings on paper need binder to maintain their integrity and to provide adhesion to the underlying base paper. The different types of binder also have different environmental effects. On the one hand there are natural binders, like starch or proteins, derived from renewable resources such as maize, potatoes or animal waste. On the other hand, latex binders are widely used, because of the better results in terms of final properties of the coating layer. However, they are a product of the petrochemical industry and, therefore, non-renewable and less environmentally friendly.

The same environmental issue is faced by the printing industry in the choice of inks used in the printing process. Traditionally, inks were based on mineral oils, which are a product of the petrochemical industry, and are not biodegradable. Hence new trends are emerging in ink formulation, favouring the use of vegetable oils. These changes make new demands on the pore structure of the coating layer and its surface chemistry.

1.4 Hypotheses

In order to understand the hypotheses for this study, it is necessary to have an understanding of the terms 'First Critical Concentration' and 'Second Critical Concentration'. When a coating dries, the particles in the coating suspension move closer together as the liquid drains or evaporates. After a certain loss of water, the 'First Critical Concentration' (FCC) is reached at which the particles touch each other. During further loss of water, the particles re-arrange themselves into an ever closer packing, until at the 'Second Critical Concentration' (SCC) their positions are locked. Further drying does not then alter the particle positions. This process is described more fully in section 1.8.7.

At the start of the project, a search of the literature showed that the main hypotheses tested in this research project were unproven or remained controversial. They are sub-divided according to process, experimentation and modelling:

Process

1. shrinkage occurs between the FCC and SCC, and the extent of shrinkage is linked to the extent of structural difference between FCC and SCC;

2. the shrinkage of a coating colour upon drying is not caused by a shrinkage of the binder(s) commonly used, but is a meniscus driven phenomenon;

3. capillaries, and, as a consequence, meniscus forces, appear on the surface of a drying paper coating layer because the dynamic rearrangement of the forming pigment network, to compensate for the water loss, is a process that requires initiation by the meniscus forces;

4. the work required to progress the rearrangement process is due to the component interactive resistance forces within the drying coating colour, which oppose the free rearrangement of the particles, and which are related to the various particulate and chemical species in the slurry;

Experiment

5. since the forces acting during shrinkage cause a coated paper formulation on an elastically flexible substrate to curl up, a quantitative measure of the degree of curl can be used to give a quantitative measure of the shrinkage forces;

Modelling

6. the shrinkage process can be realistically modelled by Pore-Cor by extrapolating backwards in drying process time from the known SCC, by increasing the porosity of the system while maintaining the same skeletal element particle size distribution;

7. the driving forces acting in the modelled process are the same as in the experimental process.

There is no experimental method available which directly probes the drying process. Therefore hypotheses 1 – 4 can only be proven by a combination of indirect experimentation and modelling. The rheology of coating colour formulations has been extensively studied, in order to measure the interactions between the different particulate and chemical species in the slurry, and hence resolves hypothesis 4. Hypotheses 5 to 7 have been probed by using a novel

experimental technique and by developing novel algorithms within the existing Pore-Cor software framework.

1.5 Pigmented coating layers

Pigments are used in the paper industry both in paper coating and as fillers, as they offer a cheaper alternative to wood fibres, whilst providing improved functional properties.

The application of a pigmented coating layer to a base sheet of paper improves its optical and printing properties. Some of the characteristics imparted by coating a paper are:

- improved uniformity in appearance,

- designed gloss or matt finish,

- increased opacity (no image show-through),

- ink absorption without blemish (improved image reproduction via increased colour spectral gamut, reduced information transfer loss and improved uniformity of print density);

- increased capillarity to promote complete ink setting within the time-scale of a modern printing operation.

The usual composition of a coating colour formulation (on a dry basis) is 80-90 w/w% mineral pigment and 10-20 w/w% binder by weight. The solid in water dispersion is usually between 50 w/w% and 70 w/w%. Other compounds, such as dispersants, stabilisers and rheology modifiers are used in the formulation of the coating colour in lower percentages to act as colloidal stabilising agents and to make the components compatible in water suspensions. The particle diameters of the mineral pigments usually range from 0.01 to 10 μm. A thin layer of coating colour is metered on the surface of the base paper, typically with a blade coater, shown in Figure 1.1, and dried.

6

(A) Coating pan
(B) Backup roll
(C) Applicator roll
(D) Blade jaw
(E) Blade
(F) Overflow
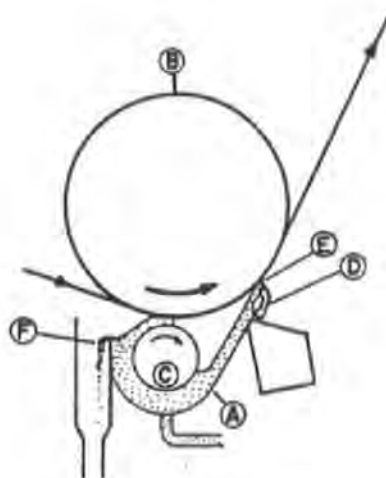
Figure 1.1 - Blade coater (Moreau S., 1994).

1.6 Pigments

Pigments are, usually, particulate minerals used on their own or in mixtures, depending on the desired properties of the coated paper. Synthetic pigments may be used as well. In this work we used ground calcium carbonate, but in order to present a full picture of the paper coating industry, a brief description of the most commonly used mineral pigments will be given.

1.6.1 Kaolin clay

Kaolin clay is widely used because it is cheap, reasonably white and easily available world-wide, the major sources being Cornwall (UK), Georgia (USA) and Brazil. Kaolin is a layered aluminium silicate represented by the stoichiometric formula:

$$(OH)_8 \, Si_4 \, Al_4 \, O_{10}$$
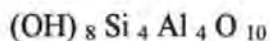
A representative structural formula is shown in Figure 1.2, and comprises alternate layers of tetrahedral and octahedral structure.

7
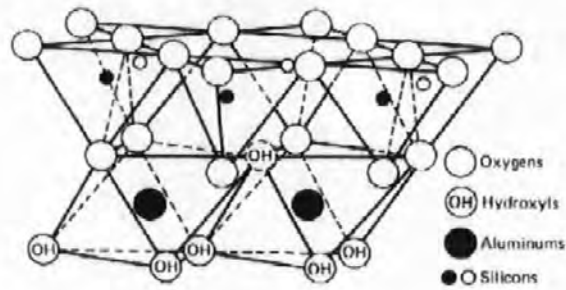
Figure 1.2 - Structural formula of kaolin (http://www.up.ac.za/academic/civil).

Individual kaolin crystals show a hexagonal shape with a defined *aspect ratio*. The aspect ratio for plate-like and acicular particles is the ratio of the major to minor particle dimensions - in the case of clay, the ratio of the diameter of the platelet face to its thickness.
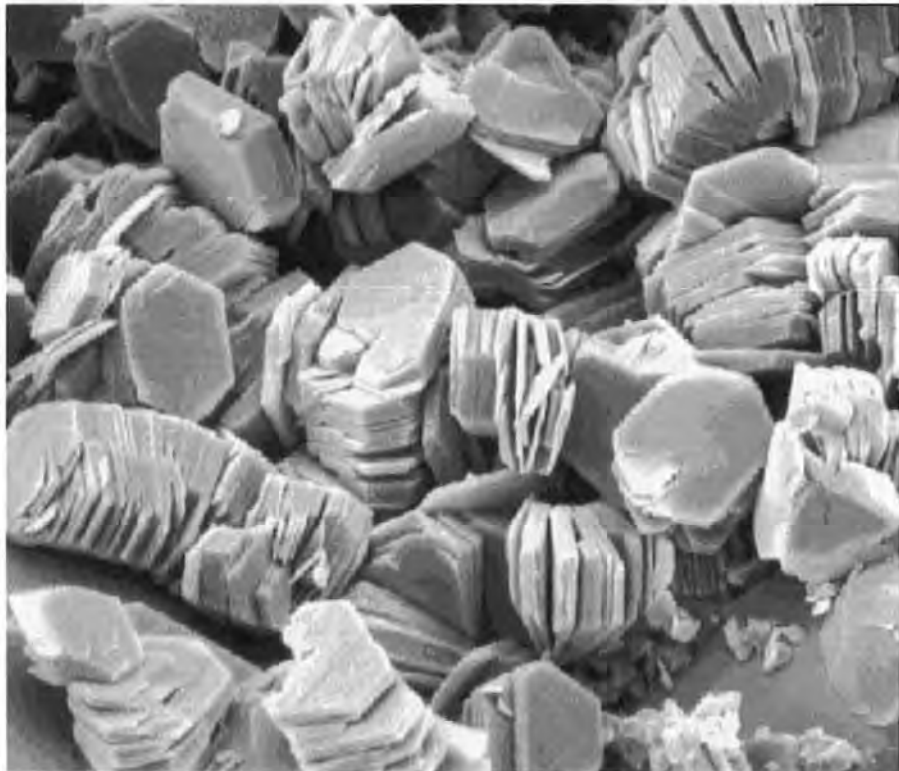
Figure 1.3 - Scanning electron micrograph of kaolin (from http://originoflife.net/information). Note the "stacks" or "booklets" of platelets which allow for further delamination.

The industrial use of kaolin clay is nowadays becoming less popular in the paper coating industry. This is mainly because of the technical and competitive market pressure exerted by calcium carbonate, which provides high brightness, good runnability and, in the case of

8

ground calcium carbonate, a more efficient production process compared to primary clay extraction.

1.6.2 Precipitated Calcium Carbonate

Precipitated Calcium Carbonate (PCC), is a chemically synthesised calcium carbonate. The production process starts with the calcination of limited resource high-purity *limestone* (95 % $CaCO_3$), producing carbon dioxide, CO_2, both from the burning of the lime itself and from the fuel used for the calcination, and CaO (quicklime). In so-called integrated plants, useful heat is extracted from the hot gases thus generated, before a proportion of the CO_2 is stored for re-use in the calcium carbonate precipitation. The quicklime is mixed with water under controlled conditions to form a slaked slurry of calcium hydroxide. Finally CO_2 is bubbled into the milk of lime, where it reacts:

$$Ca(OH)_2 + CO_2 \rightarrow CaCO_3 + H_2O.$$
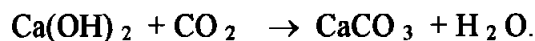
By controlling the operating conditions it is possible to obtain either calcite or aragonite (the two stable forms of calcium carbonate crystals), or a mixture of the two, and an almost monodispersed particle size distribution results. In an alternative process, the *lime soda process*, the calcium carbonate precipitates from the reaction of calcium hydroxide with sodium carbonate:

$$Ca(OH)_2 + Na_2CO_3 \rightarrow CaCO_3 \downarrow + 2NaOH$$
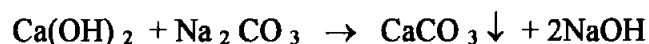
Calcite, which is the only thermodynamically stable form of calcium carbonate, belongs to the hexagonal-scalenohedral crystal class in the hexagonal system. In the commercial grades of PCC the rhombohedral, prismatic and scalenohedral (Figure 1.4) are the most commonly observed. Aragonite (Figure 1.5), which is less used than calcite due to its meta-stability, belongs to the dipyramidal crystal class and the crystals are normally elongated, with a typical needle-like shape.

9
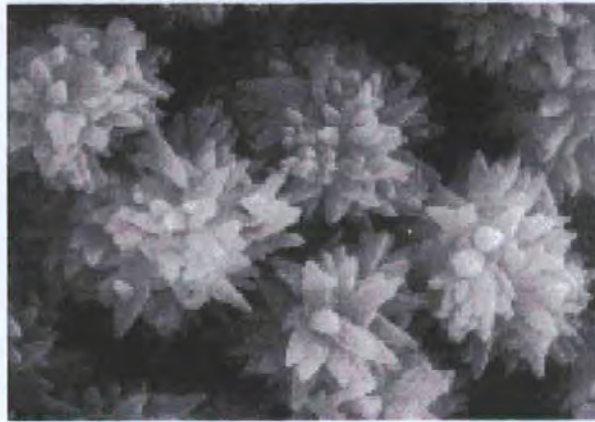
Figure 1.4 - Scalenohedral precipitated calcium carbonate (from http://www.mineralstech.com).

Figure 1.5 - Aragonite (from http://www-sop.inria.fr/agos-sophia).

The use of PCC, as well as ground calcium carbonate (GCC), is becoming more industrially relevant and the reasons are simple: better brightness and better colour than clay, together with the introduction of neutral or alkaline papermaking in which the longevity of the fibre-fibre bonds is assured. The higher pH prevents the premature ageing of paper seen when using the traditional acid kaolin-containing process.

1.6.3 Ground Calcium Carbonate

$CaCO_3$ naturally occurs as calcite (Figure 1.6) in various rock forms, namely chalk, limestone and marble.

Figure 1.6 - Calcite (from http://www.ggl.ulaval.ca).

Nowadays, the grinding of calcium carbonate is almost entirely carried out as a "wet" process, and the GCC is delivered as a slurry. This has several advantages: energy is saved, the slurry can be pumped, it is free of dust and is ready for use in water-based formulations.
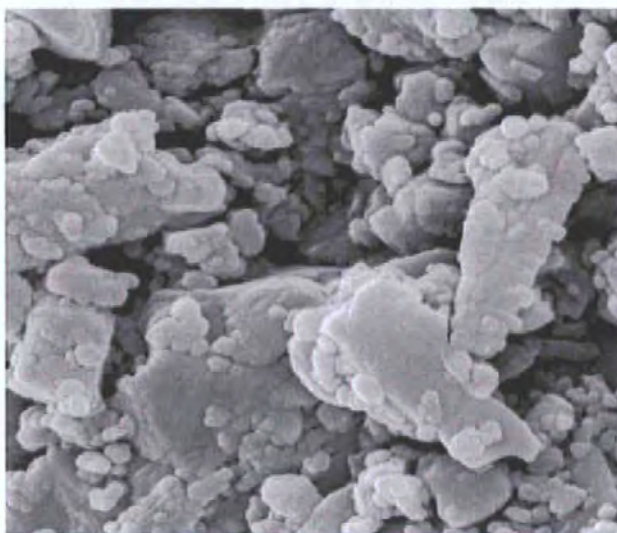
Figure 1.7 - Scanning electron micrograph of GCC.

Different grinding methods result in different particle size distributions, with typically from 40 w/w% to 98 w/w% of the particles having a diameter < 2 μm. The slurry is usually stabilised adding 0.1-1 w/w% active component of anionic dispersing agents (such as sodium poly-acrylate or sodium poly-phosphate) to avoid flocculation, aggregation or settling of the calcium carbonate, and to maximise transportation and applications solids content.

1.7 Binders

Binders are either natural (starch or proteins) or synthetic, e.g. styrene-butadiene or styrene-acrylic latex adhesives. They are used in paper coating to fix the structure formed by the mineral particles together and onto the base paper. Carboxymethyl cellulose and synthetic thickeners (usually acrylates) are also often used as co-binder(s) to provide resistance to aeration and a water retentive property.

1.7.1 Starch

The major sources of starch are corn (North America) and potatoes (Europe). Starch, as extracted from plants, forms high viscosity solutions and has the tendency to cross-link, forming a gel (Husband, 1997). In order to prevent these detrimental properties, the chain length of the starch macromolecule is reduced by acid hydrolysis, and substituent groups (anionic, such as phosphate or carboxyl, as in Figure 1.8, or non-ionic such as hydroxyethyl or hydroxypropyl, as in Figure 1.9) are attached along the chain to prevent intermolecular association.
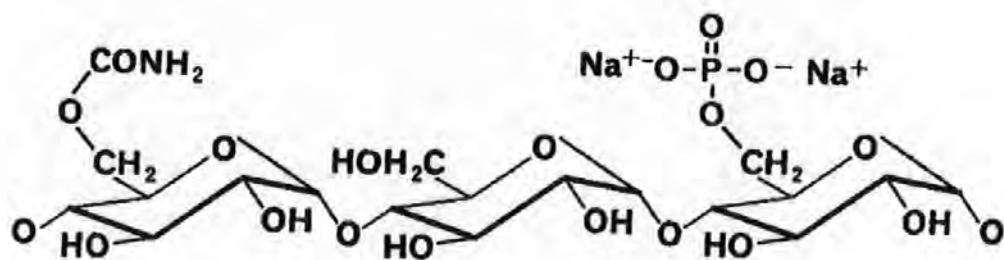
Figure 1.8 - Structural formula of phosphate modified starch.
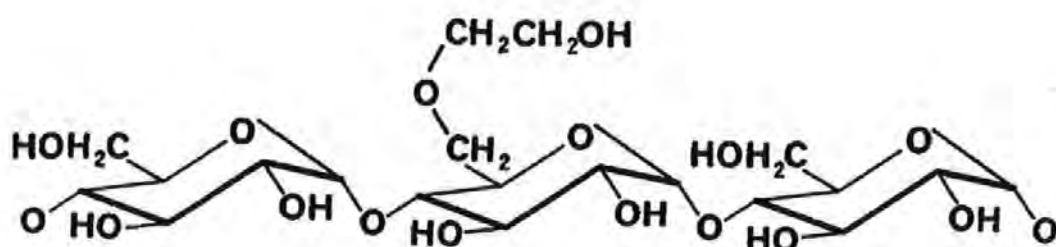
Figure 1.9 - Structural formula of starch with hydroxyethyl group.

1.7.2 Carboxymethyl cellulose

Sodium Carboxymethyl Cellulose (CMC) is widely used as thickener and water retention aid in paper coating formulations, especially when latex is the binder. Cellulose is a polymer of D-glucose, with each sugar ring linked by β 1-4 bonds as shown in Figure 1.10. CMC is synthesised from cellulose by reaction with an alkaline solution of sodium mono-chloroacetate to form the ether.
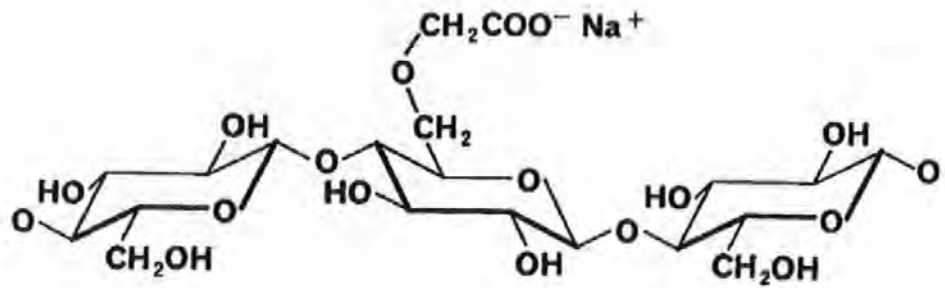
Figure 1.10 - Structural formula of carboxymethyl cellulose.

1.7.3 Synthetic binders

Synthetic binders are usually aqueous dispersions of latex particles of diameter 0.1 to 1 μm: under thermal drying conditions, depending on film forming temperature, a film, or more commonly a filament or train of coalescing particles, is formed. Chemically they are usually styrene-butadiene (Figure 1.11) or styrene/butadiene-acrylic co-polymers and they can be classified by their *glass transition temperature*, T_g, i.e. the temperature at which the filming process begins.
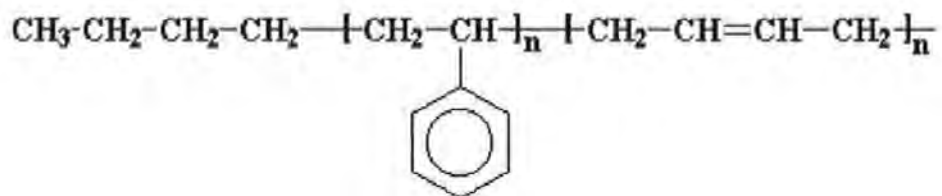
Figure 1.11 - Representative formula of styrene-butadiene latex.

In order to improve its mechanical and chemical stability, the latex polymer chains are carboxylated, as shown in Figure 1.12.

14
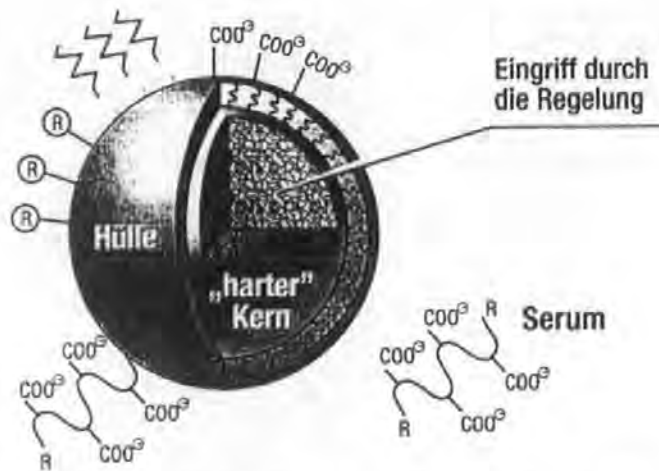
Figure 1.12 - Carboxylated latex particle. The partially polymerised species in the latex serum can be observed. (Ostrowicki and Ramthun, 1999). 1) Eingriff durch die Regelung = structure derived via controlled polymerization; 2) Hülle = outer shell; 3) harter Kern = hard core.

The progression toward the film-formation process of latex particles upon drying can be schematically represented as in Figure 1.13, showing the coalescence stage that dominates in paper coating, where the residual particulate nature of the latex is often preserved.
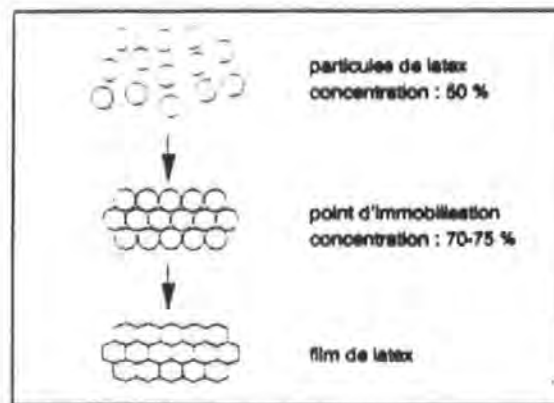
Figure 1.13 - Latex film formation (Moreau S., 1994).

1.8 Theory and literature review

1.8.1 Surface tension, surface free energy and contact angle

A full theoretical treatment of interfacial phenomena goes beyond the scope of this thesis and can be found in Adamson (1990). However, it is important to present definitions and clarify a few fundamental concepts, which represent the theoretical basis of this study.

15

Surface tension and surface free energy are, from a mathematical point of view, identical, but their definitions are different and this has led to the question of which is the more fundamental concept.

Surface tension is a force acting parallel to the surface. In order to extend the surface work must be done, and this work is equal to the surface tension multiplied by the change in area $W = \gamma dA$.

Surface free energy can be seen as the work required to bring a molecule from the interior of a liquid to its surface, and this work arises from the fact that while in the bulk of the fluid a molecule experiences no net forces, these forces become unbalanced as the molecule moves towards the surface. The total surface energy can be calculated by knowing the potential function of the interaction between molecules.

When a liquid phase comes in contact with a solid phase, as shown in Figure 1.14, the contact angle θ at the contact point of the three phases (solid S, liquid L and vapour V) describes the resultant of the mutual interaction of the different phases.

$$\gamma_{SV} = \gamma_{SL} + \gamma_{LV} \cos\theta, \qquad \text{Eq. 1.1}$$
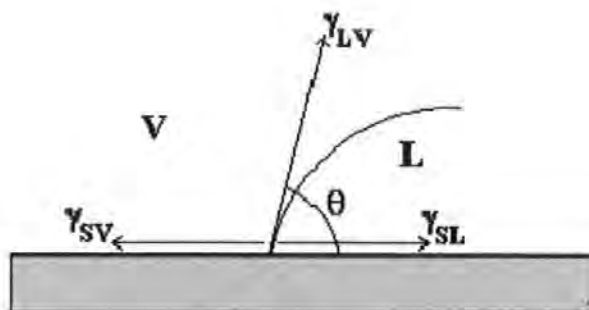
Figure 1.14 - Balance of tensions on a drop.

16

In Eq. 1.1, γ_{SV} is the surface energy for the solid-vapour interface, γ_{SL} is the solid-liquid surface energy and γ_{LV} is the liquid-vapour one. The contact angle is zero if complete wetting occurs. If the contact angle value is greater than 90° the fluid is non-wetting for the solid surface.

1.8.2 Capillarity and meniscus forces

The theory of capillarity was first given a full mathematical formulation in the early 1800s, thanks to the works of Young and Laplace. Their theory proposed that two forces, one attractive and the other repulsive, acted between fluid bodies in a surface and were responsible for the existence of interfacial tension. By calculating the work necessary to increase the surface area of the interface between two fluids of $\Delta A = x dy + y dx$ (Figure 1.15) and the change in pressure difference across such a surface, they derived the equation describing the pressure difference across the interface when mechanical equilibrium is reached (Adamson, 1990).
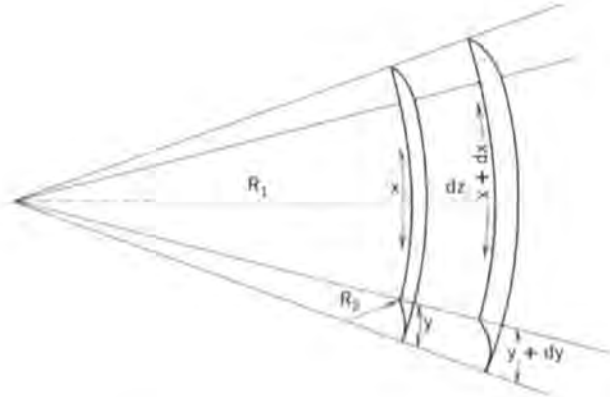
Figure 1.15 - Section of an arbitrarily curved surface.

The Young and Laplace equation,

$$\Delta P = \gamma(\frac{1}{R_1} + \frac{1}{R_2}),$$ Eq. 1.2

17

where R_1 and R_2 are the radii of curvature necessary to describe a curved surface and γ is the surface tension, represents the basis for any study involving capillarity and meniscus forces. In the case of a spherical surface the two radii of curvature are equal to each other and the Young and Laplace equation becomes:

$$\Delta P = \frac{2\gamma}{r},$$

<div align="right">Eq. 1.3</div>

such that the pressure difference across a flat surface is zero. This highlights the dependence of the capillarity upon the distortion or curvature of the meniscus. An exact solution of the capillarity problem must deal with the deviation of the meniscus from sphericity. Gaydos (Gaydos, 1996) presents a full review of the various curvature measures that have been historically employed to evaluate the degree of surface bending.

One major effect of capillarity is the insurgence of capillary forces. Capillary or meniscus forces originate from the axial component of the surface tension acting at the liquid-gas interface and the Laplace hydrostatic pressure in the interior of the bridge. The former component is positive and attractive, while the Laplace pressure can be repulsive or attractive. It is important to recognise that the Laplace pressure is a consequence and not a cause of capillarity. The primary actions are that of interfacial tension and the forced curvature of the interface. An attractive contribution to the total capillary force is seen to occur if the meniscus surface curvature is negative with respect to the interior of the meniscus (Willet et al., 2000). It is important to note that the cause of capillarity is the attractive or repulsive energy force balance between certain interfaces which causes a curvature of the meniscus and thus a potential energy. This potential energy has a gradient which defines a force. That force spread over a surface is the Laplace pressure – there is no pressure as such within the liquid itself.

The literature about meniscus forces is abundant. Most of the authors are concerned with the

calculation of the meniscus forces between two spherical particles (Figure 1.16) or between a spherical particle and a flat surface (Figure 1.18).
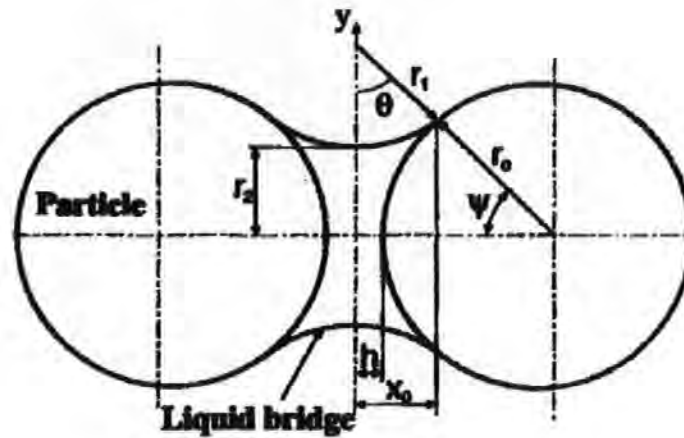
Figure 1.16 - Pendular liquid bridge between spherical particles.

The results of such studies (Muguruma *et al.*, 2000; Willet *et al.*, 2000) can be summarised with the equation:

$$F = \pi r_2^2 \gamma \left(\frac{1}{r_1} - \frac{1}{r_2} \right) + 2\pi r_2 \gamma ,$$

Eq. 1.4

where F, the force between the particles, is related to γ, the surface tension of the liquid and r_1, r_2 the radii of curvature of the liquid bridge surface. The first term represents the resulting effect of the Laplace pressure, while the second term is due to the surface tension. Muguruma *et al.* (Muguruma *et al.*, 2000) try to derive formulae to describe the geometry of a liquid bridge, i.e. the two radii of curvature, as a function of the liquid volume and separation distance between the particles, by approximating the shape of the liquid bridge as an arc of a circle and by considering a contact angle of zero between liquid and particle.

19

By numerical integration of the Laplace equation, Willet *et al.* (Willet *et al.*, 2000) show very good agreement between the capillary force values calculated using the Young-Laplace equation and those measured experimentally between synthetic sapphire spheres.

As Gao *et al.* (Gao *et al.*, 1998) point out, it is also very common to use a simplified approach of considering the meniscus surface as spherical. This approach is practically incorrect, unless the solid bodies are also spherical. They approach the problem of measurement of capillary forces in a different way (Gao, 1997; Gao *et al.*, 1998): they calculate the meniscus force acting between two surfaces having any geometry as the derivative of the total free energy of the liquid-mediated interface $F = -\dfrac{d\Delta E}{dD}$, where ΔE is the total free energy change due to the meniscus formation at the interface and dD is an infinitesimal displacement between the two solid surfaces that form the menisci. This once again requires the meniscus profile to be known. According to Pascal's law for static incompressible fluids, the pressure inside the meniscus has to satisfy this equation:

$$\frac{\gamma_{LV}}{r_m(x,y,z)} + \rho g z = P_d(z+t) - P_d(z),$$
Eq. 1.5

where the first term accounts for the local Laplace pressure due to the local liquid curvature

$$r_m(x,y,z) = \frac{1}{\dfrac{\partial^2 z}{\partial x^2} + \dfrac{\partial^2 z}{\partial y^2}},$$
Eq. 1.6

with $z = z(x,y)$ being the meniscus profile. The second term of Eq. 1.5 is the contribution from gravity, which could be ignored in most microscopic problems, and the right hand term is the disjoining pressure due to surface interactions, which generally decreases with increasing film thickness t. The disjoining pressure (Hirasaki and Yang, 2002) can be defined as the mechanical pressure that would have to be applied to a bulk substance to bring it to equilibrium with a given film of the same substance (Adamson, 1990). The meniscus profile

20

can be spherical only if both gravity and surface interactions can be neglected. The details of the solution to equation Eq. 1.5, presented in Gao *et al.* (1998), go beyond the scope of this study and will not be described, but it is interesting to notice that the calculations presented by the authors make it possible to calculate, with good accuracy, the meniscus forces acting in cases where the spherical meniscus profile approximation is not acceptable (Figure 1.17).
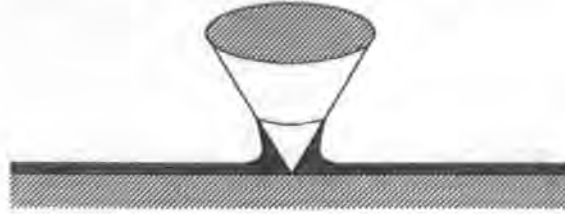
Figure 1.17 - Meniscus geometry between a conical shaped tip and a flat surface.

It is also interesting that in the case of menisci between spherical bodies or between a sphere and a plate, the spherical meniscus approximation is acceptable, as the errors it gives rise to are negligible.

Zhang and Nakajima (Zhang and Nakajima, 1999) studied the way meniscus forces between two spheres, or a sphere and a plate, deviate from the behaviour predicted by capillary theory. They observed that in very small menisci (in the order of magnitude of nanometres in thickness), the capillary forces measured differ from the expected value of $F = 4\pi\gamma R\cos\theta$. This is not due to hydrogen bonding interactions or to short range solid-solid interaction, but to the deformation of the solid surfaces due to the action of the extremely high meniscus curvature, and derived Laplace pressure, which causes a reduction of the meniscus area and further increases its curvature. In order to take into account such deformation, they modify the meniscus force equation:

$$F = 4\kappa\pi\gamma R\cos\theta,$$

Eq. 1.7

21

where

$$\kappa = \cfrac{2}{1+\sqrt{1+8\sqrt{\cfrac{2R}{h}}\left(\cfrac{\beta\gamma}{h}\right)\cos\theta}},$$ Eq. 1.8

$$\beta = \frac{2(\pi-2)}{\pi E^*},$$ Eq. 1.9

with E^* being the composite Young's modulus of the solid surfaces and h is the meniscus thickness before deformation (Figure 1.18).
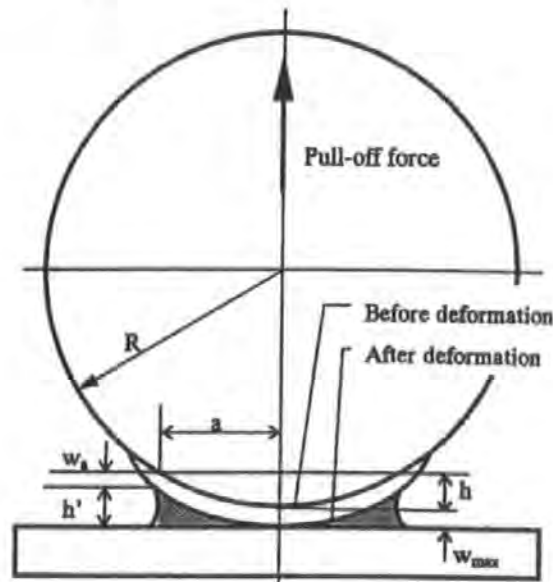
Figure 1.18 - Contact geometry between a sphere and a plane before and after deformation due to the Laplace pressure.

Lucassen (Lucassen, 1992) studied the capillary forces and thus the interaction between two particles whose edges could be represented as a sinusoidal function (Figure 1.19).
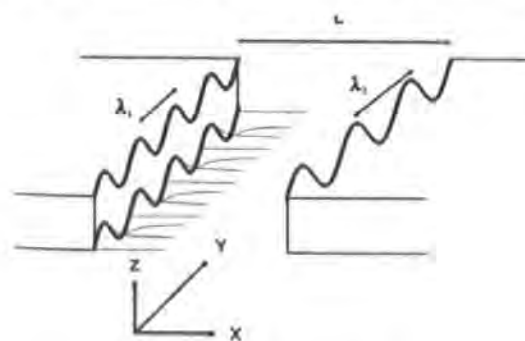
Figure 1.19 - Model system with two interacting particles with edges represented by sinusoidal function.

22

A very interesting conclusion of this study is that the action of the capillary forces between such particles could be either attractive or repulsive according to the amplitude, wavelength and phase of the sinusoidal functions describing the two particles edges.

1.8.3 Porous materials and their modelling (Matthews, 2000)

Porous media abound in everyday use, and also have industrial and engineering importance. Soil science, petroleum engineering, industrial filtration and powder metallurgy are just a few of the many research areas that rely on the study and characterisation of porous media. A porous medium can be defined as a solid body containing voids distributed throughout the material. According to Scheidegger (Scheidegger, 1974) extremely small voids can be called molecular interstices, and very large ones are called caverns. Pores have an intermediate size, between molecular interstices and caverns. The pores can be interconnected or isolated, as shown in Figure 1.20.
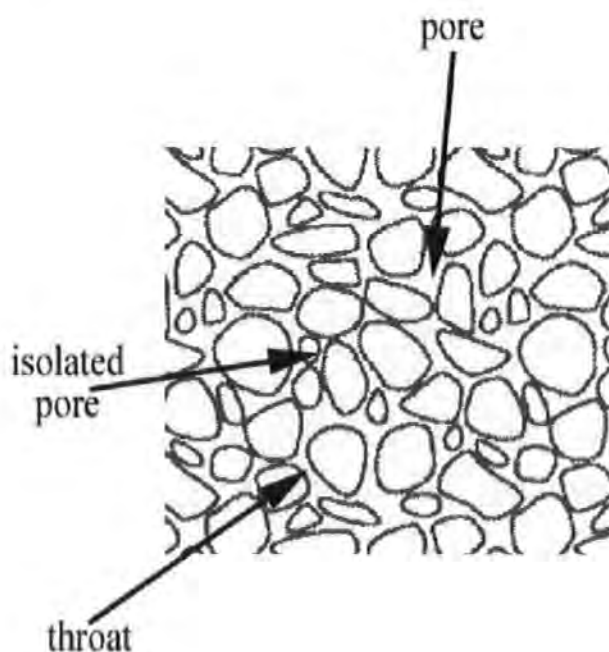
Figure 1.20 - Schematic representation of a porous medium.

As a consequence, the effective porosity of a porous medium to permeation is the void volume (or the volume %) with interconnected pores, and this is typically less than the total porosity. The void space in natural porous media and particulate structures typically comprises larger voids, which have traditionally been called pores, and smaller voids, connecting the larger ones, called throats.

Porosity is not the only parameter used for the characterisation of porous materials: pore size and throat size distribution, surface area, connectivity, tortuosity and permeability are also of fundamental importance. A good schematic representation of different categories of porous media can be found in Schoelkopf (Schoelkopf, 2002) as reproduced in Figure 1.21. Figure 1.21 (1) shows a porous material with isolated pores, while (2) shows a strongly anisotropic structure, similar to Synteape (Section 2.2). In Figure 1.21 (3) and (4) are presented two bundle-of-capillaries structures, having different average pore diameter, but similar porosity. Figure 1.21 (5) shows a structure with no connectivity and high tortuosity, while (6) shows a structure with small connectivity, high tortuosity and highly anisotropic. Figure 1.21 (7) and (8) show pore and throat network structures with different permeability.
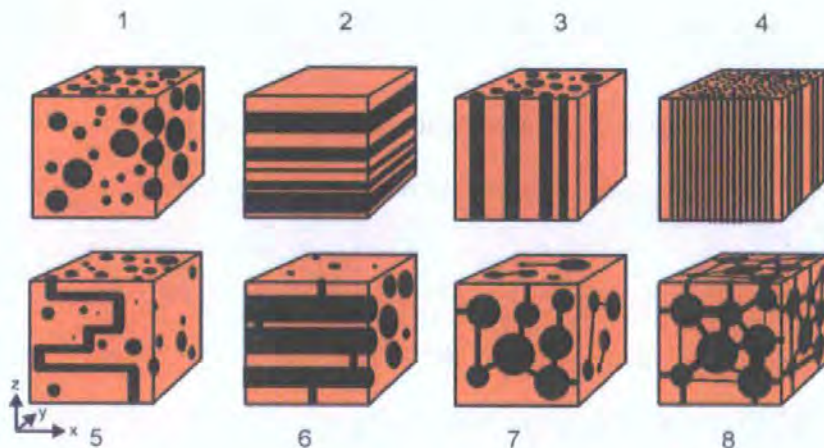
Figure 1.21 - Schematic representation of different types of porous media

24

There are several experimental techniques used to characterise porous materials. The most common is mercury intrusion porosimetry (Webb and Orr, 1997), which has been widely used in this work and will therefore be explained in detail in the next chapter. Another widely used method for the characterisation of porous material is the determination of the surface area by measuring the amount of nitrogen or helium adsorbed by the material. The results are usually analysed using the BET isotherm (from the surnames of its originators, Brunauer, Emmet and Teller (Webb and Orr, 1997). This measurement is conducted in isothermal conditions at cryogenic temperature, usually that of liquid nitrogen at its boiling point (77.35 K at atmospheric pressure).

The modelling of porous materials and their characteristics can follow substantially different approaches. The first approach is the continuum model, in which the porous structure is treated as a bulk, and the physical behaviour of the system is quantified by using bulk parameters, such as diffusion coefficients and permeabilities. These parameters are obtained as a result of phenomenological equations, through assumptions and approximations. These assumptions and approximations, despite being acceptable under the circumstances of each single study, limit the usefulness of such continuum models to a very narrow range of systems, having physical and chemical properties similar to those of the modelled systems.

A second approach is the capillary bundle approximation, where the porous material is assumed to contain aligned, separate capillaries. A typical representation for this type of porous model is shown in Figure 1.21 (3) and (4), and enlarged in Figure 1.22.

25
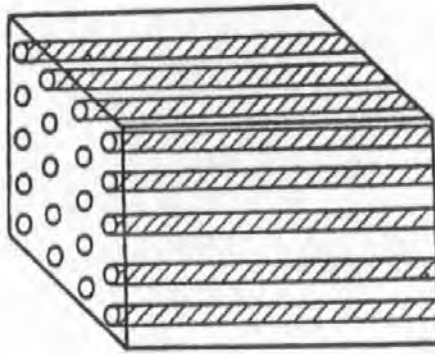
Figure 1.22 - Bundle of capillaries model for porous medium
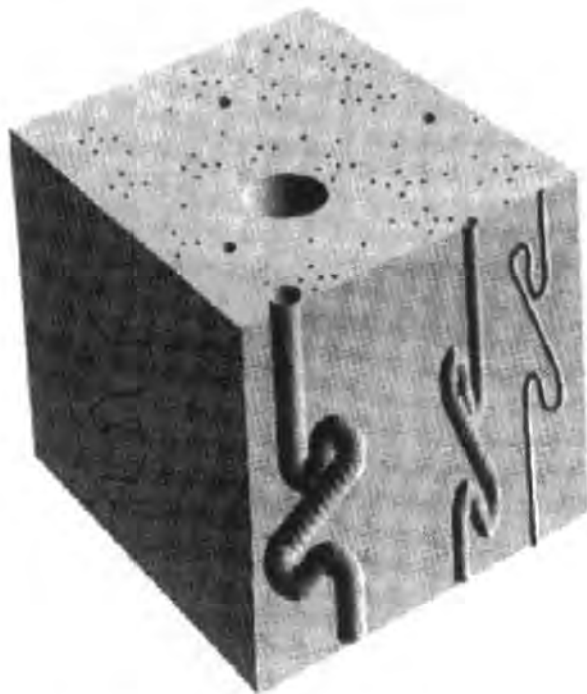
Figure 1.23 - Attempt to describe tortuosity within the one-dimensional model of a porous medium.

A capillary cross-sectional size distribution from an idealised structure such as that of Figure 1.22 can be obtained directly from a mercury intrusion curve. The mercury applied pressure is converted to a "pore" size – actually the size of the entry throat, using the Laplace equation, as discussed in more detail in Section 2.1.1. The pore size distribution for such a model void space is then assumed to be directly related to the first derivative of the mercury porosimetry intrusion curve. This can be converted to throat size distribution and an example of these

results is shown in Figure 1.24. The size distribution in Figure 1.22 corresponds to this, in that no variation in single capillary diameter can be accommodated.
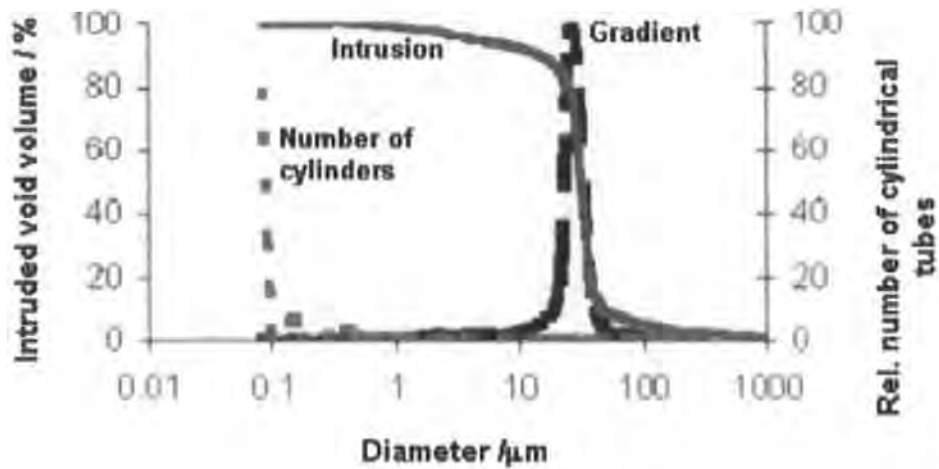
Figure 1.24 - Mercury intrusion curve, its first derivative and the corresponding pore size distribution.

It can be seen that the volume intrusion contribution artificially results in a distribution of capillary sizes that is unrealistically skewed to the small range of diameters. In reality, the pore voids are much larger. This is due to the well-known shielding effect in real porous media, (Webb and Orr, 1997), with large pores being shielded by smaller voids (throats) during the mercury intrusion process.

Figure 1.21 (5) and Figure 1.23 shows an attempt to describe the tortuosity of porous material, within a one-dimensional model of a porous medium.

The final type of approach in the modelling of porous material is the three-dimensional network modelling of the porous structure. An example of this approach can be found in the work of Pan *et al.* (Pan *et al.*, 1995), who created such a model in order to describe the migration of binder within the porous network of a paper coating, as shown in Figure 1.25.

27
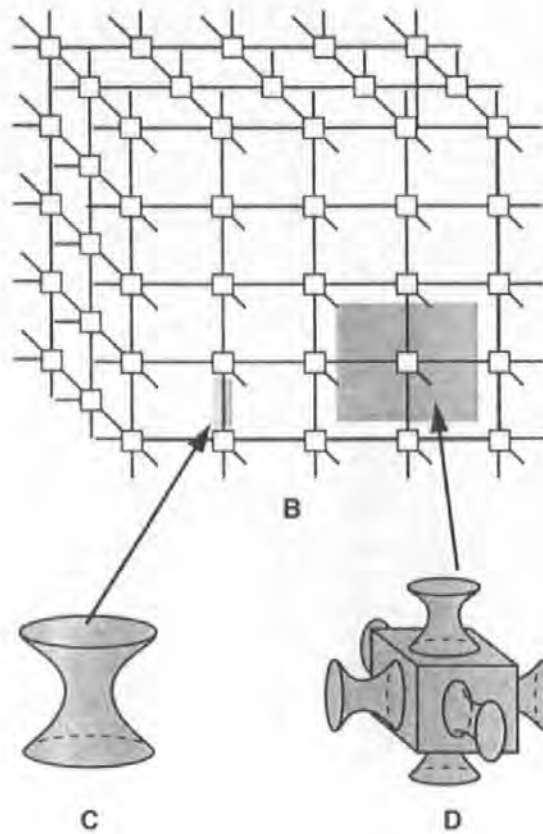
Figure 1.25 - Three-dimensional network model of a porous material (according to Pan *et al.*, 1995).

Such a model has limitations: the connectivity of the structure is fixed with a value of 6, which means that each cubical pore is connected to another pore by six throats, and the pore size distribution is completely arbitrary.

Toivakka and Nyfors (Toivakka and Nyfors, 2000) presented an attempt to describe the void space in a porous material by means of image analysis of the modelled cross-section of the material itself. They illustrated their work using a packing model of spheres and identified the pores and throats by an erosion algorithm as shown in Figure 1.26, where each successive erosion is represented by a darker colour.
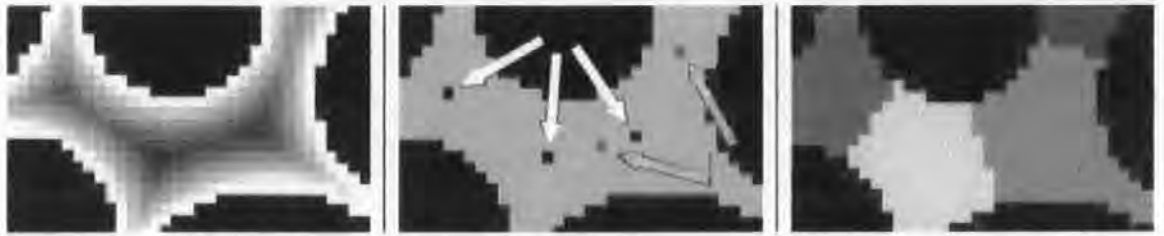
Figure 1.26 - Pore identification from a two-dimensional image and erosion of the pore space as presented in Toivakka and Nyfors (2000).

The darkest point in the void space represents the centre of a pore or a throat. Toivakka *et al.* applied their analysis to a variety of different packings of spheres (cubic, hexagonal and random) and the results for the random packing of mono-sized spheres are presented in Figure 1.27. It is obvious that such a model, though elegant in principle, has very limited use, as its application is confined to particular computer-generated packing of spheres and not real porous samples.

One of the limits of this technique in reality is the thickness of the slices of a real sample that can be studied by image analysis and then by the erosion algorithm. Even with modern techniques it is impossible to cut slices thinner that ~5 μm, which in the case of a paper coating could represent the actual thickness of the entire coating layer. It is also impossible to calculate the connectivity in the vertical direction, unless arbitrary rules are chosen for boundary and overlap conditions between the different slices.

a)

b)

c)
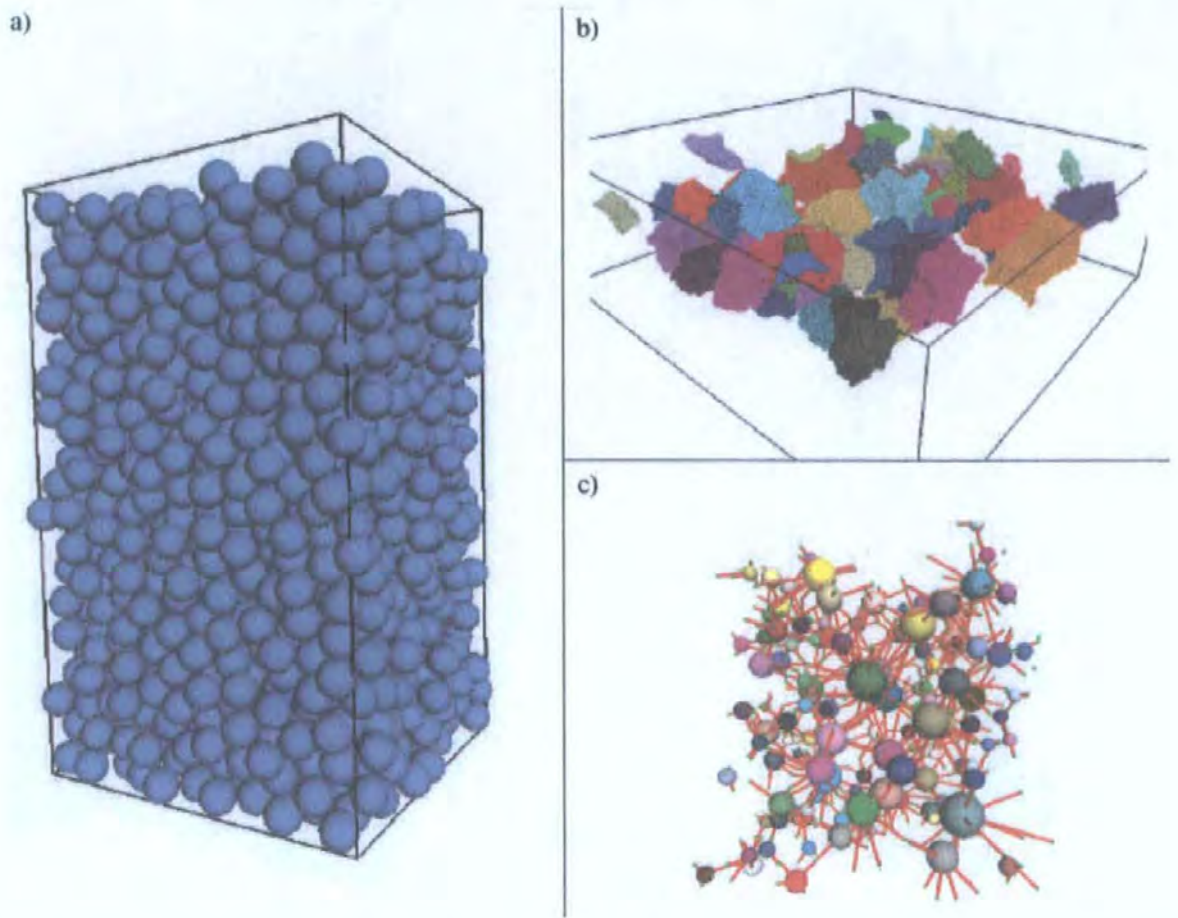
Figure 1.27 - Toivakka *et al.* (Toivakka and Nyfors, 2000) model monodispersed random packing of spheres (a), the pore space (b) and the inter-void connections (c).

Other workers (Knackstedt *et al.*, 2000; Niskanen *et al.*, 1999) focused their attention on computer models able to simulate the fibrous structure, which could be used to model the physical properties of uncoated paper. Examples of the structures generated by these models can be observed in Figure 1.28.
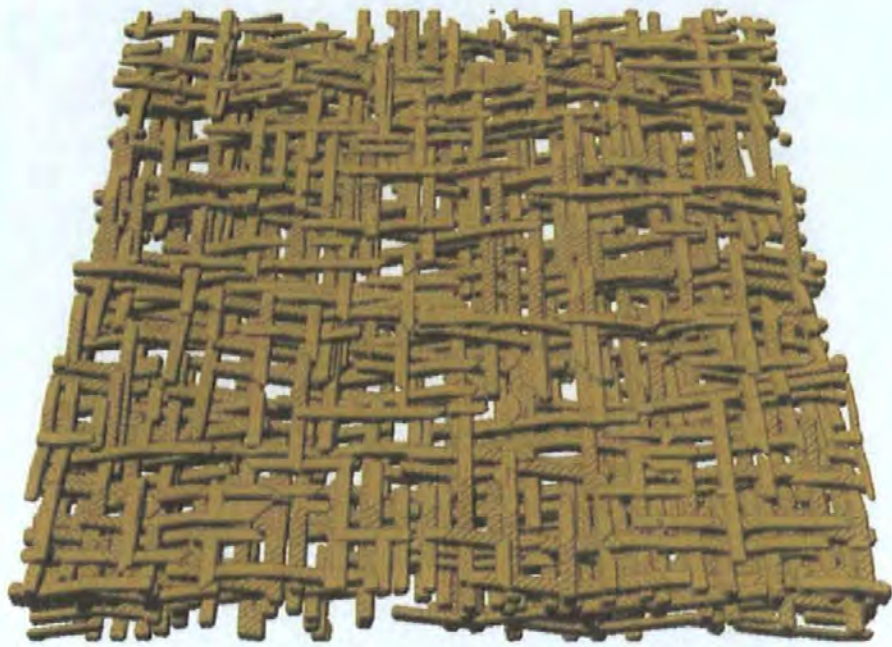
Figure 1.28 – Modelled fibrous network.

The Environmental and Fluid Modelling Group of the University of Plymouth has developed Pore-Cor, a network simulation software, which uses a different approach for the modelling of the void space in a porous material. Despite being limited to a very simplified geometry for the description of pores and throats, this model has the advantage of being free from the arbitrary choice of values for the typical parameters describing the porous material, which is the main problem of the models cited above. As this computer model has been widely used and partly improved as part of this research project, a full description of Pore-Cor will be given in chapter 5.

1.8.4 Fluid motion through porous media

1.8.4.1 Darcy's law and permeability of saturated structures

The phenomenological law presented by Henry Darcy in 1856 was based on his studies on the flow of water through granular media, used as filters in the water distribution system of the French city of Dijon. It states that:

31

$$q = \frac{K \Delta p}{L},$$

Eq. 1.10

where q represents the flow rate (m s^{-1}) through the porous bed, Δp is the hydrostatic pressure difference across the porous bed, L is its length and K is a constant depending on the properties of the fluid and the porous medium. The permeability is defined as:

$$k = K \eta,$$

Eq. 1.11

where η is the fluid viscosity. Permeability is measured either in area units or Darcy (1 Darcy = $9.87 \cdot 10^{-13}$ m^2).

1.8.4.2 Permeation

The motion of a viscous incompressible fluid through a cylindrical tube can be described with the Hagen-Poiseuille equation:

$$Q = \frac{\pi \Delta p \, r^4}{8 \, h \, \eta},$$

Eq. 1.12

where Q is the volume flow rate passing through the cylindrical tube of radius r and length h, with a pressure difference from end to end of Δp.

If a porous medium is represented as a bundle of straight capillaries, as in Figure 1.22, with n capillaries per unit of cross sectional area, the flow per unit of area through the porous medium will be, according to the Hagen-Poiseuille equation:

$$q = \frac{n\pi d^4}{128\eta}\frac{dp}{dx},$$ Eq. 1.13

where $\frac{dp}{dx}$ is the pressure gradient across the capillaries. But, according to Darcy's law, the same volume flow rate per unit of area is given by $q = \frac{k}{\eta}\frac{dp}{dx}$. It follows that

$$k = \frac{n\pi d^4}{128}.$$ Eq. 1.14

If d is an average value if pore diameter for the porous medium, Eq. 1.14 can also be expressed in terms of porosity ϕ as:

$$k = \frac{\phi d^2}{32}.$$ Eq. 1.15

This is obviously a very simplified model of permeation through porous media and its results have to be often corrected to take into account tortuosity and other factors. A full description of these correction terms and their justifications can be found in Bodurtha (2003).

The permeability of pigmented paper coating layers has been studied by Schoelkopf *et al.* (Schoelkopf *et al.*, 2003). The permeability, measured experimentally by the authors, is seen under certain conditions not to obey the linearity of the Darcy relation as a function of applied liquid pressure differential (Figure 1.29). This it is argued is due to incomplete saturation during the initial imbibition phase of the experiment, caused by inertial selection of preferred pathways during absorption.
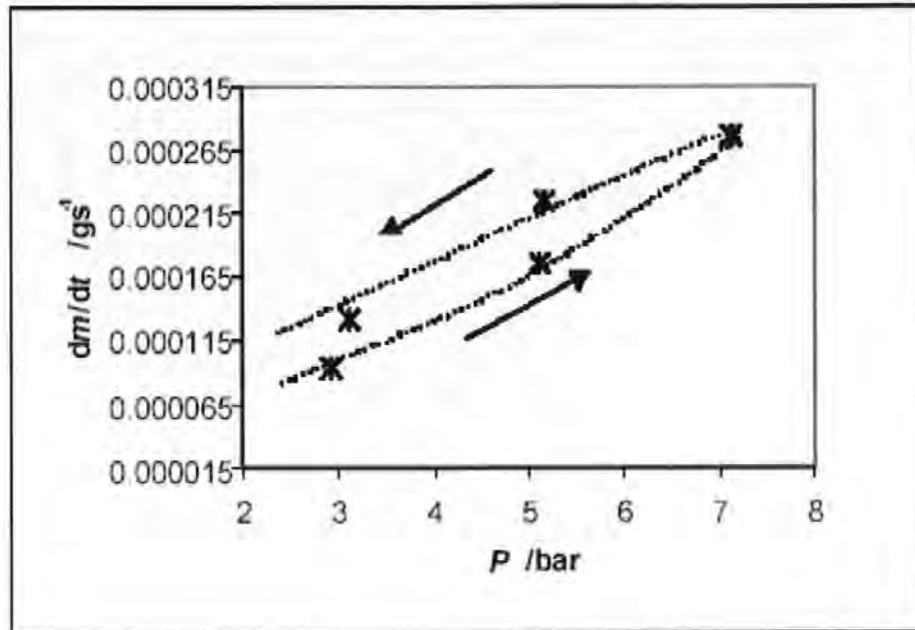
Figure 1.29 - Hysteresis of the permeation flow as a function of applied pressure.

They also observe that there is no direct linear correlation between porosity of their samples and their permeability.

1.8.4.3 Dynamic fluid motion during absorption into porous media

The equilibrium fluid motion during absorption into a capillary tube, under the action of the imbibition force, can be described to a first approximation by incorporating the Laplace equation with the Poiseuille equation for laminar flow.

The result of this formulation is the Lucas-Washburn equation:

$$x^2 = \left(\frac{rt}{2\eta}\right)\gamma_{LV}\cos\theta,$$ Eq. 1.16

where x is the distance travelled by the liquid front at the time t in an horizontal capillary tube.

The $\sqrt{t}$ proportionality of the Lucas-Washburn equation is adequate to describe the dynamic fluid motion in porous media at long time-scale, but the assumed parameters of interfacial

34

tension and pore radius are not adequate when considering the pore networks in real porous media. At each change of geometry or dimension, there are short term phenomena occurring within the network imbibition. Under these circumstances for selected pores, an imposed $\sqrt{t}$ dependence of the wetting front matches neither the experimental measurements of the surface interfacial energy nor the pore sizes (Schoelkopf et al., 2002). By adding the effect of inertia of the fluid mass, Bosanquet (Bosanquet, 1923) derived an equation describing the movement of the wetting front in a capillary at short time-scales, in which the greater accelerated mass of liquid entering a large pore leads initially to a retardation of imbibition. The Bosanquet equation can be derived by a force balance equation (Eq. 1.17), between capillary, inertial, viscous forces and applied external pressure:

$$\frac{d}{dx}(\pi r^2 \rho x \frac{dx}{dt}) + 8\pi\eta x \frac{dx}{dt} = P_a \pi r^2 + 2\pi r \gamma \cos\theta .$$ Eq. 1.17

After approximations assuming continuity in the limit $t \to 0$, and with no external pressure applied (P_e=0), it was shown by Schoelkopf et al. (Schoelkopf et al., 2000) that Eq. 1.17 yields:

$$x^2 = \frac{2\gamma \cos\theta \ t^2}{r\rho},$$ Eq. 1.18

as the major term in a Maclaurin expansion, which applies preferentially to the finest pores. The authors refer to this as inertial plug flow filling of the finest low aspect ratio pores, which, together with the inertial retardation in the larger pores, leads to a preferred pathway flow driven by the interconnection of fine pores with larger reservoir pores. It is important to recognise that in volume terms at equilibrium this still reflects a $\sqrt{t}$ dynamic, due to overall effective viscous drag, but significantly alters the pore size dependence of imbibition.

This approach is highly relevant to the paper coating industry because processes such as printing occur over an extremely short time-scale, and longer term absorption phenomena

35

involved in ink drying are also strongly related to pore size distribution and connectivity, in which preferred-pathway dynamics prevail. Such dynamics have been extensively investigated by Schoelkopf, Ridgway and Gane (Gane *et al.*, 2000; Schoelkopf *et al.*, 2001; Schoelkopf *et al.*, 2002; Ridgway and Gane, 2002) and it has been found to give results in accord with experimental measurements.

1.8.5 Particles - size and shape

The sizes of particles play a very important role in the rheology of a coating formulation, in the packing and structuring of the coating layer and, therefore, in the final appearance and printability of the paper coating layer. The distribution of particle sizes can be investigated using various techniques. The most appropriate, but at the same time most expensive and time consuming, would be image analysis, which would allow the study of both particle size and shape. Other more rapid methods used in particle size analysis are based on sedimentation and dynamic or low angle static light scattering. In the first two techniques the particle size is measured as an equivalent spherical diameter, which is that diameter of a spherical particle showing the same behaviour, relative to the technique in use, as the real particle.

The sedimentation method is based on Stokes' law, which relates the equilibrium velocity, u, of the particle having mass m and diameter d, through a fluid of viscosity η, under the action of the force of gravity:

$$m\,\mathbf{g} = -3\,\pi\,\eta\,d\,\mathbf{u}\,.$$ Eq. 1.19

By measuring the time necessary for the sedimentation of a particle, its equivalent spherical diameter can be calculated. The validity of this technique is strongly limited by the size of the particles under examination. For particles with diameters of 0.2 µm or less, random Brownian

36

motion will start to play a significant role (Allen, 1981), making sedimentation measurements irreproducible.

In all methods described, the shape of the particle is a very significant factor. In low angle light scattering, for example, the scattering pattern is well-defined only in the case of perfectly spherical particles.

The particles of many mineral pigments, as pointed out in section 1.8.5, are not spherical and their shape is defined in terms of aspect ratio. For platey particles, like kaolin or talc, the aspect ratio is the ratio of the diameter across the face of the particle to the thickness, while in the case of needle-shaped particles, like aragonitic PPC, the aspect ratio is the ratio of the length to the diameter.

In Jennings and Parslow (1988) a method is presented for the evaluation of the shape factor of platey and needle-like particles. The results of two different size-measuring instruments are compared, based respectively on sedimentation and light scattering. A mathematical model is then used, which uses oblate spheroids to represent platey particles and prolate spheroids (Figure 1.30) to represent the needle-like particles. This approach was also used in a recent study by Lohmander (Lohmander, 2000a).
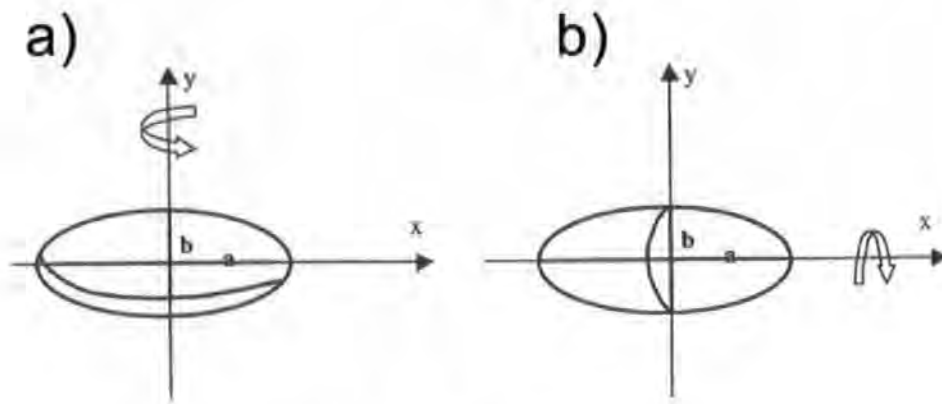
Figure 1.30 - Oblate (a) and prolate (b) spheroids.

1.8.6 Evaporation in porous media

Evaporation and other transport phenomena in porous media can be studied by two different approaches: the *continuum* and the *discrete* approach. The continuum approach to the evaporation from porous media is simpler, but its results often do not match or explain some of the experimental observations. It is also impossible to predict the heat and mass transfer coefficient, needed by the continuum approach, which must therefore be obtained experimentally obtained for each different situation.

The network approach is based on a representation of the pore space as a network of interconnected pores and throats. An interesting study of evaporation from capillary porous media can be found in the studies by Laurindo and Prat (Laurindo and Prat, 1996; Laurindo and Prat, 1998a; Laurindo and Prat, 1998b). They study evaporation as a displacement between two immiscible fluids. As evaporation results in the invasion of the medium by a non-wetting phase (vapour), the similarity with drainage is evident. They create a two-dimensional network model, trying to describe isothermal evaporation, controlled mainly by mass transfer (ignoring the heat transfer) and neglecting the viscous forces (which is acceptable if the evaporation is slow). In terms of drying rate their model agrees with the experimental observations only on a qualitative level, as the drying is significantly faster in the experiments

38

due to the presence of liquid films that the model neglects. In terms of phase distribution the model gives results consistent with the experimental ones.

1.8.7 Consolidation of paper coating and binder migration

The structure of a pigmented coating layer influences all the properties of the final product, such as the ink receptivity and the gloss. It is therefore essential to understand what happens during the process of drying and consolidation of a paper coating. Despite the importance of a full understanding of the consolidation process very few studies on the subject have been published. An attempt to follow this process of consolidation has been made by Watanabe and Lepoutre (Watanabe and Lepoutre, 1982) who followed the drying of a paper coating based on clay and latex by gloss and diffuse reflectance (light scattering) measurement, and by electron microscopy analysing the coating by freezing it at various stages. Their experiments showed that, after a certain drying time, the gloss of the coating layer drops sharply when the water film on the surface of the drying coating layer ceases to be continuous and menisci form on the surface. As the drying proceeds, the reflectance of the coating sharply increases and, at the same time, the gloss reaches a constant value. Such a sharp increase in diffuse reflectance can be explained in terms of air entering the structure. The results can be represented in terms of gloss or diffuse reflectance vs. solid volume content %, and the trends are shown in Figure 1.31.
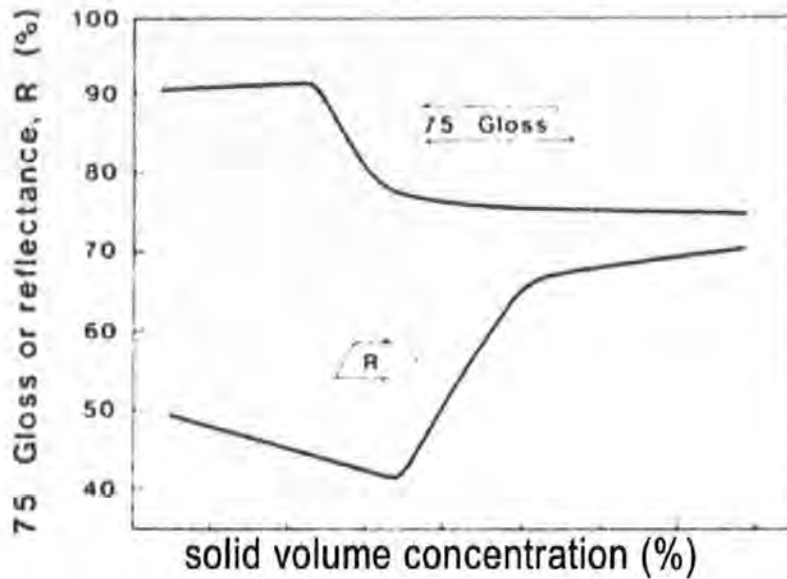
Figure 1.31 - Coating gloss and diffuse reflectance as a function of the solid volume concentration in the wet coating. The top curve represents the gloss of the sample and the bottom one represents its reflectance. "75 Gloss" refers to the Tappi Hunter Gloss measurement using a grazing angle of 75° to the coating surface.

On the basis of these experimental results, the authors describe the drying process as consisting of three phases, separated by two critical concentrations. The application of the coating is followed by a first phase of water evaporation at the liquid-air interface. This phase is unaffected by the solid content in the liquid phase. At the *first critical concentration* (FCC), a three-dimensional network is formed and particle motion is greatly restricted. The water-air interfaces recede into the surface capillaries, creating a capillary pressure that causes shrinkage of the network. This goes on until the *second critical concentration* (SCC) is reached: the network is fixed and air enters the rigid structure. They used both filming and non-filming latex observing that:

- the solid volume concentration at the FCC for filming latex-based coating colours is larger than that of the non-filming latex (61.5 % vs. 58.0 %)

- the solid volume concentration at the SCC is much larger for filming latex-based coating colours than for non-filming ones (79.0 % vs. 64.0 %)

40

- the difference in solid volume concentration between FCC and SCC is much larger in the case of filming latex.

- the final gloss and porosity of the coating layer containing a film-forming latex is less than that of a coating colour containing non-filming latex.

They explain this phenomenon by taking into consideration the rigidity of the latex polymer: as the surface tension of water within the surface capillaries acts as a compressive force, the soft latex particles which are squeezed between the clay particles can absorb the compressive force by deforming. The latex coalescence has been observed to take place over a relatively narrow concentration range after the FCC and is completed at the SCC. The shrinkage that occurs between the FCC and the SCC was much larger for the filming latex because it is associated with the phenomenon of coalescence and flow of latex polymer.
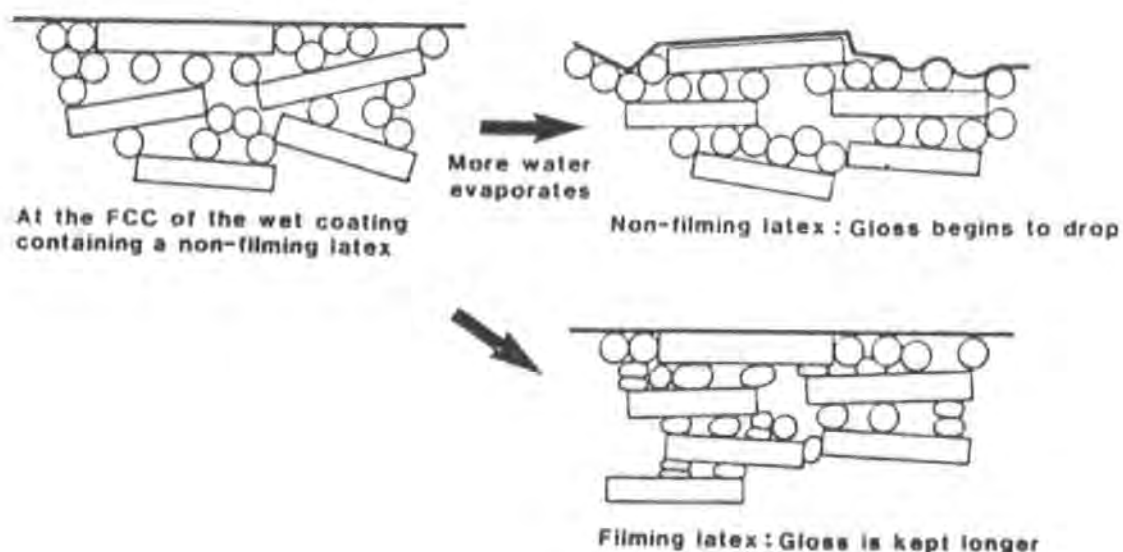
Figure 1.32 – Schematic representation of a clay-latex network at and beyond the FCC.

The authors also focused their attention on binder migration. They observed that the amount of binder in the top 10 % of the coating layer can increase at low solid content, when compared with the latex content of the coating colour bulk. It reaches the bulk value when the solid content in the drying coating layer reaches the FCC. This implies that the binder, according to

41

Watanabe and Lepoutre, can migrate toward the surface, along with the evaporating water, and toward the absorbing paper substrate, only before the FCC has been reached. After the FCC, the movement of latex particles within the network structure becomes impossible. These measurements were carried out by ashing the top section of the coating layer and analysing its carbon content. This technique, as explained by Groves *et al.* (Groves *et al.*, 2001) and later on in this section, is of questionable validity as carbon content measurement does not only indicate binder but also soluble polymers such as non-adsorbed dispersant.

Pan, Davis and Scriven (Pan *et al.*, 1995) created a model to describe the moisture distribution and soluble binder migration in drying paper coatings. They modelled the consolidated paper coating as a three-dimensional network of 1000 pore bodies and interconnecting throats, as previously described in section 1.8.3 and shown in Figure 1.25. In order to describe the distribution of the binder and of the moisture, they used equations describing the pore-level physics of the water flow (capillary forces), vapour diffusion and binder transport and deposition. In particular the binder transport in the coating is characterised by two dimensionless numbers: a capillary number (Ca), that describes the competition between capillary driving force and viscous resistance to flow, and a Peclet number (Pe) that describes the competition between convection toward and diffusion away from evaporating pores. These numbers are related to the drying rate and binder diffusivity. This model has not been tested in a quantitative way by its authors and therefore its results cannot be validated against experimental results.

Bernada and Bruneau (Bernada and Bruneau, 1997; Bernada and Bruneau, 1996) created another model to describe the drying of a paper coating, focusing their attention on the migration of water soluble binders. Their model is based on diffusive liquid transport, and

takes into account the shrinkage of the coating and the migration of the different solid components during drying. They divide the drying processes into three phases: liquid, gel and solid, similar to Watanabe's phases. The modelling results are compared with experimental results obtained with an experimental device to simulate the de-watering (water penetration into the base sheet) of the coating during the drying process (Figure 1.33).
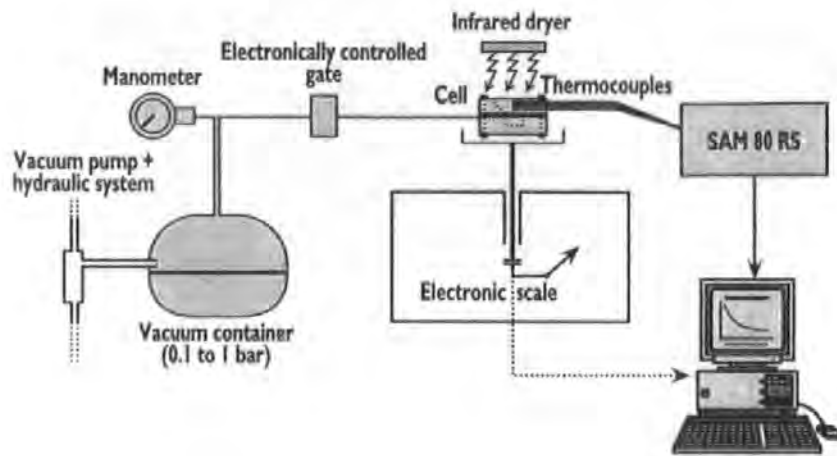
Figure 1.33 - Experimental device used in order to simulate the dewatering of the coating through the base sheet.

The results of their model show that the migration of water soluble binder continues long after the FCC (in opposition to the latex migration, which stops at the FCC, as shown by Watanabe and Lepoutre). The major limit of this model is that the set of equations used to describe the mass balance for the species in the coating colour, and their diffusive motion within the coating colour formulations, is solved using a set of semi-empirical parameters. Another problem of this study is that a latex–starch blend has been used in the coating formulations, making it impossible to distinguish between the effects of the two different binders.

In an extensive experimental work, Groves and Lanham (Groves and Lanham, 1991) studied the influence of latex on the final coating structure. They studied the effect of the amount of

latex in the coating colour formulation, of the drying temperature and of the coating thickness, focusing their attention on volumetric shrinkage, porosity, binder migration and ink absorption of the final coating colour. In order to minimise the number of unknown factors in the system, they decided to use a laboratory-prepared carboxylated styrene-butadiene (SBR) latex with known composition, instead of a commercial one. Their experiments show that keeping constant the amount of latex in the coating colour formulation, and increasing the thickness of the coating layer, causes a reduction in void volume and in ink absorption. They also observed that by drying the samples at lower temperature, the final porosity and ink absorption of the coating layer increases. Another interesting result is that an increasing amount of latex in the coating colour formulation causes an increasing volumetric shrinkage of the coating upon drying. This occurs up to a limiting value of latex content, above which the shrinkage remains constant (Figure 1.34).
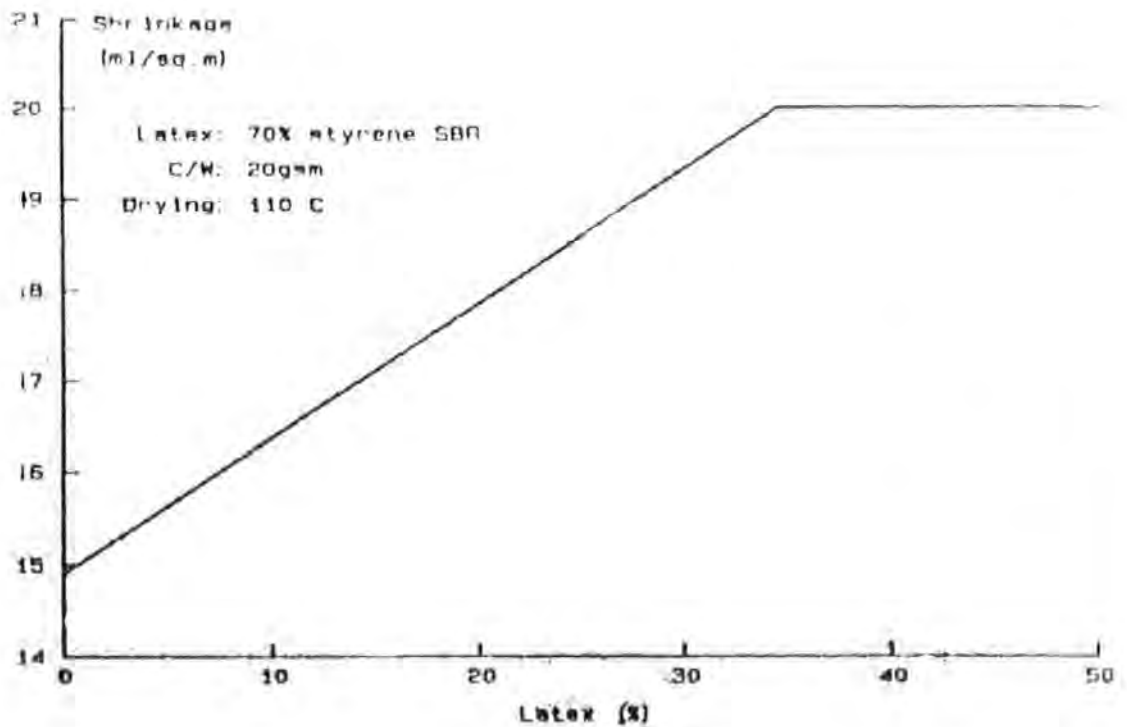
Figure 1.34 - Volume shrinkage of coating on drying as a function of latex level, expressed in w/w% (Groves and Lanham, 1991).

44

As the authors of this work point out, the role and behaviour of latex upon drying of a paper coating layer is not clear. Two hypotheses can be made: one is that the binder acts simply as a void filler, replacing air within the pigment structure, but without changing the structure itself. The other is that well-coalesced, void-free latex micro-domains form, dispersed within the pigment matrix. The experimental void volume of the coating layer does not follow either of these hypotheses, as shown in Figure 1.35.
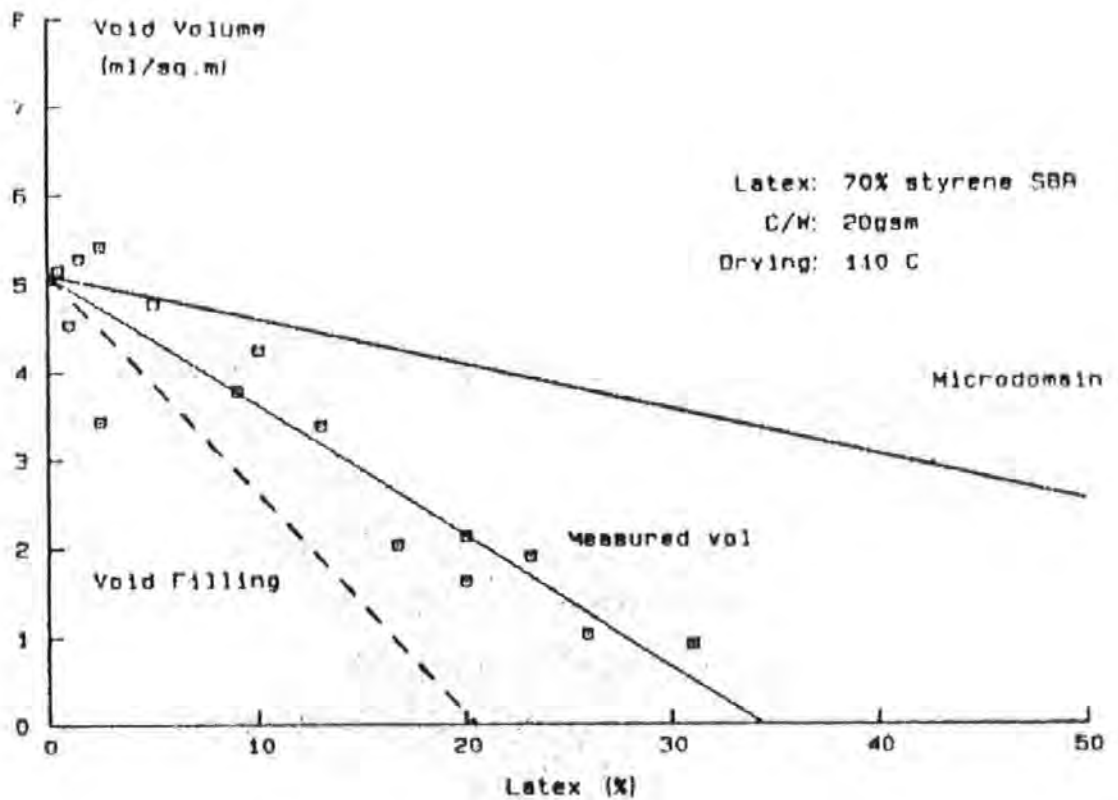
Figure 1.35 - Theoretical void filling, theoretical microdomain and experimentally measured voids as a function of latex level, expressed in w/w% (Groves and Lanham, 1991).

These theories also fail to explain the reduction in volumetric shrinkage for a thinner coating layer and for a lower drying temperature. The authors suggest that the shrinkage of the coating layer is mainly caused by shrinkage of the latex upon drying and that different drying conditions can affect the extent of such latex shrinkage. They also hypothesise that the latex and pigment interact in the wet state, causing a flocculation effect, which, in turn, causes an

45

expansion of the coating structure. However, the results of their experiments are not conclusive. Also the measurements of binder concentration at the surface of the coating layer do not prove the existence of binder migration upon drying of the coating colours.

A similar study has been carried out by Xiang and Bousfield (Xiang and Bousfield, 2001), who studied the effect of coat weight and drying conditions on the final porosity and ink absorption of the coating. They wished to find a relationship between the amount of coating applied and the drying temperature, and the appearance of non-uniform coating surface which can lead to backtrap mottle, a major printing problem. The results of their experimental work show that paper coating porosity and ink receptivity decrease as the coating layer thickness increases, while the different drying conditions do not seem to affect the final properties of the coating layer. The authors of this work explain the different results for different coating thickness in terms of different packing of the system particles upon drying. With a low coating thickness, and, as a consequence, a low coating weight, the water is rapidly removed from the coating by the absorbing paper and a filtercake is formed, without enough time for further orientation of the pigment particles (kaolin was used). The structure of this filtercake tends to reflect that of the original suspension, as it is applied on the base sheet, with a random orientation of the particles and, hence, a more open structure. If, on the other hand, the coating layer is thicker, the flow of water to the base paper is slower, due to higher resistance to such flow in the forming filtercake. This makes it possible for the particles to rearrange for a longer time, creating a more efficiently packed structure, with lower porosity and lower permeability.

In another very extensive study, Groves *et al.* (Groves *et al.*, 2001) studied the effect of drying conditions and dewatering on binder migration. In the first part of this publication the authors focus on the different methods and techniques used in the past to investigate the migration of

46

binding systems upon drying, pointing out the weaknesses and strong points for each. The authors then present the results of several drying experiments carried out on a thick coating layer (2.5 mm), when compared with the average industrial coating thickness of about 10-20 μm. The drying process has been carried out at different temperature and in different conditions: by evaporation only, or simulating the dewatering in a pressure cell similar to that of Bernada (Bernada and Bruneau, 1997). The results of this study show a great difference in the behaviour of starch and latex. No evidence of the latex migration on the surface of the coating has been found, while a significant surface enrichment of starch, in the case of evaporative drying, or a significant loss of starch, in the case of dewatering simulations, has been shown. It has been seen also that an increased concentration of water-soluble species (surfactants and dispersant) flows at the surface of the coating. In earlier studies, this might have been incorrectly interpreted as the result of latex migration. However, Groves *et al.* conclude that the migration can occur only for water soluble species; latex particles, whilst remaining particulate, cannot migrate as they are trapped within the network structure formed by the pigment particles. The authors also propose a simple model describing the migration of soluble species, taking into account only the rates of water removal and diffusion of the soluble species. They treat the binder migration as a one-dimensional convection/diffusion problem. The drying coating layer is approximated to 10 infinitely wide sheets of finite thickness (Figure 1.36).

Water evaporates at surface.
Evaporation is zero if the surface is covered.

Top surface

Sheet 0

x=0

Starch undergoes convection and diffusion from layer to layer

Sheet *i*   Sheet thickness h_i Clay does not move from its original layer

Water moves from layer to layer in response to the evaporative loss of water from the top layer

As a layer loses water, it shrinks. The shrinkage is expressed as a function of the water content of the layer

Sheet *l*   x=h_0+h_1+...+ h_i +... + h_l

Bottom surface

Figure 1.36 - Mathematical model of starch migration.

The boundary condition for the water evaporation at the surface layer is:

$$-D_s \frac{\partial w_0(t)}{\partial x} = \alpha(w_0(t) - w_a),$$ Eq. 1.20

where $w_0(t)$ is the concentration of water in the surface layer at time t, w_a is the concentration which would be in equilibrium with the vapour pressure in the atmosphere remote from the surface, D_s is the surface diffusion coefficient and α is a coefficient which quantifies the efficiency of the evaporative process, and x as in Figure 1.36. The solution of the equation describing the diffusion of a species in a semi-infinite composite material during the time step Δt is:

$$\frac{w(t+\Delta t) - w_0(t)}{w_a - w_0(t)} = \text{erf} \frac{x}{2\sqrt{D_s \Delta t}} - \exp(hx + h^2 D_s \Delta t)\text{erfc}(\frac{x}{2\sqrt{D_s \Delta t}} + h2\sqrt{D_s \Delta t}),$$ Eq. 1.21

where $h = \frac{\alpha}{D_s}$.

The model also allows the calculation of the starch concentration in each of the layers. By running the simulation with one hour time-steps the results of the simulation and the experiments are very close, as shown in Figure 1.37.

48
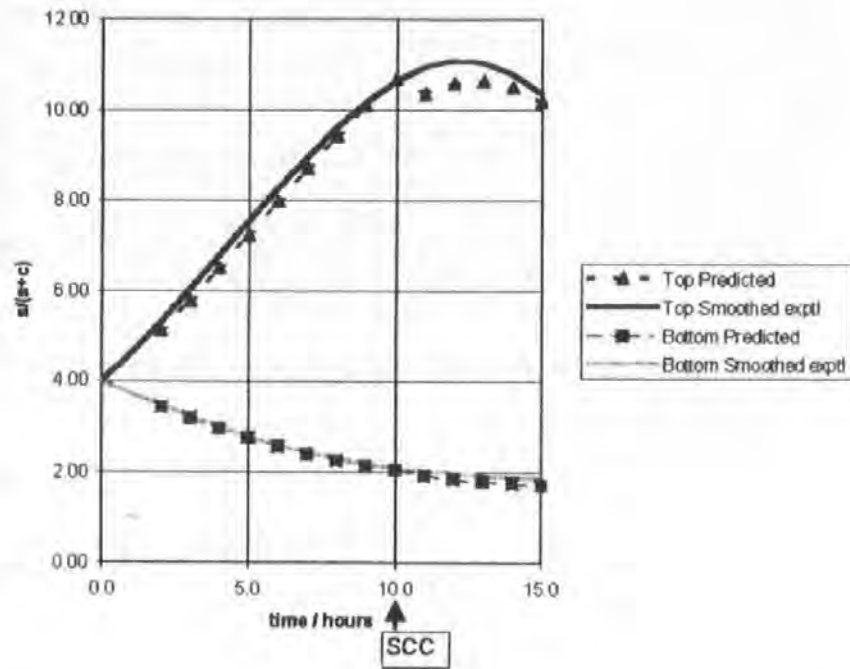
Figure 1.37 - Comparison of experimental and predicted starch/starch+clay ratio in the top and bottom layers of the coating.

This seems to support the authors' hypothesis of a diffusion driven migration of the water soluble species in a coating colour formulation.

1.8.8 Rheology

1.8.8.1 Viscosity

Viscosity is the measure of the internal friction of fluids. The model in Figure 1.38 represents two plates of area A, a distance dx apart, separated by fluid (the actual apparatus is described in Section 2.1.3). When a force F is applied to the top plate, the two plates will move parallel to each other with a relative speed dv.

49
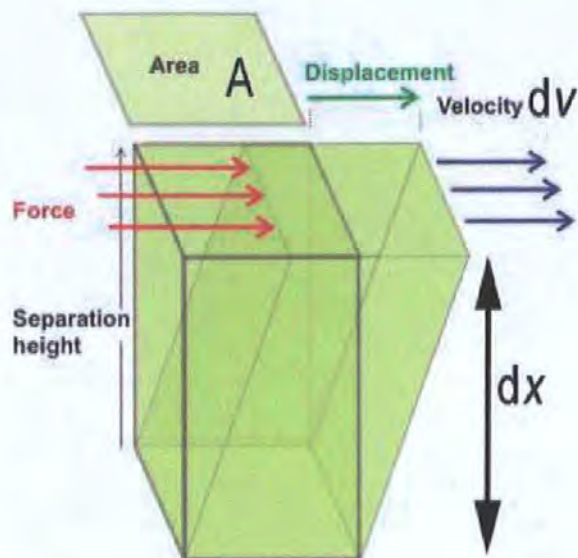
Figure 1.38 - Viscosity.

The force per unit of area required to make the displacement is called shear stress τ and its effect is the amplitude of displacement or shear strain γ, representing the displacement per unit of height. The rate of change of shear strain, $\dot{\gamma}$, is therefore the velocity per unit of height dv/dx. For Newtonian liquids under isothermal conditions, the shear stress is proportional to the shear rate for all stress/strain conditions. For viscoelastic or pseudo-plastic materials (discussed in more detail below), the proportionality is valid only over infinitesimal rates of change. The proportionality constant for the Newtonian case is called the shear viscosity η and for the non-Newtonian case the complex or dynamic viscosity μ^*. These values represent the tendency of the fluid to resist flow.

Shearing of a fluid occurs whenever the fluid is physically moved or distributed, as in mixing, spraying or spreading; hence the importance of this parameter for the paper coating industry. Newtonian fluids in the paper coating industry are a rare exception. Most formulations are highly viscoelastic and show a distinct progressive reduction in viscosity as they are initially

50

sheared, exhibiting on occasion a further disruption of packing uniformity at high shear rates, known as dilatancy, resulting in large increases in viscosity.
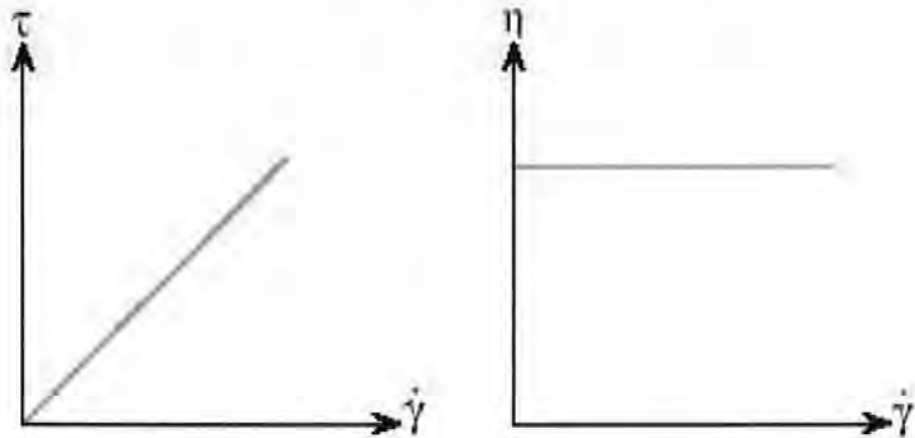
Figure 1.39 - Newtonian behaviour.

Due to the large range of behaviours possible it is worthwhile to list them here. The viscosity of a fluid can be affected both by its temperature and by the applied shear rate. There are several types of non-Newtonian behaviour:

- Pseudoplastic fluids display a decreasing viscosity for increasing shear rate and their behaviour is also called shear-thinning (typical of many paper coating colours).

- Dilatant fluids are shear thickening, as their viscosity increases for increasing shear rates. This is usually an indication of problems, if this phenomenon occurs at solids contents typical of those during application of the coating colour onto the base paper.

- Plastic fluids behave as a solid under static conditions and a certain amount of strain must be applied to the fluid in order to produce viscous flow. Once the fluid starts flowing it can show Newtonian, pseudoplastic or dilatant behaviour.

51
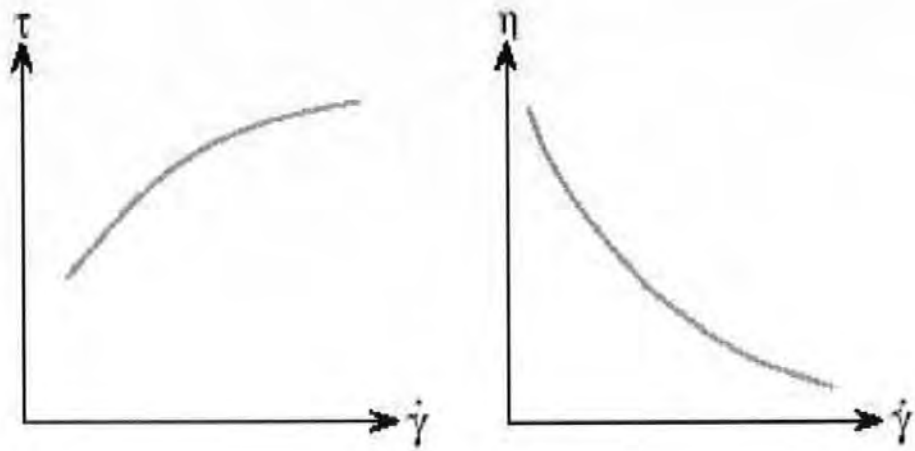
Figure 1.40 - Pseudoplastic behaviour.
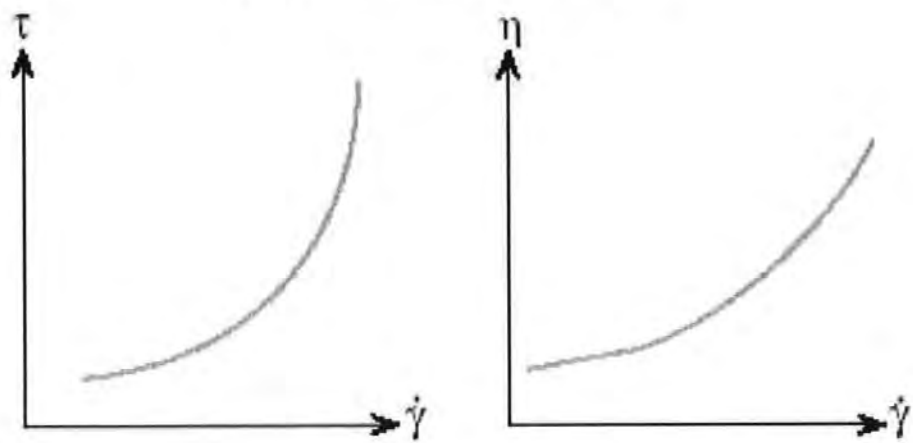
Figure 1.41 - Dilatant behaviour.
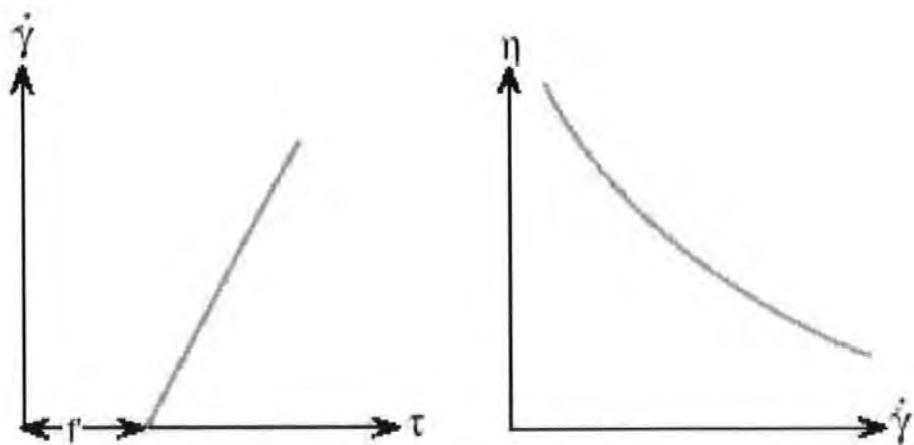
Figure 1.42 - Plastic behaviour.

52

Some fluids also show different values of viscosity at constant shear rate and temperature: thixotropic fluids show viscosity decreasing with time, when a constant shear rate is applied, while the opposite behaviour is called rheopectic.
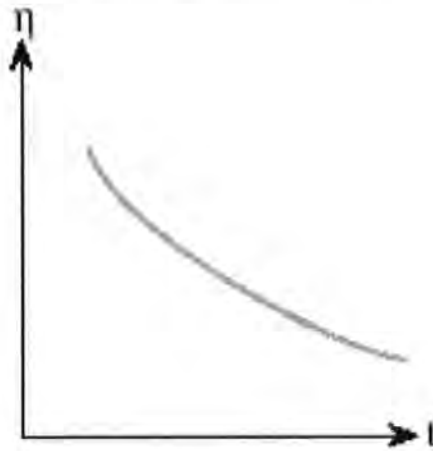
Figure 1.43 - Thixotropic behaviour.

Figure 1.44 - Rheopectic behaviour.

We shall now go on to discuss the phenomenon of viscoelasticity in more detail as it describes the interactions and deformation characteristics of coating colours under the conditions of study in this thesis.

1.8.8.2 Viscoelasticity

The rheological behaviour of complex colloidal systems, including dispersions of mineral pigment particles with stabilisers and polymeric binder systems, is too complex to be described only in terms of viscosity.
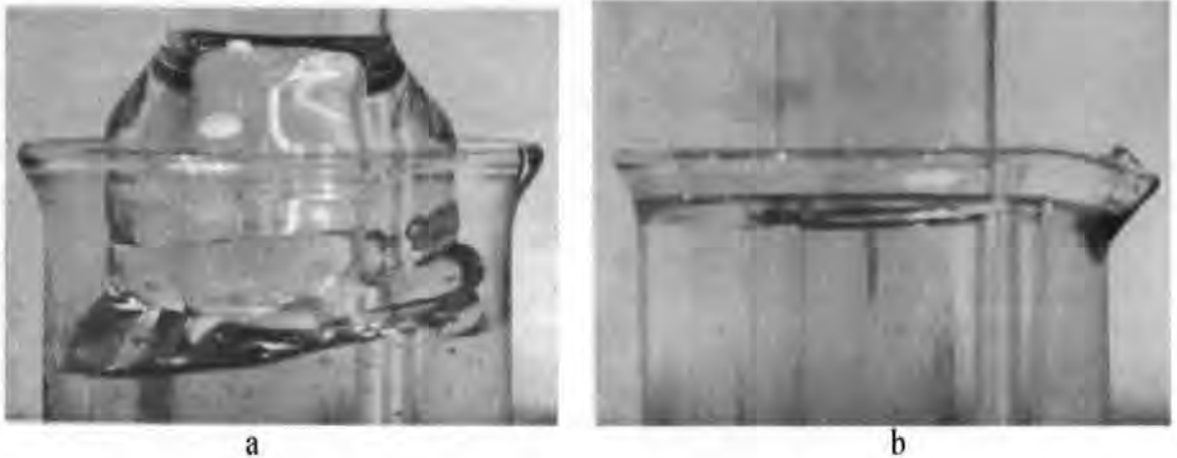
Figure 1.45 - Weissenberg effect: a) shows the rise towards the inner stirring rod or cylinder of the visco-elastic fluid, while b) shows the behaviour of a Newtonian fluid with similar viscosity.

For example Figure 1.45 (Lodge, 1964) shows the behaviour of liquids with similar viscosity, when sheared between concentric cylinders. If the fluid between the cylinders is Newtonian, a slight rise of the liquid horizontal surface towards the outer cylinder, under the action of centrifugal forces, can be observed. Some polymer solutions, undergoing the same test, show an unexpected rise of the free liquid surface towards the inner cylinder, increasing with the concentration of the polymer in solution. This is called the Weissenberg effect and it is due to the fact that viscoelastic materials show normal stresses in steady shearing flows.

Another interesting effect is the die swell, shown in Figure 1.46 (Lodge, 1964); when a solution of material of viscoelastic behaviour flows out of a tube, the diameter of the emerging liquid stream increases, in some cases by three or four times the diameter of the tube. For a

54

purely viscous incompressible Newtonian fluid, with similar values of viscosity, the theory would predict that the diameter should decrease of about 13 %.

Figure 1.46 - Die swell effect. On flowing out of a capillary tube, a stream of viscoelastic liquid increases in diameter by 200 %, while a Newtonian liquid (on the left) shows a contraction of its diameter.

The behaviour of viscoelastic materials is affected by many factors including the volume occupied by the solid particles in the aqueous suspension and the physical and chemical interactions between all the different species present in the suspension.

When shear strain is applied to a colloid or micro-particulate suspension, such as a coating colour, part of the induced stress is elastic and will return to zero either as soon as the strain is released (purely elastic) or will decay gradually as the viscous part of the flow (viscoelastic) allows rearrangement of the structure. The viscous component, however, remains as long as stress is sustained, usually by application of a continuous rate of change of strain (shear rate). This combination of elastic and viscous behaviour allows the description of viscoelastic materials under deformation. The behaviour can be probed using methods based on oscillation, where an applied oscillatory strain, often defined to induce a constant stress within the material, is used to measure the stress response.

Modern rheometers apply a sinusoidal oscillating force, either by applying a controlled strain rate, or by maintaining a controlled stress response in the material. This is conveniently done

55

between two cylindrical surfaces. The response of the fluid to the applied force is then determined using a measure of torque on either the oscillating element or the stationary element (the effect being symmetrical). The sample will react either to the applied sinusoidal strain rate by displaying a sinusoidal stress (controlled strain), or by allowing a certain amplitude of sinusoidal strain rate to occur whilst suffering a sinusoidal stress (controlled stress). The latter is shown in Figure 1.47.
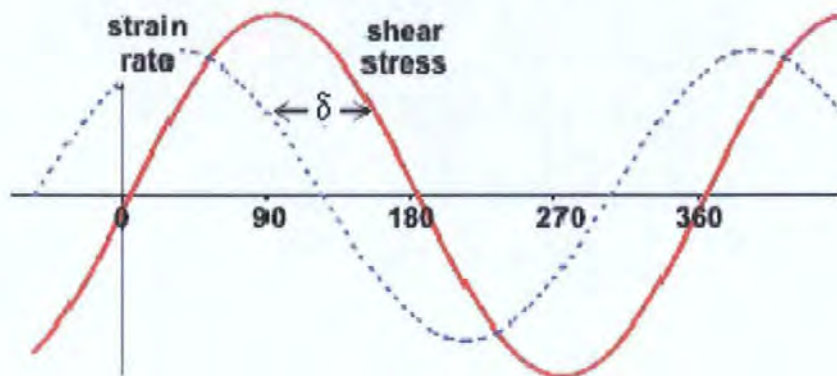
Figure 1.47 - Sinusoidal oscillating stress within the fluid is controlled by the rheometer (full red line), and the sinusoidal strain rate of the viscoelastic material results (dotted blue line).

If the strain rate is perfectly in phase with the experienced stress, the behaviour of the sample is perfectly elastic, while if the phase angle δ is 90°, the behaviour is purely viscous. The stress and strain are related by a complex modulus G^*.

$$\tau = G^*\gamma.$$

Eq. 1.22

The complex shear modulus G^*, representing the viscoelastic behaviour, can in turn be expressed as a vectorial sum of the elastic modulus G' and the viscous modulus G'' (often described also as storage and loss modulus, respectively).
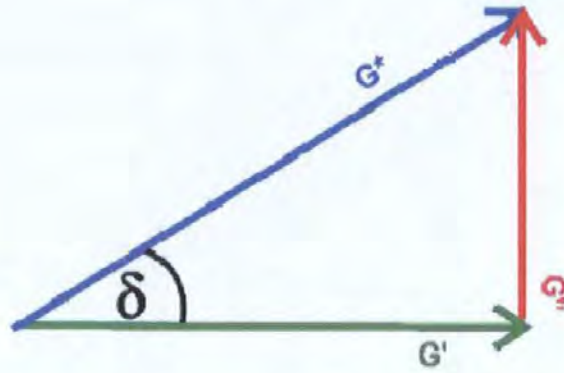
Figure 1.48 - Vectorial representation of the viscous and elastic modulus and their relation to the shear modulus.

The ratio between viscous and elastic modulus gives the phase angle:

$$\tan \delta = \frac{G''}{G'}.$$

Eq. 1.23

If the phase angle is less than 45°, the elastic behaviour is predominant.

An important feature of viscoelastic fluids is that they show normal stresses even in steady shearing flows. The first and second normal stresses Ψ_1 *and* Ψ_2 are given by:

$$\Psi_1 = \frac{\tau_{11} - \tau_{22}}{\dot{\gamma}^2}$$

Eq. 1.24

$$\Psi_2 = \frac{\tau_{22} - \tau_{33}}{\dot{\gamma}^2},$$

Eq. 1.25

where $\dot{\gamma}$ is the shear rate and τ_{ii} are the normal stresses shown in Figure 1.49.

57
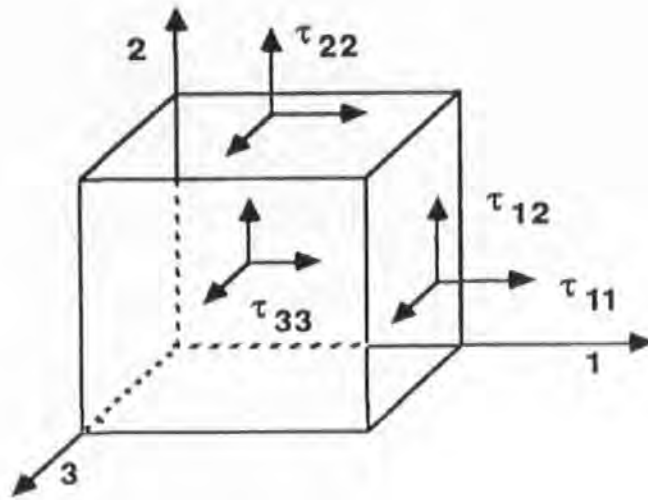
Figure 1.49 - Stresses acting in a cubical element of viscoelastic material.

The existence of normal stresses means that viscoelastic materials, under steady shearing flow, can show elastic or viscous behaviour depending on the dimensionless Weissenberg number:

$$We = \frac{\tau_{11} - \tau_{22}}{\tau_{12}}.$$
Eq. 1.26

Large values of this dimensionless parameter mean that the elastic effects dominate the rheology of the fluid under examination.

In the study of viscoelastic materials, time also plays a very important role: the Deborah number (*De*) describes the significance of elastic stresses in rapidly changing flow and it is the ratio between the relaxation time for the fluid, λ, and the time of residence, t, of the fluid in a given flow field of a process.

$$De = \frac{\lambda}{t} = \lambda \dot{\gamma}.$$
Eq. 1.27

When the Deborah number is greater than 1, the fluid behaves predominantly as an elastic material, i.e. the time in the flow field is short in relation to the relaxation time (the ability to

58

re-arrange) and so the material behaves more elastically. This viscoelastic description follows a Maxwell spring and dashpot model (Figure 1.50) and the relaxation time is $\lambda = \dfrac{\mu}{E}$.
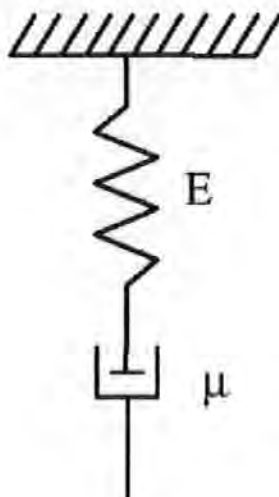
Figure 1.50 - Maxwell elastic spring and viscous dashpot model

The rheological properties of coating colour formulations have been the object of many studies, mostly related to the runnability of the coating colour under the very high speed (2000 mmin^{-1}) and high shear rates ($10^6 - 10^7$ s^{-1}) of an industrial coater, but also related to the final properties of the coating layer. Viscoelastic measurements at small deformation, for example, can give important information about the extent of particles' association and the strength of polymer-pigment interactions. They can also give insights into the structuring in the coating colour slurry, which in turn affects the final structure of the coating layer (Triantafillopoulos, 1996).

1.8.8.3 Rheology of coating colours

As previously described, the interactions between the different components of a coating colour formulation are extremely complex, and each particle is subject to different forces, both hydrodynamical and non-hydrodynamical. The rheology of a coating colour is closely related

to these complex interactions. An attempt to describe and model the relationship between rheology and particle motion has been made by Bousfield (Bousfield, 1993) for very low solid-volume fractions, compared to those used in a coating colour suspension. Bousfield reached the conclusion that non-hydrodynamic forces (electrostatic, short range dispersive forces and Born repulsion) are responsible for the time-dependent rheology of coating colours.

A similar approach has been used by Toivakka (Toivakka and Eklund, 1995) in order to study the effect of the size distribution of the particles on the suspension rheology. In this study, the authors simulated the behaviour of mono- and bi-modal size distributions for particles larger than 100 μm, far larger than those used in paper coating. The results showed shear thickening behaviour for the mono-dispersed particle size distribution, while the presence of small particles seemed to break the stress chain formed between the particles, reducing the viscosity.

The effect of a very narrow particle size distribution has been studied experimentally by Backfolk *et al.* (2003). A very narrow particle size distribution can improve the optical properties of the coating layer, by creating a more open packing of the structure with a higher number of air-pigment contact points and therefore higher light scattering. However, the lack of fine particles has two main detrimental effects: a poor water holding, mainly due to the reduction in the maximum packing of the structure in the wet state, and a high viscosity, both of which contrive to create runnability problems. The results of this study seem to show that the introduction of a lubricant, calcium stearate, can improve the runnability of the coating colour formulations containing pigments with narrow particle size distributions. In the same study, the authors went on to test the effect of the addition of the surfactant used in the calcium stearate emulsion. This alone was shown to induce a boundary slip effect, which is a depletion of solid content in the vicinity of the boundaries. This effect improves the

runnability of the coating colour, showing that the calcium stearate was not acting as a lubricant, as previously thought. The latex also suffered from interactions induced by calcium ions, bridging via dispersant molecules that adsorb onto the latex. This is due to the pigment particles with a narrow size range having a less strongly adsorbed low molecular weight fraction of dispersant than finer pigment particles.

In Husband (2000), an interesting experimental study of the interactions between calcium carbonate particles and latex can be found. The author focuses his study on the observation that GCC-latex suspensions have a higher viscosity than similar suspensions containing clay as pigment. This higher structuring of the coating colour in the wet state can cause problems in terms of runnability of the coating under the blade and final sheet quality. The author studied both Brookfield viscosity (low shear rate) and final gloss of the coated paper and the results show that the interactions in the coating colour between latex and GCC can change the viscosity by a factor of 20. These interactions were found to be mainly due to the interactions between the dispersant agents, used in order to obtain high concentration GCC suspensions, and partially polymerised species present in the latex serum, which are by-products of the polymerisation and the carboxylation process. Figure 1.12 shows a latex particle and the partially polymerised species in the latex serum. This detrimental increase in viscosity can be controlled by washing the latex or by controlling the level of dispersant in the GCC suspensions. This confirms the fact that polymers present in the coating colour formulation have a major influence on the runnability. The dispersant used by Husband in this study and the surfactant used to emulsify calcium stearate in the work by Backfolk *et al.*, act to sequester the Ca^{2+} ions which bridge the latex particles.

A similar study by Ostrowicki and Ramthun (Ostrowicki and Ramthun, 1999) show that changes in the parameters controlling the latex emulsion polymerisation can be used to control the viscoelasticity of the coating colours and therefore the final result of the coating process. The rheology of a coating colour formulation can be affected also by the order in which the different components are mixed, as shown by Persson, Järnström and Rigdahl (Persson et al., 1995).

The relationship between rheology and surface defects in blade coating has been investigated in Triantafillopoulos and Grankvist (1994). The results show that clay-based coating formulations are more elastic than calcium carbonate ones and that the use of cationic starch in the formulations can increase the elasticity, due to the affinity of the cationic starch to the anionic charges on the surface of clay particles; this causes a flocculation of the clay suspension which can lead to coating defects. Defect-free high-speed coated runnability requires that the magnitude of elasticity be controlled, so that it is enough to provide an action of levelling, but not enough to exceed the Deborah number of the application dwell time.

The rheological behaviour of clay and PCC-based coating colour formulations have been extensively studied by Lohmander (Lohmander, 2000b), by examining the viscosity of coating colours at both low and high shear rate, with a controlled stress rheometer and a capillary viscometer, including the use of a slit geometry, respectively. The results show that a broad shape factor distribution results in a lower viscosity than a narrow one, especially for needle shaped PCC particles, in agreement with Backfolk et al. (2003). He also showed that the passage through a slit makes the needle particle-containing coating formulation more susceptible to dilatancy.

Capillary viscometers are often used in order to study the behaviour of the coating colours under high shear rates, above 10^5 s^{-1}, which are similar to those applied to the coating colour under a so-called bent blade application. Under normal stiff blade operations, however, the method is erroneous according to Gane (Gane, 1997) as a viscoelastic colour will always have a large Deborah number under the impulse conditions of the very short dwell time at a fast running blade. This means that the colour experiences enormous stresses under small strains. The constant very high shear rate of a capillary viscometer is therefore considered irrelevant. It is more applicable to so-called bent blade operations where the gap under the blade is large and shear can be established.

A review of capillary rheometry and of the different geometrical effects that can affect its results can be found in Faure *et al.* (1991).

Capillary viscometers can be used to study not only viscosity at high equilibrium shear rates, but also other phenomena, such as the pressure loss at the entrance of the capillary and the apparent wall slip (Willembacher *et al.*, 1997). But, as the authors of this study point out, it is impossible to correlate the runnability of the coating colour to only one of these rheological parameters, which change simultaneously with the different coating colour formulations. This confirms the irrelevancy to blade coating operation of the high shear rate measurement of capillary viscometry, as suggested by Gane (Gane, 1997).

Roper *et al.* (Roper and Attal, 1993) combined experimental results from rotational viscometers and capillary viscometry to generate a single flow curve covering a wide range of shear rates (from 1 to 10^6 s^{-1}). This study also shows how increasing values of viscosity cause increasing values of blade pressure in order to obtain the desired coating weight. But, in turn,

increasing blade pressures on an industrial blade coater could result in paper web breaks and downtime on the machine. In order to avoid these problems, the relationship between the speed of an industrial coater, the blade pressure and the rheology of the coating colour formulations have to be tested on a pilot plant, which is an expensive and time consuming operation. The authors suggest that by combining the rheological data, obtained experimentally, with increasingly sophisticated computational fluid dynamics simulations, it will be possible to create a predictive tool able to minimise the need for such time consuming pilot tests. Once more, this approach is of dubious validity because of the questionable relevance of capillary rheometry for high-speed impulse blade coating.

2 EXPERIMENTAL TECHNIQUES

2.1 Existing techniques

2.1.1 Mercury porosimetry

Mercury intrusion porosimetry is widely used in the study of different porous materials (Webb and Orr, 1997). In recent years, it has also been used in the paper coating industry for characterisation of the porous structure of a dry paper coating layer (Johnson *et al.*, 1999). A sample, evacuated of trapped gases and moisture, is immersed in mercury, which is a non-wetting fluid for most materials. The mercury displacement caused by the sample allows the calculation of the bulk volume of the sample itself, V_{bulk}. The external pressure is then gradually increased. The amount of mercury intruding the void space of the sample is measured as a function of pressure; the volume of mercury intruded into the sample increases as the pressure increases and the mercury is forced into ever smaller voids. The result is a mercury volume intrusion curve per unit weight of sample as a function of applied pressure, which, knowing the interfacial tension and contact angle of mercury with the solid, can be converted into a void size distribution by the Laplace equation:

$$D = \frac{-4\gamma_{LV}\cos\theta}{P},$$
<div align="right">Eq. 2.1</div>

where γ_{LV} is the interfacial tension between mercury and air, P is the applied pressure, θ is the contact angle and D is the throat or assumed capillary diameter. A similar procedure, but with pressure reduction, allows the drainage, or extrusion, curve to be obtained, as the mercury emerges from the sample. The commonly used values of γ_{LV} and θ, for mercury entering an evacuated sample, are 0.485 N m^{-1} and 140° respectively. There are, however, uncertainties and variations in these values, the consequences of which have been reviewed by Webb and Orr (1997).

The void size distribution obtained by taking the first derivative of the intrusion curve and then applying the Laplace equation is representative of a one-dimensional model of a porous solid, as described in section 1.8.2. However, this "bundle of capillaries" model of a porous material cannot fully explain some of the results of mercury intrusion porosimetry. For example, the intrusion and extrusion curves differ. This hysteresis effect is caused by the "shielding" of larger void spaces, or pores, by narrower void spaces, or throats. The shielding therefore requires a higher than expected pressure for many of the features to fill. Such problems in the interpretation of the mercury intrusion measurements can be, at least partially, overcome by using a void space network model, such as Pore-Cor, which will be described in full in Chapter 5.

The results of this technique have to be carefully interpreted and many correction factors have to be applied in order to obtain a true measure of the void space of a sample.

If the sample was completely incompressible, the experimentally observed mercury intruded volume, V_{obs}, would include the volume of mercury intruded into the sample, V_{int}, the volume expansion of the analysis chamber or penetrometer, δV_{pen}, and the compression of the mercury δV_{Hg} (Gane *et al.*, 1995):

$$V_{obs} = V_{int} + \delta V_{pen} + \delta V_{Hg}.$$

Eq. 2.2

The term representing the expansion of the chamber can be evaluated by running a blank run with no sample in the penetrometer, while the term representing the compressibility of the mercury itself can be evaluated by using experimentally derived equations, which relate the volumetric compression of mercury as a function of pressure. The working equation for an incompressible sample becomes:

$$V_{int} = V_{obs} - \delta V_{blank} + \left[0.175(V^1_{bulk})\log_{10}\left(1 + \frac{P_{app}}{1820}\right) \right],$$

Eq. 2.3

where δV_{blank} is the change in the blank run volume reading, V^1_{bulk} the sample bulk volume at atmospheric pressure and P_{app} the applied external pressure.

Paper coating, as explained in the previous chapter, consists mainly of finely ground mineral pigment particles or synthetic pigment particles, bound together and to the base-paper by latex and/or natural binders. Due to this composition, a paper coating layer is partially compressible, because of the compressibility of the latex particles, the compaction of pigment particles, or in the case of synthetic pigments, collapse of the particles. In order to obtain a correct interpretation of the mercury porosimetry intrusion curves one has to take into account this compressibility and apply another correction to the observed intruded volume. If ψ_{ss} is the compressibility of the sample and M_{ss} its bulk modulus, then:

$$M_{ss} = \frac{1}{\psi_{ss}} = \frac{dP}{\left(\dfrac{-dV_{ss}}{V_{ss}}\right)},$$

Eq. 2.4

and the final expression for the fully corrected intruded volume is:

$$V_{int} = V_{obs} - \delta V_{blank} + \left[0.175(V^1_{bulk})\log_{10}\left(1+\frac{P_{app}}{1820}\right)\right] - V^1_{bulk}(1-\Phi^1)\left(1-\exp\left[\frac{(P^1-P_{app})}{M_{ss}}\right]\right),$$

Eq. 2.5

where Φ^1 is the porosity at atmospheric pressure and P^1 is the atmospheric pressure.

Mercury porosimetry can be used to determine the pore size distribution of porous materials even when these are supported by a laminate substrate (like Synteape) or by a fibrous substrate (like paper).

mercury occlusion

mercury meniscus

surface

debonded or ruptured fibre
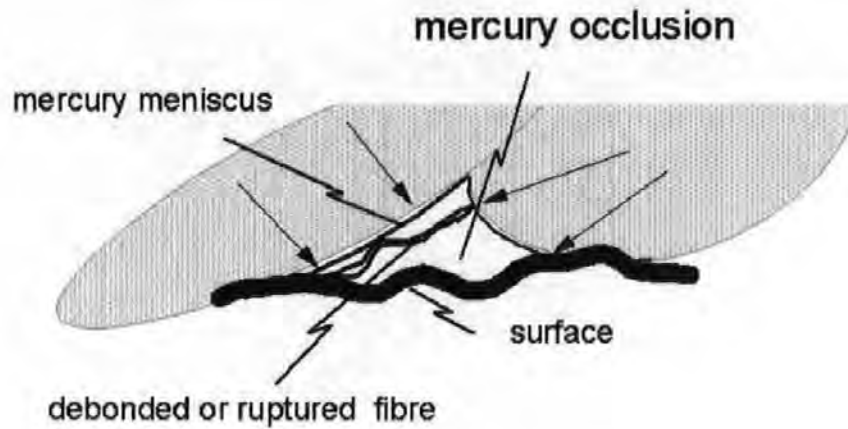
Figure 2.1 - Schematic of low pressure mercury occlusion from sample surface or edge features. Mercury shown light grey.

Ridgway and Gane (Ridgway and Gane, 2003) describe a technique which, by using hexadecane absorption coupled with mercury porosimetry, allows the correction of the saturation values of the mercury porosimetry, so that the contribution of the substrate and the occlusion effect (Figure 2.1), caused by surface features of the substrate, are taken into account. This effectively normalises the total intrusion value by an independent method.

The analysis of the samples discussed here has been carried out using a Micromeritics Autopore III mercury porosimeter (Figure 2.2), able to apply a maximum pressure of mercury of 60 000 psia (414 MPa), corresponding to a diameter of 4 nm via the Laplace equation (Eq. 2.1).

Figure 2.2 - Micromeritics Autopore III mercury intrusion porosimeter

2.1.2 Scanning electron microscopy

In a typical SEM configuration, electrons are emitted from a cathode filament towards an anode. The electron beam is focused by successive magnetic lenses into a very fine spot (about 5 nm in diameter). As the electrons strike the surface they are inelastically scattered by atoms in the sample. Through these scattering events, the beam spreads and fills a teardrop-shaped volume extending about 1 μm into the surface. Interactions in this region lead to the subsequent emission of electrons and X-rays, which are then detected. The electrons are emitted from the surface of the material and are used to produce an image. Such backscatter cross-sectional images can be used to view the particle and pore-size arrangement, and connectivity of the pigment coatings. The X-rays, on the other hand, emerge from within the teardrop volume and can be used to characterise the elemental content of the material. They provide a spatial mapping, depending in resolution on the teardrop dimensions and subsequent X-ray absorption of the various elemental/chemical constituents. The X-ray emission is

69

usually limited to inorganic materials containing elements higher than C, H and O, in the periodic table, unless specialist equipment is used.

This application is extremely useful in order to obtain visual images and qualitative information on the coating surface pore level structure. By applying image analysis procedures (Toivakka and Nyfors, 2000) to the scanning electron micrographs, quantitative information on particle size distribution and/or void structure can also be obtained. However such procedures are very time consuming, and limited, as previously discussed, to the dimensions achievable when producing ultra-thin sections.

2.1.3 Brookfield viscometry

The Brookfield viscometer is a rotational viscometer and it measures the torque required to rotate an immersed element, the spindle, in a fluid. For a given viscosity, the viscous drag, or resistance to flow, is proportional to the spindle's speed of rotation and is related to the spindle's size and shape.
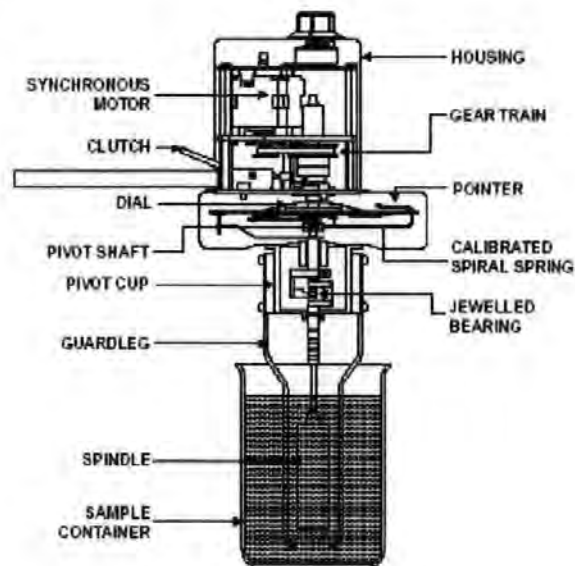
Figure 2.3 - Brookfield viscometer
(http://www.brookfieldengineering.com/download/files/more_solutions.pdf).

The spindle can be of variable shape and size, Figure 2.4, according to the type of measurement and the viscosity range of interest. The experiments of relevance to this work were carried out using cylindrical spindles of different lengths for single point measurements, in which the viscosity is measured at constant temperature and constant shear rate, $\sim 30\ s^{-1}$ for a spindle rotation speed of 100 min^{-1}, termed the Brookfield 100 value.
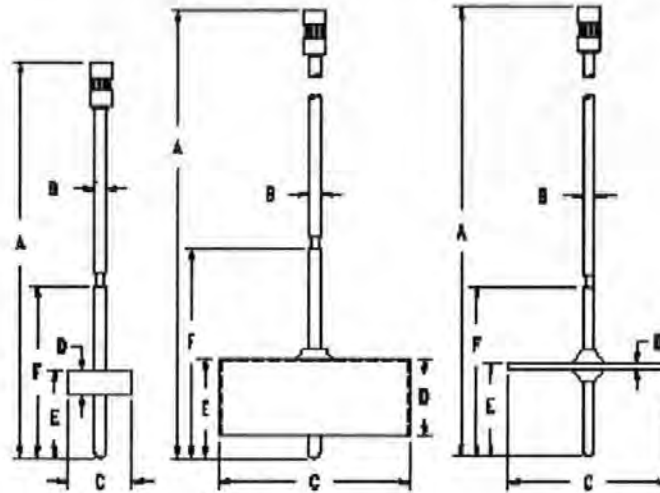
Figure 2.4 - Brookfield viscometer cylindrical spindles

2.1.4 Other rheological measurements

The theory of rheological measurement on viscoelastic fluids has been extensively explained in section 1.8.7.2.

Such measurements have been carried out using a StressTech controlled stress/strain rheometer (ATS RheoSystems and Reologica Instruments AB, Figure 2.5).

71

Figure 2.5 - StressTech rheometer

The measurements are carried out using two concentric cylinders, with a rotating/oscillating bob and a fixed cup (Figure 2.6).
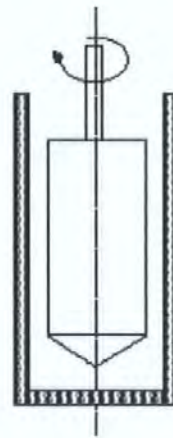
Figure 2.6 - Rotating/oscillating bob and fixed cylinder in the StressTech rheometer.

The inner cylinder of the rheometer oscillates at a constant frequency (data used here apply 0.5 Hz) while the amplitude of its oscillation, and, as a consequence, the stress experienced by the coating colour, progressively increases until a controlled value of shear stress has been reached. For different values of induced shear stress the values of the elastic (or storage)

72

modulus G', the viscous (or loss) modulus G'' and the phase angle δ are measured. The method subsequently provides data over a range of controlled stress values, i.e. via a stress sweep.

The instrument can also be used to run constant shear rate viscosity measurements, similar to the Brookfield viscosity measurements, but over a wider range of shear rates. The yield stress, stress below which no observable flow will occur, can also be measured with this instrument, by increasing the applied shear stress and monitoring the changes in measured viscosity.

These methods when combined are particularly useful to determine the result of interactions within the coating colour suspension leading to viscoelasticity, shear thinning and ultimately shear-induced effects, such as dilatancy.

2.2 Coating application

In order to obtain accurate and reproducible coating layer thicknesses, the samples used in this study were prepared by applying the coating colour onto the substrate with an automated draw down film applicator, shown in Figure 2.7.

Figure 2.7 - Automated film applicator.

The accuracy in applied coating thickness is obtained by the metering bars. These are produced by winding a stainless steel wire around a stainless steel rod, resulting in a pattern of identically shaped grooves (Figure 2.8).
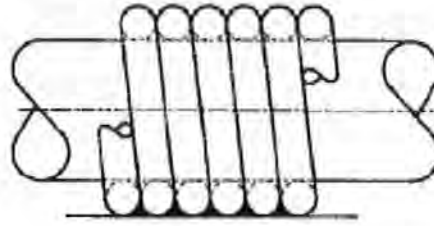
Figure 2.8 - Section of a metering bar or rod.

These grooves then precisely control the wet film thickness, and rods with larger wound wire diameters apply a thicker coating layer.

2.3 Existing and new techniques for measuring surface stress

2.3.1 Existing techniques

Due to the complexity and the small dimension of the system in the out-of-plane direction, the measurement of the forces acting upon drying could not be carried out with any direct method. These forces were therefore measured by observing how an elastic material reacts to them.

A similar approach has been used by Perera (Perera, 1995) and is standard in the paint industry. In Perera's work the measurement of the stresses acting upon drying of paint layers have been measured by applying the paint on a freely supported steel beam in a commercial apparatus (CoRI stressmeter, Braive Instruments, Liège, Belgium). Figure 2.9 shows the steel beam, painted on its top side, placed on two supports. The supported length of the beam is l, the overlap is l_0, and the extent of deformation is d^t.
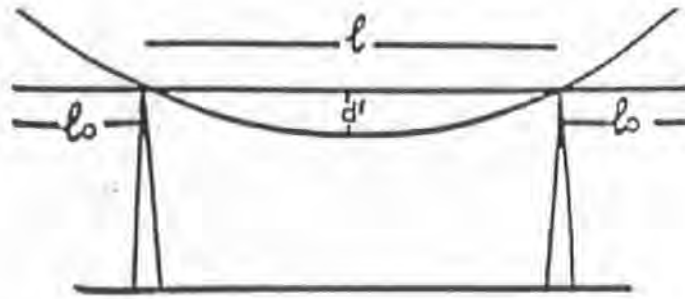
Figure 2.9 - Schematic description of a freely supported beam (Perera, 1995).

Paper coatings and paints are similar to the extent that they both consist of a pigment and a binding agent. However the types of binding systems are very different and, while paper coatings are water-based, the paints investigated by Perera were organic solvent-based systems. These major contrasts cause order-of-magnitude differences in the shrinkage stresses exerted by paper coating layers (Pascals) and paints (MPascals) upon drying and the time required for the drying process to complete. The critical pigment volume concentration (cPVC) plays a very important role in the development of shrinkage stress in solvent-based paint (Figure 2.10). The cPVC is the volume percentage of pigment in a coating below which the pigment particles are completely surrounded by binding resin so that no free void space exists. A preliminary set of experiments, carried out on paper coating formulations with the technique described later on in this section, has shown that the effect of binder is proportional to its content within the pigment dosage range above the cPVC (so that the final structures present voids), and so the increased binder quantity is a useful experimental parameter to apply without influencing the basic mechanisms themselves. The value of the cPVC for pigments dispersed in water with particulate latex binders which remain stable in water suspension is much lower than in systems where the latex shows solvent-dependent film forming. This is confirmed by Groves and Lanham (Groves and Lanham, 1991), who investigated the gloss variation and volumetric shrinkage for latex-clay coatings. They measured a minimum value of gloss for coating colours containing 30 w/w% and a maximum

75

volumetric shrinkage for 35 w/w% of latex in the coating formulations. These measurements show that the critical pigment concentration for the coating used in their experiments is 65-70 w/w% corresponding to more than 50 % in volume of latex in the coating colour formulation. Their measurement showed proportionality between latex content and volumetric shrinkage above the cPVC (structure with voids), while the shrinkage was constant below the cPVC (structure without voids).
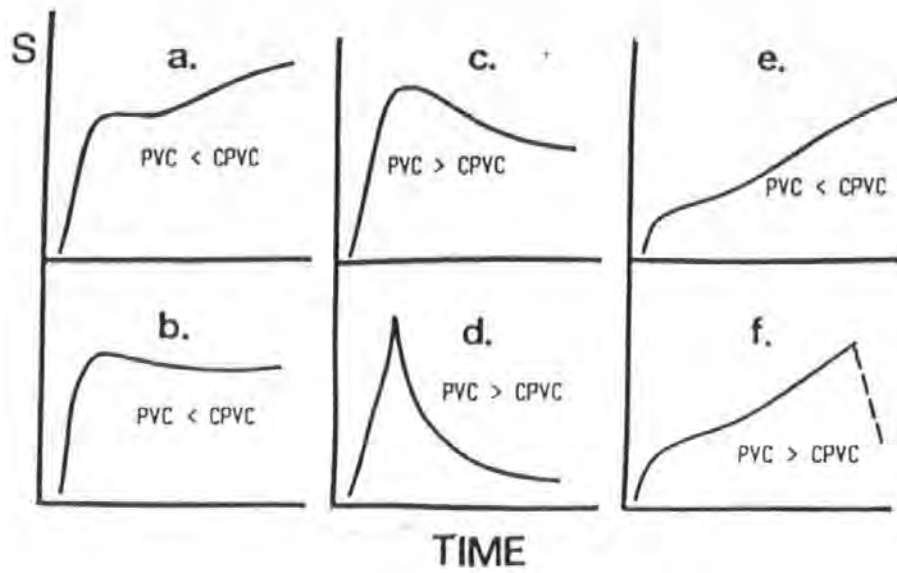
Figure 2.10 - Development of stress S with time for paint coatings for different relationships between pigment volume concentration (PVC) and critical pigment volume concentration (cPVC): (a) and (b) PVC < cPVC; (c) and (d) PVC > cPVC; (e) and (f) in the presence of a poor coalescent.

Similar methods for the measurement of bending stiffness of papers and card and packaging boards, based on the measurement of bending under know stress conditions, are considered standard in the paper and board industry (Tappi Test T836 om-02 or Tappi Test T820 cm-00, Tappi, 2000).
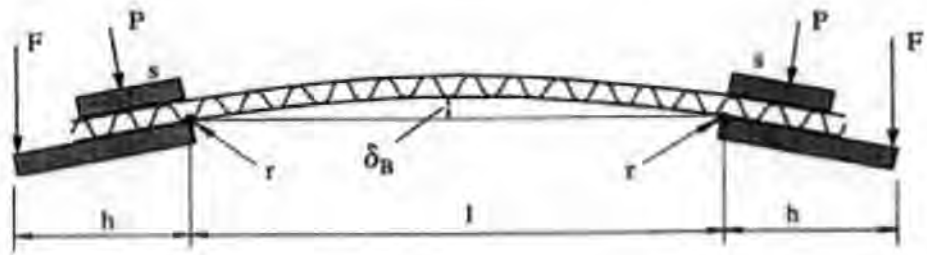
Figure 2.11 – Measurement of the bending stiffness of a corrugated cardboard under the action of a know force *F*.

Figure 2.11 shows a standard method (Tappi Test T836 om-02) for the measurement of the bending stiffness of a cardboard, similar to the test used in our experiments to measure the mechanical properties of Synteape (section 2.3.6).

2.3.2 New techniques

Due to the obvious differences between paints and paper coatings, the technique had to be completely redesigned in order to fit our purposes and allow the measurement of all the parameters involved in the drying process of paper coating layers.

The forces could not be calculated from the application of coating colours to a natural base paper. The fibres of a base paper rearrange under the forces caused by the drying coating layer, especially under high moisture conditions during the initial part of the drying. The fibres deform in the plane of the paper, but display no measurable bending other than the action of wetting on the in-built stress relaxation properties of the fibrous mat. This planar deformation, however, cannot act to alleviate any non-uniformities in the coating caused by coating shrinkage. It was therefore necessary to identify a more suitable potential substrate.

A series of tests on several polymeric materials led to the choice of Synteape (Arjo Wiggins) as substrate for our experiments. Synteape is a synthetic laminate substrate made of stretched polypropylene sheets filled with calcium carbonate. Its slightly rough surface, which enables

77

the adhesion of the coating colour, makes it a useful substrate in the study of paper coating in isolation from fibrous base sheets. This roughness, together with the laminate elasticity, makes it an ideal substrate for paper coating shrinkage experiments.
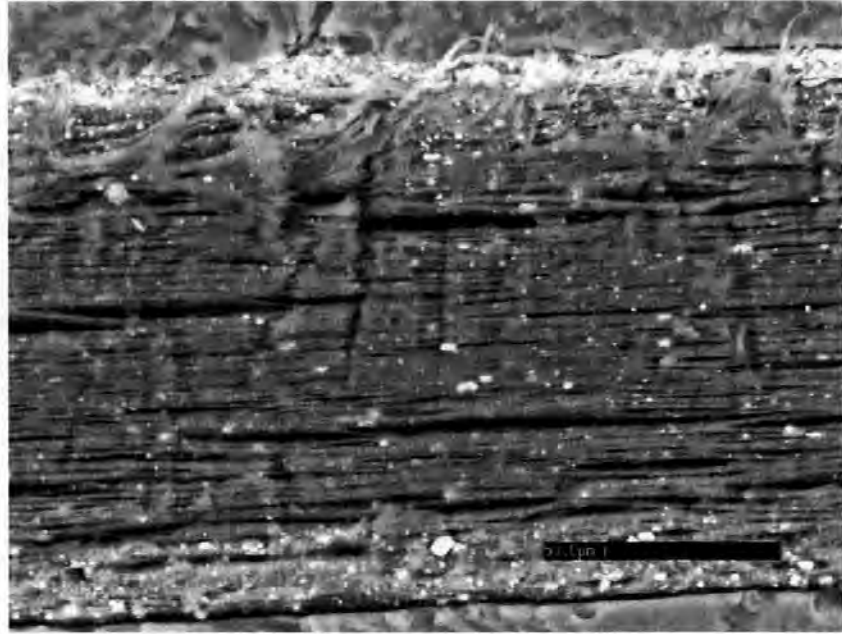
Figure 2.12 - SEM micrograph of the cross section of Synteape showing the laminated structure, white CaCO₃ particles, and surface roughness. Scale bar 50 μm

Each coating colour was applied to a strip of the synthetic base, and the deflection of the strip upon drying was measured as a function of weight loss. The elementary beam theory was then used to calculate the forces acting on the substrate's surface.

The substrate strips used in the experiments were 4.5 cm long, 0.5 cm wide and 0.01 cm thick. These dimensions formed the designated coordinates x, y and z respectively. The weight of the strips was considered negligible when compared with the forces acting to cause the deflection of the beam.

The mechanical properties of the coated substrate were assumed to be constant during the drying of the coating layer. This is an approximation as the coating structure develops some

mechanical resistance as it changes from the FCC to the SCC, i.e. the coating layer changes its mechanical properties upon drying, from plastic, through viscoelastic to brittle. However, the exact mechanical transitions between these states of the coating are not the target of investigation, rather the roles of the various force components as a function of time and solids concentration. Furthermore, the shrinkage forces which drive this change must, by definition, be greater than the physical resistance to change. The coating layer was therefore assumed to act only as a *stress deliverer*, whilst itself having little or no stress growth as a direct result of the resulting bending strain. The internal stress of the coating layer is released in the x direction causing the sample to curl, as shown in Figure 2.13 and Figure 2.14. Curling in the y direction also occurs, but as the sample is narrow, this has a much smaller measurable effect, which is not monitored.
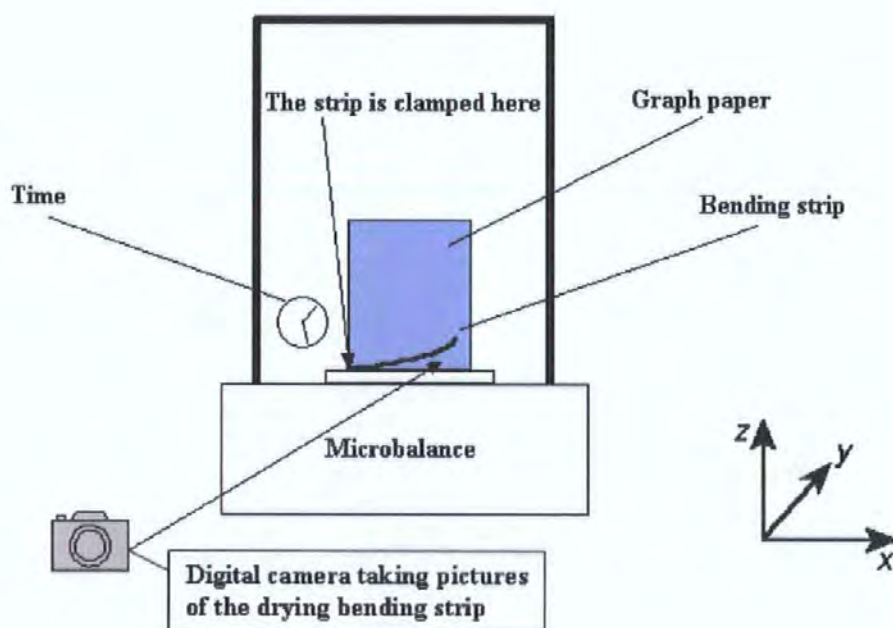
Figure 2.13 - Diagram of the experimental apparatus, viewing in the xz plane as shown.

79
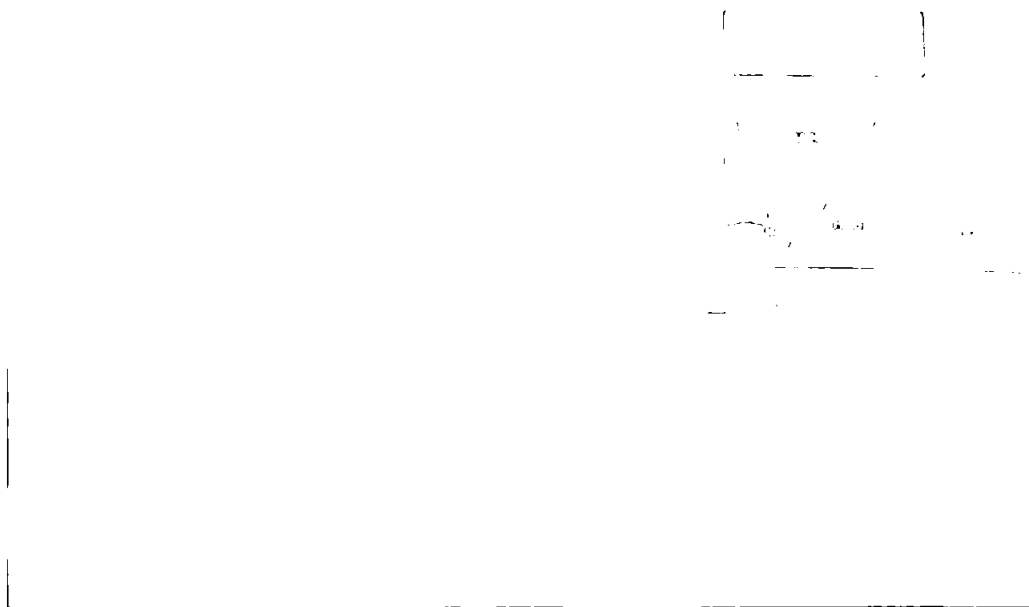
Figure 2.14 - A Synteape strip bending while the coating on its surface dries. The strip is on a microbalance that measures its weight loss and its white profile can be seen in front of the graph paper.

The experimental apparatus, presented in Figure 2.13, was designed and built in order to take pictures of the sample deflection during the drying process and simultaneously to measure its weight loss. This arrangement made it possible to find the forces acting on the surface of the substrate as a function of % weight (water) loss. It consists of a microbalance, connected to a computer in order to acquire and store the weight of the samples while the drying occurs. The apparatus is a development of that described in (Schoelkopf *et al.*, 2000), which comprised a microbalance only used for measuring the uptake of liquid during wicking. The coated strips were clamped to the plate of the microbalance and the chamber above the plate was closed, in order to avoid external disturbances of the evaporation and weighing processes.

80

2.3.3 Application of the Elementary Beam Theory (Frenner, 2003)

An outline of elementary beam theory is presented as a guideline for carrying out the full derivation of the working equation for the present experiment.

The elementary beam theory gives:

$$M = \frac{EI}{R},$$

Eq. 2.6

where M is the bending moment (the torque which develops in a loaded beam as shown in Figure 2.17), E is the elastic or Young's modulus (the ratio between the stress applied and the subsequent strain), I is the second moment of inertia (a geometrical property of a beam related to its ability to resist bending) related to the z axis (with z as indicated in Figure 2.15), and R is the radius of curvature of the deformed beam.

2.3.4 Effect of the coating layer

It is possible to assume that the coating gives rise to a total surface traction T and, hence, to a bending moment $M = Td$, where $2d$ is the thickness of the beam. From Eq. 2.6:

$$\frac{EI}{R} = Td,$$

Eq. 2.7

where $I = b(2d)^3/12$, b is the width of the beam and the product EI is called the "beam stiffness" or "flexural rigidity".
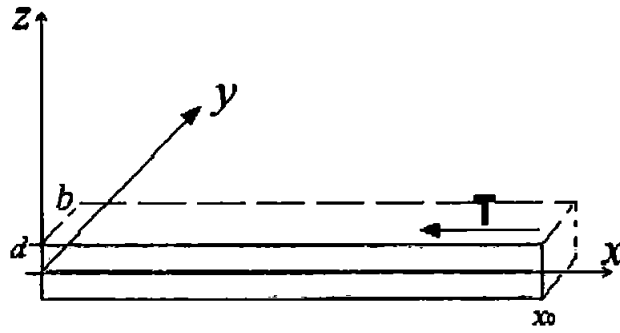
Figure 2.15 – Beam of thickness 2*d*, width *b* and length x_0 with a total force T acting on its surface.

2.3.5 Radius of curvature of the bending beam

For a generic function $z = f(x)$ the radius of curvature is

$$\frac{1}{R} = \frac{z''}{(1+z'^2)^{\frac{3}{2}}},$$

Eq. 2.8

where $z' = dz/dx$ and $z'' = d^2z/dx^2$. For small z', $1/R \cong z''$. If we have a circular deformation through (x_0, z_0), then:

$$\frac{1}{R} = \frac{2z_0}{x_0^2 + z_0^2},$$

Eq. 2.9

Eq. 2.8 and Eq. 2.9 are consistent if $x_0^2 >> z_0^2$, i.e. for small deformation. If a deflection z_0 is measured, substituting from Eq. 2.7:

$$T \cdot d = \frac{2EIz_0}{x_0^2 + z_0^2}.$$

Eq. 2.10

If x_0, z_0 and EI are known, T can be calculated from Eq. 2.10. The stress acting on the surface of the beam can be calculated as $\tau = T / b \cdot x_0$. Since $T \propto I \propto b$, the stress τ is independent of the strip width b.

82

2.3.6 Evaluation of the stiffness of the beam

The standard beam theory is also helpful if the stiffness of the beam is unknown. The deflection of the strip is measured due to its own weight, as shown diagrammatically in Figure 2.16. The effect of the sample weight is assumed negligible when compared to the stress caused by the drying coating layer, but is nevertheless enough to cause a small deflection. Then it is possible to determine the value of the product EI.
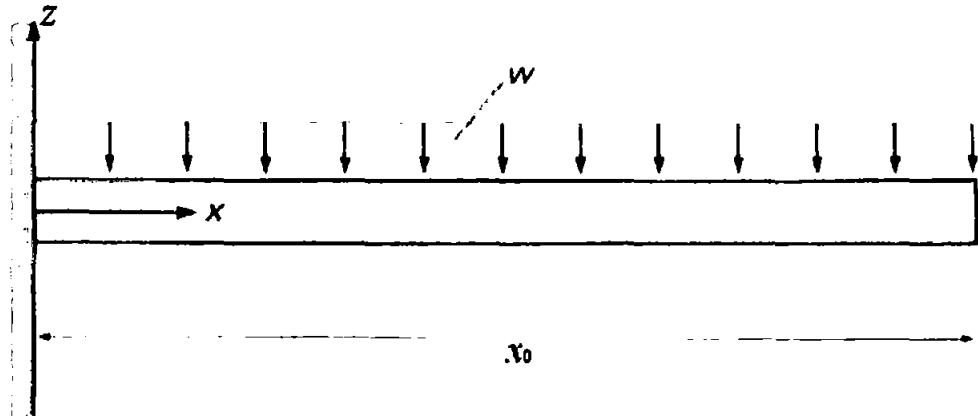
Figure 2.16 – Evaluation of the stiffness of a beam, by measurement of the deflection of the beam under the action of its own weight w.

For each section of the beam between x and $x+dx$ (Figure 2.17) the elementary beam theory gives $dM/dx = S$ and $dS/dx = -w$, where w is the weight per unit of length, M is the bending moment and S shear force.
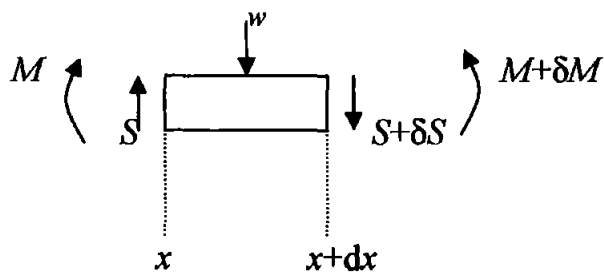
Figure 2.17 – Schematic of a section of a beam with the stresses and torque acting on it.

Setting $1/R \cong z''$ and eliminating S from the previous equations, Eq. 2.6 gives:

83

$$EI \frac{d^4 z}{dx^4} = -w ,$$

<div align="right">Eq. 2.11</div>

Successive integrations lead to:

$$EI \cdot z(x) = -\frac{w \cdot x^4}{24} + \frac{w \cdot x_0 \cdot x^3}{6} - \frac{w \cdot x_0^2 \cdot x^2}{4} + A \cdot x + B .$$

<div align="right">Eq. 2.12</div>

The boundary conditions are $z(0) = z'(0) = 0$

This leads to:

$$z(x) = \frac{1}{EI} \left\{ -\frac{w}{24} \left(x^4 + 6x_0^2 \cdot x^2 - 4x_0 \cdot x^3 \right) \right\}$$

<div align="right">Eq. 2.13</div>

which, for $x = x_0$, will become:

$$z_1 = z(x_0) = \frac{1}{EI} \left(-\frac{3x_0^4 \cdot w}{24} \right) = -\frac{x_0^4 \cdot w}{8EI} ,$$

<div align="right">Eq. 2.14</div>

and finally:

$$EI = -\frac{w \cdot x_0^4}{8z_1} .$$

<div align="right">Eq. 2.15</div>

3 EXPERIMENTAL (Laudone *et al.*, 2004)

The experimental work was divided in two parts: in the first part the shrinkage forces, developed upon drying of a paper coating layer, were measured using the method described in section 2.2, and the dry structures of the coating layers were characterised by mercury intrusion porosimetry and electron microscopy. This made it possible to quantify the shrinkage forces and infer some important ideas on the drying mechanism and how different binders, coating thicknesses or pigment particle sizes can affect the final properties of the coating layer.

In the second part, the interactions between the different components of a coating colour formulation in the wet state were investigated by measuring rheological properties. The results of this second experimental section are presented in chapter 4.

3.1 Sample preparation

3.1.1 Substrate

The synthetic substrate was the synthetic laminate, Synteape (Arjo Wiggins), described in chapter 2, manufactured by filling polypropylene with calcium carbonate and stretching it. Its slightly rough surface allowed the coatings to adhere. Its elastic behaviour, so important for the measurement of coating shrinkage forces, was shown to be anisotropic, due to the unidirectional stretching during the last stage of its manufacture. It was found necessary to cut the strips parallel to this stretch direction to establish a reproducible elastic behaviour. The strips were formed 4.5 cm long (x axis) and 0.5 cm wide (y axis). The thickness of the substrate was 100 μm and its elastic modulus 1.73 GPa, calculated by measuring the deflection of Synteape strips under the action of their own weight, as described in section 2.2.4.

3.1.2 Pigments

The pigments were based on ground calcium carbonate (GCC). This choice of pigment avoided complications such as the anisotropy of clay platelets and the acicularity of aragonitic precipitated calcium carbonate (PCC) (Bodurtha *et al.*, 2001; Lohmander, 2000a). The GCC was a dispersed limestone from Orgon, France, ground to two particle size ranges, named Hydrocarb 60 and Hydrocarb 90 (Omya AG, Switzerland). The samples contained, respectively, 60 w/w% and 90 w/w% of particles with diameter < 2 μm, and with a maximum diameter of around 5 μm.

For a control experiment, the GCC was substituted by a polystyrene pigment with very fine monosize spherical particles, 98 % in volume with a diameter less than 0.5 μm (DPP 3710, Dow Chemicals).

3.1.3 Binders

The binder for each sample was selected from one of the following:

- thermally modified maize starch C-film 07321 (Cerestar, France);

- high glass transition temperature (T_g = 23 °C) acrylic latex Acronal S320D in the form of spherical particles of diameter 0.2 μm (BASF, Germany);

- high T_g (22 °C) styrene-butadiene latex DL940 (Dow Chemical, USA) with spherical particles of diameter 0.14 μm;

- low T_g (5 °C) styrene-butadiene latex DL930 (Dow Chemical, USA) with spherical particles of diameter 0.15 μm .

Both latex types are designed for stability in the presence of calcium ions and so the different chemical nature of the acrylic and styrene-butadiene (SB) latices was assumed not to interfere with the study.

The minimum film-forming temperatures are given by the manufacturers as 1 °C above T_g. Therefore the low T_g latex was expected to show some film-forming, as much as the coating structure would allow, at the temperature of the experiment (20 ± 1 °C), whereas the high T_g latices were not.

3.1.4 Thickness and composition

The coating colours were prepared by mixing the pigment and the binders under high shear mixing conditions, in order to ensure that the final mixtures were homogeneous and all the pigment agglomerates were broken down.

The preparation of the starch solution was carried out by slowly adding the starch to water at 70-75 °C under high shear mixing, in order to avoid the formation of starch lumps.

Two different compositions were used, either 10 or 25 w/w% binder on a dry basis, the remaining being pigment. 25 w/w% is above the maximum binder concentration used in commercial paper coating (typically less than 20 w/w%). However this composition is included here to demonstrate the dependence of the method to latex level, independent of critical pigment volume concentration, when emulsion polymers are used (contrary to what might have been expected from solvent-based paint technology). Experiments were performed on (i) binders only, (ii) pigment with dispersant only, and (iii) pigment with dispersant and binders.

It is important to point out that usually, in the paper coating industry, the paper coating composition is represented as parts of every component per 100 parts of pigment on a dry

basis. This means that 25 w/w% corresponds to about 33 parts of binder per 100 parts of pigment and 10 w/w% corresponds to about 12 parts of binder per 100 parts of pigment.

The strips were coated using an automated laboratory coater, described in section 2.2, and two different draw-down rods, which control the amount and thickness of coating colour applied: rod 2 (applying about 10 g m^{-2} of dry coating corresponding to a dry coating layer thickness of about 5 µm) and rod 3 (about 20 g m^{-2} and 10 µm respectively).

3.2 Mercury porosimetry

Coating layers were prepared by applying the coating colour formulations described above onto non–porous aluminium foil. They were then dried under the same conditions as for shrinkage testing, before being subjected to mercury intrusion porosimetry. Aluminium foil was chosen as substrate, instead of Synteape, to prevent confusion caused by mercury intrusion into the edges of the substrate, and substrate compression. The mercury intrusion results were corrected using Pore-Comp (following the analysis of Gane *et al.* (Gane *et al.*, 1995), described in section 2.1.1), in order to take into account compressibility of mercury and compressibility of the sample skeletal materials themselves. All the mercury intrusion curves showed bimodality in their first derivative (Figure 3.1) with mercury intrusion for pressures below 1 MPa, corresponding to Laplace diameters larger than 1.5 µm, while, usually, paper coating layers show pore sizes smaller than 1 µm (Kettle and Matthews, 1993).
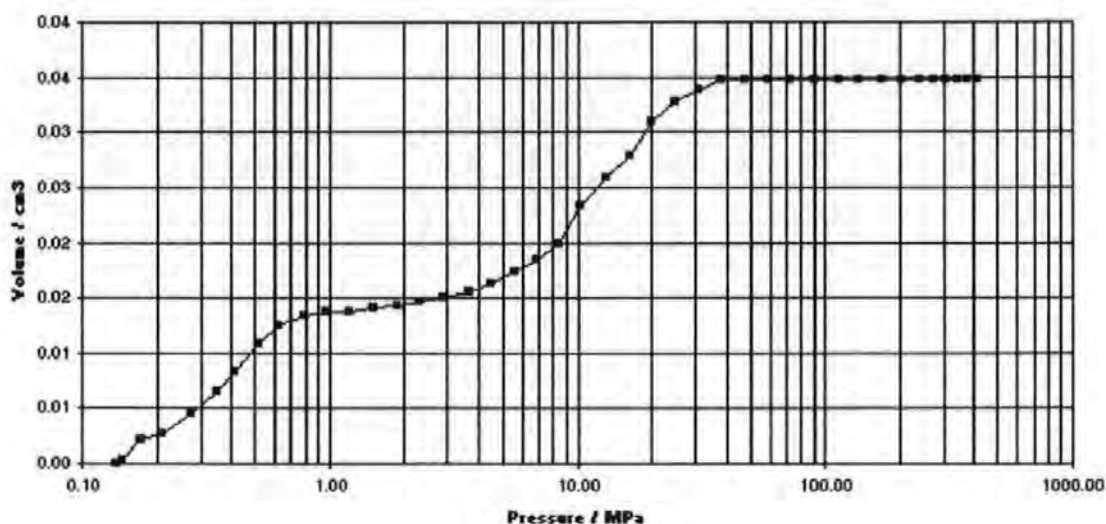
Figure 3.1 - Mercury porosimetry intrusion curve for a starch-based coating colour. The pore diameters range for the pressure of 0.1 – 1 MPa is 1.5 - 13 µm.

For a correct interpretation of the mercury intrusion porosimetry results, the experimental intrusion curves showing bimodality had to be split into two different distributions, as explained later in this section. The finer pore-size distribution curves were scaled to represent the region of interest, so that the intrusion measurements started from zero at the beginning of this range. The two different pore-size ranges can be observed in the micrographs presented in Figure 3.9 to Figure 3.12.

Table 3-1 shows the values of porosity of the dry coating layers after the mercury intrusion curves were split and re-scaled.

Table 3-1 - Porosities of dry samples measured by mercury porosimetry (volume %) after the intrusion curves were split and re-scaled.

Sample :	Acrylic high T_g latex	Acrylic high T_g latex	SB high T_g latex	SB high T_g latex	SB low T_g latex	SB low T_g latex	Starch	Starch
Coating weight :	low	high	low	high	low	high	low	high
HC60 + 10 % binder	26.1	24.8	30.8	25.8	21.8	18.7	17.4	15.7
HC60 + 25 % binder	19.8	18.9	24.2	19.6	14.2	12.8	14.3	8.0
HC90 + 10 % binder	38.4	24.5	39.9	32.2	28.5	24.9	26.5	22.5
HC90 + 25 % binder	37.7	23.2	35.1	21.9	15.5	13.9	17.0	10.2
DPP + 25 % binder	-	-	-	-	42.5	33.2	19.3	17.7

It can be observed that the porosity of the coating layer based on the coarser calcium carbonate, Hydrocarb 60 (HC60) are lower than the corresponding coating layers prepared using finer calcium carbonate Hydrocarb 90 (HC90). When the synthetic Dow Plastic Pigment (DPP) is used in the coating colour formulation, the samples show higher porosity than in the corresponding cases with calcium carbonate. This is to be expected when one considers the packing differences between the nearly log-normal tightly packing particle size distributions of the GCC compared with the monomodal distribution of the plastic pigment, DPP.
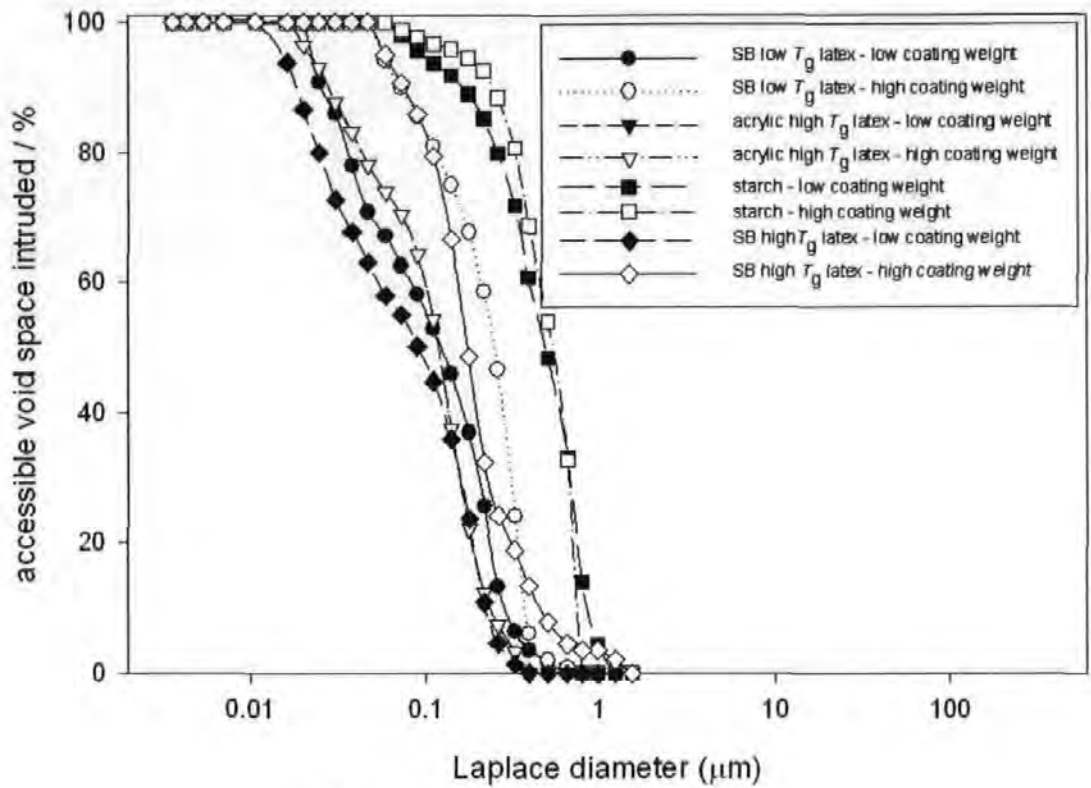
Figure 3.2 - HC60 + 10 w/w% binder.
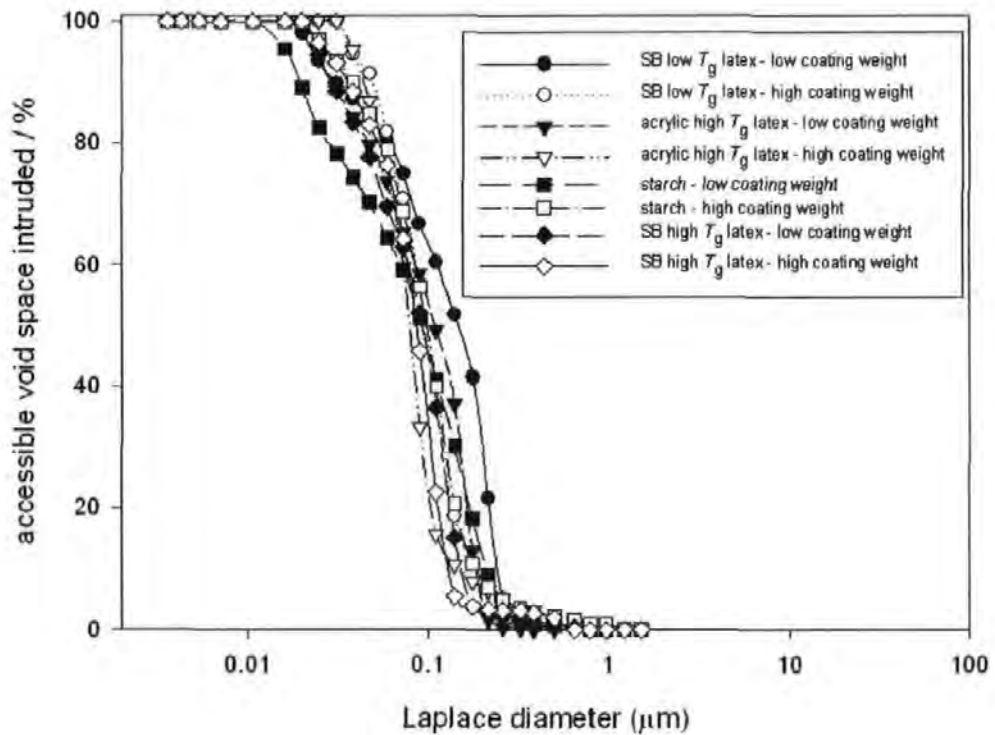
Figure 3.3 - HC90 + 10 w/w% binder.

91

Figure 3.2 and Figure 3.3 show the mercury intrusion curves for HC60 and HC90 with 10 w/w% of binder in the coating colour formulation.
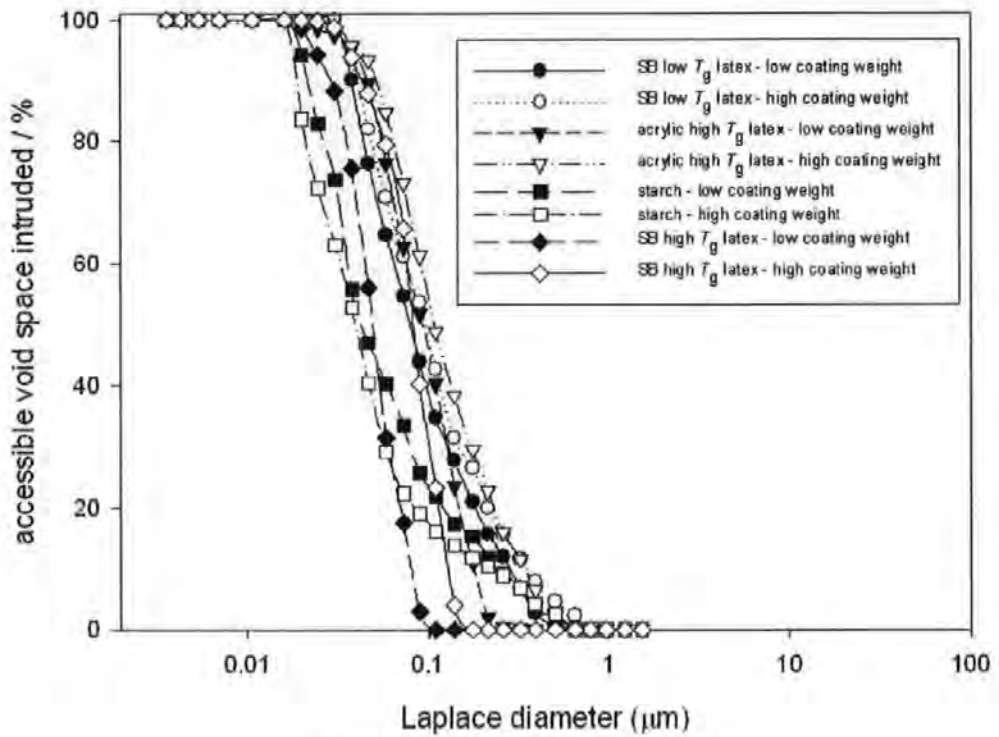
Figure 3.4 - HC60 + 25 w/w% binder
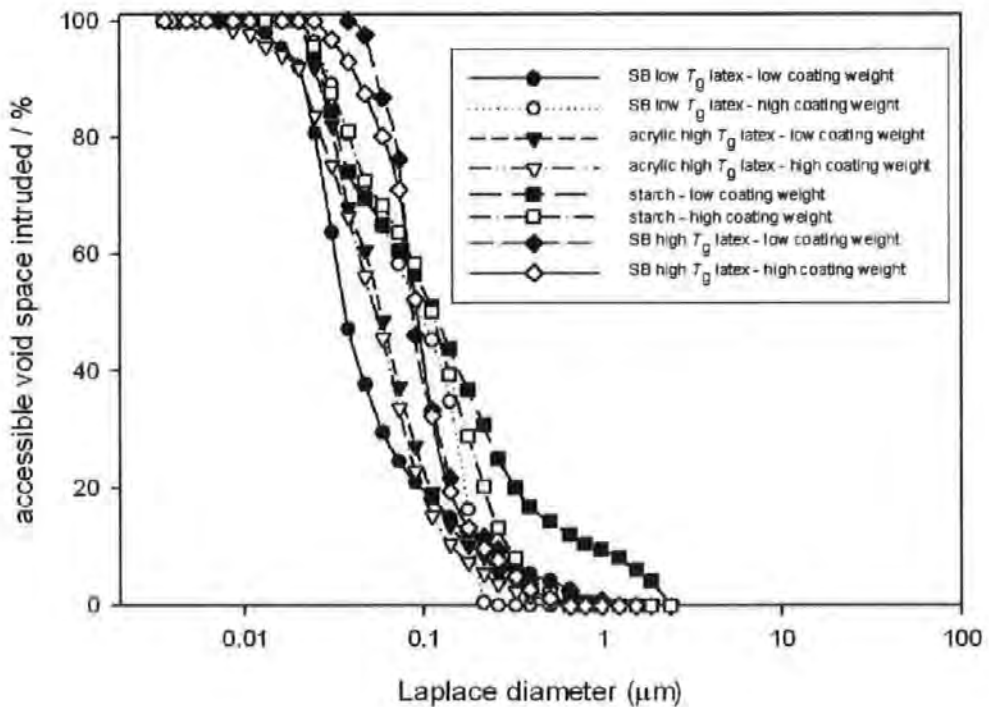
Figure 3.5 - HC90 + 25 w/w% binder.

Figure 3.4 and Figure 3.5 show the mercury intrusion curves for HC60 and HC90 with 25 w/w% of binder in the coating formulation. A higher concentration of binder in the coating formulation causes, as expected, a decrease in the value of porosity of the dry sample. It also causes an increase in the pressure required for intrusion, interpreted as a decrease in Laplace throat diameters.
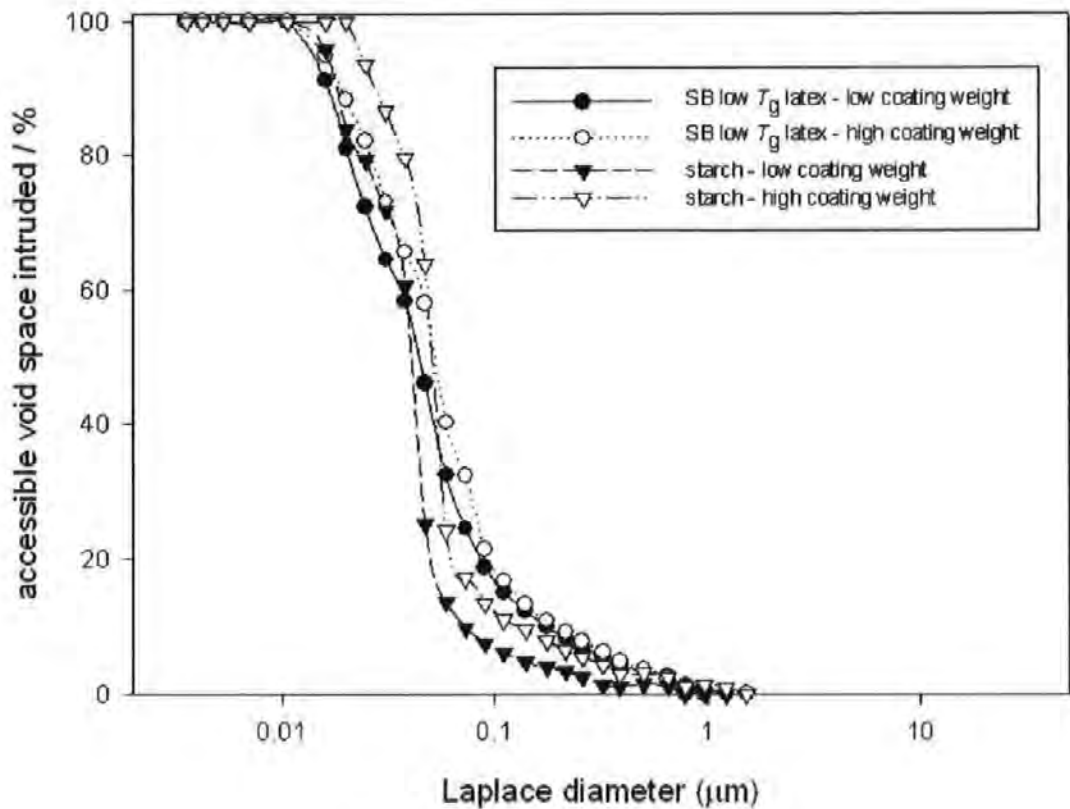
Figure 3.6 - DPP + 25 w/w% binder.

In Figure 3.6 the mercury intrusion curves for DPP-based coating formulations with 25 w/w% of either starch or SB low T_g are shown.

The mercury intrusion curves in Figure 3.2 to Figure 3.6 are used to model the network void structure of the dry paper coating layer with Pore-Cor. The modelling and results are presented in Chapter 5.

In the paper coating industry it is well known (Xiang and Bousfield, 2001) that the higher the coat weight, the lower the light scattering, which implies loss of porosity and reduction of layer thickness per unit weight of coating, i.e. densification. The original intrusion curves, before splitting and re-scaling, showed, in the case of low T_g latex and starch, higher values of porosity for higher coating weight applied. This anomalous trend in the porosity for low T_g latex and starch-based coating colours could be explained with the appearance of surface "mud-cracks" (Figure 3.9 to Figure 3.12) with size in the order of magnitude of micrometres. This "pore size" measured by the porosimeter and due to surface cracks lies outside the light scattering pore size and outside the pore size range that affects absorption, i.e. they are really discontinuities and therefore do not describe the compacted coating regions which have undergone shrinkage.

The porosities of the dry samples, after splitting and re-scaling, Table 3-1, all decreased on increasing the layer thickness from rod 2 to rod 3, an effect also observed by other workers (Xiang and Bousfield, 2001). The thinner coating layers had a thickness of the same order of size as the largest particles in the layer (5 µm), and so packing was constrained in respect to the lack of movement of the largest particles. In the thicker coatings, there was a greater possibility of particle movement during drying, and the resulting more efficient packing gave a lower porosity.

3.3 Electron microscopy

In order to confirm the presence of surface cracks, causing the observed bimodality of mercury intrusion curves, and to gather information on the coating layers, the surfaces of the dry samples with 25 w/w% binder were examined under scanning electron microscopy. HC90-based samples with 25 w/w% binder showed the larger bimodality in the mercury intrusion

curves, so they are chosen as illustrative samples of interest for this visual analysis in Figure 3.7 to Figure 3.12, where the scale bar is 5 μm.

It is interesting to notice that in Figure 3.7 the larger pigment particles protrude from the coating surface. These large particles act as a restraint to the freedom of particle-particle rearrangement in layers of limited thickness.
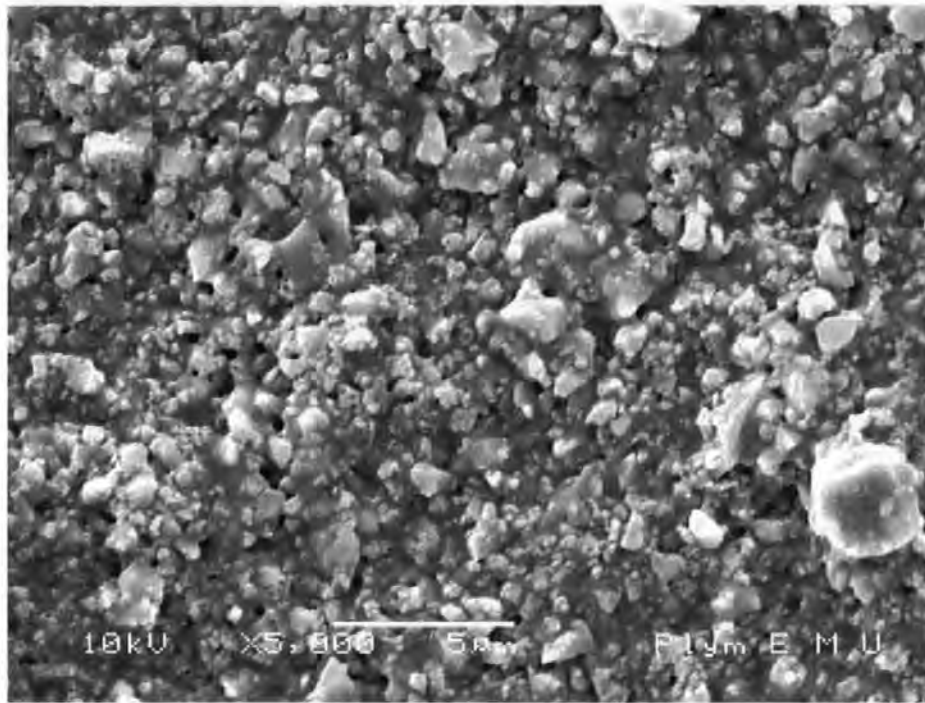
Figure 3.7 - Micrograph of a HC90 + 25 w/w% styrene-butadiene low T_g latex coating applied with rod 2.

Figure 3.8 shows that when the coating layer is thicker, there is much less protrusion from the coating layer surface. The particles are free to move, as none of them is larger than the coating layer thickness, and the filming latex then has the potential to hold the shrunken structure in place.

Figure 3.9 and Figure 3.10 show the surface of coating prepared using high T_g acrylic latex as binder. It appears that, on the surface of the coating, the latex has film-formed. It can also be noted that cracks begin to form as a relief of stress within the rigid structure provided by the acrylic high T_g latex. The latex used in the preparation of these samples should not film-form in the experimental condition (too low drying temperature). By analysing under higher resolution, it can be seen that the cracks here go deep into the coating structure and that the film-forming is a phenomenon localised on the surface of the coating layer. This effective filming is then probably related to soluble chemical species in the latex serum, like monomers or oligomers of the latex, and in the liquid phase of the carbonate slurry, which are able to migrate to the surface of the coating layer. The filming is probably not because the latex is raised above its glass transition. This evidence supports the previous claim (section 1.8.7) that observed organic species on the surface of dried coatings do not necessarily imply that latex binder has migrated.
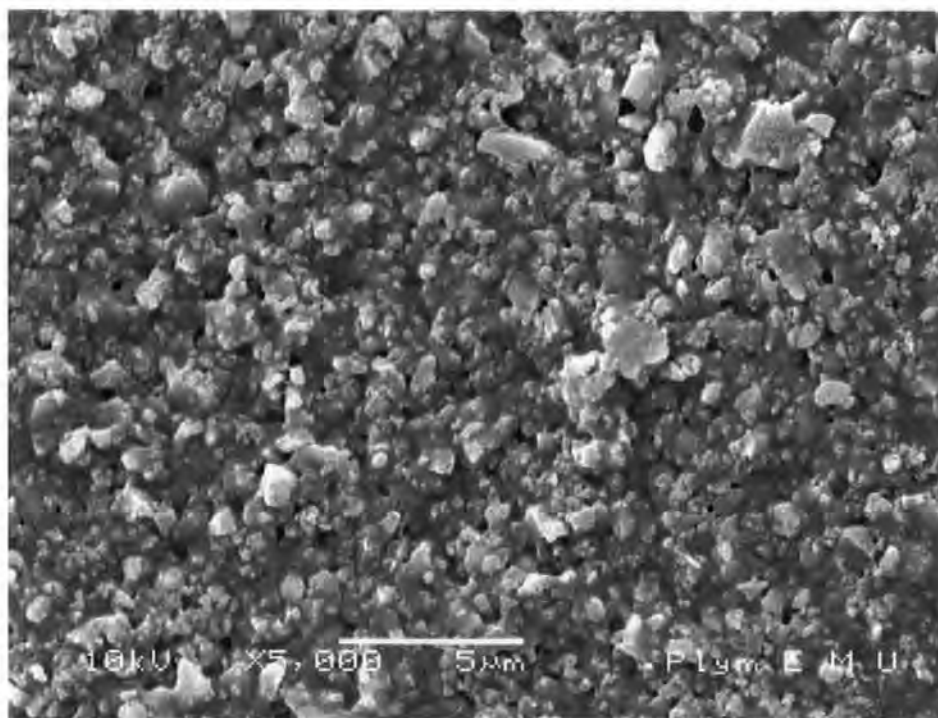
Figure 3.8 - Micrograph of a HC90 + 25 w/w% styrene-butadiene low T_g latex coating applied with rod 3.
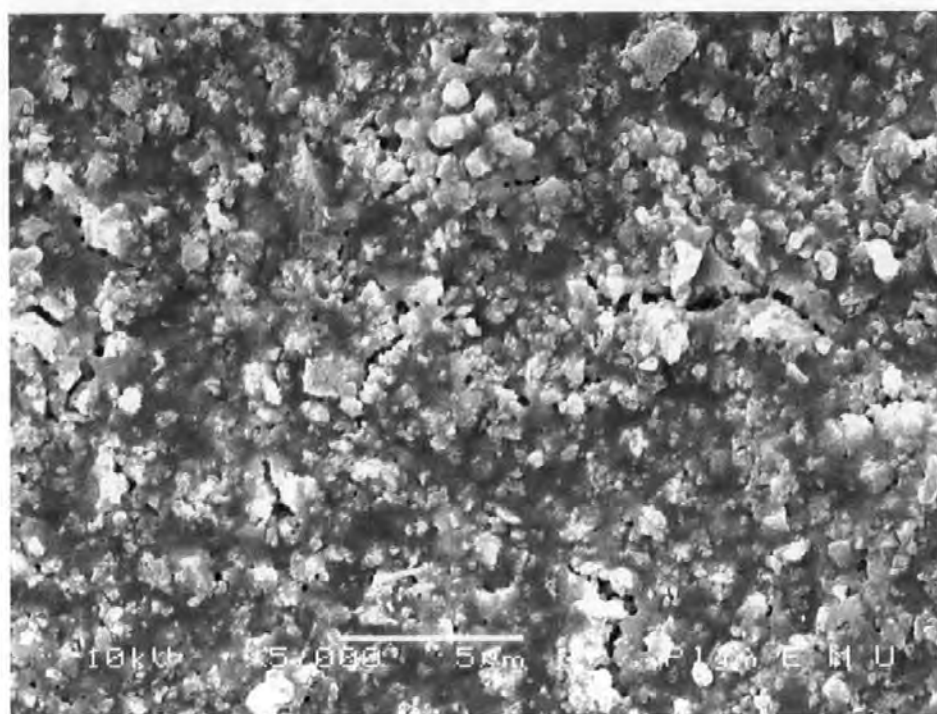
Figure 3.9 - Micrograph of a HC90 + 25 w/w% acrylic high T_g latex coating applied with rod 2.
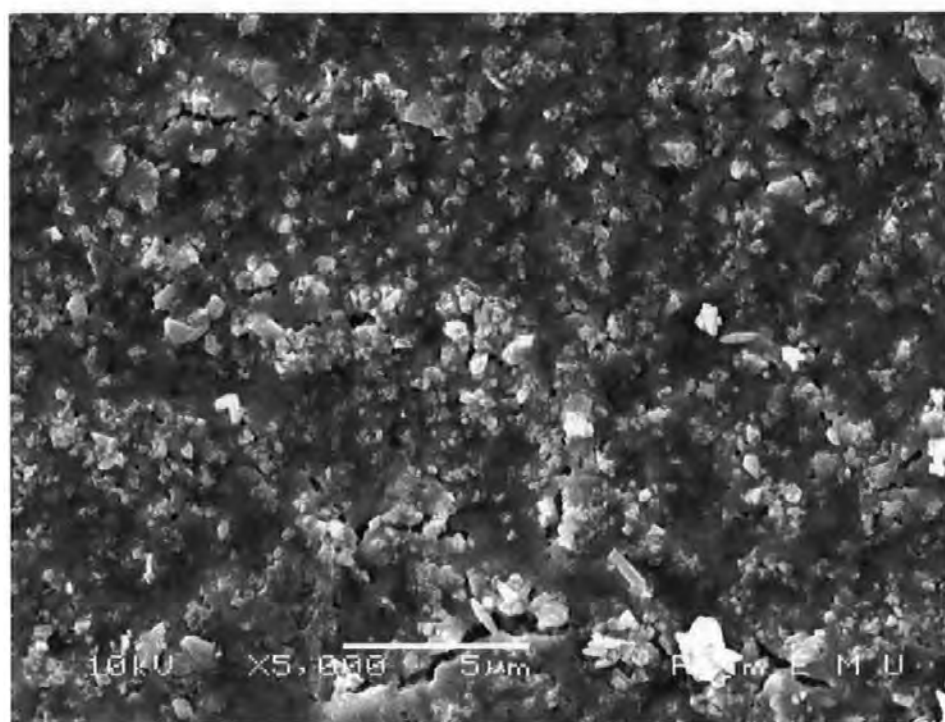
Figure 3.10 - Micrograph of a HC90 + 25 w/w% acrylic high T_g latex coating applied with rod 3.

97
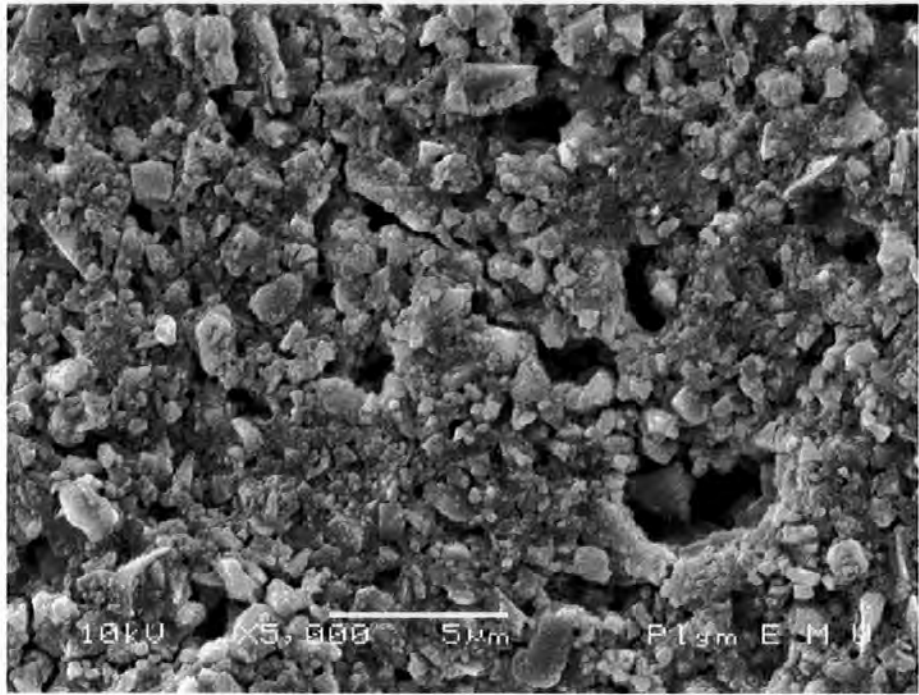
Figure 3.11 - Micrograph of HC90 + 25 w/w% starch coating applied with rod 2.
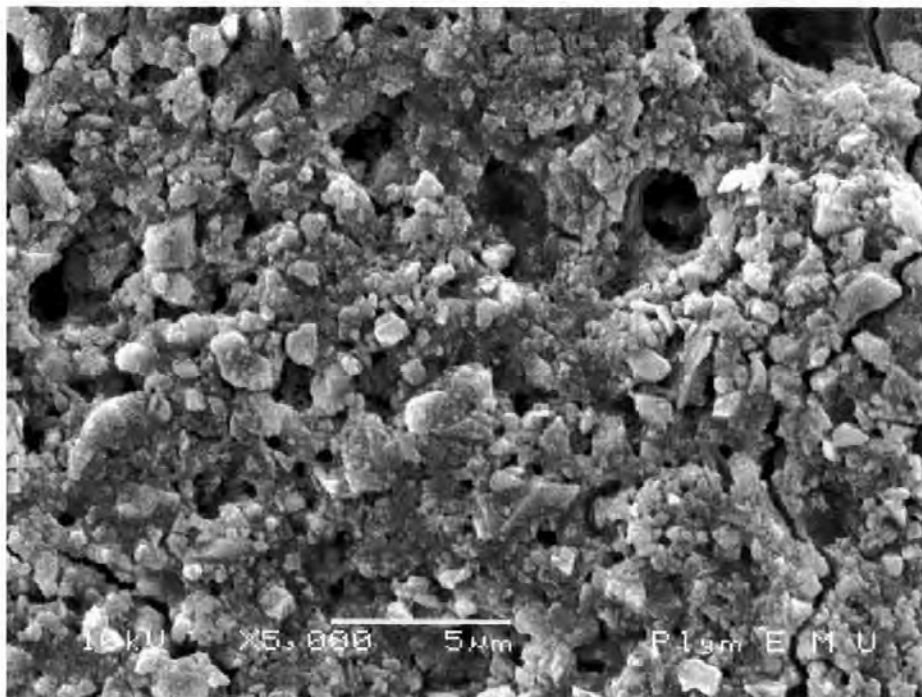
Figure 3.12 - Micrograph of a HC90 + 25 w/w% starch coating applied with rod 3.

Figure 3.11 shows the surface of a low coating weight HC90 and starch based coating layer. It can be observed that the particles on the coating layer surface appear larger in size than those

observed in latex-based coating formulations. The voids between the particles are also larger. At this stage some form of aggregation or flocculation could be suspected. 'Mud cracks' can be seen on the surface and many of the larger particles are protruding from the coating layer surface. These larger particles represent a serious constraint to rearrangement at light coat weight application on this substrate. The structure in Figure 3.12 is more consolidated and closely packed, as the restraint to the freedom of rearrangement of the particles, by elements larger than the coating thickness, plays a less important role in thicker coating layers.

3.4 Shrinkage stress measurements

3.4.1 Results

Using the novel experimental method described in section 2.2, the progressive extents of curl as a function of drying were converted to shrinkage force per unit of coated area, i.e. shrinkage stress, τ. Weight losses were expressed as % weight loss relative to the infinite time ($t \to \infty$) asymptote. Figure 3.13 and Figure 3.14 show the results obtained for five replicates for two different coating formulations. For further analysis of the formulation behaviour, the data from the replicate that most closely followed the average fitting curve was chosen (replicate 3 in both Figure 3.13 and Figure 3.14). The average deviation of the experimental points from these curves, relative to the maximum value of the representative curve, were 3.3 % and 3.5 % respectively. The same procedure was repeated for each curve shown in Figure 3.15 to Figure 3.24.
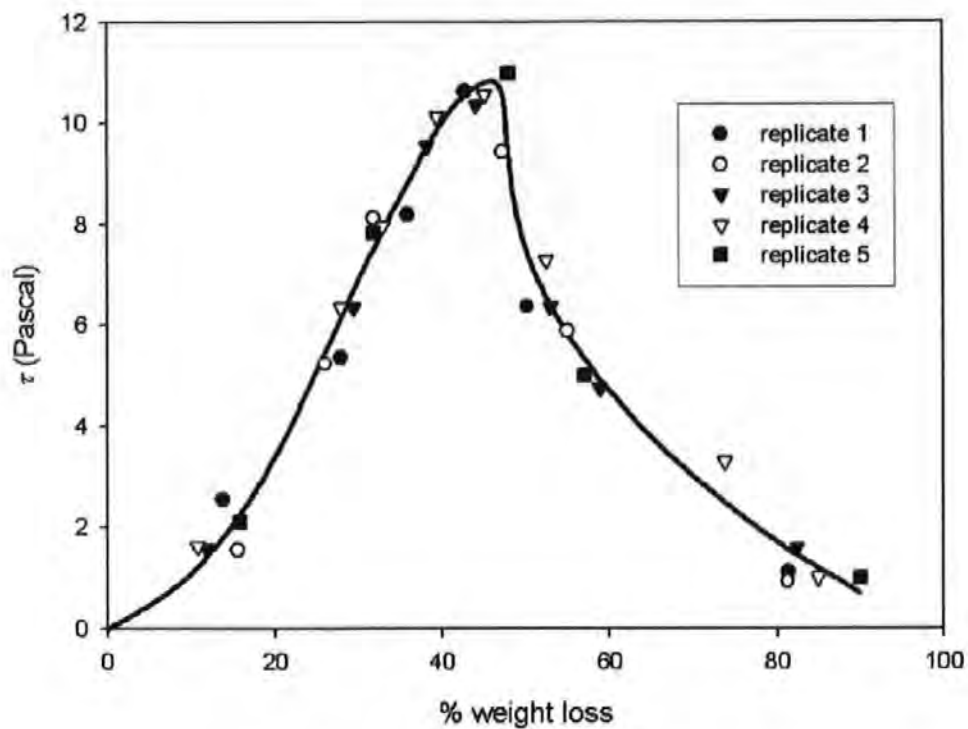
Figure 3.13 - Hydrocarb 90 with 25 % acrylic high T_g latex – low coating weight.
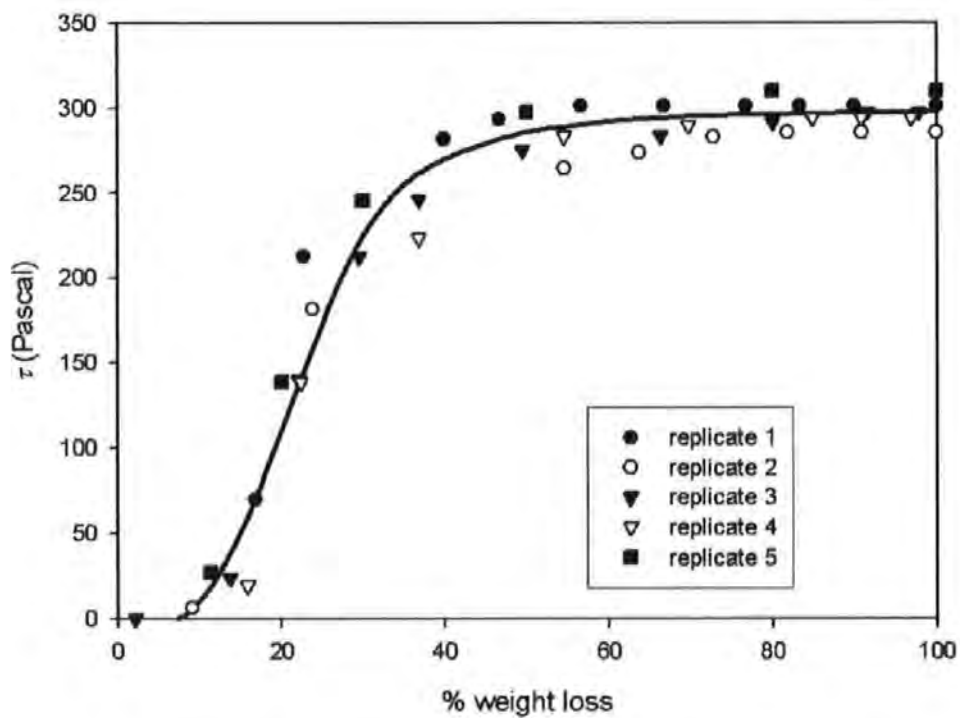
Figure 3.14 - Hydrocarb 90 with 25 % starch – low coating weight.

100

First we consider the control experiments containing singly each component of the coating colour alone. The bending of the samples coated with $CaCO_3$ slurry or with the latex suspensions alone at low coat weight (using rod 2) was too rapid and too small to be observed with the apparatus. The strips coated with $CaCO_3$ only retained no stress and so did the strips coated with high T_g latices. The low T_g latex- and starch-coated strips did not return to their original position, retaining part of the stress. The starch data series refers to a starch solution with a 15 w/w% solid content.
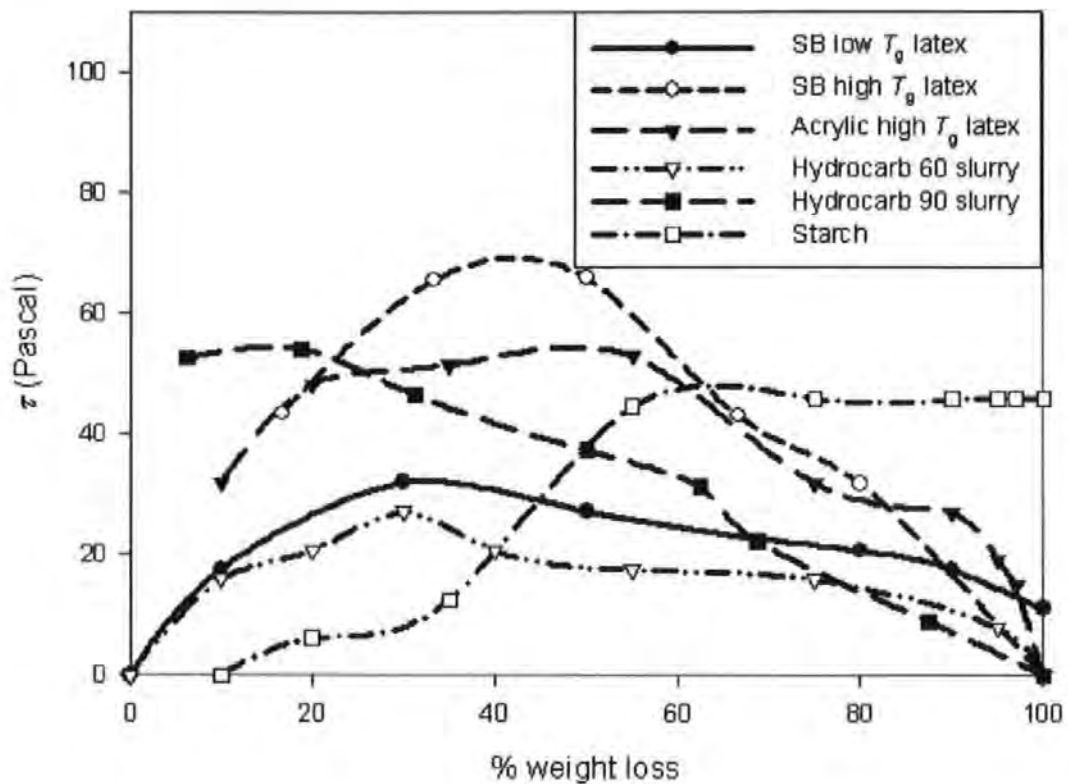
Figure 3.15 - CaCO₃ slurries only; binders only.

Figure 3.15 shows the results for the $CaCO_3$ slurries at higher coat weight (rod 3) without binder. The stresses reached a peak of about 50 - 60 Pa in the case of the finer mineral pigment (HC90) and 30 Pa in the case of the coarser one (HC60). As the weight loss continued, the stresses in the samples returned to zero.

101

Also shown in Figure 3.15 are the control experiments with binder suspensions only. The high T_g latices gave rise to a maximum stress of about 50-60 Pa and ultimately no stress retention, while the low T_g showed a smaller stress peak value (30 Pa) and a very small stress retention. It is interesting to notice that the starch solution gave rise to a maximum stress of 46 Pa, which is lower than the stress generated by the high T_g latex. The starch layer retained 100 % of the maximum stress.
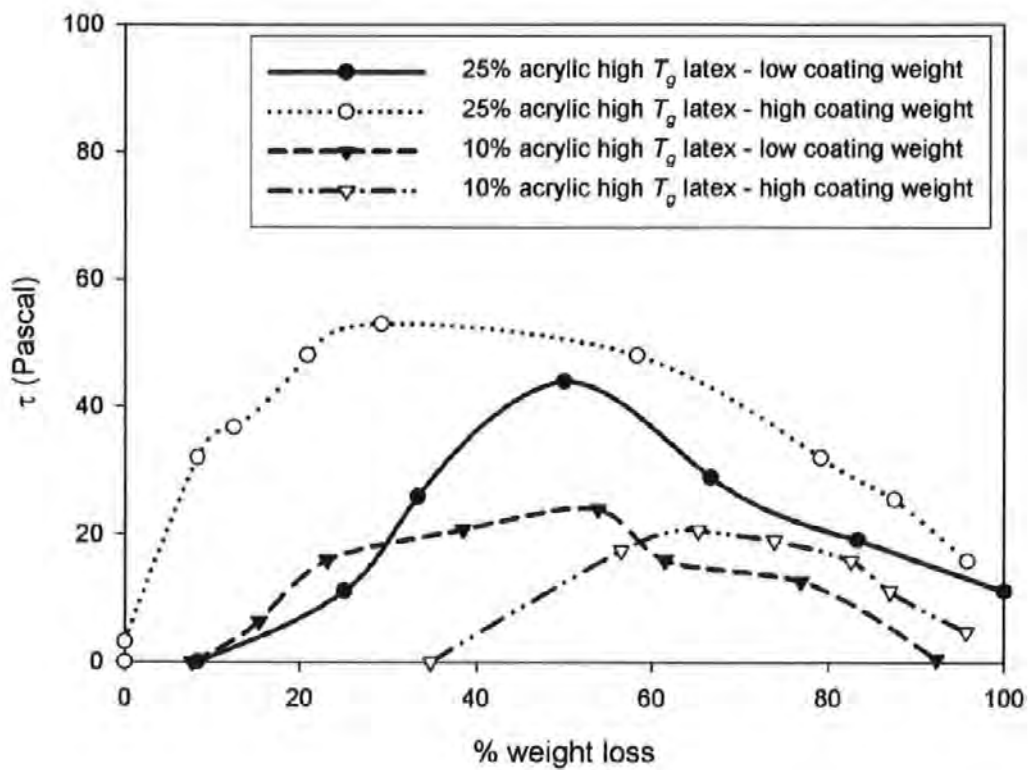
Figure 3.16 - HC60 (coarse) with acrylic high T_g latex.
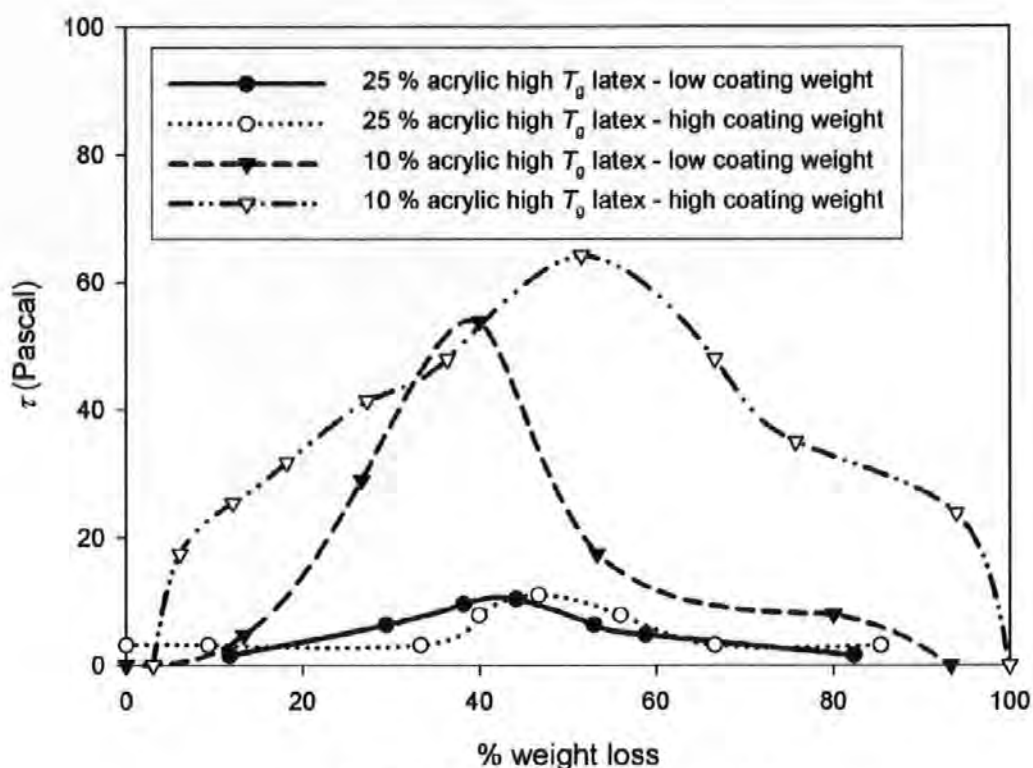
Figure 3.17 - HC90 (fine) with acrylic high T_g latex.

The graphs in Figure 3.16 and Figure 3.17 show the results for complete coating colours. All the samples contain the high T_g acrylic latex. It can be seen that the stresses are insensitive to the coat weight and hence thickness of the coating layer. The amount of latex affected the two different mineral pigments in opposite ways. In the case of the coarser pigment, Figure 3.16, the maximum stress was around 20 Pa in the case of low binder content and 45-55 Pa in the case of high binder content. For the finer pigment, Figure 3.17, the maximum stress was very low (11 Pa) for higher binder content, and about 50-60 Pa for the lower binder content. In all these cases with the high T_g acrylic latex there was minimal stress retention at the end of the drying process. The maximum measured stress, the retained stress and the % water loss at the SCC are summarised in Tables 3.2 to 3.4.
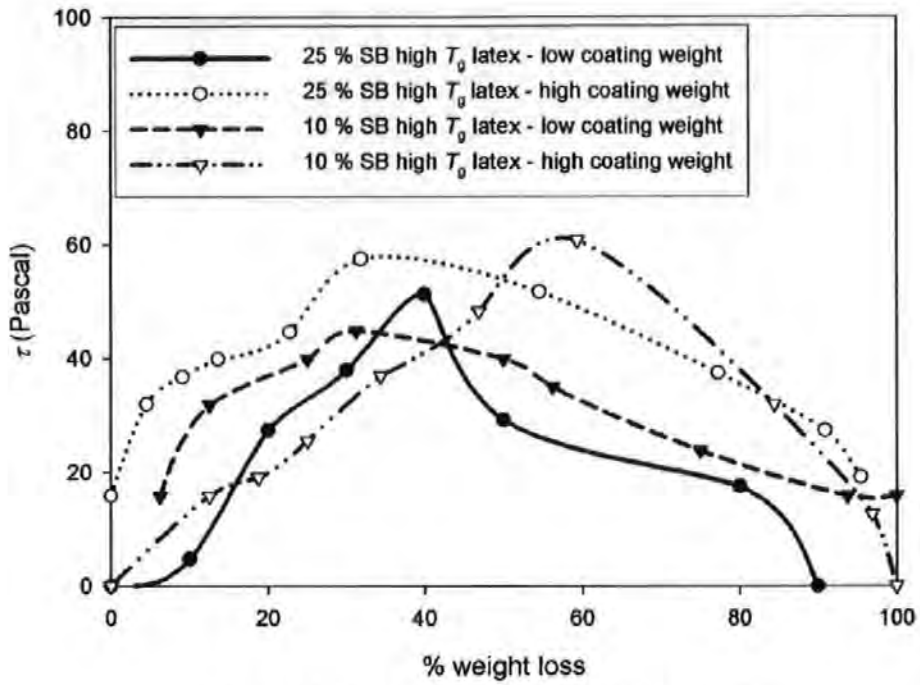
Figure 3.18 - HC60 (coarse) with SB high T_g latex.
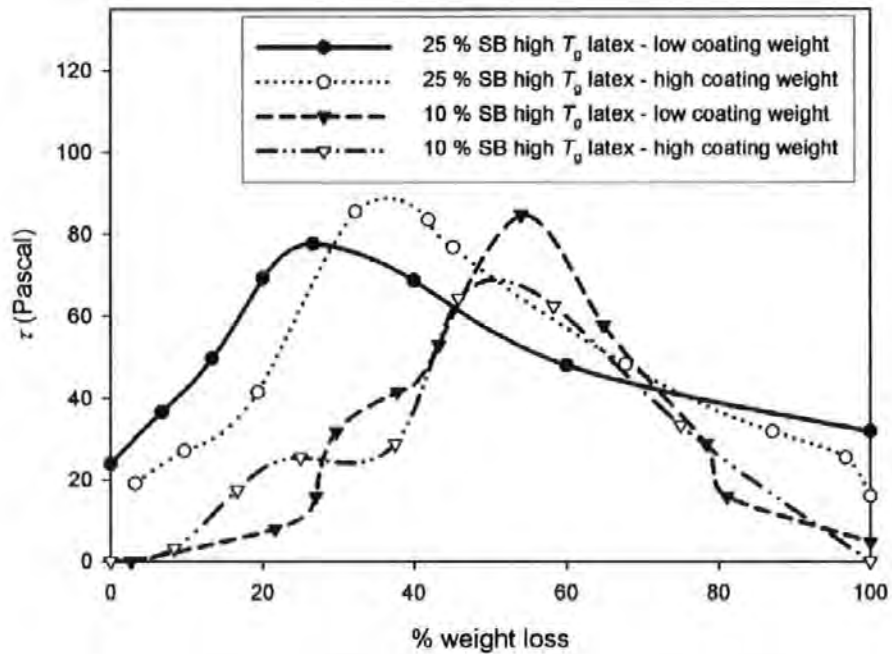
Figure 3.19 - HC90 (fine) with SB high T_g latex.

Figure 3.18 and Figure 3.19 show the results for the pigments together with the high T_g styrene

butadiene (SB) latex. The stresses were relatively insensitive to the thickness of the coating

layer and the amount of binder used. There was a small but significant difference between the

104

maximum stress for the coarse calcium carbonate (50-60 Pa), Figure 3.18, and the fine calcium carbonate (80-90 Pa), Figure 3.19, as was seen for the $CaCO_3$ slurries alone. There was once again minimal stress retention for high T_g latex.

Figure 3.20 and Figure 3.21 show the results for $CaCO_3$ in the presence of low T_g SB latex. The coarser mineral pigment (Figure 3.20) shows similar trends for similar coating compositions, with the coatings prepared with 25 w/w% latex showing maximum stresses far larger than those with 10 w/w%. Coating thickness had relatively little effect. Figure 3.21 shows a mixed behaviour: at low % weight loss the shrinkage stress is determined by the amount of binder whereas at higher weight loss the effect of coating weight becomes more important. The most significant difference is that all the samples containing the SB low T_g latex stayed curled indefinitely and retained between 39 % and 96 % of the maximum stress during drying.
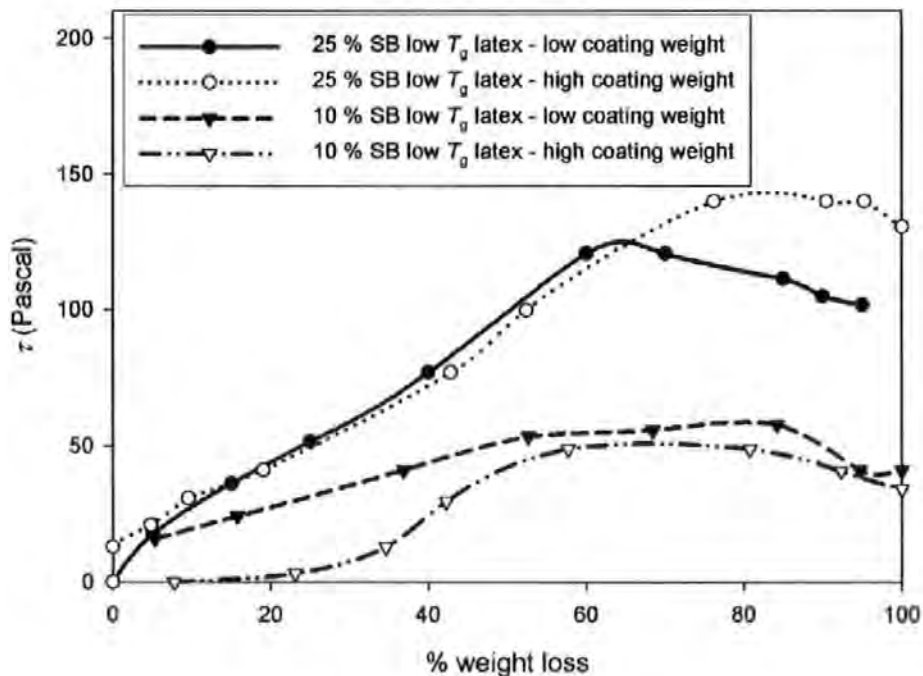
Figure 3.20 - HC60 (coarse) with SB low T_g latex.
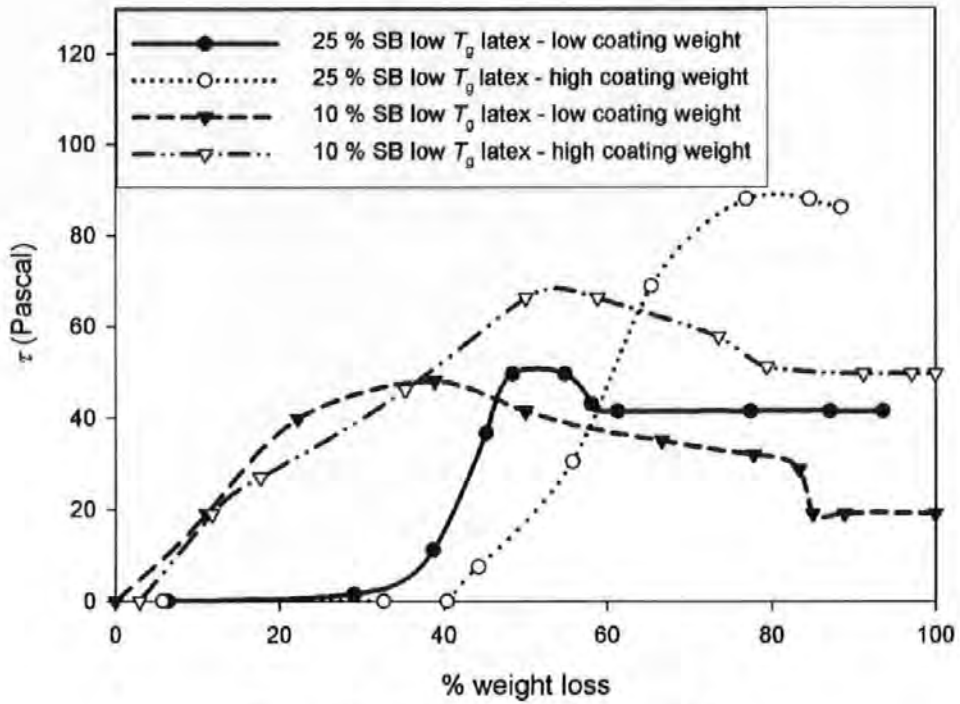
Figure 3.21 - HC90 (fine) with SB low T_g latex.

Figure 3.22 and Figure 3.23 show the stresses measured on drying of colours bound with starch. The stresses are an order of magnitude higher than those with latex, and, unlike in the cases of slurry only or with latex, those with the coarser calcium carbonate (Figure 3.22) are higher than those with the finer (Figure 3.23). The stresses are highly dependent on coating weight. The amount of starch is seen to affect the coarse pigment samples (Figure 3.22) but not the fine (Figure 3.23). All the samples show a high degree of stress retention, up to 100 % of the maximum stress.
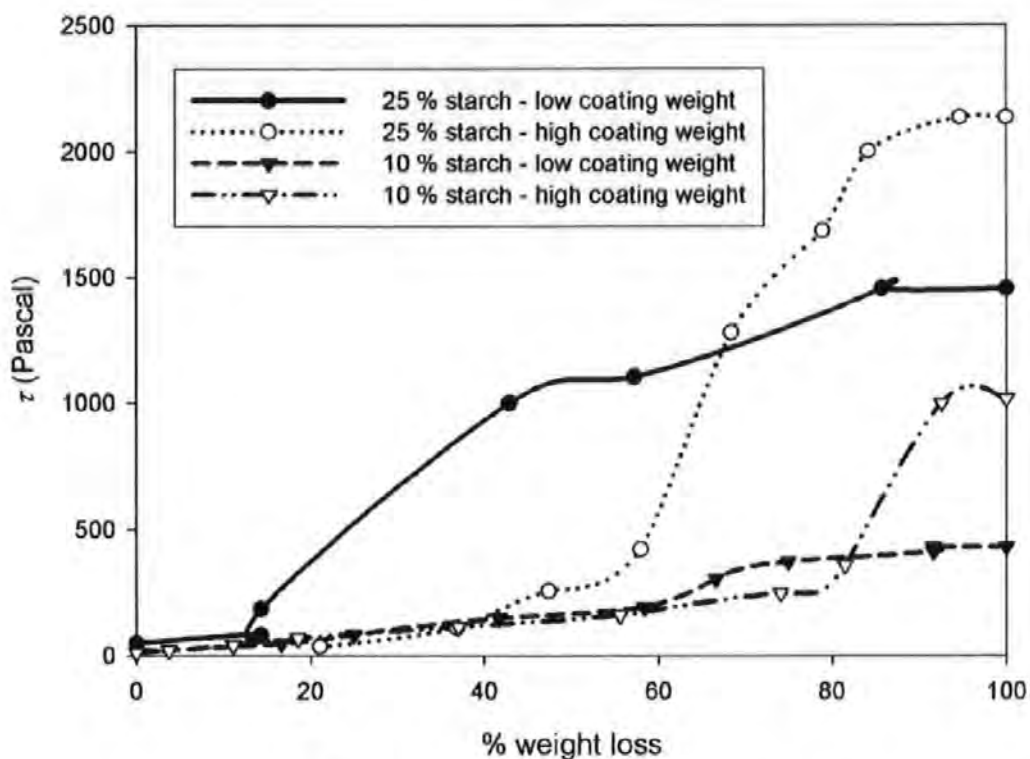
Figure 3.22 - HC60 (coarse) with starch.
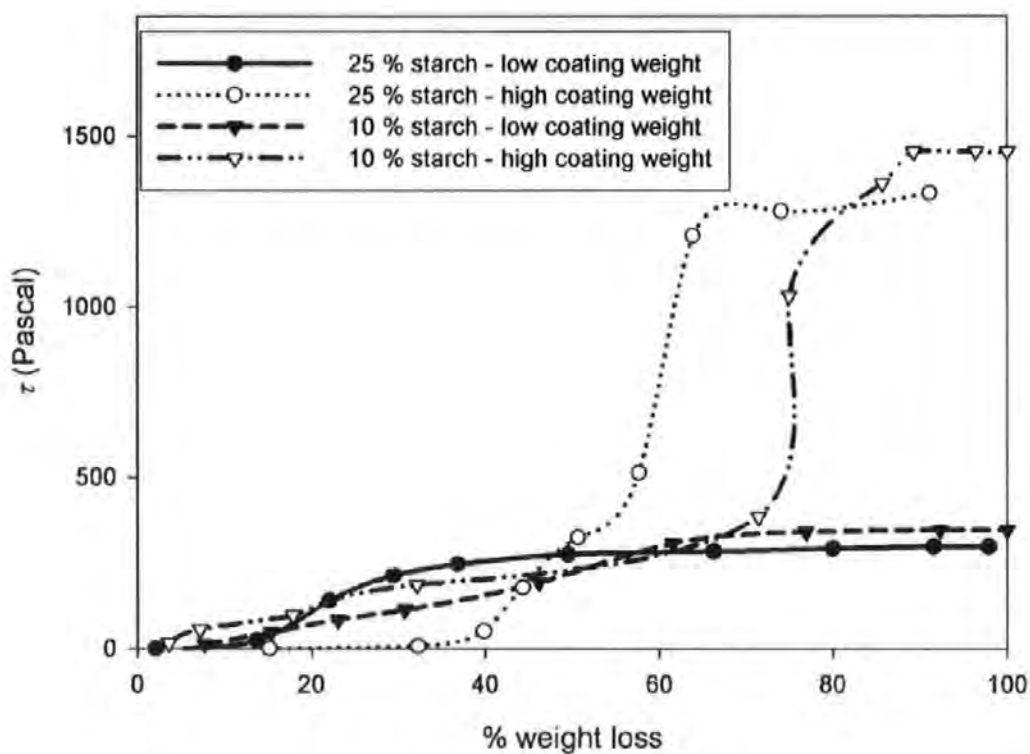
Figure 3.23 - HC90 (fine) with starch.

As a final control experiment, to test potential interaction phenomena and the effect of the particle size distribution, the broad size distribution calcium carbonate pigments were replaced by the monosized polystyrene pigment DPP 3710, Figure 3.24, with either 25 w/w% SB low T_g latex or 25 w/w% starch. Unlike the case of starch-containing CaCO$_3$-based colours, the thickness of the coating layer did not affect the stress acting upon drying. The maximum stress measured was 230-260 Pa in the case of starch-containing coating colours and 45 Pa, with a stress retention of about 30 Pa on drying, in the case of low T_g latex–containing coating colours.
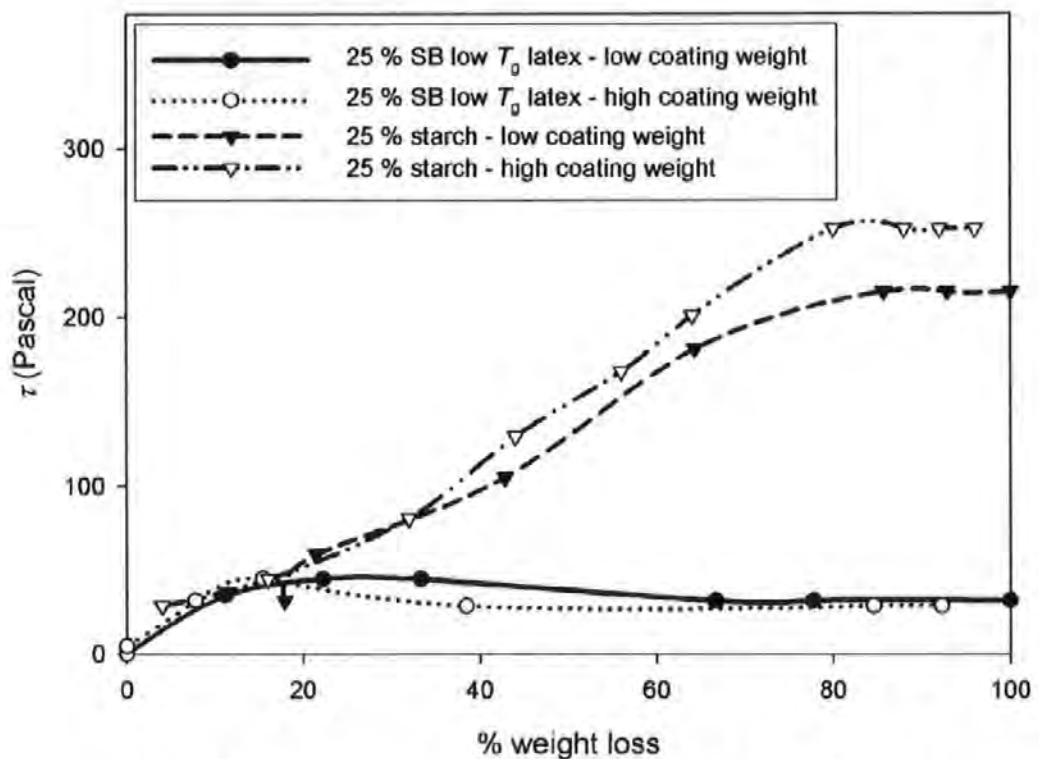
Figure 3.24 - Polystyrene pigment with either SB low T_g latex or starch.

3.4.2 Discussion

First let us consider the control experiment with the calcium carbonate only, Figure 3.15. As water evaporates from the structure, menisci recede through it and exert capillary forces. Summed over the whole sample, these forces rise to a stress of nearly 60 Pa between the finer

HC90 particles (smaller capillaries and hence high forces), and 30 Pa between the coarser HC60 particles. There is nothing to retain the stress which, therefore, disappears completely as the sample dries.

Latex on its own produced shrinkage stresses of between 50 and 70 Pa for high T_g latex, and 30 Pa for low T_g latex. So menisci forces acted amongst these arrays of spheres, but as expected were relieved by the deformability and film-forming tendencies of the low T_g latex. Starch produced a maximum shrinkage stress of 45 Pa. Starch is a dissolved binder, and therefore any shrinkage is due to the shrinkage of the tertiary structures of the polymer chains, a factor not relevant to the mixed polymer-carbonate systems which are the focus of this work. It is interesting to notice that the starch layer retained 100 % of the maximum shrinkage stress, which is less than that produced by high T_g latex, confirming that polymer shrinkage plays only a minor role in the shrinkage of a paper coating layer.

Deducing the processes occurring in the pigment systems with binder is much more difficult, because there is no way of measuring the void structures at the FCC. From the definition of SCC, we can assume that the SCC skeletal structure is the same as that of the dry sample. So we have to make educated guesses of the FCC structures, and match the change from the guessed FCC to the known SCC with the experimental stress and porosity results. The maximum measured stress, the retained stress and the % water loss at the SCC are shown in Figures 3.16 to 3.23 and also summarised in Tables 3.2 to 3.4.

First we compare the HC60 results in Figure 3.15 (∇) with all those in Figure 3.16. It can be seen that the addition of 10 w/w% high T_g acrylic latex reduced the maximum stress from around 30 Pa to around 20 Pa, whereas increasing the amount of latex to 25 w/w% increased

the maximum stress to between 40 and 50 Pa, dependent on coating thickness. A possible cause of this is that the binder particles, which are around an order of magnitude smaller than the HC60 particles, create their own secondary porosity. This secondary porosity increases the meniscus forces and hence stresses during shrinkage. However, in doing this the binder fills gaps within the porous structure. So, increasing the binder concentration from 10 w/w% to 25 w/w% reduces the porosity from 24.8 % to around 18.9 %, Table 3-1.

For the finer HC90, with a low coat weight, there are very high porosities of around 38 %, Table 3-1, but increasing the amount of binder from 10 w/w% to 25 w/w% has little effect. An explanation is that the HC 90 particles are finer, and more similar in size to the binder, so that there is no dual porosity system as was formerly postulated for the coarser pigment system. The binder and pigment particles pack to give a very open, highly porous structure of 38 % or 25 % porosity at 10 w/w% binder, with stresses similar to those in the HC90 slurry, Figure 3.15 (■), and around three times larger than for HC60 alone. However, unlike HC60, increasing the amount of binder makes the stresses disappear. This suggests that the binder acts to prevent a change in structure between FCC and SCC. The high T_g latex spherical particles have a diameter between 0.15 and 0.20 μm, as stated by the manufacturer. The mercury porosimetry experimental data show intrusion of mercury for pressures corresponding to the same size range as the latex particles. This supports the fact that the latex particles can occlude part of the void structure formed by the mineral pigment particles and, being below their film-formation temperature and having a higher bulk modulus than low T_g latex particles, they do not allow the structure to deform under the action of the surface capillary forces. The micrographs (Figure 3.9 and Figure 3.10) suggest that there is some partial film-forming, and surface-cracking, after the drying has been completed. This is a phenomenon probably related

110

to soluble chemical species in the latex serum, as previously explained, and the values of bulk porosity measured for the high T_g based coatings tend to confirm this interpretation.

The contribution made by the chemical rather than physical properties of the latex can be inferred by substituting the second high T_g latex. Comparison of Figure 3.18 and Figure 3.19 with Figure 3.16 and Figure 3.17 shows that the stress effects are broadly similar, except that the dependence on amount of binder is now much reduced. Table 3-1 shows that the porosity effects are also broadly similar for the two types of high T_g latex.

Figure 3.20 and Figure 3.21 show that the effect of the film-forming SB low T_g latex is very different. All the samples now retain the stress when dry. For the coarser HC60, Figure 3.20, the amount of binder matters, but not the coat weight. For the finer HC90, Figure 3.21, both the amount of binder and the coating weight have an effect. We postulate that the first part of the drying process follows the same mechanism as for the high T_g latices. However, when the FCC has been reached, the latex particles, which are above their minimum film-forming temperature, begin to deform. Being more compressible than the high T_g latex particles under the forces of capillary action, they allow the deformation of the coating layer (and hence bending of the substrate). The FCC and SCC structures are therefore significantly different from each other in both structure and porosity than for the high T_g case. Once the structure has reached the SCC, the deformed latex retains a high fraction of the stress. The latex film occludes much of the pore structure, giving the lower porosities relative to the high T_g latices seen in Table 3-1. The values of τ measured for the two different coating weights applied can be explained as follows: in the case of higher applied coating weight and, therefore, higher thickness of the coating layer, the rearrangement of the particles under the capillary forces has more freedom and is not so influenced by the size of the particles in relation to the coating

thickness, while in the case of a thinner coating layer the maximum diameter of the mineral pigment particles, ~ 5 μm, is very close to the thickness of the layer, not allowing the free rearrangement of the structure in the x direction due to constraints in the z direction. When the structure is free to rearrange, the surface forces act freely for longer and the final dry structures show a lower value of porosity.

Figure 3.22 and Figure 3.23, when compared to the previous graphs, show that the addition of starch increases the stress by more than an order of magnitude relative to the addition of latex. For the coarser HC60, the stress depends on both coating weight and amount of added starch, whereas for the finer HC90, Figure 3.22, only the coating weight is important. An explanation is that partial adsorption of the starch on the pigment particles (Järnström *et al.*, 1995b; Järnström *et al.*, 1995a) and/or the relative solubility effect (Yan *et al.*, 2000) causes a depletion flocculation of the pigment particles, producing an open, loosely packing structure in which groups of flocs touch one another. The lack of close-packing reduces the effective number of fine capillary-like voids in the drying coating at the initial FCC. However, once the surface menisci form, the loose floc packing at FCC transforms to the tighter SCC packing as shown by lower values of dry porosity, Table 3-1. The change in dimension from loose to tight packing in this system is large and so the measured stress is correspondingly high.

If a monosized plastic pigment rather than a broad particle size distribution mineral pigment is used, Figure 3.24, starch produces much lower stresses. This indicates that there is a similarity between FCC structures and SCC structures when monosized pigments are used, and also suggests that with broad size particle distributions there is selective flocculation of different particle sizes of the mineral. With low T_g SB latex the stresses formed in the plastic pigment-containing colour are much the same as when $CaCO_3$ is present, although the structures have

even higher porosities, Table 3-1. All samples retain stress, as expected.

Table 3-2 - Maximum shrinkage stress (Pascal).

Sample :	Acrylic high T_g latex	Acrylic high T_g latex	SB high T_g latex	SB high T_g latex	SB low T_g latex	SB low T_g latex	Starch	Starch
Coating weight :	low	high	low	high	low	high	low	high
HC60 + 10 % binder	23	20	39	60	58	48	429	1015
HC60 + 25 % binder	43	52	51	57	120	140	1454	2132
HC90 + 10 % binder	53	64	84	64	48	66	347	1455
HC90 + 25 % binder	10	11	77	85	50	88	297	1333

Table 3-3 - Retained shrinkage stress (Pascal).

Sample :	Acrylic high T_g latex	Acrylic high T_g latex	SB high T_g latex	SB high T_g latex	SB low T_g latex	SB low T_g latex	Starch	Starch
Coating weight :	low	high	low	high	low	high	low	high
HC60 + 10 % binder	0	4	15	0	41	34	429	1015
HC60 + 25 % binder	11	12	0	16	101	130	1454	2132
HC90 + 10 % binder	0	0	4	0	19	49	347	1455
HC90 + 25 % binder	0	0	22	14	41	84	297	1333

Table 3-4 - % water loss by evaporation at the SCC.

Sample :	Acrylic high T_g latex	Acrylic high T_g latex	SB high T_g latex	SB high T_g latex	SB low T_g latex	SB low T_g latex	Starch	Starch
Coating weight :	low	high	low	high	low	high	low	high
HC60 + 10 % binder	54	65	50	59	84	57	91	92
HC60 + 25 % binder	50	30	40	32	60	76	85	91
HC90 + 10 % binder	40	51	54	46	39	50	78	87
HC90 + 25 % binder	44	47	27	32	49	76	80	92

4 RHEOLOGY AND FLOW PROPERTIES OF COATING COLOURS

4.1 Introduction

This chapter is divided into four different sections, presenting the results of four different experiments. The first experiment (section 4.2) was carried out with a Brookfield viscometer (section 2.1.3) in order to measure the interaction between calcium carbonate and latex particles at different latex volume concentrations. Section 4.3 shows the second series of results of the rheological analysis, carried out with the StressTech instrument (section 2.1.4), on the coating colour formulation used in the bending strip experiments (section 3.4). Yield stress measurement (section 4.4) and controlled stress sweep measurements (section 4.5) were included using the StressTech instrument on the same set of samples.

4.2 Effect of latex volumetric concentration on Brookfield viscosity

4.2.1 Samples

The interactions, packing and flow behaviour between latex and $CaCO_3$ in the coating colour have been studied by Brookfield viscosity measurements. The aim of this study was to investigate how the latex particles and the $CaCO_3$ behave when mixed together in suspension and how their interaction is affected by the volumetric fraction of latex in the coating suspension.

A series of coating colours was prepared by mixing, as described in more detail in section 3.1.4. They were HC90 or HC60 slurries, respectively, with the same latices used in the preparation of the samples studied in Chapter 3. The volumetric fraction of mineral pigment was kept constant ($\phi_P = 0.2$), while the volumetric fraction of latex (ϕ_L) was increased from 0

(suspensions of $CaCO_3$ only) to 0.2, corresponding to a coating colour with 25 w/w% binder on a dry basis as also used in the bending strips experiments (Chapter 3). By using this technique, it was possible to keep the carbonate volume concentration constant while the solids content was raised by the addition of the latex volume fraction. The resultant measurement of Brookfield viscosity shows effectively how the latex particles in the coating colour suspension gradually fill the gaps between the pigment particles and how this affects the packing interactions between latex and pigment particles. If the viscosity rises linearly over the initial range of latex addition then it is possible to conclude that the latex particles are small enough to exist between the carbonate particles without disrupting their equilibrium packing and without establishing any other sorptive or chemical interaction. The viscosity then follows the Einstein volume fraction equation (Einstein, 1906; Einstein, 1911)

$$\eta_r = \frac{\eta}{\eta_0} = (1 + 2.5\phi), \qquad \text{Eq. 4.1}$$

where η_r is the relative viscosity defined as the ratio of the suspension viscosity, η, to the liquid phase viscosity, η_0, and ϕ ($=\phi_P + \phi_L$) is the volume fraction of solid particles, i.e. the viscosity is seen to be proportional to the total volume fraction, and corresponds to the linearity as a function of latex volume fraction addition.

At the concentration where the viscosity rises sharply with the addition of latex, then the latex is disrupting the mutual packing of the components or is taking part in some inter-particle interaction.

4.2.2 Results

The results are shown in Figures 4.1 to 4.6. It can be observed that the measured values of Brookfield viscosity (HA1 spindle at 100 min^{-1}, corresponding to a shear rate of 22 s^{-1}) for HC60- and HC90-based coating colours are similar at low latex volumetric fractions, when the

same latex is used, and that the increase in viscosity is almost linear with the volumetric concentration of binder in the suspension. This confirms that no significant interaction of a chemical nature is occurring between the latices and the pigments. In the case of HC60 this linear increase in viscosity continues throughout the range of binder volumetric concentration investigated, as can be observed in Figures 4.1, 4.3 and 4.5. However, in the case of HC90-based coating colours (Figures 4.2, 4.4 and 4.6), when the latex volumetric fraction reaches a value of 0.10-0.15, a steeper rise of the viscosity of the suspension can be observed. It can thus be deduced that the finer pigment, with its tighter packing per unit solids content, is more easily disrupted by the addition of latex once the latex level rises to a volume fraction of 0.10-0.15.
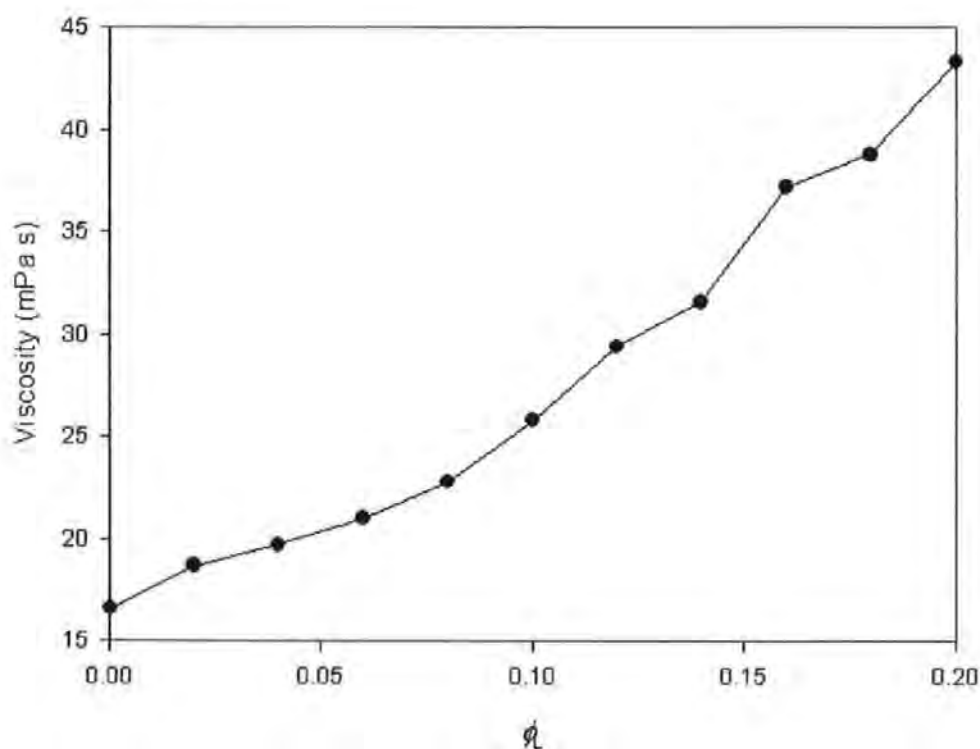
Figure 4.1 - Brookfield viscosity at 22 s^{-1} shear rate for HC60 and increasing volumetric fractions, ϕ_L, of acrylic high T_g latex. The curve follows the linearity of the Einstein model.

It is also interesting to observe that the values of Brookfield viscosity measured for different types of latex, when the same pigment was used, were all of the same order of magnitude,

116

independently from the chemical formulation and the film-forming properties of the latex. The only exception to this (Figure 4.6) is the styrene-butadiene low T_g with HC90 at high volumetric fractions of latex, which shows a higher value of viscosity.
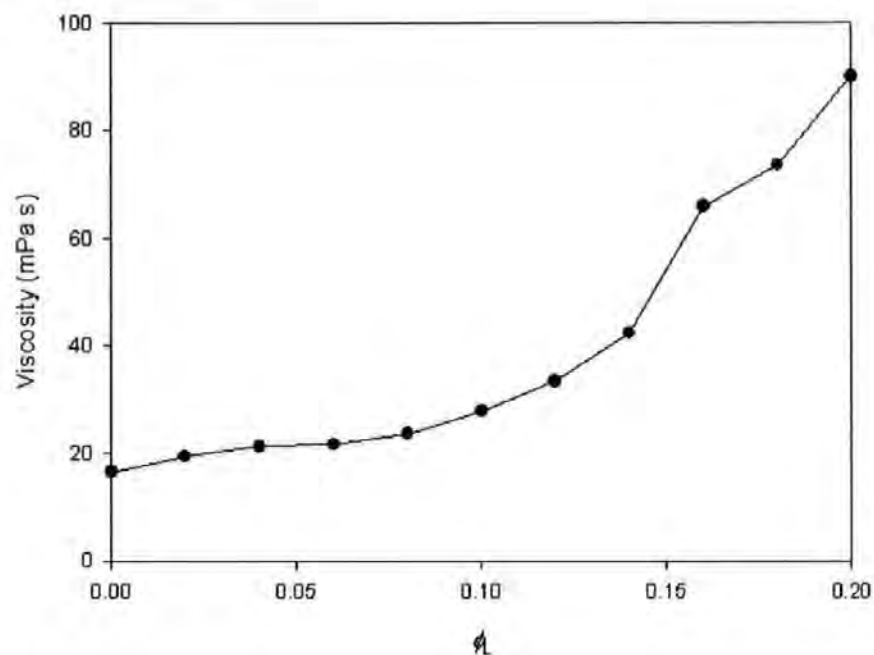
Figure 4.2 - Brookfield viscosity at 22 s^{-1} shear rate for HC90 and increasing volumetric fractions, ϕ_L, of acrylic high T_g latex. Note the rapid increase in viscosity above the volume fraction of ~0.15.
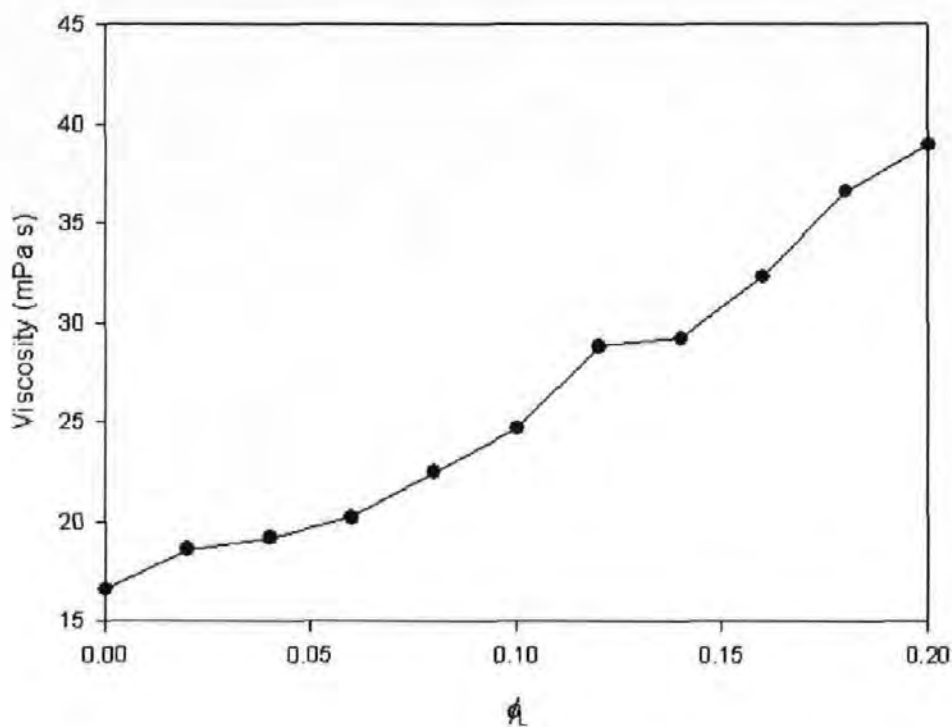
Figure 4.3 - Brookfield viscosity at 22 s⁻¹ shear rate for HC60 and increasing volumetric fractions, ϕ_L, of styrene-butadiene high T_g latex.
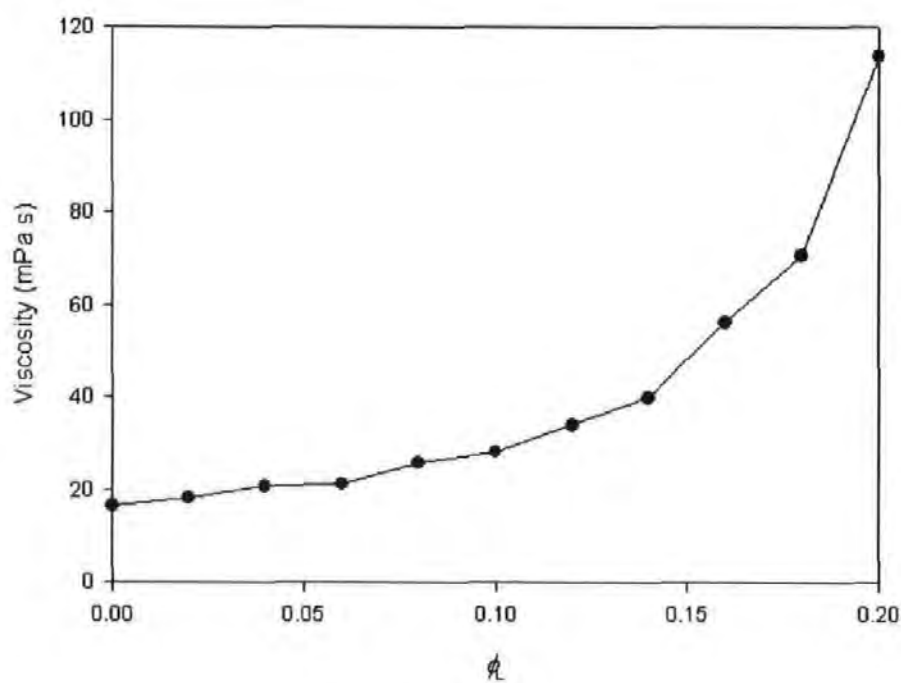
Figure 4.4 - Brookfield viscosity at 22 s⁻¹ shear rate for HC90 and increasing volumetric fractions, ϕ_L, of styrene-butadiene high T_g latex. Once again displays the increased viscosity due to packing disruption at higher latex volume fractions.

118
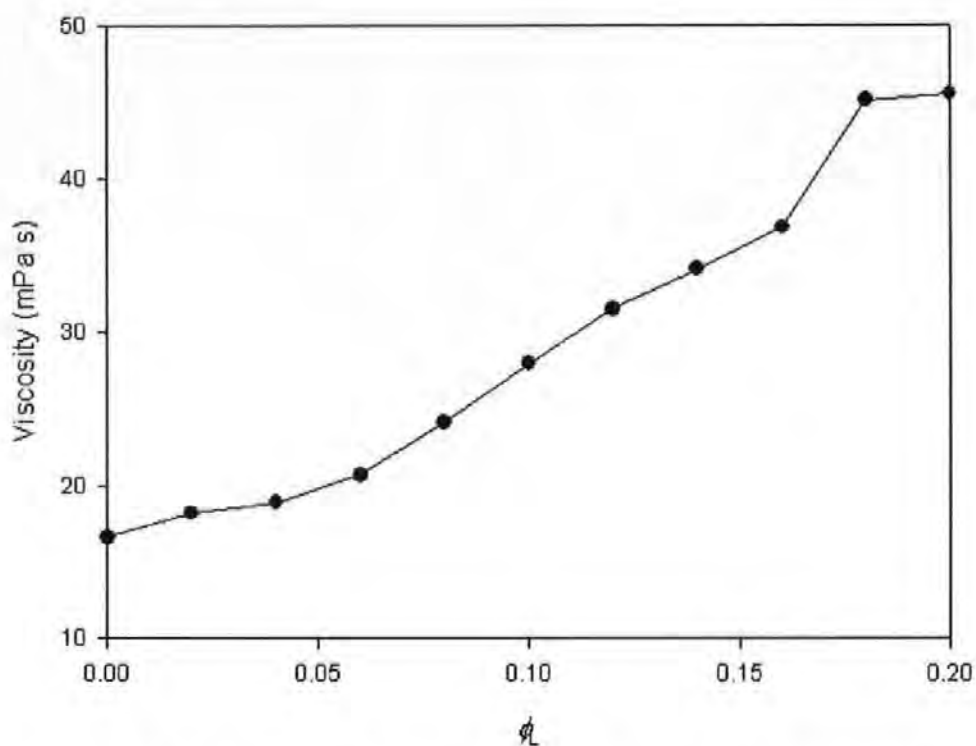
Figure 4.5 - Brookfield viscosity at 22 s^{-1} shear rate for HC60 and increasing volumetric fractions, ϕ_L, of styrene-butadiene low T_g latex.
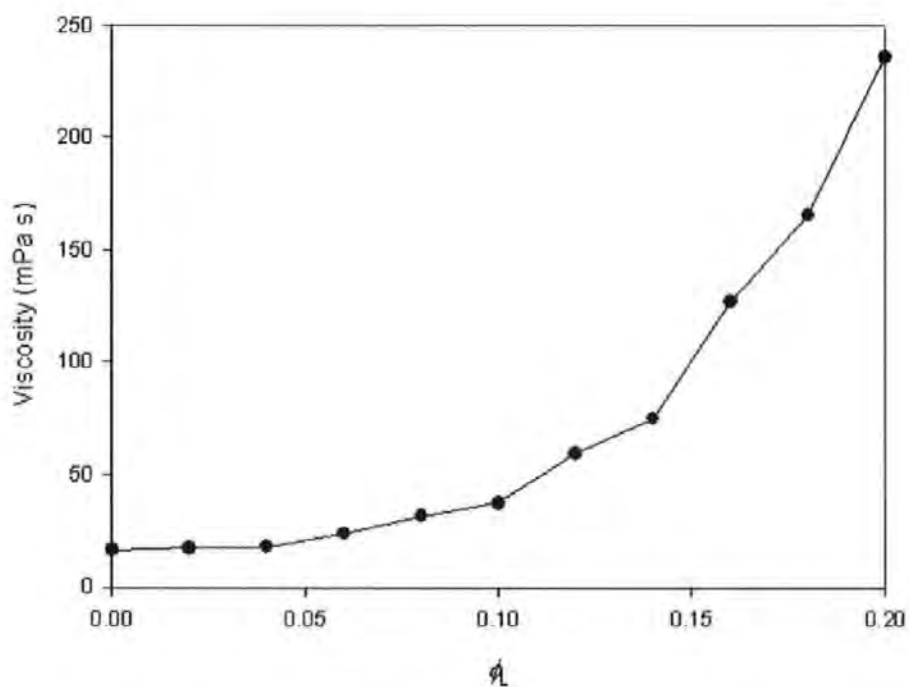
Figure 4.6 - Brookfield viscosity at 22 s^{-1} shear rate for HC90 and increasing volumetric fractions, ϕ_L, of styrene-butadiene low T_g latex. In this case, the disruption in packing due to the latex is the greatest in the series.

119

4.2.3 Discussion

As we have now seen, using the method of volume fraction, it is possible to determine the point at which there is an onset of packing or interactive disruption as latex is added to calcium carbonate. In the case of the coarse pigment HC60 (Figures 4.1, 4.3 and 4.5), there is apparently sufficient space between the pigment particles to allow for the additional volume fraction of latex without any additional disruption of the equilibrium packing properties, i.e. viscosity is a simple function of volume fraction content. Consequently, during the drying of such a mixture, it is expected that the structure will maintain similarity throughout the drying process if the process only involves the removal of water. This assumes that concentration of soluble species will have a minor role to play.

In the case of the finer HC90 (Figures 4.2, 4.4 and 4.6), on the other hand, higher volume fractions of latex induce a packing disorder or interaction with the pigment. This could be argued purely on the basis of particle packing or could be due to other interactions. From this test it is not possible to determine the exact nature of the interaction, though it is interesting to see that the low T_g styrene butadiene latex generates the most interaction. Given that the chemistry of the two carbonate pigments is the same, it is unlikely that the interaction is chemical, and we can assume that the rise in viscosity on addition to the HC90 is most likely to be due to packing.

The particle sizes of the different latices have been presented in section 3.1.3, and range from 0.14 for the SB high T_g latex to 0.2 μm for the acrylic high T_g latex. As later shown in section 6.5.2, HC90 has an average particle size, in terms of number percent of particles, of about 0.1 μm, while HC60 has an average particle size of about 0.5 μm. The latex particles are therefore of the same size or larger than the average HC90 particle and this will obviously

cause a disruption of the calcium carbonate packing. In the case of HC60, the latex particles are smaller than the average carbonate particle and do not cause disruption of the packing.

Once the packing disruption occurs, it is likely that the latex will be seen to play a very important role in determining the packing behaviour difference between that of a coating colour, containing pigment and latex, compared with the pure slurry of pigment alone as solids rises during the drying. The shrinkage properties will thus be strongly dependent on the latex particle size and physical properties, such as glass transition temperature, T_g, as well as any physico-chemical interactions that might be taking place.

4.3 Constant shear rate

The coating colour formulations containing HC60 or HC90 as mineral pigments and 25 w/w% of binder on a dry basis, used in the study of the shrinkage forces and fully described in section 3.1, were also studied using a StressTech controlled stress/strain rheometer (section 2.1.4). The solid content of these coating colour formulations was 55 w/w%. First a series of measurements of viscosity and shear stress at constant shear rate were carried out, over a range of shear rates from 5 to 1 000 s^{-1}. Yield stress and stress sweep measurements were also carried out and the results will be presented in section 4.3 and 4.4.

4.3.1 Results

Figure 4.7 and Figure 4.8 show the viscosity and shear stress measured at constant shear rate for coating colours containing 25 w/w% on a dry basis of acrylic high T_g latex with HC60 and HC90, respectively. It can be observed that the coating colour containing the finer calcium carbonate (HC90) shows higher values of viscosity and higher shear stress in the whole range of shear rate investigated.
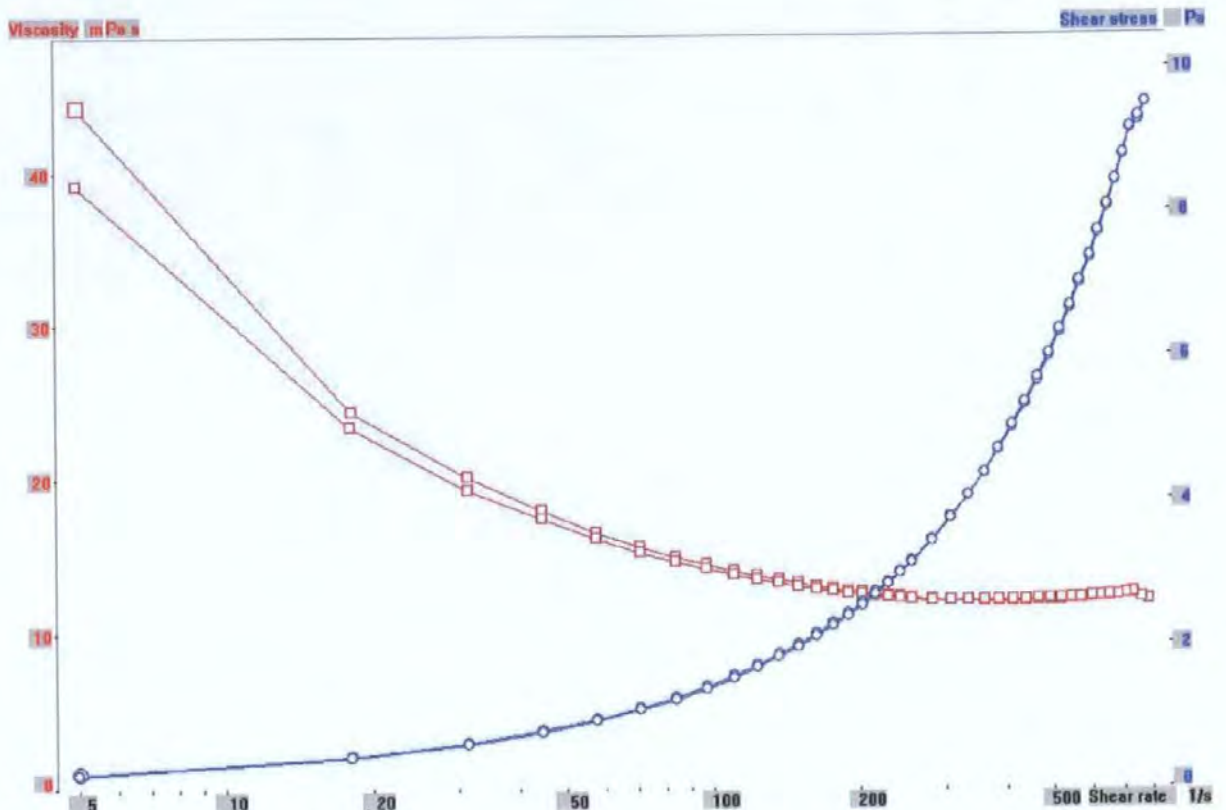
Figure 4.7 - Viscosity (red) and shear stress (blue) for HC60 + 25 w/w% acrylic high T_g latex as a function of shear rate.
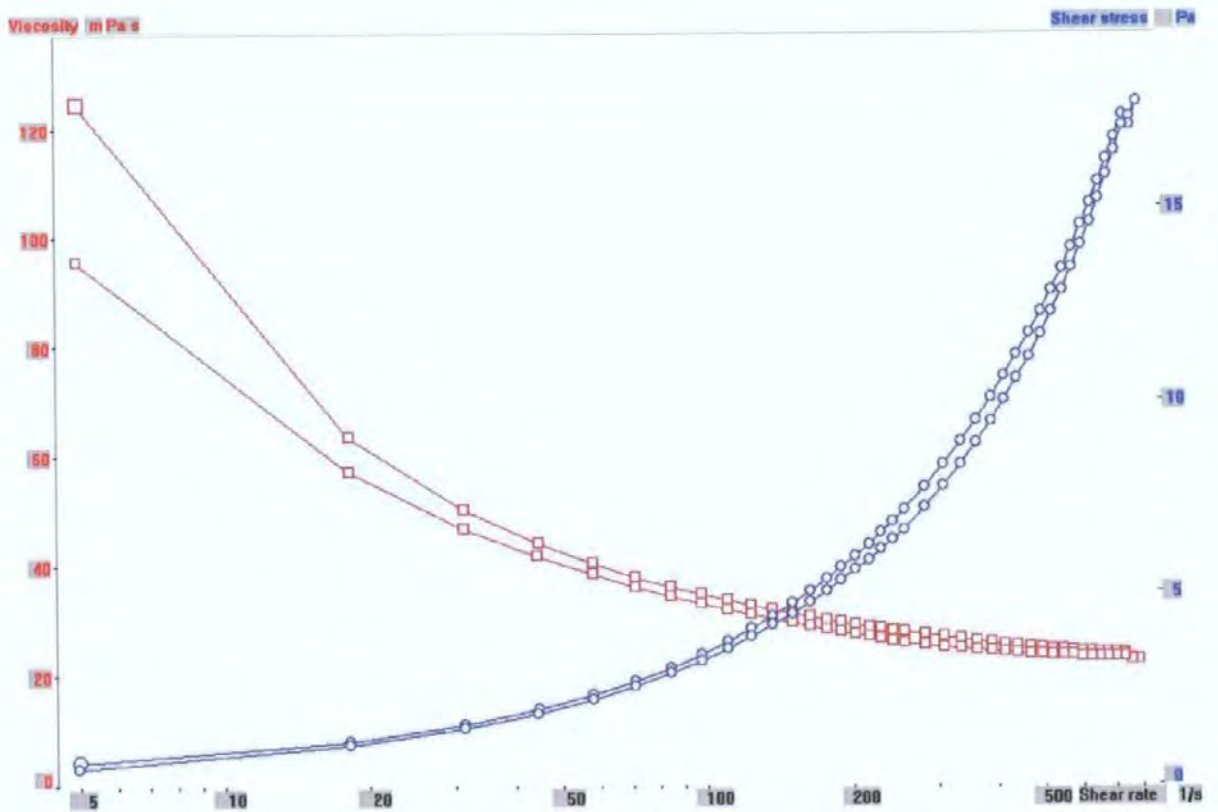
Figure 4.8 - Viscosity and shear stress for HC90 + 25 w/w% acrylic high T_g latex as a function of shear rate.
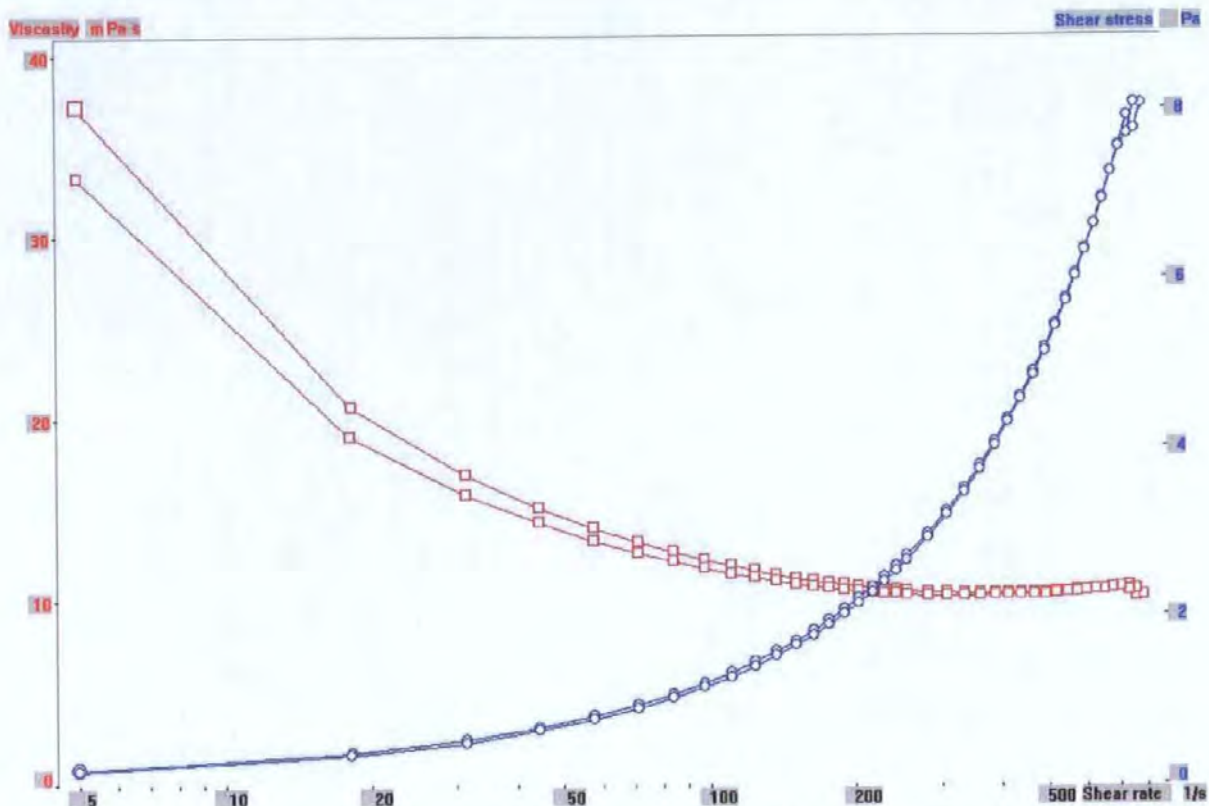
Figure 4.9 - Viscosity and shear stress for HC60 + 25 w/w% styrene-butadiene high T_g latex as a function of shear rate.
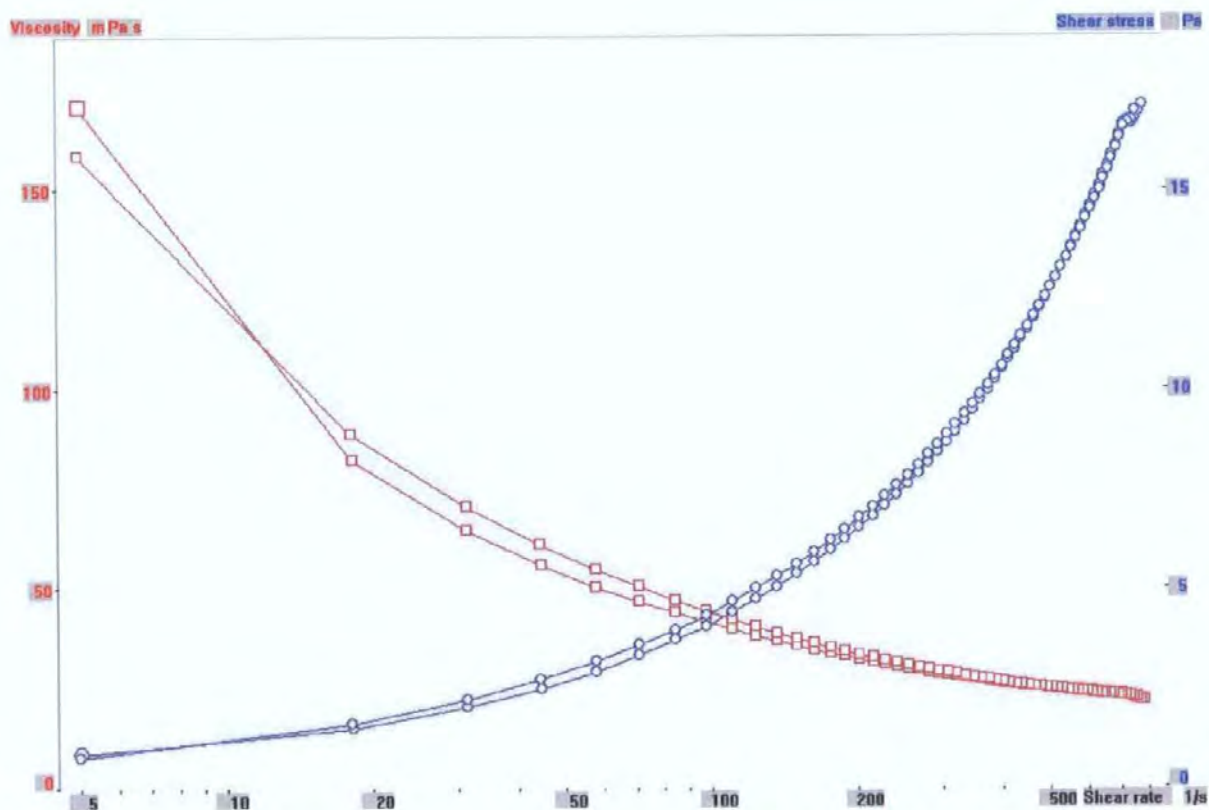
Figure 4.10 - Viscosity and shear stress for HC90 + 25 w/w% styrene-butadiene high T_g latex as a function of shear rate.

Similar behaviour can be observed for SB high T_g based coating colours (Figure 4.9 and Figure 4.10) and SB low T_g based coating colours (Figure 4.11 and Figure 4.12).
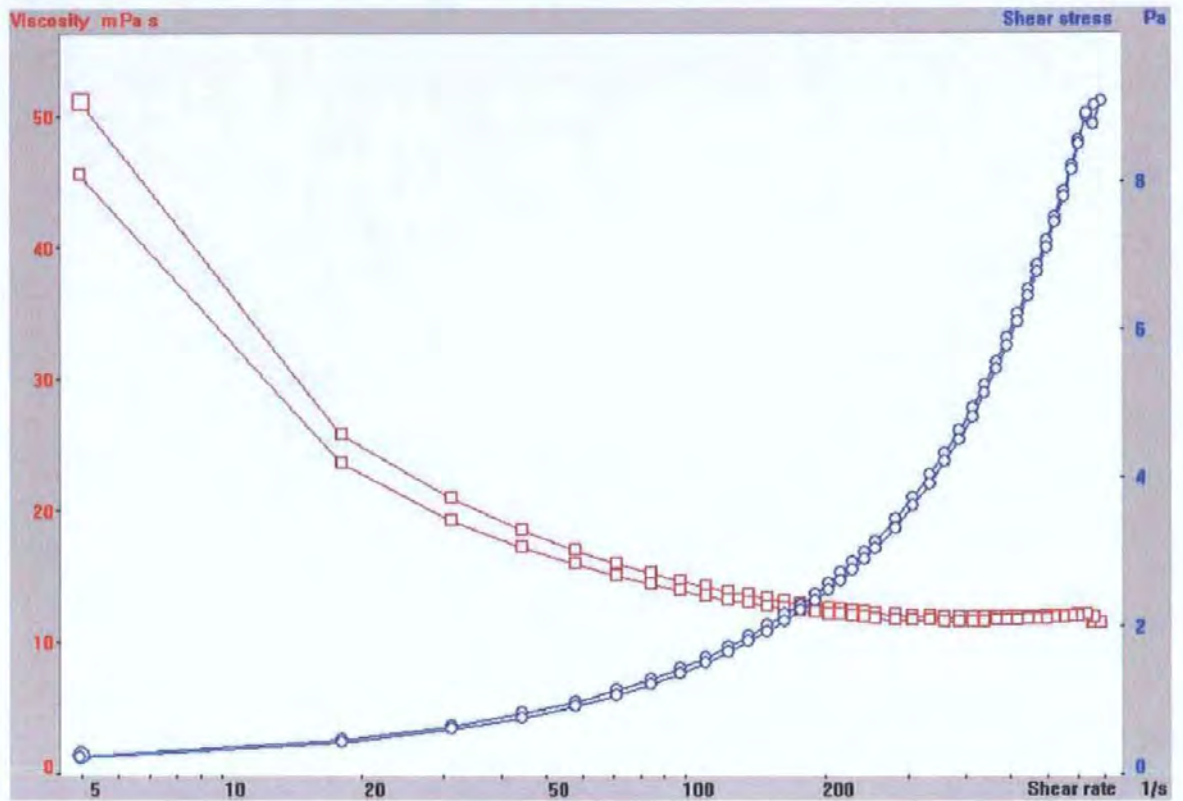
Figure 4.11 - Viscosity and shear stress for HC60 + 25 w/w% styrene-butadiene low T_g latex as a function of shear rate.
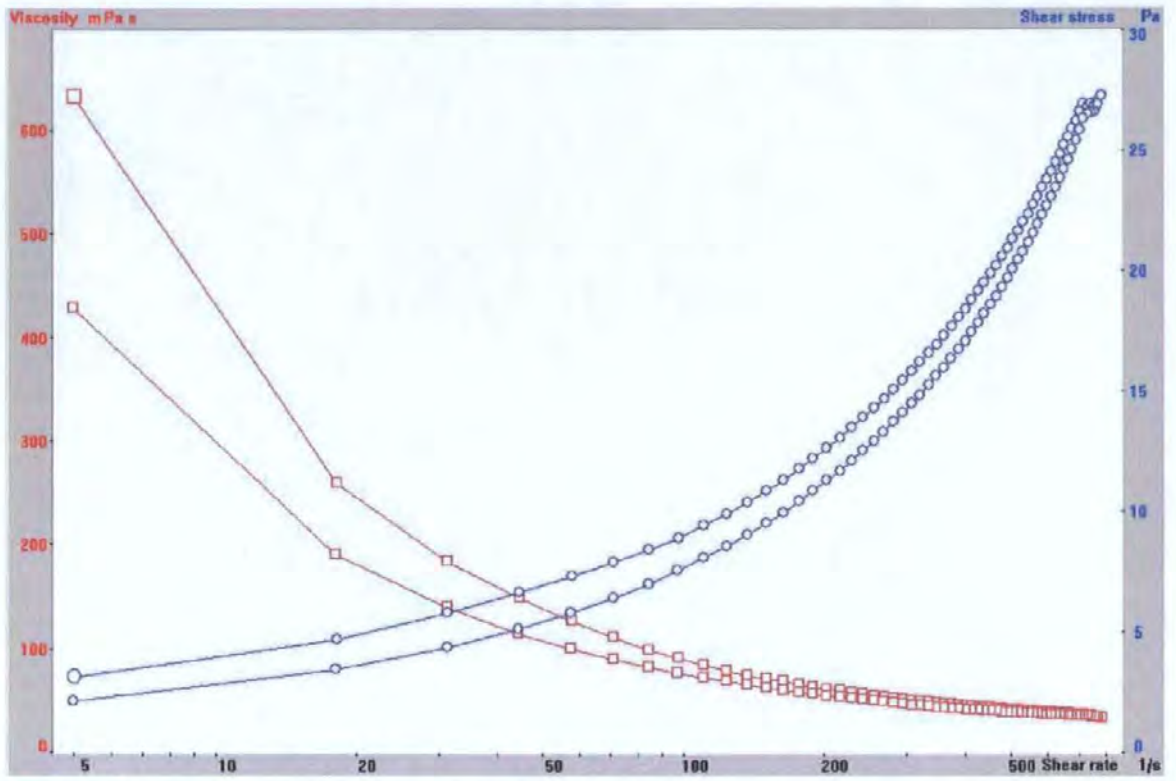
Figure 4.12 - Viscosity and shear stress for HC90 + 25 w/w% styrene-butadiene low T_g latex as a function of shear rate.

When starch was used in the coating formulation, the drop in viscosity with increasing shear rates was markedly less steep than in the case of latex-based coating colours and the behaviour of HC90 and HC60 starch-based coating colours are very similar, especially at high shear rates.
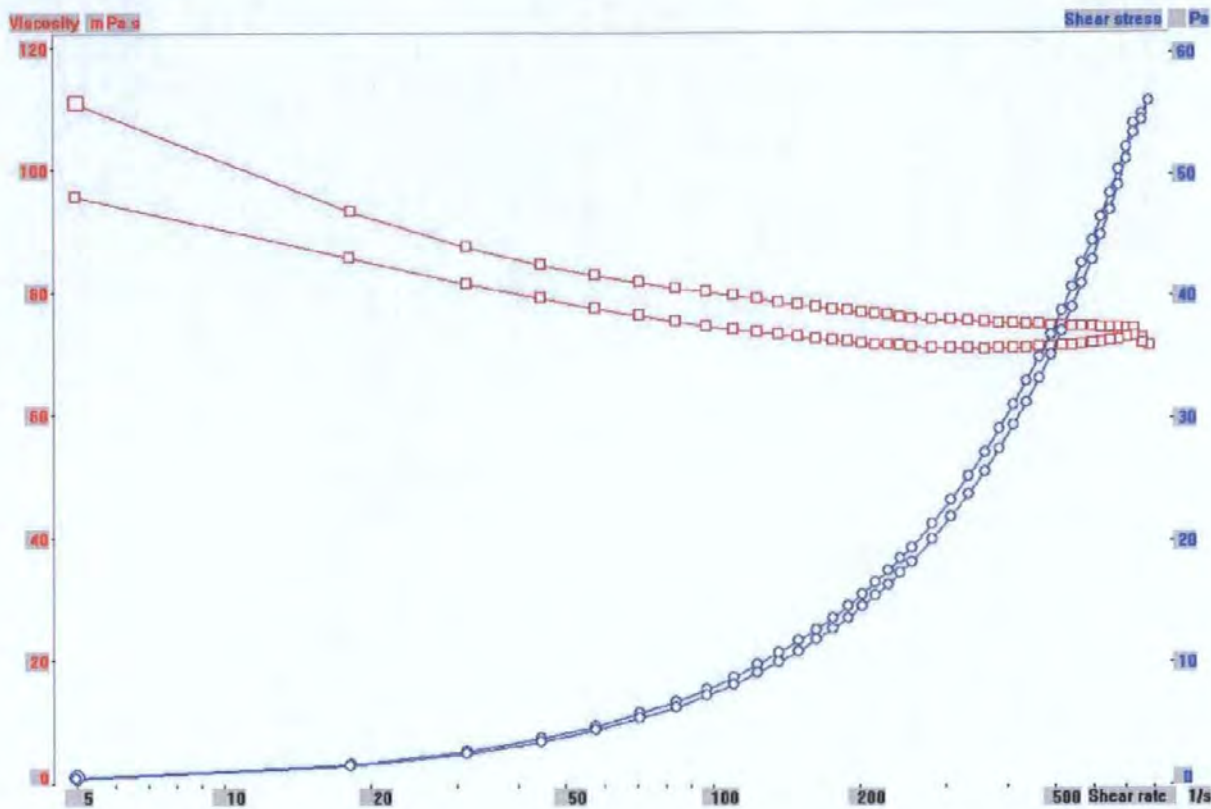
Figure 4.13 - Viscosity and shear stress for HC60 + 25 w/w% starch as a function of shear rate.
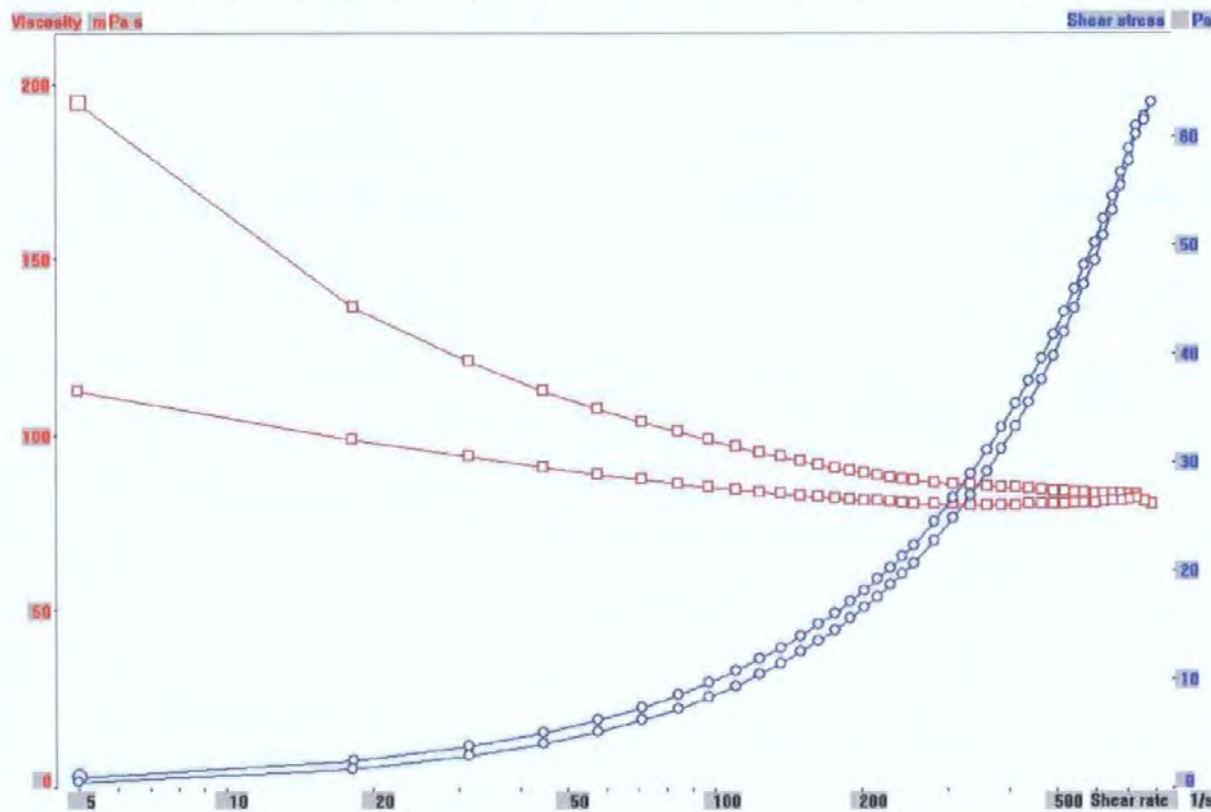
Figure 4.14 - Viscosity and shear stress for HC90 + 25 w/w% starch as a function of shear rate.

4.3.2 Discussion

Over a range of shear rates, it is possible to investigate the impact of both shear-induced structure and packing. Since all colours with latex are shear thinning, we can assume that there is no shear-induced packing disorder as particles are moved past each other. This is an important finding as it indicates that continuous motion of the mixture of particles is allowed, once any static structure is destroyed (yield). That the HC90 with latex (Figures 4.8, 4.10 and 4.12) generally shows higher viscosity reflects the more crowded packing of that combination. This latter effect is most marked in the case of HC90 with the low T_g styrene butadiene latex, thus confirming the assumptions made using the Brookfield data, i.e. over the whole range of shear rate, the packing dominates. If this had not been the case, the shear thinning of the colour showing the highest viscosity (Figure 4.12) would have been discontinuously greater at lower shear rates as interactions became broken down.

The difference between the initial sweep in increasing shear and the return sweep as shear rate is once again reduced is a measure of the hysteresis in the system. The greater the hysteresis, the more likely it is that slow processes have led to a stationary equilibrium structure, which gets progressively broken down as the shear rate increases and fails to re-form as fast as the timescale of the return shear rate sweep. Such processes are often osmotic in nature, reflecting a potential depletion flocculation effect. The greater the number of particles (finer size per unit solids content, for example), together with any disruptive packing ensuring particle-particle contact, will lead to the greater likelihood of such interactions. This we see in the data for the finer HC90 especially with the low T_g styrene butadiene latex (Figure 4.12).

Starch addition, on the other hand, is seen to result in a greatly increased viscosity of the coating, which is maintained largely throughout the shear rate range (Figures 4.13 and 4.14). The nature of this viscosity component will be explored in more detail studying

127

viscoelasticity. Starch is soluble, so there is a rise in the viscosity of liquid phase supporting the particulate suspension. However, the effect may be more complicated, involving adsorption or flocculation.

4.4 Yield stress measurements

The yield stress properties of the samples, described in section 4.2, have also been studied by increasing the applied shear stress from low levels and monitoring the change in viscosity of the samples.

4.4.1 Results

Figure 4.15 and 4.16 show the result of yield stress measurements for coating colours prepared using acrylic high T_g latex as binder. It can be seen that the viscosity shows an initial rise with shear stress to a maximum value of about 2 Pa s and then it falls. In the case of HC60-based coating colour, the fall is sudden and occurs at a value of shear stress of about 40 mPa, while in the case of HC90-based coating colour the fall occurs more gradually at around 100 mPa.
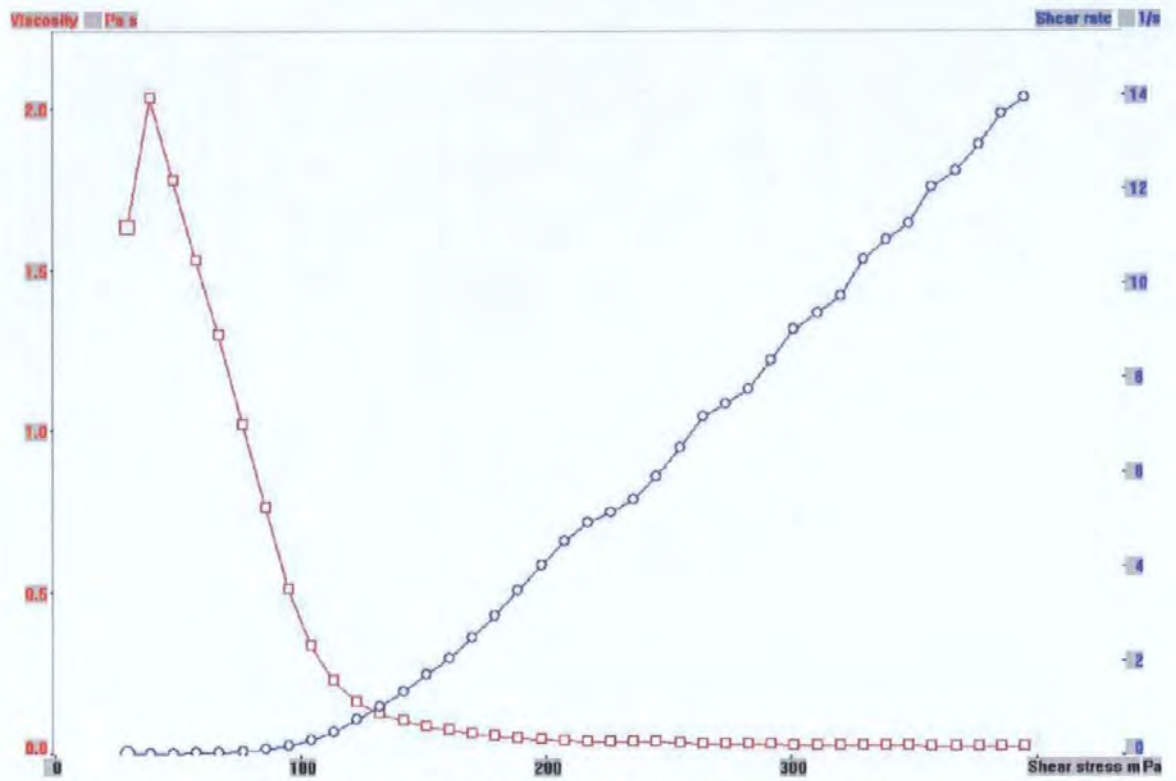
Figure 4.15 - Viscosity (red) and shear rate (blue) for HC60 + 25 w/w% acrylic high T_g latex as a function of the induced shear stress.
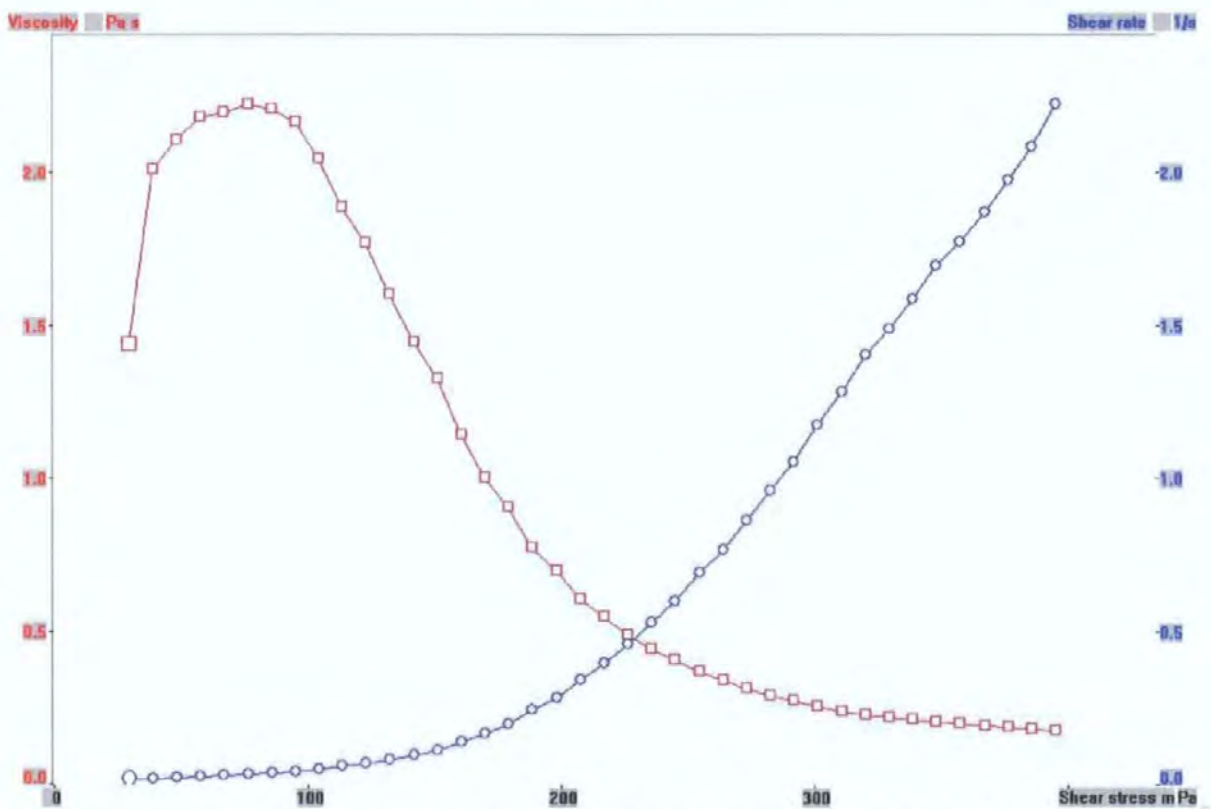
Figure 4.16 - Viscosity (red) and shear rate (blue) for HC90 + 25 w/w% acrylic high T_g latex as a function of shear stress.
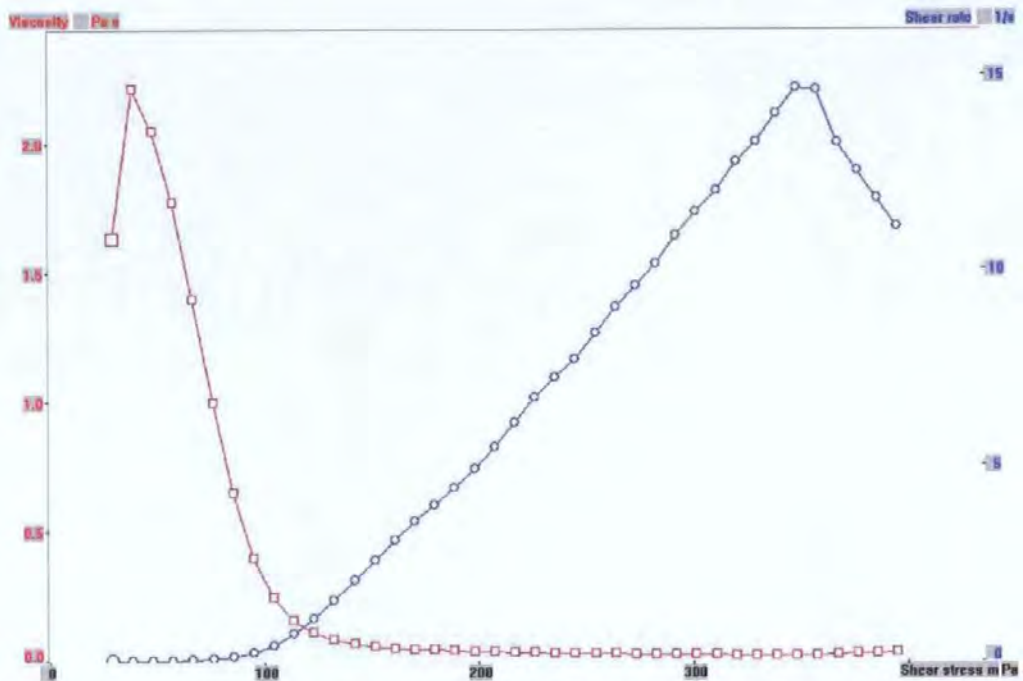
Figure 4.17 - Viscosity (red) and shear rate (blue) for HC60 + 25 w/w% styrene-butadiene high T_g latex as a function of shear stress.

The behaviour of HC60 in combination with SB high T_g latex (Figure 4.17) is similar to that of HC60 with acrylic latex (Figure 4.15), while the use of this binder with HC90 (Figure 4.18) results in a higher maximum viscosity and a much less steep drop in the value of viscosity.
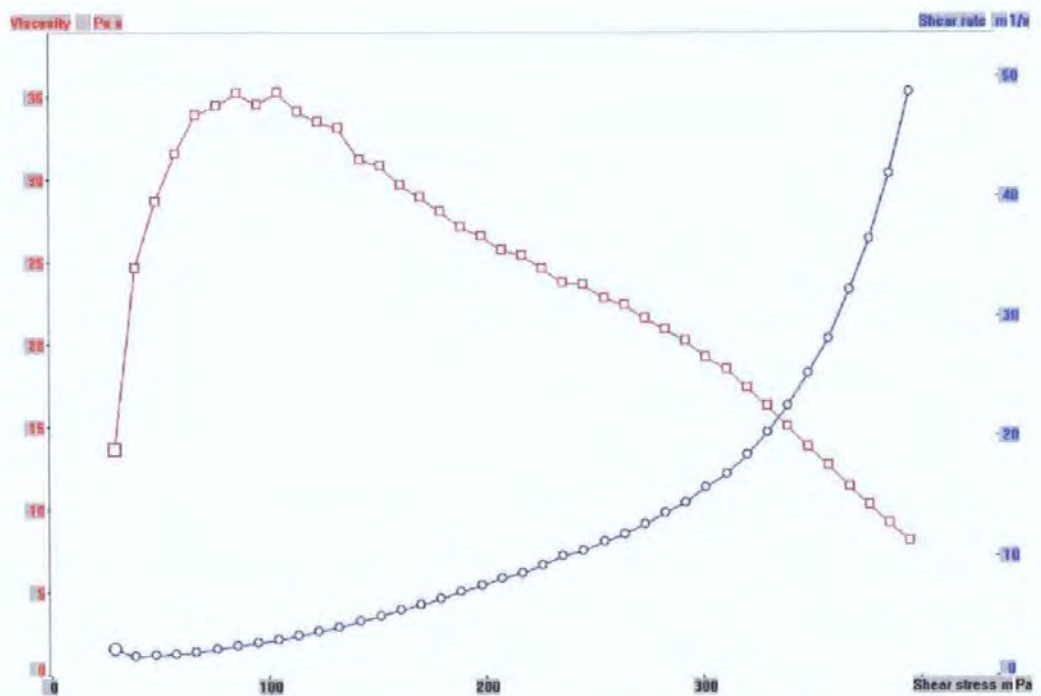
Figure 4.18 - Viscosity (red) and shear rate (blue) for HC90 + 25 w/w% styrene-butadiene high T_g latex as a function of shear stress.

130
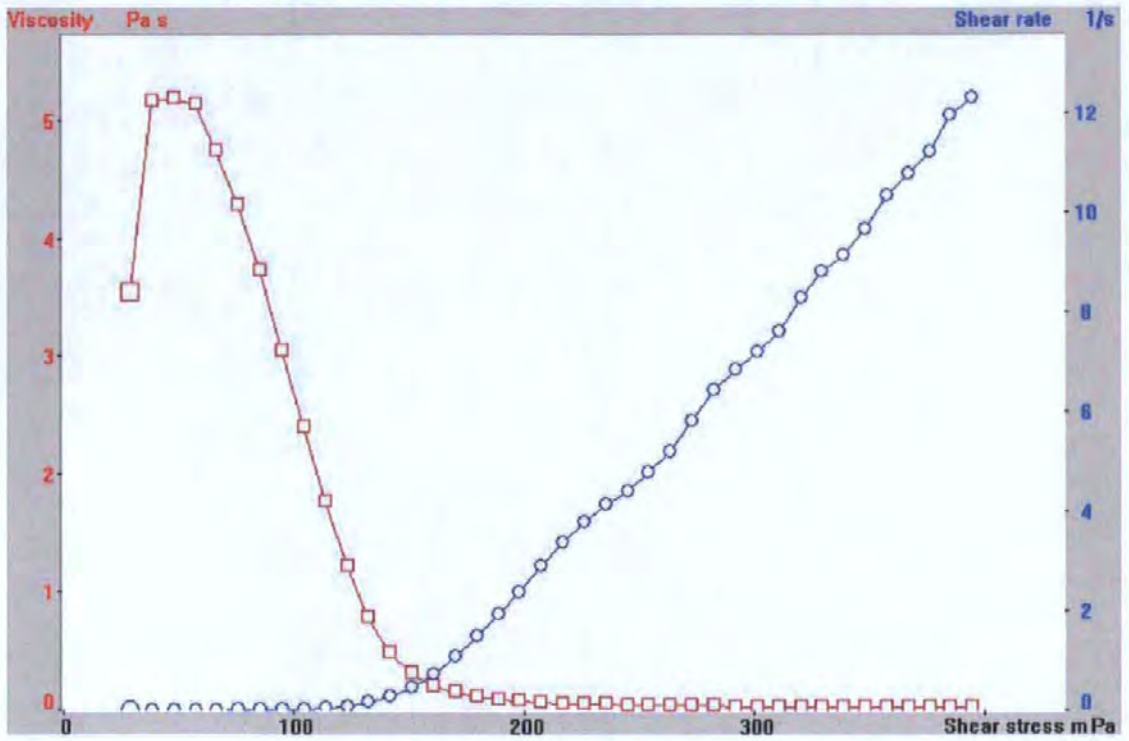
Figure 4.19 - Viscosity (red) and shear rate (blue) for HC60 + 25 w/w% styrene-butadiene low T_g latex as a function of shear stress.

HC60 and HC90 show a different behaviour when SB low T_g latex is used in the formulation. The HC60-based coating colour shows a slightly higher value of maximum viscosity and a drop in viscosity for a shear stress of about 100 mPa (Figure 4.19), whereas the HC90-based coating colour shows a continuous rise in the value of viscosity in the range of shear stresses investigated (Figure 4.20).
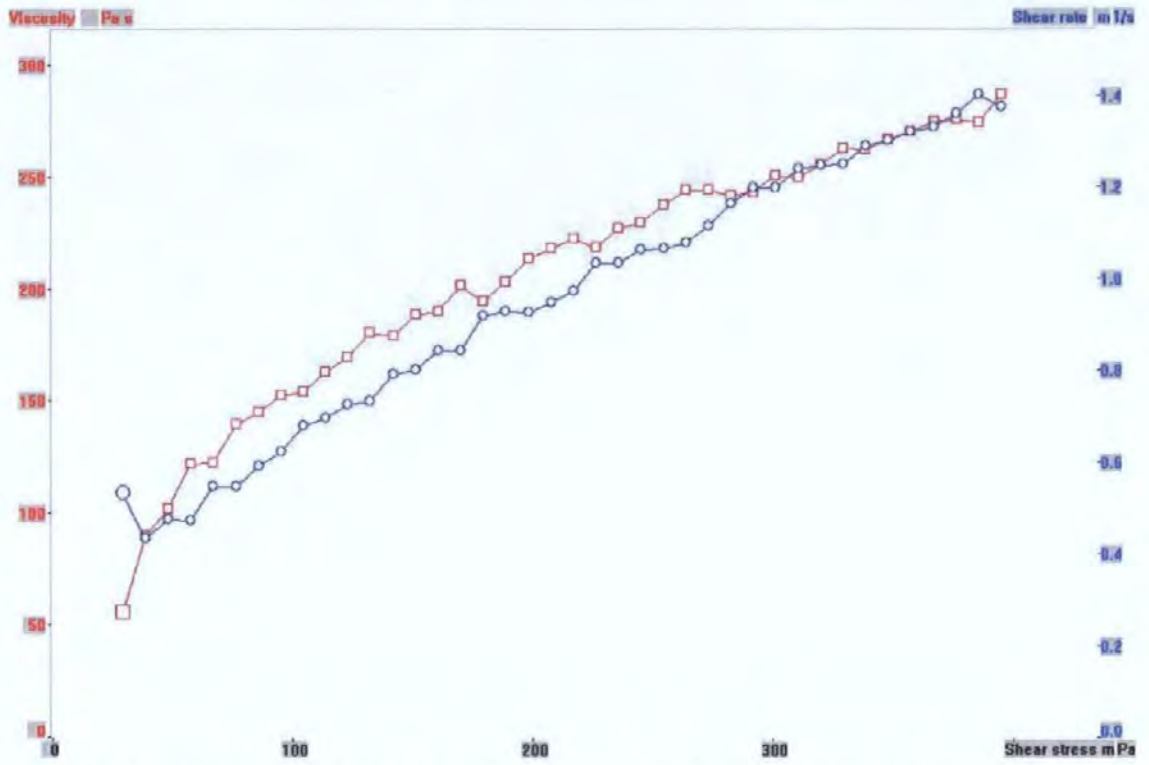
Figure 4.20 - Viscosity (red) and shear rate (blue) for HC90 + 25 w/w% styrene-butadiene low T_g latex as a function of shear stress.
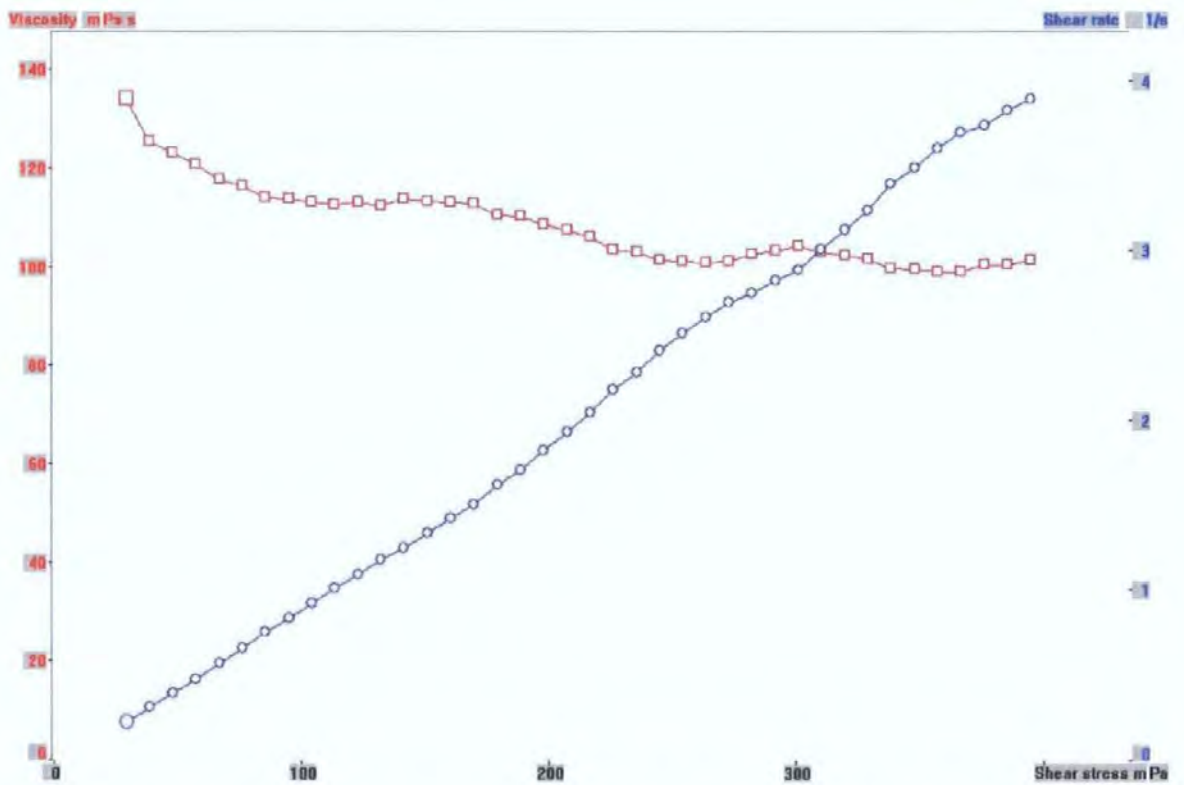
Figure 4.21- Viscosity (red) and shear rate (blue) for HC60 + 25 w/w% starch as a function of shear stress.

Figure 4.21 shows the yield stress measurement for an HC60 + 25 w/w % starch coating colour. It can be observed that the viscosity value is the highest measured for the HC60 series of samples and that the drop in viscosity is very slow.

A similar behaviour is shown in the case of HC90 + 25 w/w% starch coating colour (Figure 4.22), but with higher values of viscosity.
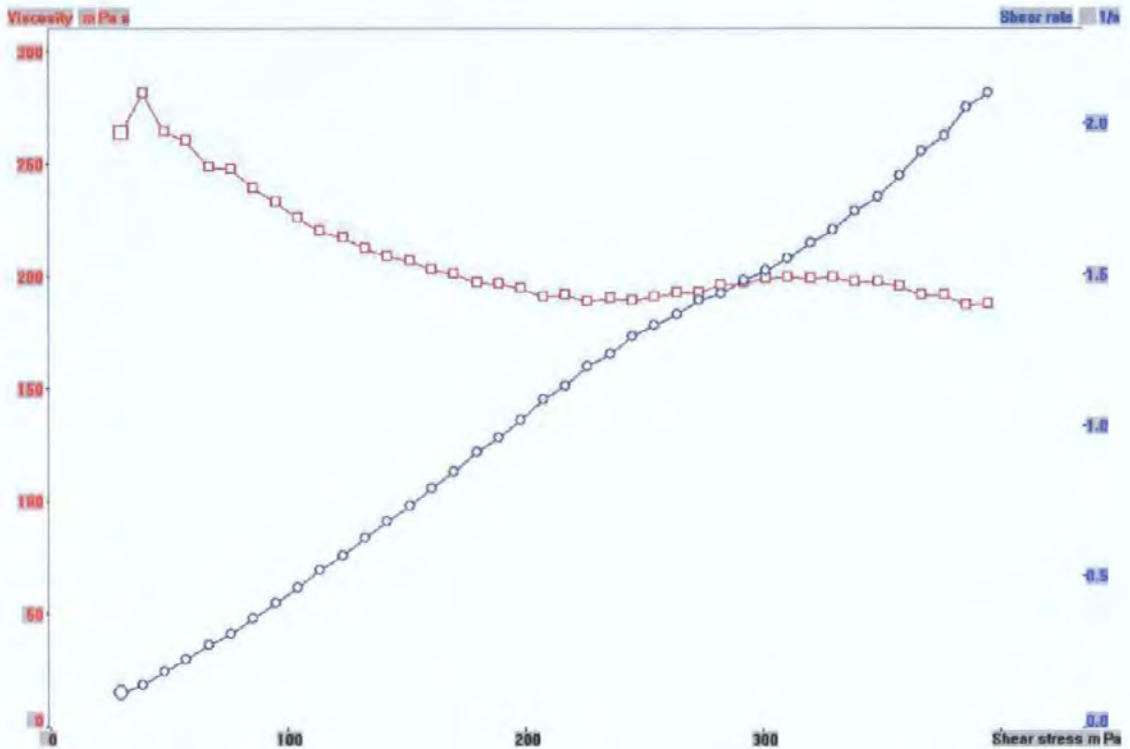
Figure 4.22 - Viscosity (red) and shear rate (blue) for HC90 + 25 w/w% starch as a function of shear stress.

4.4.2 Discussion

In the case of HC60-based coating colours, with all the different latices used in the formulations, the particle-particle interactions appear to be weak and small increases in the internal shear stress cause a steep drop in the measured viscosity (Figures 4.15, 4.17 and 4.19). These interactions, in contrast, appear to be larger in the case of HC90-based coating colours (Figures 4.16, 4.18 and 4.20), with larger shear stresses needed to cause the drop in viscosity.

133

This can be seen as an effect of the number density of particles in the coating colour, which is larger for the finer calcium carbonate.

As explained more extensively in section 4.4.2, the interpretation of the results for starch-based coating colour is not as simple as in the case of latex-carbonate mixtures, due to the high values of viscosity of starch solutions. However, it can be observed that in the case of the finer carbonate HC90 the measured values of viscosity are larger than for the corresponding HC60-based coating colour.

Figures 4.15 to 4.22 also show the shear rate as a function of shear stress data. These can be interpreted as an indication of how much the system is physically moving. In the cases of starch-based coating colours and HC90 with SB latex, shown in Figures 4.20, 4.21 and 4.22, it can be observed that the colours flow proportionally to the shear stress. The latex-based coating formulations show an initial region where the system is not flowing, despite the growth in internal shear stress. This represents not only an indication of high viscosity until the yield stress is reached, but an actual immobility of the system. It is necessary to overcome an energy barrier in order to get the system flowing. It appears therefore that the latex-containing systems show hard-sphere interactions, while starch-containing systems show long range interactions allowing the collective movement of the material. These observations support the idea, presented in more detail in section 4.5.2 and Chapter 8, of a 'stick-slip' phenomenon, where the interactions between the particles in the coating colour formulation can hold the system in place, not allowing the flow and rearrangement of the particles, until an energetic barrier is overcome.

4.5 Controlled stress sweep measurements

As previously described in section 1.8.8.2 and section 2.1.4, information about the viscoelastic behaviour of a coating colour can be obtained by inducing a controlled oscillating shear stress within the coating colour, over a range of stress values, and determining the elastic and/or viscous behaviour by measuring the phase angle δ, the elastic modulus G' and the viscous modulus G''. A phase angle δ of $0°$ shows perfectly elastic behaviour, and a phase angle of $90°$ indicates perfectly viscous behaviour.

This stress sweep measurement was carried out on the same samples studied in the previous section and the results are presented below.

4.5.1 Results

First of all it can be observed that the trends in the curves describing the phase angles for HC60 with high T_g latex coating colours (Figure 4.23 and Figure 4.25) are not as well defined at low stress as in the other cases. These samples, due to low interactions, other than hard sphere interaction and viscosity, probably expose the physical limit of the measuring instrument at low stress values, making it difficult to carry out reliable measurements under suspected slip-stick conditions. The remaining parts of the curves, however, are reliable and show a progressive breakdown of weak elastic structures moving through to a more purely viscous flow as stress increases.

This behaviour of elasticity at low stress is common to all pigment-latex coating colours and the magnitude of the rate constant for the structure formation is responsible for the hysteresis seen earlier in the shear rate curves.

135
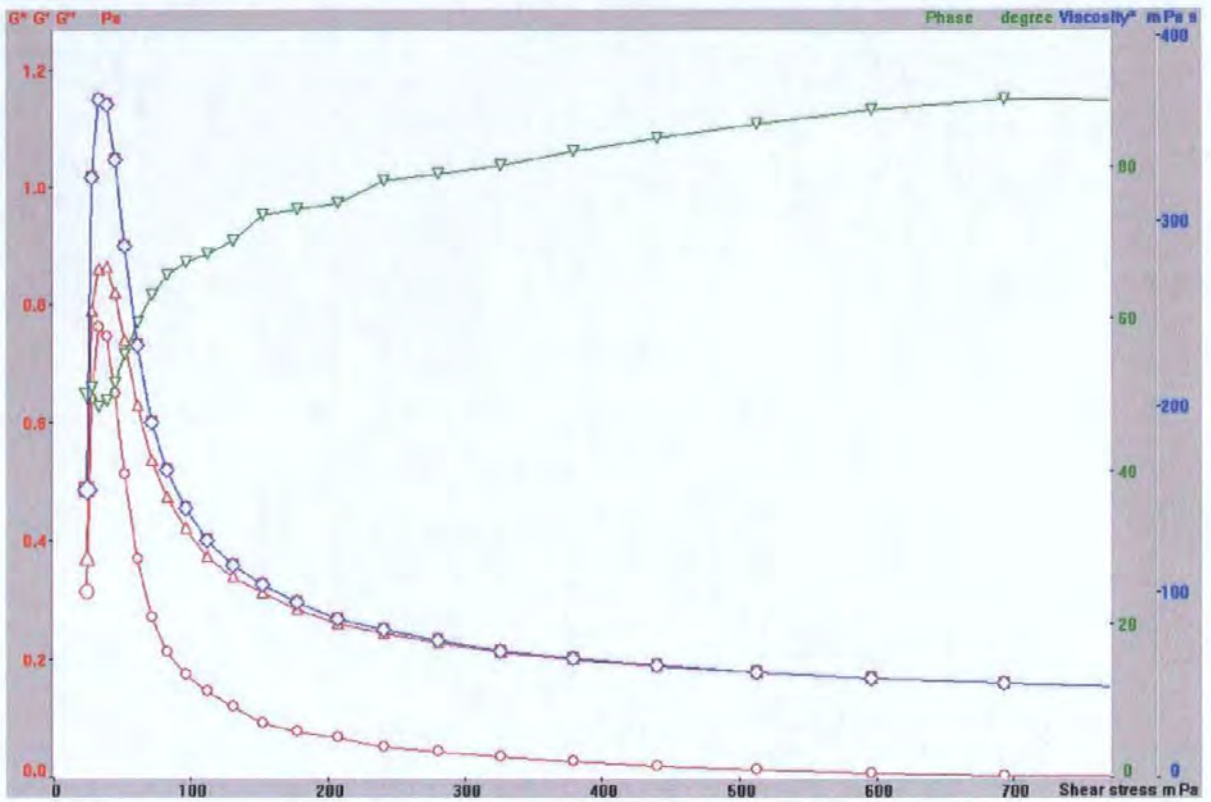
Figure 4.23 - Elastic modulus G' (red ○), viscous modulus G'' (red Δ) and phase angle δ (green) for HC60 + 25 w/w% acrylic high T_g latex as a function of shear stress.

It is interesting to notice that HC90-based coating colours show higher values of elastic modulus than the corresponding coating colours based on the coarser calcium carbonate when latex is used as binder. Also, the phase angle reaches a value of 45°, the middle point between perfectly elastic and perfectly viscous behaviour, later in the stress sweep, i.e. at larger applied strain.
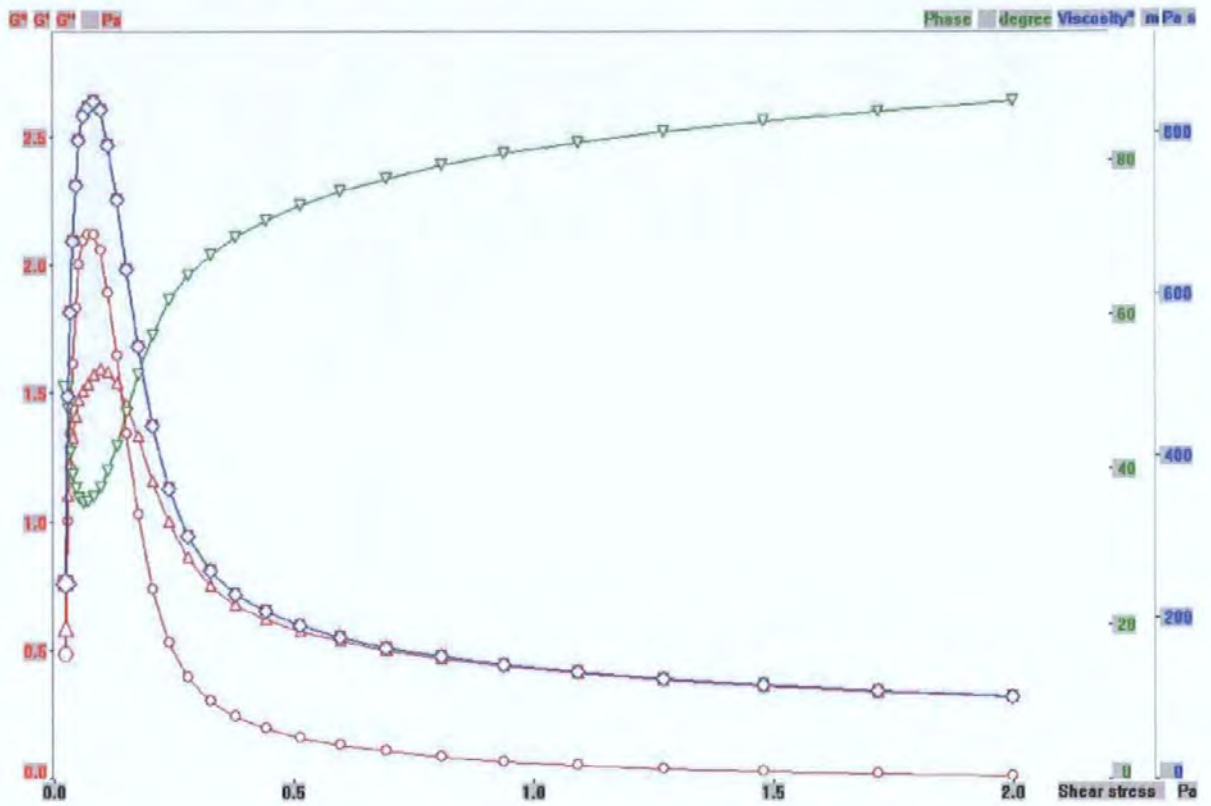
Figure 4.24 - Elastic modulus G' (red ○), viscous modulus G'' (red Δ) and phase angle δ (green) for HC90 + 25 w/w% acrylic high T_g latex as a function of shear stress.
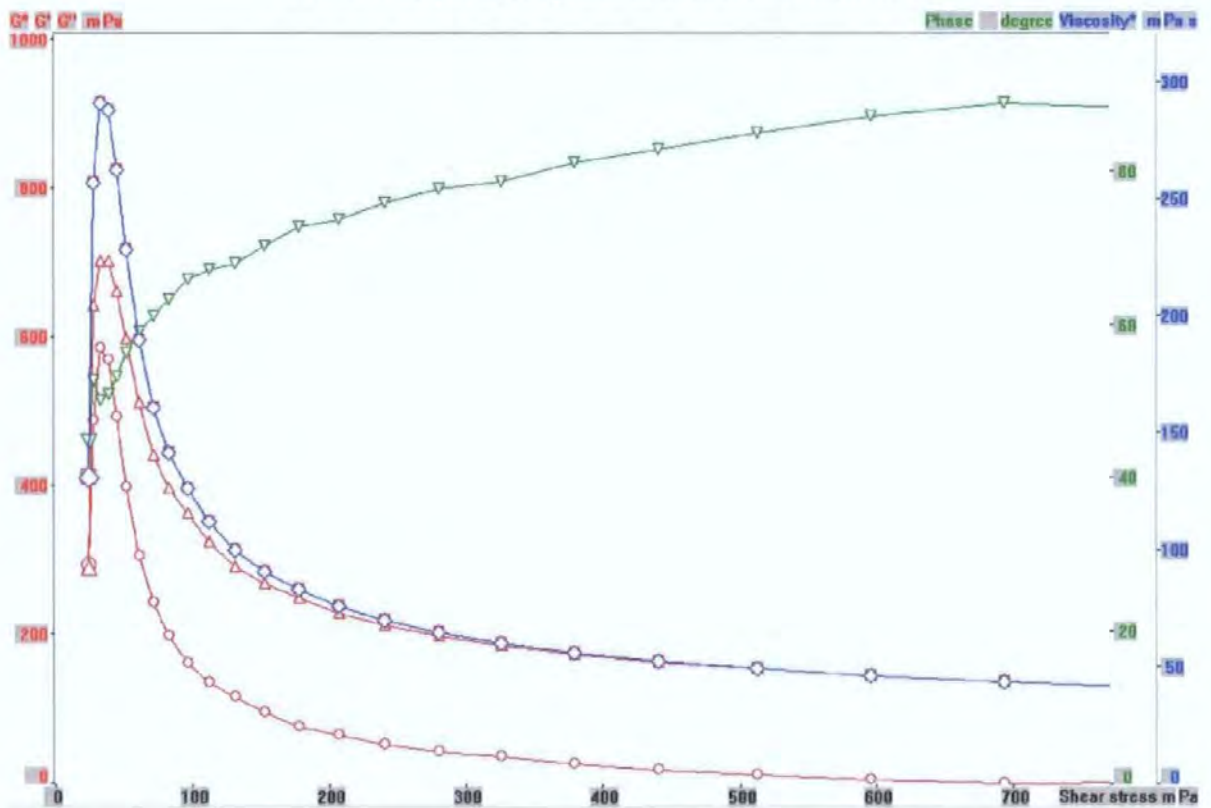
Figure 4.25 - Elastic modulus G' (red ○), viscous modulus G'' (red Δ) and phase angle δ (green) for HC60 + 25 w/w% styrene-butadiene high T_g latex as a function of shear stress.

137
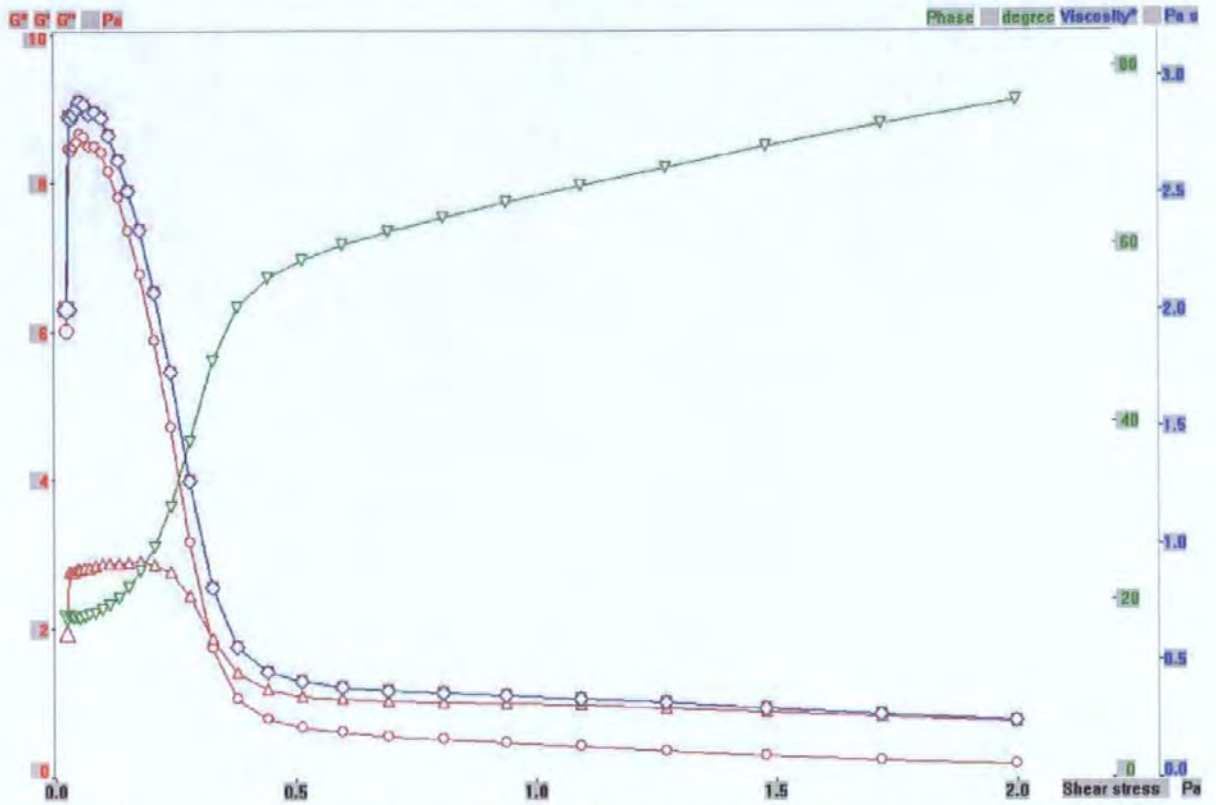
Figure 4.26 - Elastic modulus G' (red $\circ$), viscous modulus G'' (red Δ) and phase angle δ (green) for HC90 + 25 w/w% styrene-butadiene high T_g latex as a function of shear stress.

When styrene-butadiene latex is used in the coating formulations, the measured value for the elastic modulus is higher at low shear stress than for any other type of latex, especially when the finer calcium carbonate (HC90) is used as pigment.
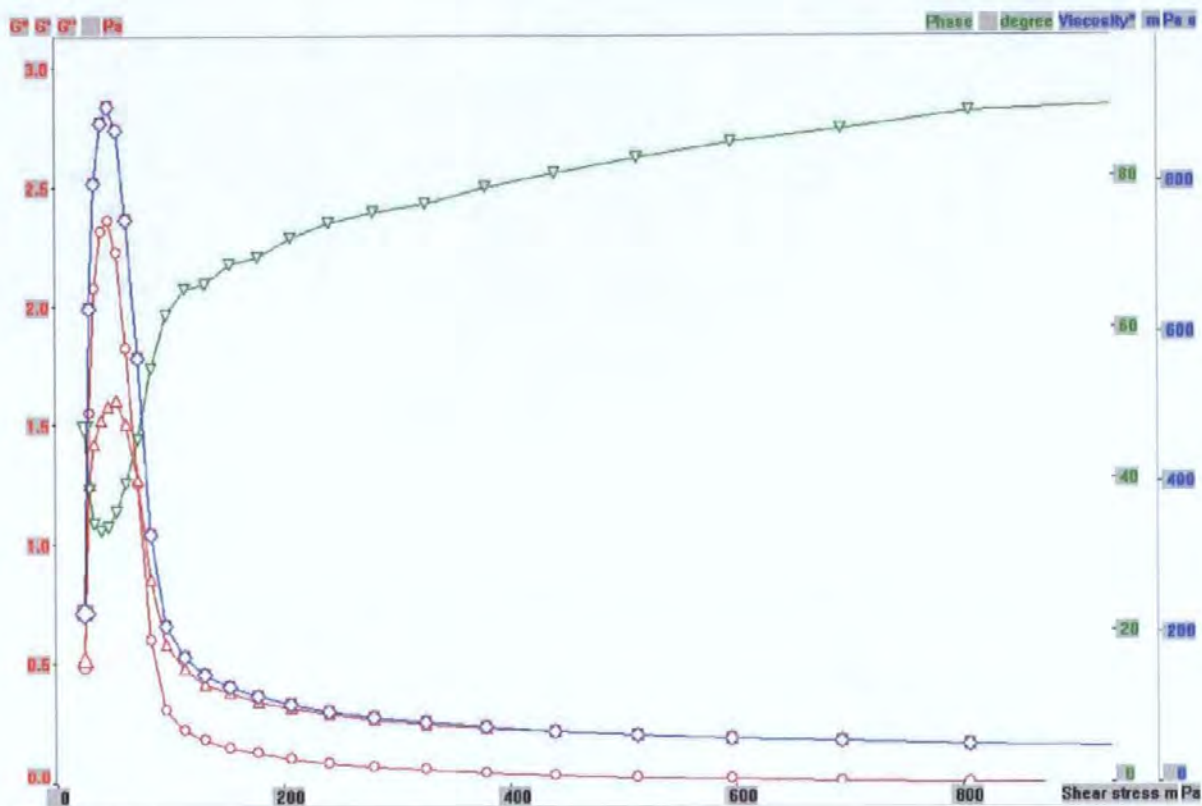
Figure 4.27 - Elastic modulus G' (red ○), viscous modulus G'' (red Δ) and phase angle δ (green) for HC60 + 25 w/w% styrene-butadiene low T_g latex as a function shear stress.
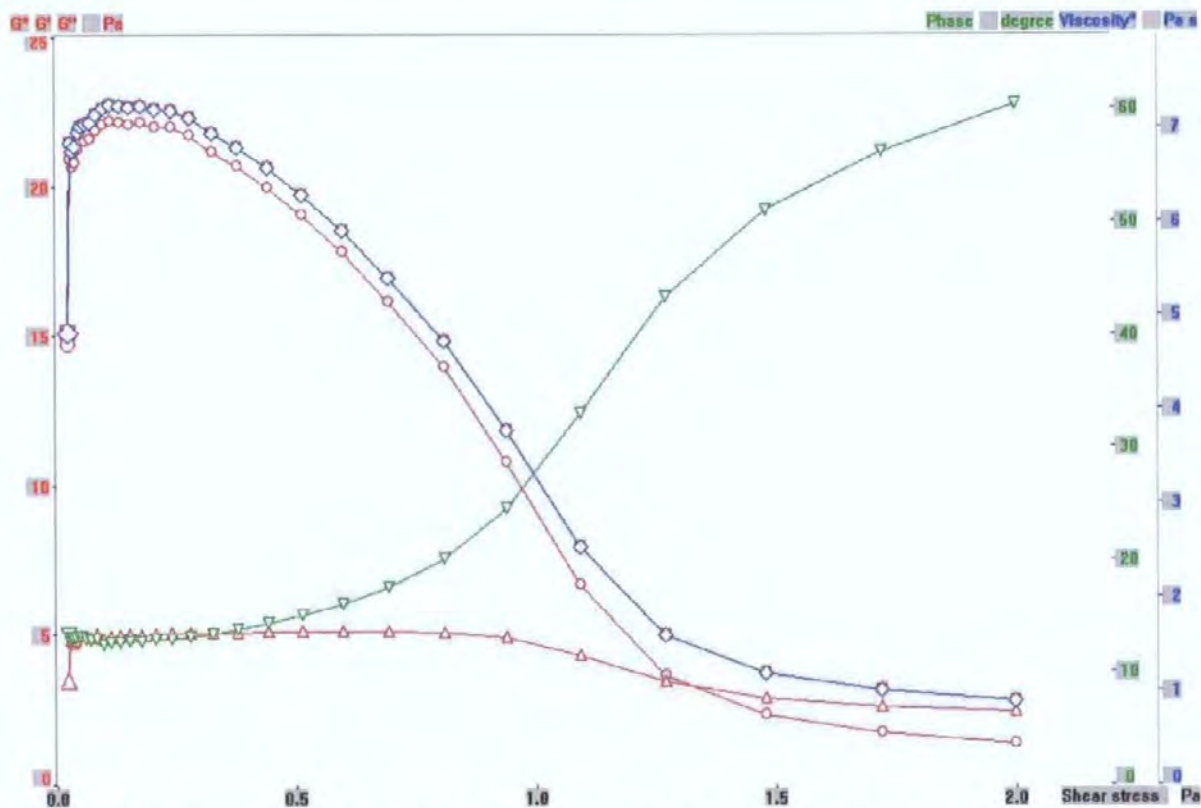
Figure 4.28 - Elastic modulus G' (red ○), viscous modulus G'' (red Δ) and phase angle δ (green) for HC90 + 25 w/w% styrene-butadiene low T_g latex as a function of shear stress.

The use of starch in the coating formulations leads to a highly viscous behaviour even for very low applied shear stress, with phase angles between 60° and 90° and far larger values of viscous modulus (500 to 700 mPa) when compared with latex based coating colour. The two different types of calcium carbonate used in the coating formulations lead to almost identical results (Figure 4.29 and Figure 4.30).
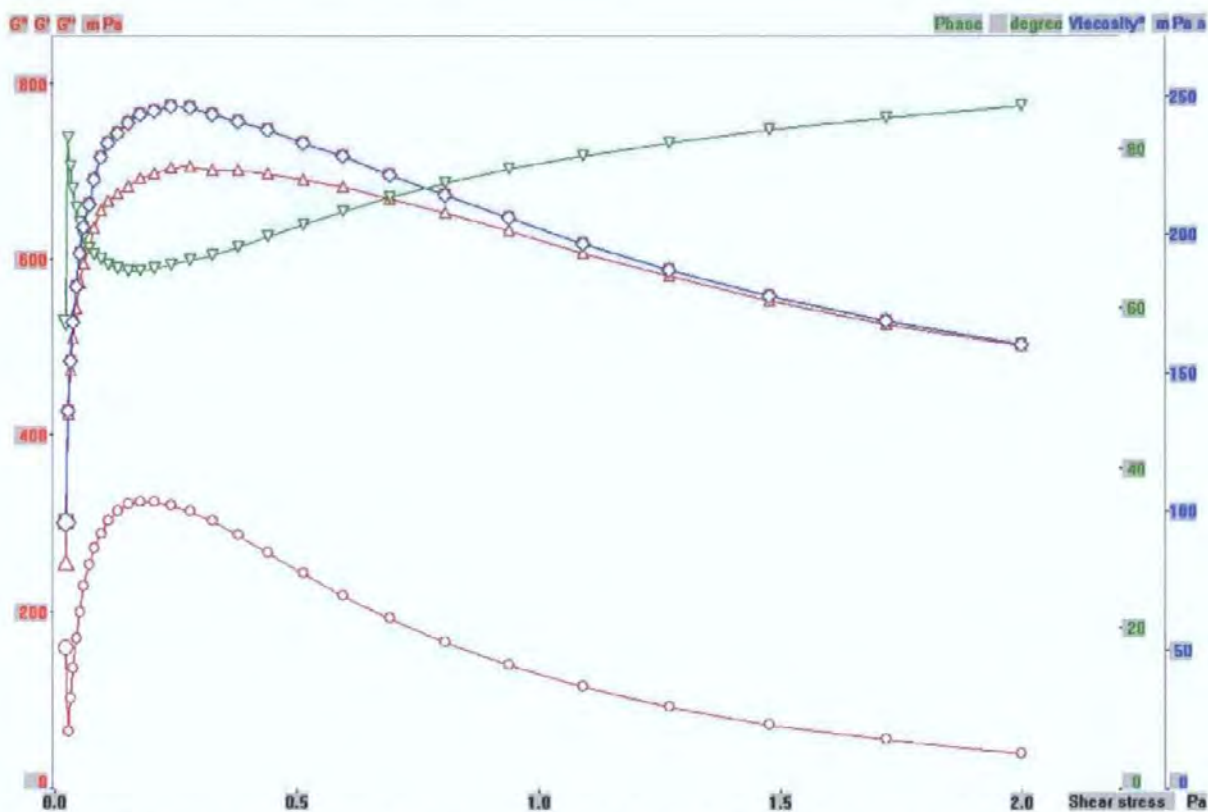
Figure 4.29 - Elastic modulus G' (red ○), viscous modulus G'' (red Δ) and phase angle δ (green) for HC60 + 25 w/w% starch as a function of shear stress.
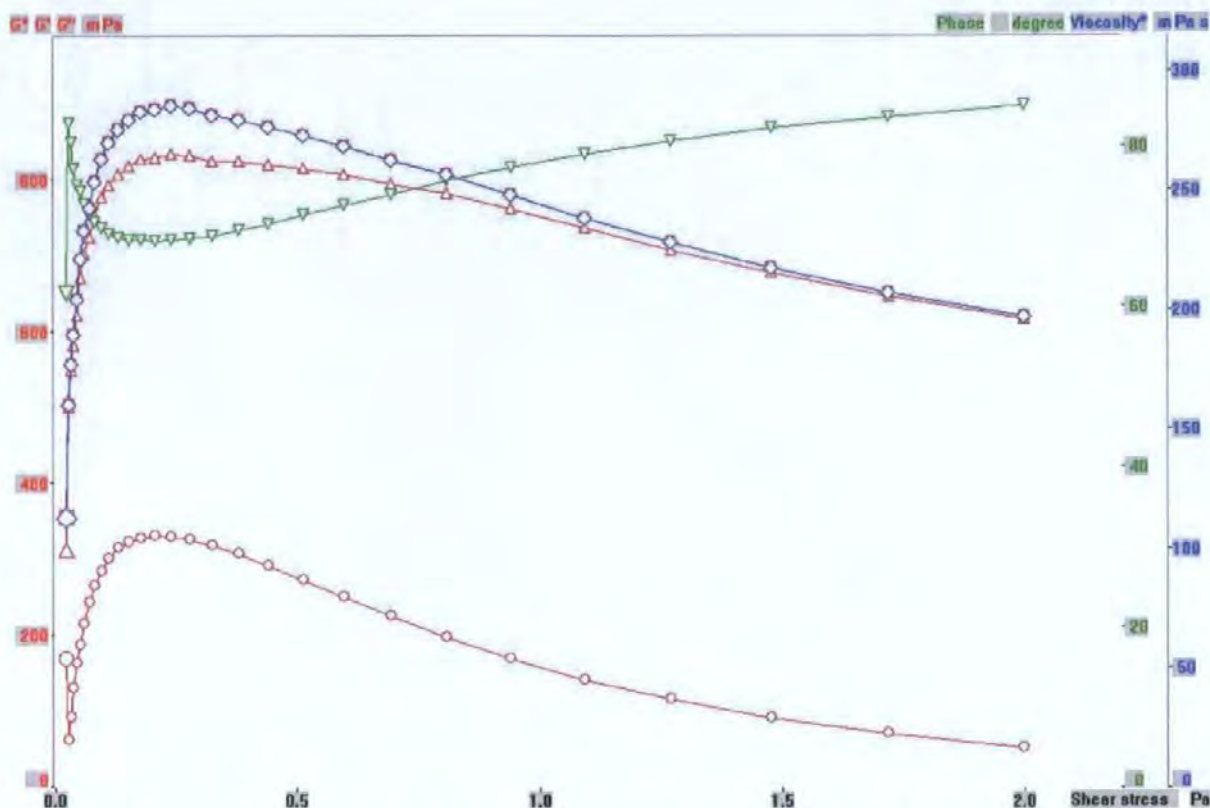
Figure 4.30 - Elastic modulus *G'* (red ○), viscous modulus *G"* (red Δ) and phase angle δ (green) for HC90 + 25 w/w% starch as a function of shear stress.

4.5.2 Discussion

We are now in a position to consider the viscoelastic results in the light of the previous shear measurements.

The first point of interest concerns the latex-based colours. The application of low strain, resulting in low stress in the samples, induces a rapid rise in elasticity and a corresponding drop in phase angle. The action of distorting the packing and thereby inducing a reactive structuring is most pronounced for the HC90 coating colours. This interaction reflects the particle number density per unit solids content, it being higher for HC90 than in the case of the coarser HC60. The particle-particle interactions are therefore magnified in the case of HC90. The strength of this distortion-induced structure is reflected in the delay of the rise of phase angle as a function of internal stress. This delay is most marked, as expected, for the most disrupting system, i.e. that of HC90 plus latex, and in particular the low T_g styrene butadiene

141

latex. This was shown using the volume fraction method (section 4.2), and was reflected in the reluctance to flow (non-linear shear rate response to internal stress).

The principal interest of this project, the drying process, occurs in a static coating colour. Therefore, the low strain data are most important. As solids increase, the internal stress will increase, as will the strength of the elastic structure. Then the structure will yield to the stress. Then, once again, the structural interactions will build elastically as the local stress rises. It will yield only as the stress increases, and the phase angle rises through 45°. It will then begin to flow into a new configuration. This behaviour is referred to as 'stick-slip'.

The induction of structure as a response to induced stress is also responsible for determining the first critical concentration (FCC), i.e. immobilisation of the wet colour. Furthermore, the greater the need for high internal stress to cause the consolidation of the coating colour, the more likely the system is to collapse critically during the slip-stick action.

Starch at high concentration is a viscous medium. The passage of the particles of pigment through this medium is reflected in high drag viscosity. One must, therefore, be careful in interpreting the curves in the case of starch due to this background viscous drag. Although the *average* behaviour is favouring viscous flow, it is important to note that the elastic modulus, G', rises significantly and extends far as a function of stress. In fact the elastic modulus behaviour is similar in the case of both HC60 and HC90 together with starch, and interestingly follows that of the HC90 with low T_g styrene butadiene latex. This induced elasticity, which remains under increasing stress until finally broken down, seems to be a common factor between the most interacting combinations, and, as we see during drying, is a common factor in respect to the magnitude of shrinkage. Thus, although the long-range forces in the starch-

containing colours dominate the flow behaviour, the local hard sphere interaction is still present.

Structure is, therefore, likely to be a key element in determining the response of the coating colour to drying. Firstly, in respect to the onset of FCC and, secondly, in respect to the internal stress needed to progress consolidation, with an increasing likelihood of catastrophic collapse of the structure the more the elastic modulus extends into the higher stress regime.

This overall study of rheology gives clues as to the mechanism of shrinkage and the interactions involved. The induced distortion of the packing structure leads to an elastic interaction, which must be broken down before the sample can "flow". The induced packing distortion is greatest for the finer pigment, which is logical based on particle-particle number interactions, and for those binders that give the most deviation from a non-interacting hard sphere model – low glass transition temperature latex and starch seem to provide the longest lasting elasticity as a function of stress. Deviation from a non-interacting hard sphere model is, therefore, probably the clue in determining the magnitude of shrinkage.

The concept of slip-stick and deviation from non-interacting hard sphere behaviour will be pursued further during the modelling of the shrinkage phenomenon.

5 MODELLING PAPER COATING WITH PORE-COR

5.1 Pore-Cor

As previously explained in section 1.8.3, there are many examples of different network models for the study of porous media. The Environmental and Fluid Modelling Group of the University of Plymouth has developed, during the past 13 years (Spearing, 1991), its own network model, Pore-Cor, trying to address many of the problems and arbitrary choices presented by other models. Pore-Cor has been successfully used for the modelling of a wide range of porous materials including sandstones (Matthews *et al.*, 1993), medicinal tablets (Ridgway *et al.*, 1997) and soil (Peat *et al.*, 2000).

Pore-Cor generates a three-dimensional structure, which matches the experimentally determined porosity and the percolation characteristics measured by mercury porosimetry. The simulated structure, consisting of a repeated unit, or unit cell, is made up of a 10 x10 x 10 cubic array of 1 000 cubic pores, equally spaced in a three-dimensional matrix by a distance defined as the pore-row spacing, and interconnected by up to 3 000 throats. The number and arrangement of throats dictates the connectivity, defined as the average number of throats connected to each pore, between 0 and 6 (Figure 5.1). Both the pore size and throat size distributions are initially linearly distributed over a logarithmic scale, with equal numbers of pores and throats in each respective logarithmic interval, the maximum individual throat size being determined by the smaller of the two pores it joins.

The simulation is performed by optimising, with a Boltzmann-annealed Simplex algorithm (Johnson *et al.*, 2003), sets of 4 adjustable parameters: the connectivity, correlation level, pore and throat skews.

Figure 5.1 - Cubical pore with six cylindrical throats.

Correlation level is a parameter with value between 0 and 1 and represents the level of ordering of the structure: the more the structure is spatially ordered (vertically, as in Figure 5.2, or horizontally banded, as shown in Figure 5.3), the more the value of the correlation level tends to 1. When modelling a sample with Pore-Cor, the type of structure banding which gives the best matches of porosity and percolation properties of the sample must be investigated. A set of similar samples must be modelled with the same chosen structure type for meaningful comparisons to be made.

145
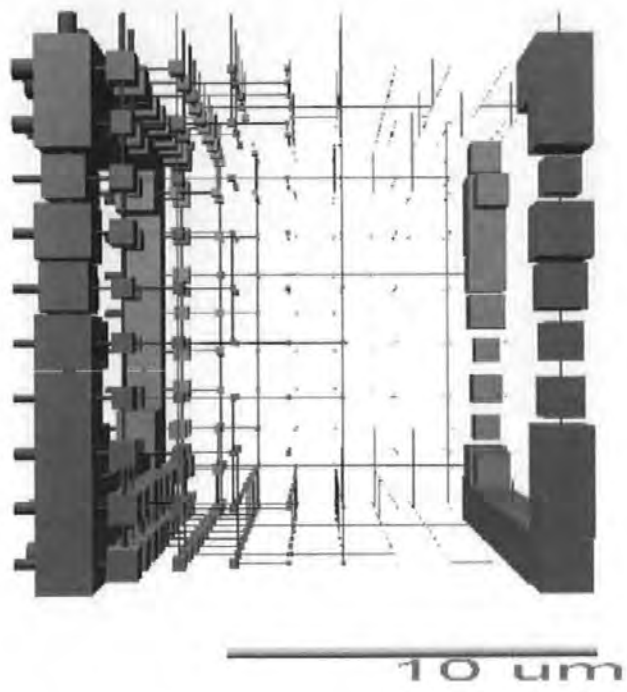
Figure 5.2 - Vertically banded Pore-Cor unit cell.
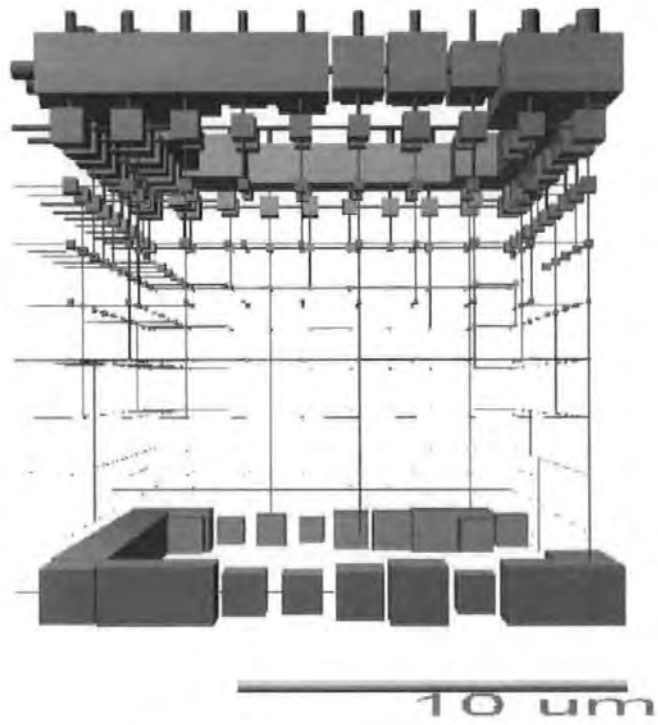
Figure 5.3 - Horizontally banded Pore-Cor unit cell.

146

The throat skew changes the percentage number of throats of the smallest size (Figure 5.4), and so "tilts" the distribution, while pore skew is a scaling factor applied across the originally linear logarithmic distribution, which increases the sizes of the pores by a constant ratio, up to a cut-off value, the cut-off value being defined by the limitation of the pore-row spacing for adjacent pores.
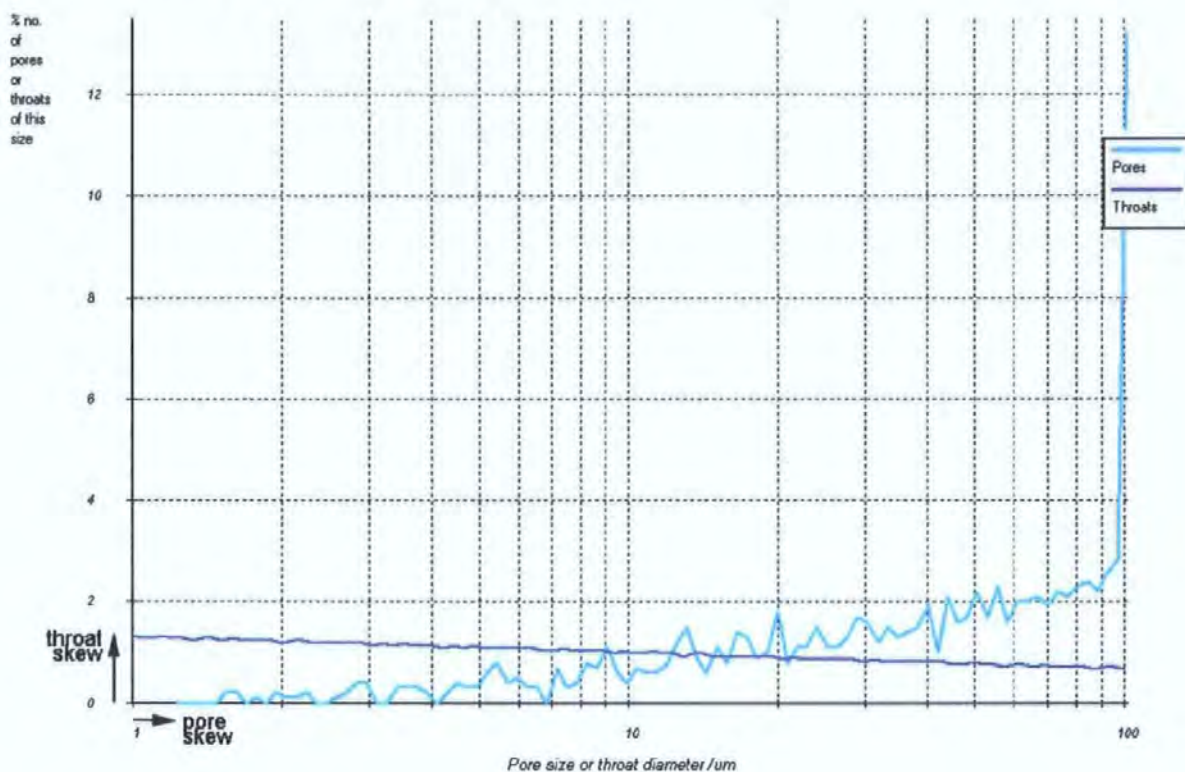
Figure 5.4 - Pore and throat size distribution in a Pore-Cor unit cell with throat skew = 1.31 and pore skew = 1.23.

It is clear that the simulated void space generated by Pore Cor is very simplified, especially when compared, for example, to the Toivakka model (Toivakka and Nyfors, 2000) discussed in section 1.8.3, but the great advantage of Pore-Cor is that the porosity and the percolation characteristics of the simulated structures match closely those measured experimentally. Also the size and the distribution of sizes for the voids are in a realistic range, as the shielding effect of large voids by small voids is taken into account. This has been shown by Schoelkopf *at al.*

147

(Schoelkopf *et al.*, 2003) and Ridgway *et al.* (Ridgway *et al.*, 2002) to be a crucial advantage when predicting the absorption and permeation characteristics of network structures.

5.2 Property inversion problem and the representative elementary volume

The Pore-Cor model is dealing with a property 'inversion' problem. Although any single porous structure will give rise to a single mercury intrusion curve and a single value for its permeability, the opposite is not true; the real structure to the porosimetry curve is a many-to-one mapping. There are an infinite number of simulated unit cells that could give rise to the same value of permeability or have the same percolation characteristics. This problem can be avoided by applying arbitrary restrictions to the network structure: the one-dimensional bundle of capillaries model is an extreme example of this. But, by doing so, the usefulness of the model decreases, as the resulting structure has to fit various arbitrary constraints. Pore-Cor applies fewer restrictions to the simulated network structure and therefore generates a large number of structures corresponding to a single intrusion curve.

To cope with this problem, the model creates groups of stochastic realisations known as stochastic generations. Each stochastic generation is created by using a different set of pseudo-random starting numbers. If the unit cell is the same size as the Representative Elementary Volume (REV) of the sample, and its complexity is equivalent to the complexity of the experimental void structure, then different stochastic generations will all have the same properties, as the random effects will average out across the unit cell. Usually the model does not fulfil the criteria of representing the REV of the sample, and the variability of the results for different stochastic generations must be analysed statistically. However it has been shown by Schoelkopf *et al.* (Schoelkopf *et al.*, 2000) that, in the modelling of paper coating, the

148

properties of different stochastic generations are similar, as the REV and the actual size of the unit cell are similar.

5.3 Recent applications and developments of Pore-Cor with regard to paper coating

Pore-Cor has been widely used by Schoelkopf (Schoelkopf *et al.*, 2002; Schoelkopf *et al.*, 2001; Schoelkopf *et al.*, 2000 and Schoelkopf, 2002) to model how a wetting fluid imbibes through a void structure. It has been experimentally shown that, on very short time scales within the pore network structure, i.e. as each throat starts to fill, the wetting front does not follow the $\sqrt{t}$ proportionality described by the Lucas-Washburn equation. This is manifest on average in a failure to scale the absorption rate, based on a $\sqrt{t}$ observation, with the pore size, despite keeping surface chemistry and, to a large extent, geometry constant.

In section 1.8.4.3 the theory of the Bosanquet equation and its application to the field of paper coating has been explained in detail. According to the Bosanquet equation, the fluid accelerated on entering a large capillary is retarded because of the larger mass of fluid involved, and, therefore, the larger inertia compared with fluid entering smaller capillaries. Fluid entering the finest capillaries wets with plug-like flow proportional to t, which lasts for up to ~10 ns (nanoseconds). This is just long enough for water and many oils to fill a low aspect ratio ≤ 0.1 μm pore, i.e. a fine pore approximately as long as its diameter. Such pores are often found in paper coating structures, especially those made from GCC.

Schoelkopf *et al.* (Schoelkopf *et al.*, 2000) used Pore-Cor to simulate the network structures of several calcium carbonate tablets. They simulated the imbibition of wetting liquid by such structures, using both the Lucas-Washburn and the Bosanquet equations. For example, in

149

Figure 5.5, it can be observed that, at a very short time scale, the fluid imbibing into the structures can reach some pores deep in the structure (as indicated by the arrow) before others closer to the surface. The results of the simulation and the experiments, carried out during the Schoelkopf research project, have shown very good correlation and reproducibility, giving a great contribution to the understanding of the permeation of porous structures by wetting fluid, as in the case of ink applied onto paper coating. The Bosanquet equation has now been included in the Pore-Cor software package, alongside the Lucas-Washburn one, and the wetting of a porous structure can now be simulated according to either equation.
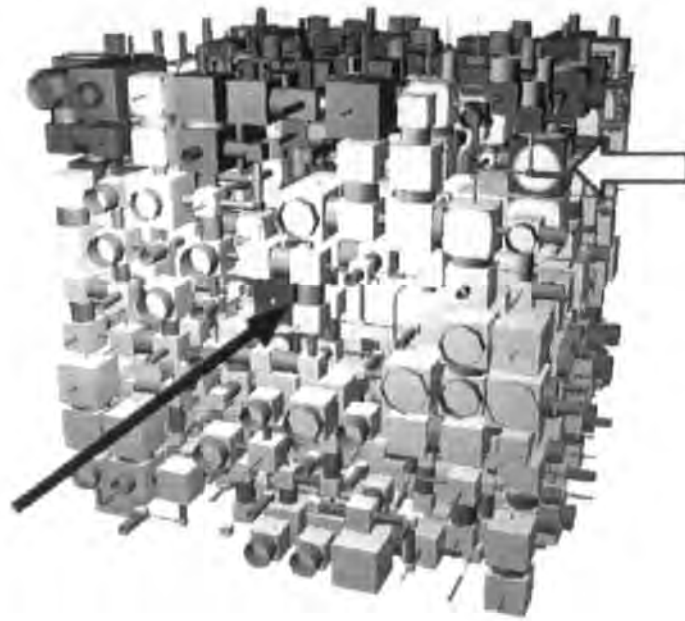
Figure 5.5 - Non-uniform wetting front. Water, shown dark, entering a unit cell representative of a compressed calcium carbonate tablet. The black arrow shows an advanced pathway, while the white arrow shows a partially filled throat and some of the surface features are empty (Schoelkopf, 2002).

The throats in the simulated porous network generated by Pore-Cor have traditionally been represented by cylinders, and the fluid-dynamics through such throats have been assumed similar to that through a cylindrical capillary tube. Ridgway (Ridgway *et al.*, 2001) simulated the behaviour of a porous structure having double-conical throats (Figure 5.6). This has several advantages: it can simulate the velocity changes for a wetting fluid, caused by the

geometry changes within the network void structure, it can simulate the hold-up of non-wetting fluid under external pressure, and it makes it possible to generate structures with porosity matching the experimentally measured one, without arbitrarily bulking up the pore size by using the pore-skew parameter.
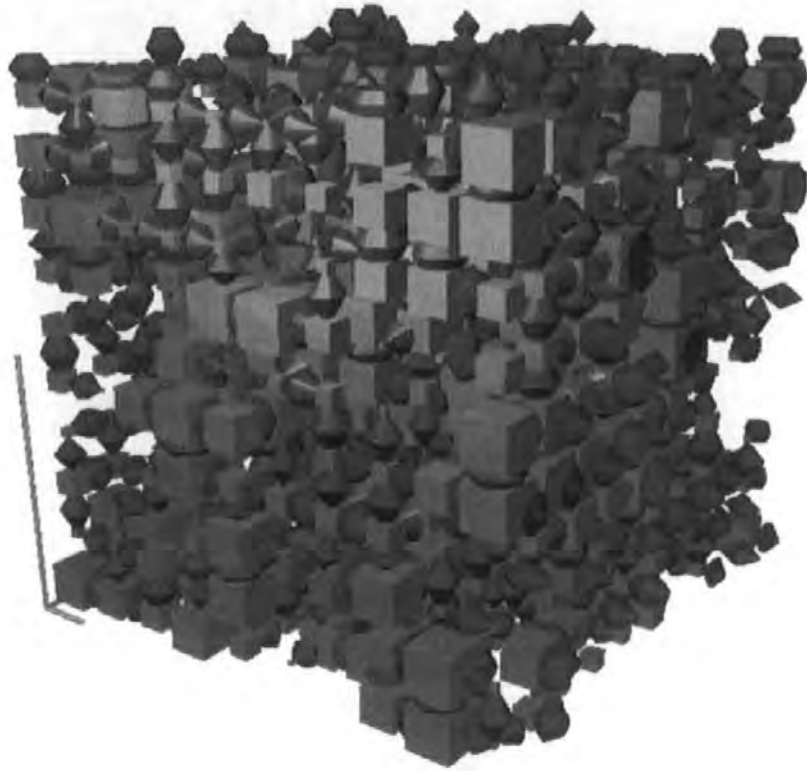
Figure 5.6 - Pore-Cor unit cell with double conical throats.

The geometry of the conical throats is shown in Figure 5.7.
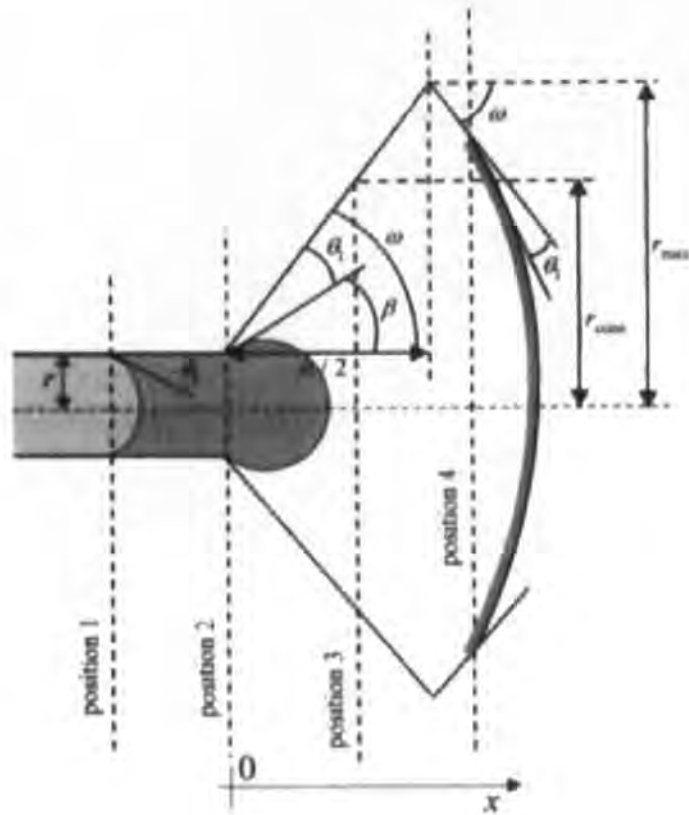
Figure 5.7 - Cross-sectional view of a non-wetting fluid entering a conical throat.

The imbibition of liquid into the structures with double-conical throats has also been studied by the same authors with the Bosanquet equation.

Bodurtha (Bodurtha *et al.*, 2001; Bodurtha, 2003; Bodurtha *et al.*, 2005) focused on the study of anisotropic paper coating structures, as might be found when platey-like clay or needle-like PCC particles are used as pigments. In his work, the structure of the unit cell was modified to make it anisotropic, by re-scaling the z axis relative to the x and y axes. When the z axis is re-scaled to make the feature smaller, the pores become rectangular in cross-section, and the x and y throats gain elliptical cross-sections. A structure representing a clay-based paper coating is shown in Figure 5.8.

152
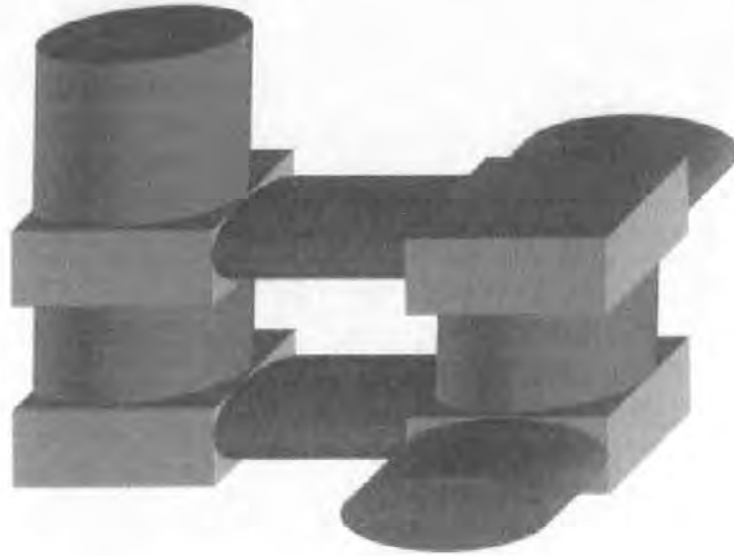
Figure 5.8 - Anisotropic structure showing throats with elliptical cross-section and plate like pores with rectangular cross-section.

By re-scaling the z axis to make features larger in this direction results in pores having a rod-like shape, again of rectangular cross-section, with throats once again having an elliptical cross section. Such a structure would be representative of that obtained by using aragonitic PCC as pigment (Figure 5.9).

Figure 5.9 - Anisotropic structure showing throats with elliptical cross-section and rod-like pores with rectangular cross-section.

Bodurtha has also developed and applied the wetting algorithm for these anisotropic structures and studied the imbibition of wetting fluids into such structures, in order to simulate the behaviour of ink applied on clay or aragonitic PCC based coating layers, as shown in Figure 5.10.
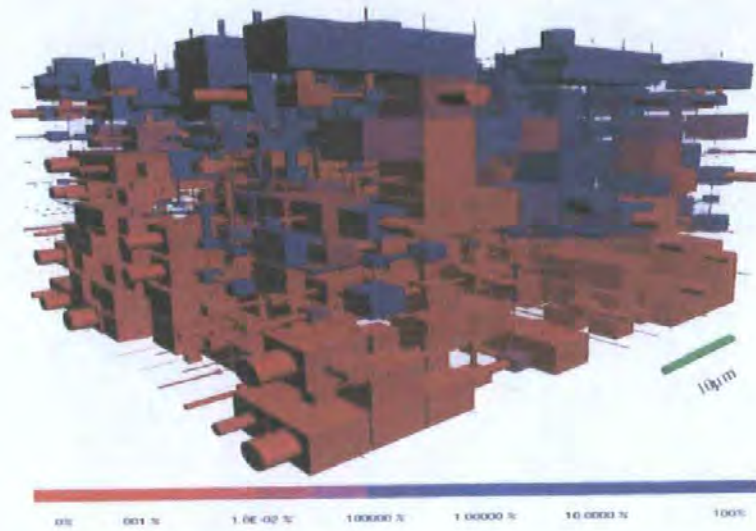
Figure 5.10 – Simulation of hexadecane absorption into a clay-based paper coating. The red voids are empty of wetting fluid and the dark blue ones are full.

These latest developments in the Pore-Cor model have not been applied in this work as the mineral pigments used in the preparation of the samples for this study are neither platey nor needle-like, and therefore the final dry structures are not expected to show anisotropy, provided the shrinkage on drying is not opposed more strongly in any one dimension.

The effective solid elements algorithm, describing the size distribution of the skeletal material between the pores, and presented in Chapter 6, has not yet been implemented for structures with double conical throats or structures which are anisotropic.

5.4 Modelling the bimodal intrusion curves

An initial attempt to fit the complete bimodal mercury intrusion curves with Pore-Cor (section 3.3), for HC90-based samples with 25 w/w% of binder, gave rise to a series of horizontally banded structures with large surface throats. This was the only way the software could accommodate the observed surface "mud-cracks".

Table 5-1 - Simulated correlation level for the bimodal intrusion curves.

	SB low T_g latex rod 2	SB low T_g latex rod 3	Acrylic high T_g latex rod 2	Acrylic high T_g latex rod 3	Starch rod 2	Starch rod 3
Simulated correlation level	0.16	0.20	0.03	0.31	0.37	0.28

The values of simulated correlation level resulting from the attempt to fit the bimodal intrusion curves are shown in Table 5-1. It is interesting to observe how thinner (rod 2) latex-based coating layers have a more random structure; the acrylic high T_g with low coating weight has a completely random structure, as shown by Figure 5.11, while the thicker (rod 3) acrylic high T_g structure is horizontally banded (Figure 5.12). This can be interpreted taking into account the diameters of the biggest pigment particles, which are ~ 5 μm, in relation to the thickness of the coating layer. In the case of the thin coating layer, the dimension of the biggest particle is larger or equal to the thickness of the layer; this limits the freedom of movement and rearrangement of the particles while the structure is drying, leading to a random structure. If the coating layer is thicker than the biggest particle of calcium carbonate, the structure is free to rearrange and this leads to more order and, therefore, to a higher correlation level. This phenomenon seems to affect less the starch-based coating colours, which both show a highly correlated structure, suggesting that the surface forces acting upon drying when starch is used as binding system are able to overcome the restraining action of the larger pigment particles.
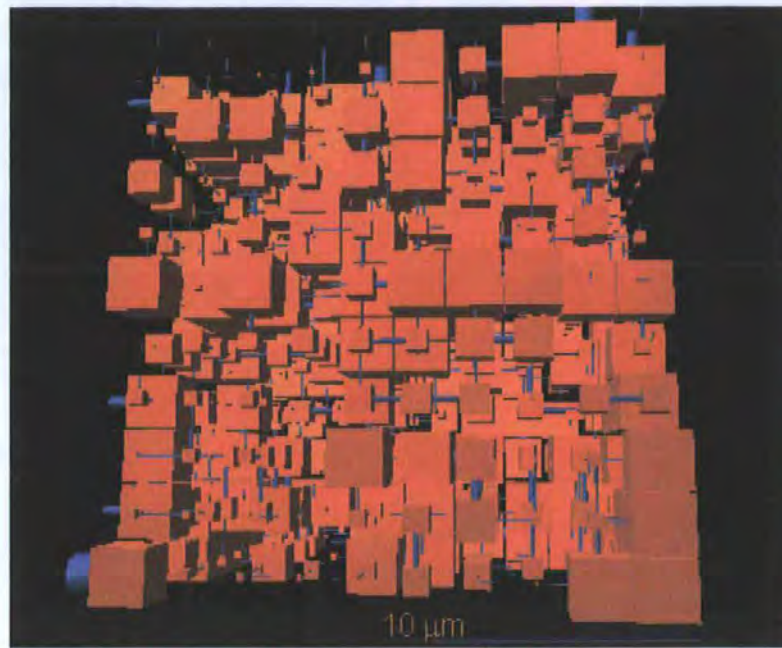
Figure 5.11 - Modelled structure of HC90 and acrylic high T_g latex-based coating applied with rod 2, generated by fitting the original bimodal mercury intrusion curve: the structure results show it to be completely random.
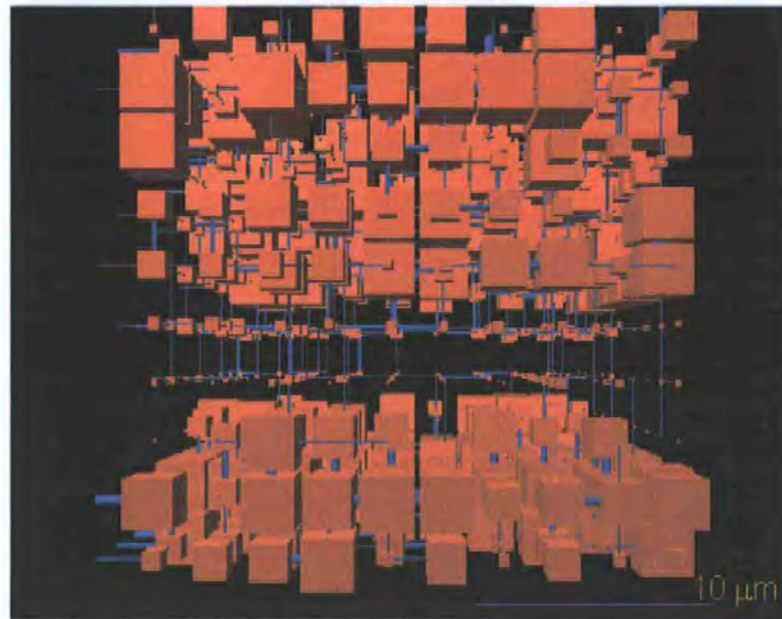
Figure 5.12 - Modelled structure of HC90 and acrylic high T_g latex-based coating applied with rod 3, generated by fitting the original bimodal mercury intrusion curve: central zone of small throats and pores.

5.5 Modelling of Hydrocarb 90-based samples

The re-defined mercury intrusion curves, obtained by splitting the original intrusion curves, as explained in section 3.3, omitting the larger crack-related pores, were subsequently used as

input data for the network simulator to describe the microstructure during unconstrained drying. For each sample, 10 different "stochastic generations" were used and Paired Student *t*-tests were performed on the mean values of each of the fitting parameters of the modelled coating layers in order to determine if there were any significant differences in their values. The stochastic generation having fitting parameters closer to the calculated average fitting parameters was chosen as representative of the sample. This process is also repeated below for coatings with different formulations.

The mercury intrusion curves were fitted with vertically banded structures, which were found to be more versatile and able to give simulation results fitting very closely the experimental intrusion curves.

The results of the software simulation for HC90-based coating colours with 25 w/w% of binder are presented in Table 5-2.

The simulated three-dimensional structures generated by the software model are shown in Figure 5.13 to Figure 5.20. Although the simulated void structures are a gross simplification of those actually existing in the real samples, they nevertheless reveal some interesting and fundamental properties which are highlighted below.

Table 5-2 – Simulation parameters resulting from the modelling of coating colours prepared with HC90 and 25 w/w% binder.

Sample	Experimental and simulated porosity / %	Simulated connectivity	Simulated correlation level	Simulated throat skew	Simulated pore skew	Figure number
SB low T_g latex rod 2	15.50	4.96	0.16	2.24	4.47	5.13
SB low T_g latex rod 3	13.96	5.08	0.17	2.15	3.06	5.14
SB high T_g latex rod 2	35.09	4.53	0.01	1.49	2.67	5.15
SB high T_g latex rod 3	21.86	3.75	0.06	1.35	1.63	5.16
Acrylic high T_g latex rod 2	37.72	5.36	0.24	1.84	3.34	5.17
Acrylic high T_g latex rod 3	23.15	4.01	0.29	1.31	3.61	5.18
Starch rod 2	17.01	4.16	0.25	1.26	3.47	5.19
Starch rod 3	10.17	5.04	0.22	1.36	2.36	5.20

Figure 5.13, which represents a thin coating prepared with fine HC90 and 25 w/w% SB latex, shows regions of small pore size illustrating the close packing and filling of pores by the deformation of the latex between the pigment particles. A similar situation can be observed for the thicker coating layer (Figure 5.14), where the pore structure becomes even tighter, as shown by lower values of porosity.
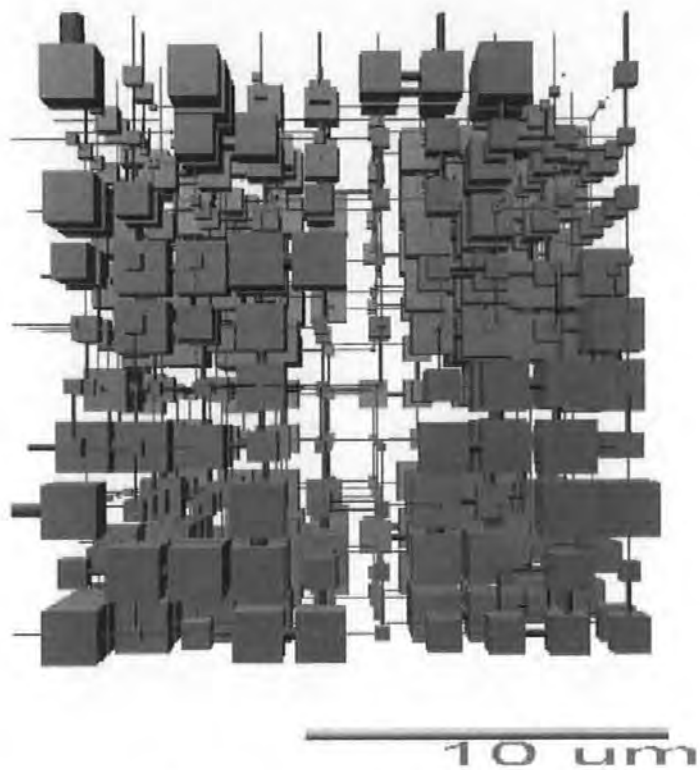
Figure 5.13 - Modelled structure of an HC90 + 25 w/w% styrene-butadiene low T_g latex coating applied with rod 2.
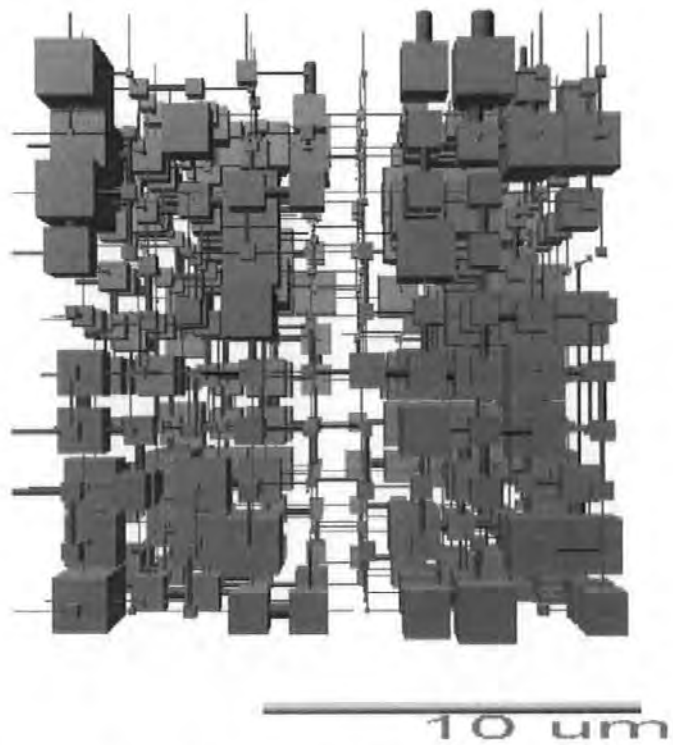
Figure 5.14 - Modelled structure of an HC90 + 25 w/w% styrene-butadiene low T_g latex coating applied with rod 3.

It is interesting to notice that the use of non-filming latex, as shown in Figure 5.15 to Figure 5.18, leads to a structure with larger voids, showing the resistance of the high T_g latex to the shrinkage action (notice the difference in the scale bar in the figures).
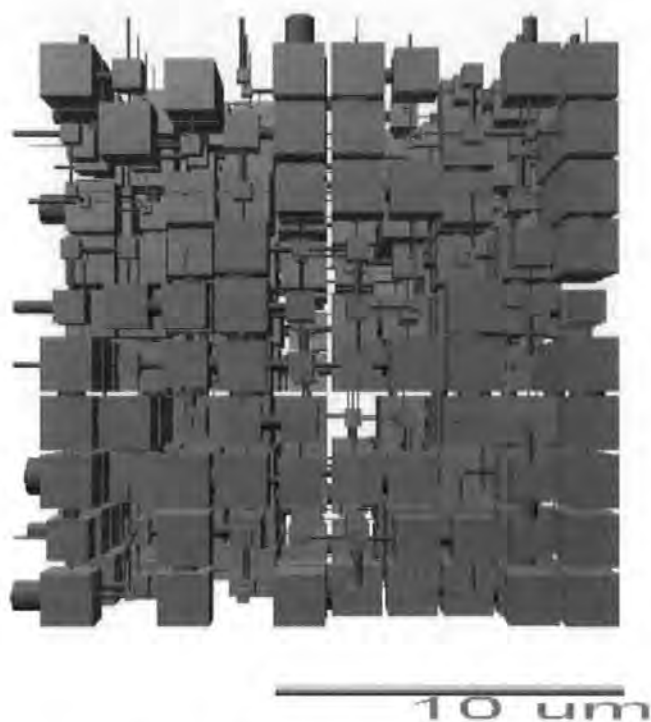
Figure 5.15 - Modelled structure of an HC90 + 25 w/w% styrene-butadiene high T_g latex coating applied with rod 2.

This becomes even more evident in the thicker coating layers, applied with rod 3 (Figures 5.16 and 5.18), as the extra freedom of movement of the particles in the thicker layer allows for a very uniform structure to be developed whilst resisting shrinkage via the high T_g latex. The lower values of the connectivity for high T_g latex-based coating layers applied with rod 3, when compared with those of coating layers applied with rod 2, is an indication of better packing of the structure.

161
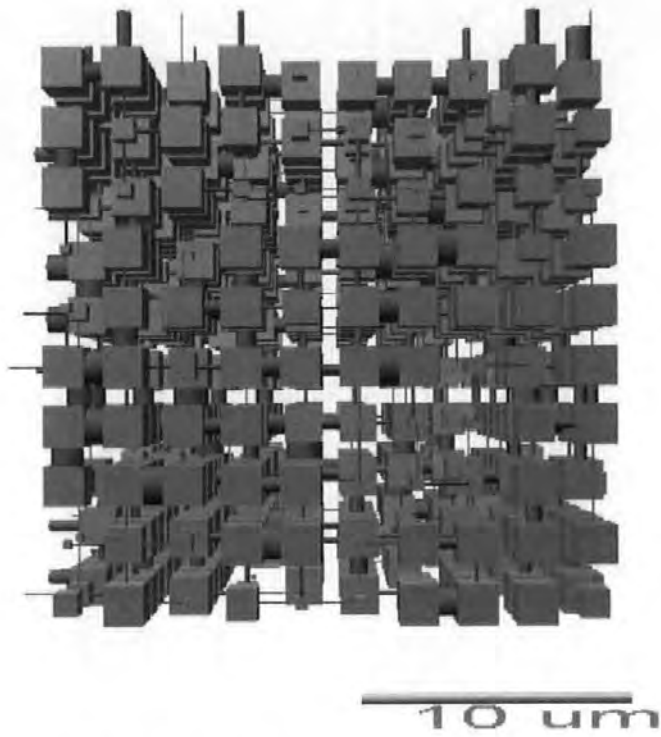
Figure 5.16 - Modelled structure of an HC90 + 25 w/w% styrene-butadiene high T_g latex coating applied with rod 3.
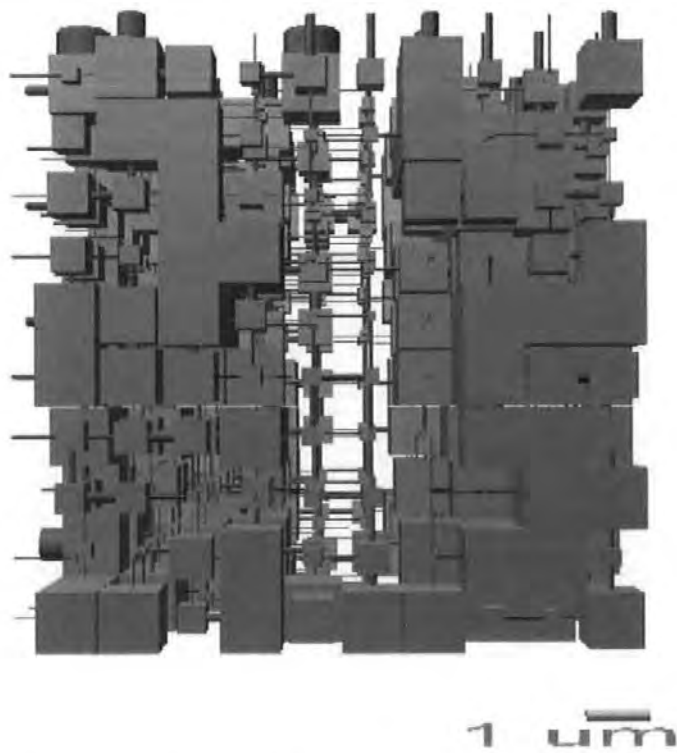
Figure 5.17 - Modelled structure of an HC90 + 25 w/w% acrylic high T_g latex coating applied with rod 2.

162
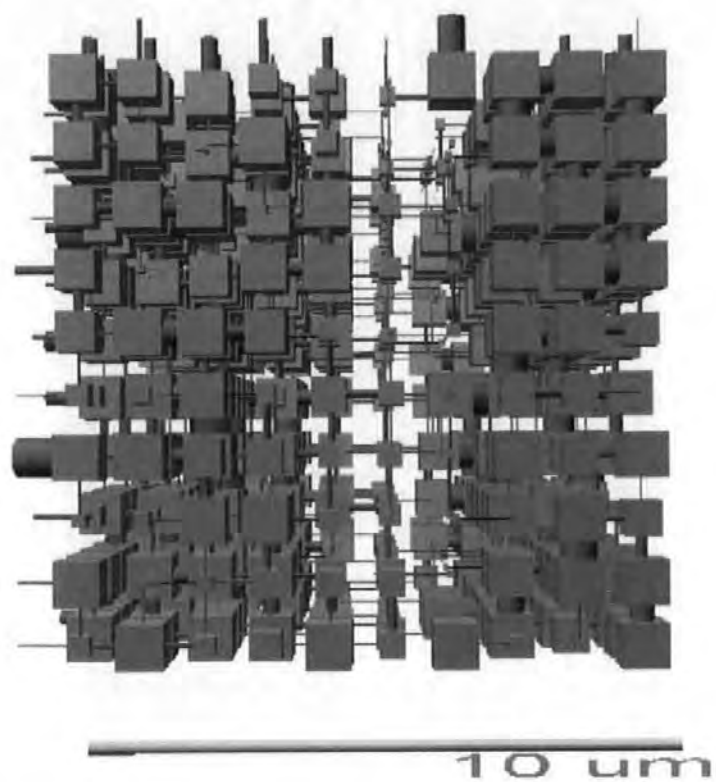
Figure 5.18 - Modelled structure of an HC90 + 25 w/w% acrylic high T_g latex coating applied with rod 3.
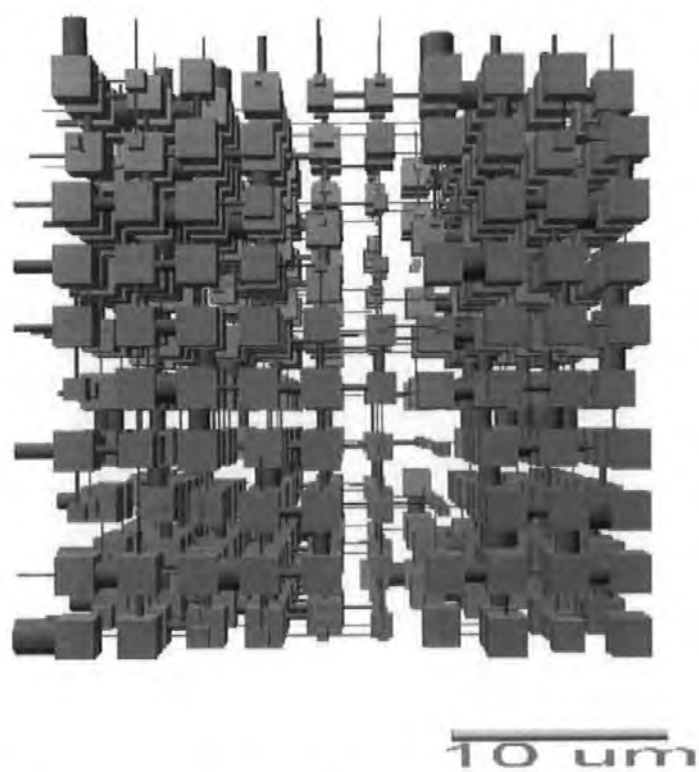
Figure 5.19 - Modelled structure of an HC90 + 25 w/w% starch coating applied with rod 2.

The final dry structures of coating layers prepared with HC90 and 25 w/w% starch are shown in Figure 5.19 and Figure 5.20. Both show a fairly uniform pore distribution, but the pores are smaller than in the latex-based coating layers. This supports the proposition of starch-induced flocculation, explained in detail in section 3.5. In the thicker coating layer, the freedom of rearrangement of the particles leads to the formation of even smaller pores. Some of the throats are completely cut off whereas others remain large, typical of a mobile binder, and the skeletal particle size is large. The modelling parameters, shown in table 5.2, are very similar for the two starch-based coating layers, but the coating layer applied with rod 3 shows a lower value of porosity.
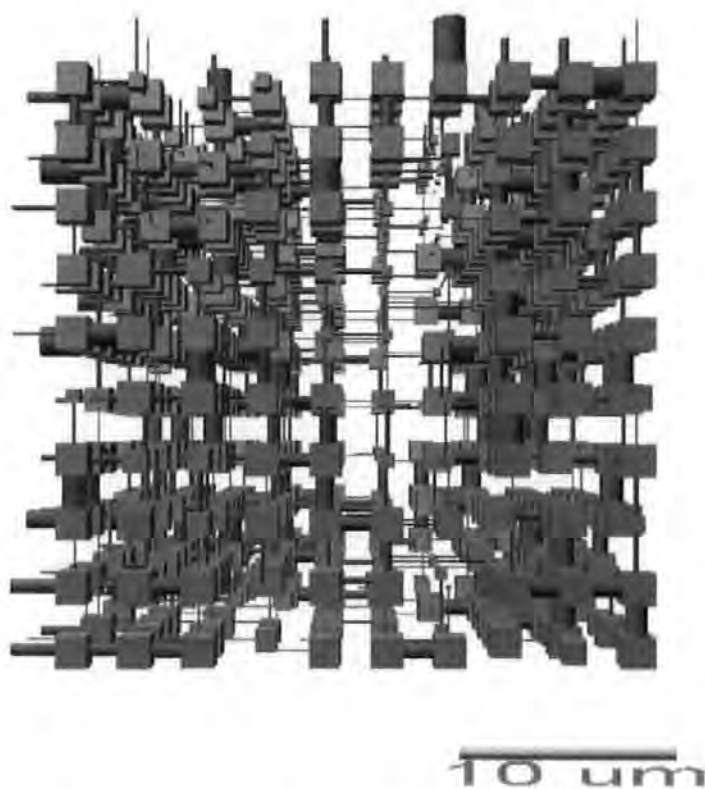
Figure 5.20 - Modelled structure of an HC90 + 25 w/w% starch coating applied with rod 3.

As Figure 5.19 and Figure 5.20 show very similar structures, a more detailed qualitative analysis can be carried out by comparing the number of features of a certain size normalised per cm^3 of sample. This confirms that in the case of the thicker coating layer the pores are smaller in size, while the throat size distributions are similar and uniform.

164
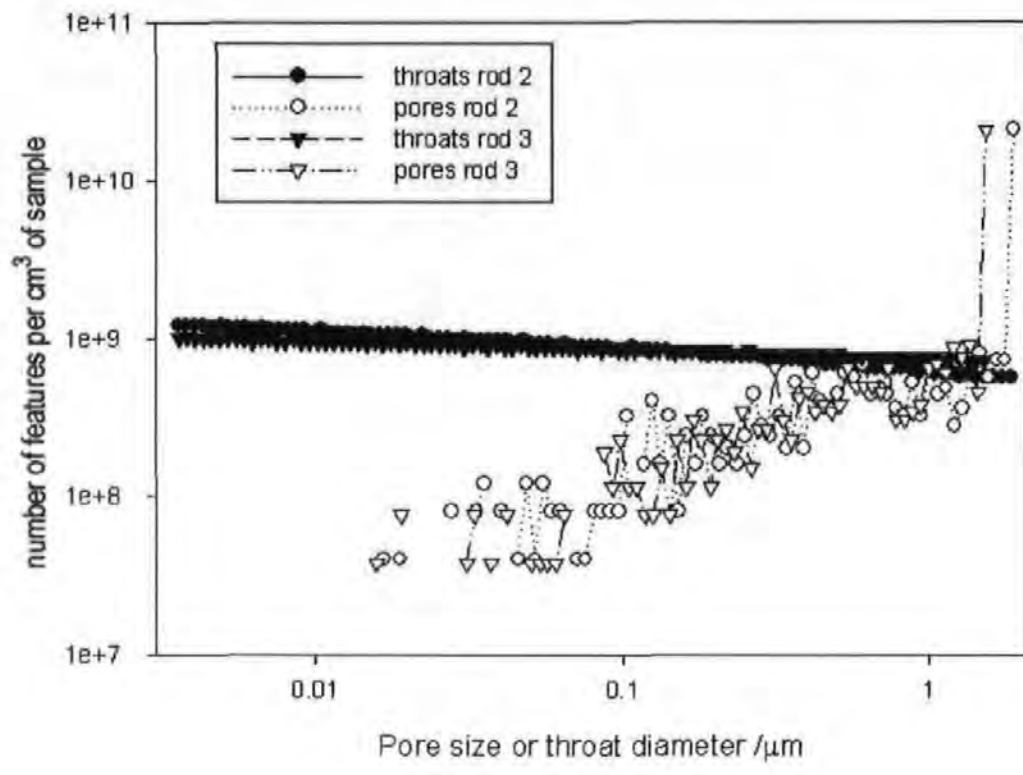
Figure 5.21 - Pore and throat size distribution in a cm³ of HC90 + 25 w/w% starch coatings.

The results of the software simulation for HC90-based coating colours with 10 w/w% of binder are presented in Table 5-3.

Table 5-3 - Simulation parameters resulting from the modelling of coating colours prepared with HC90 and 10 w/w% binder.

Sample	Experimental and simulated porosity / %	Simulated connectivity	Simulated correlation level	Simulated throat skew	Simulated pore skew	Figure number
SB low T_g latex rod 2	28.47	3.07	0.31	1.79	4.50	5.22
SB low T_g latex rod 3	24.93	4.65	0.14	1.00	4.91	5.23
SB high T_g latex rod 2	39.94	3.78	0.23	1.58	4.88	5.25
SB high T_g latex rod 3	32.25	3.71	0.21	1.79	4.70	5.26
Acrylic high T_g latex rod 2	38.43	4.76	0.18	1.81	3.52	5.27
Acrylic high T_g latex rod 3	24.51	3.44	0.11	2.02	3.01	5.28
Starch rod 2	26.52	4.22	0.34	1.91	3.16	5.29
Starch rod 3	22.46	4.57	0.23	1.66	1.96	5.30

The coating layers prepared with HC90 and a lower level of SB low T_g latex (Figure 5.22 and Figure 5.23) show a more random and uniform structure than the corresponding ones containing a higher level of latex, as shown by their lower values of correlation level. The coating layer thickness does not affect the final structure of the coating layer as much as when 25 w/w% of latex was used. The throats appear to be larger when a thinner coating layer is applied.
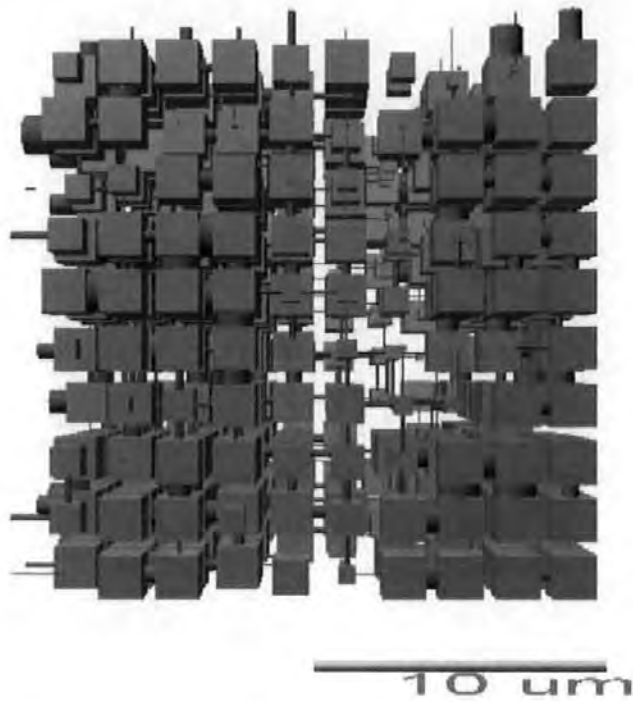
Figure 5.22 - Modelled structure of an HC90 + 10 w/w% styrene-butadiene low T_g latex coating applied with rod 2.
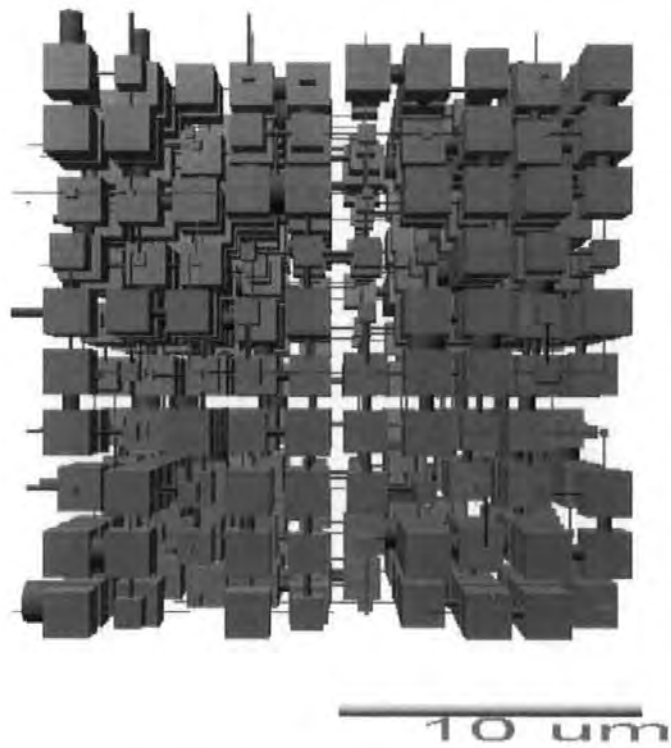
Figure 5.23 - Modelled structure of an HC90 + 10 w/w% styrene-butadiene low T_g latex coating applied with rod 3.

Figure 5.24 shows that the pore sizes have a very similar distribution in the two samples, while the throats are larger in the case of the thinner coating layer.
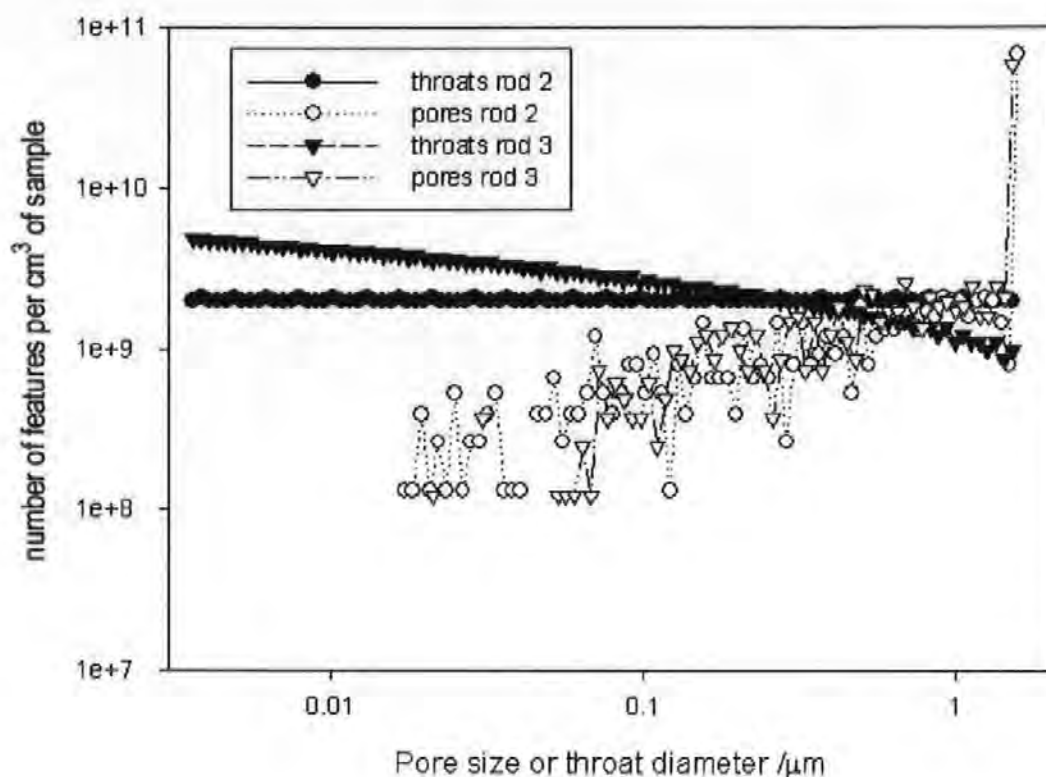
Figure 5.24 - Pore and throat size distribution in a cm³ of HC90 + 10 w/w% styrene-butadiene low T_g latex coatings.

When a hard (non-filming) latex, either acrylic or styrene-butadiene, is used in the coating formulation, the resulting modelled structures are again very similar across the coat weight range (Figures 5.25 to 5.28). They show large pores and smaller skeletal elements, confirming that the latex is not film-forming in the experimental conditions and it is resisting the shrinkage acting upon drying. The value of connectivity for thicker (rod 3) coating layers is lower than that obtained for thin ones (rod 2). This can be seen as an indication of better packing of the structure.
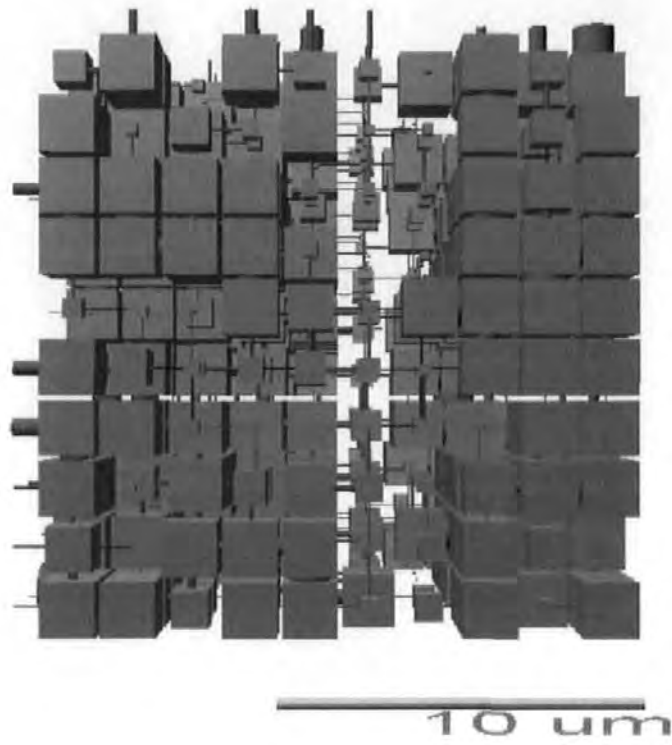
Figure 5.25 - Modelled structure of an HC90 + 10 w/w% styrene-butadiene high T_g latex coating applied with rod 2.
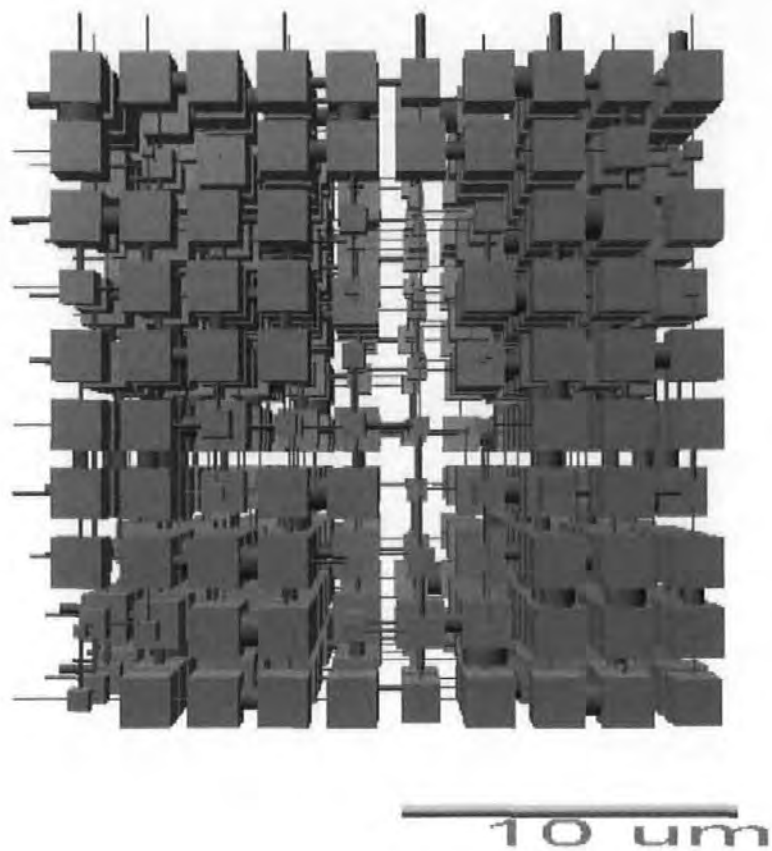
Figure 5.26 - Modelled structure of an HC90 + 10 w/w% styrene-butadiene high T_g latex coating applied with rod 3.
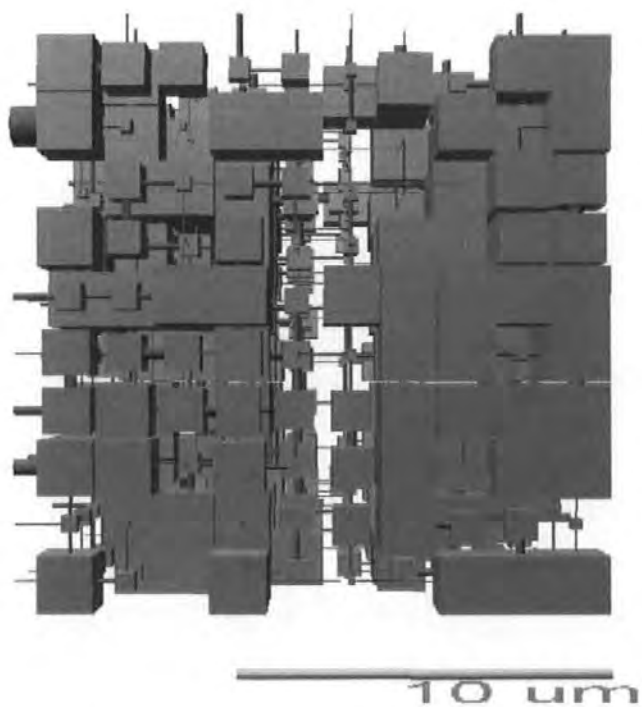
Figure 5.27 - Modelled structure of an HC90 + 10 w/w% acrylic high T_g latex coating applied with rod 2.
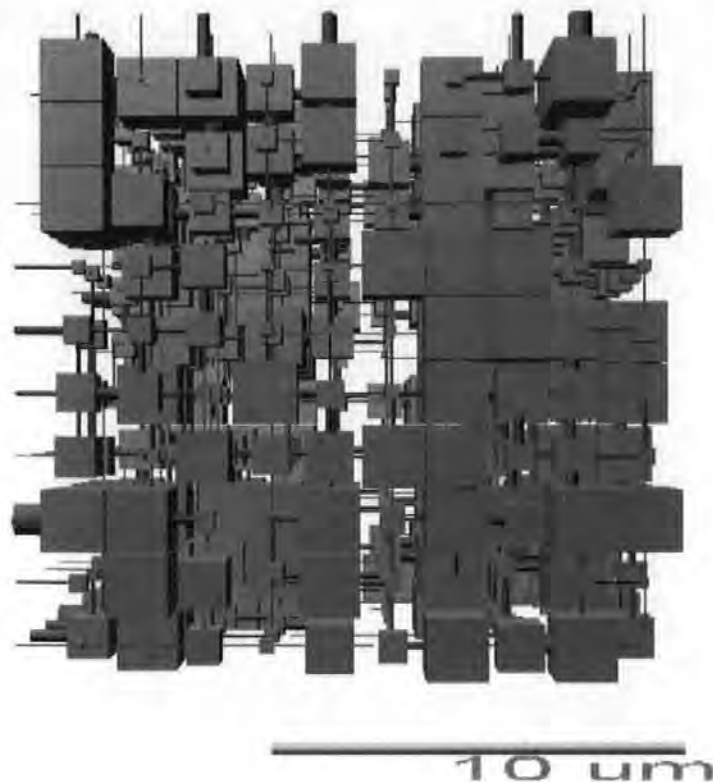
Figure 5.28 - Modelled structure of an HC90 + 10 w/w% acrylic high T_g latex coating applied with rod 3.

Figure 5.29 and Figure 5.30 show the modelled three-dimensional structures generated by Pore-Cor in the case of coating layers prepared with HC90 and 10 w/w% starch. When a lower amount of starch is used in the coating colour formulation, the resulting modelled structure shows a central area of very small pores. The starch-induced flocculation is therefore non-uniformly distributed in the whole unit cell, but localised in certain areas of the structure, while, when a higher level of starch was used, this flocculation effect could be observed across the whole unit cell. This is unlikely to have originated from an inhomogeneous distribution of flocculated particles in the diffusion-controlled mobile wet colour but rather indicates the strength of flocculation. A weakly flocculated structure can deform and the deformation is heterogeneous depending on the localised stress generated during drying.
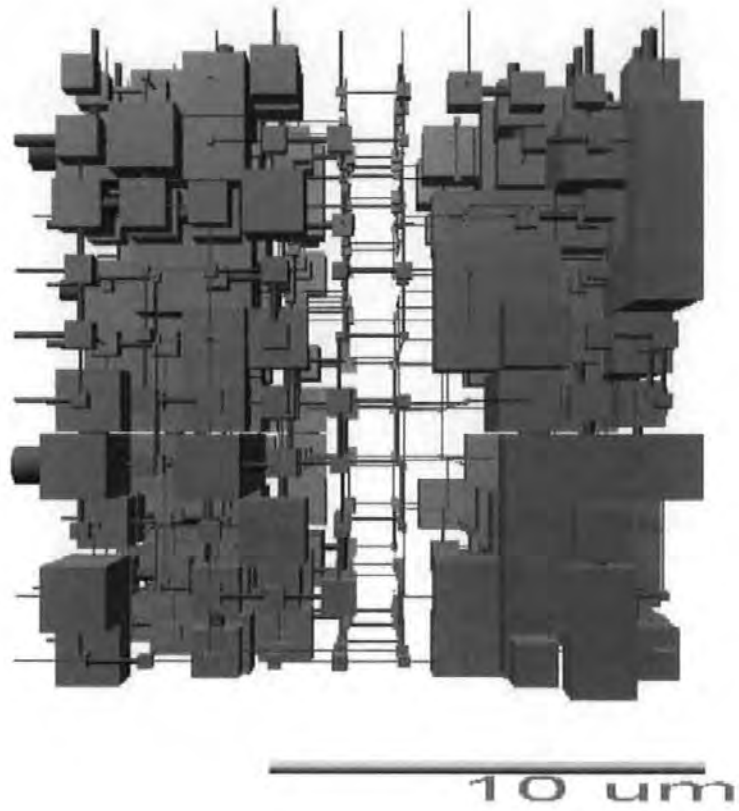
Figure 5.29 - Modelled structure of an HC90 + 10 w/w% starch coating applied with rod 2.
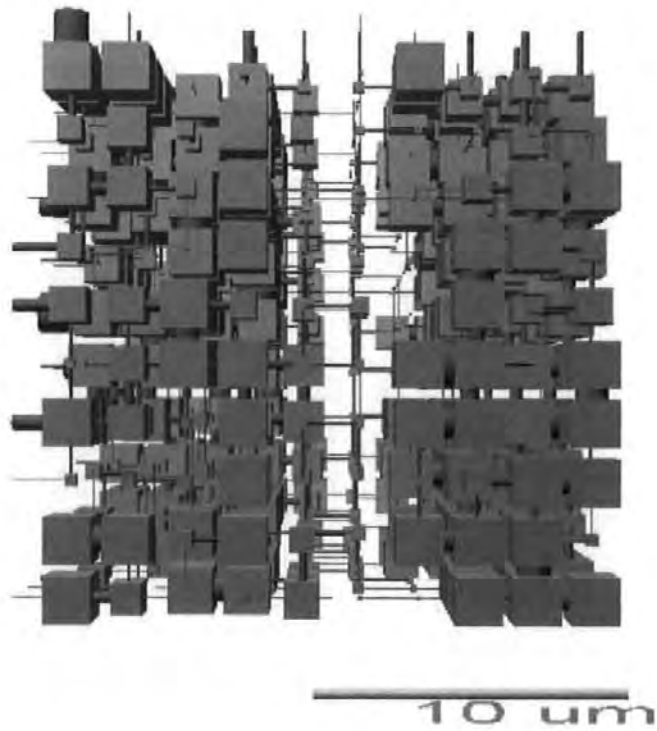
Figure 5.30 - Modelled structure of an HC90 + 10 w/w% starch coating applied with rod 3.
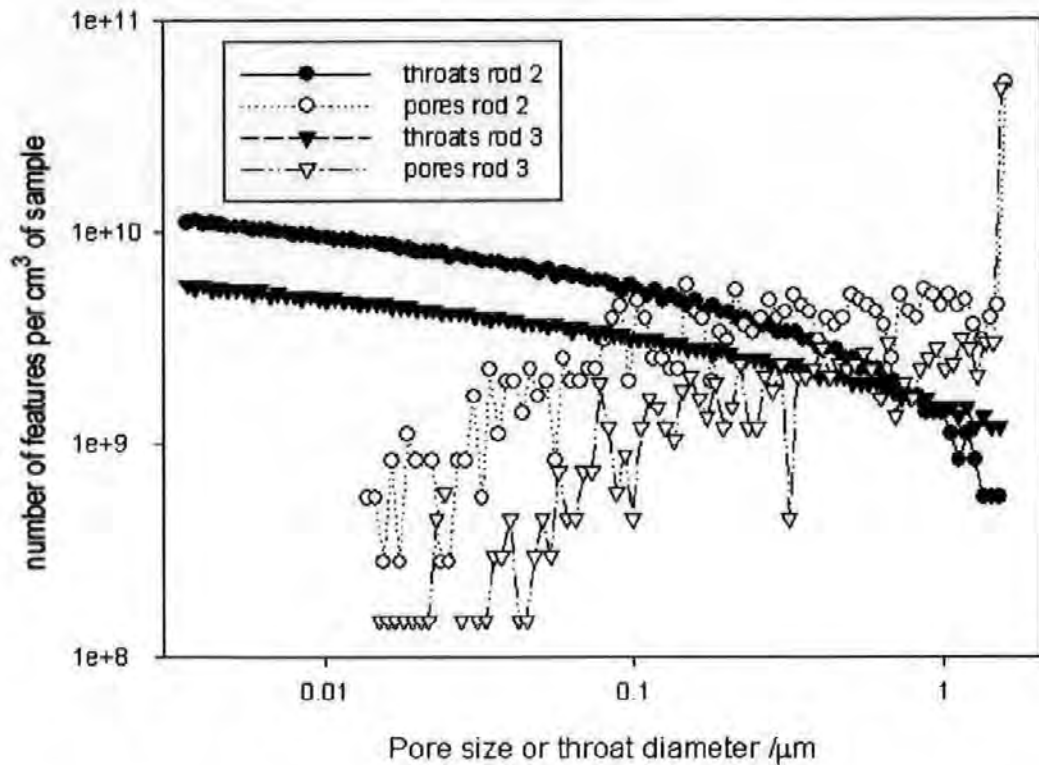
Figure 5.31 - Pore and throat size distribution in a cm³ of HC90 + 10 w/w% starch coatings.

Figure 5.31 shows that, in the case of a thinner coating layer, there is a larger number of smaller throats and smaller pores.

5.6 Modelling of Hydrocarb 60-based samples

Table 5-4 shows the results of the Pore-Cor modelling carried out on dry coating layers prepared with the coarser calcium carbonate, HC60, and 25 w/w% binder.

Table 5-4 - Simulation parameters resulting from the modelling of coating colours prepared with HC60 and 25 w/w% binder.

Sample	Experimental and simulated porosity / %	Simulated connectivity	Simulated correlation level	Simulated throat skew	Simulated pore skew	Figure number
SB low T_g latex rod 2	14.25	3.30	0.14	1.95	4.23	5.32
SB low T_g latex rod 3	12.76	4.49	0.28	2.22	3.43	5.33
SB high T_g latex rod 2	24.17	4.45	3.00E-02	1.95	4.57	5.34
SB high T_g latex rod 3	19.57	5.53	0.13	1.92	2.01	5.35
Acrylic high T_g latex rod 2	19.75	5.52	0.18	2.05	4.21	5.36
Acrylic high T_g latex rod 3	18.90	2.76	0.12	0.28	1.73	5.37
Starch rod 2	14.31	3.16	0.25	1.57	2.29	5.39
Starch rod 3	8.01	2.79	0.32	1.53	3.63	5.40

Figure 5.32 and Figure 5.33 show the modelled structures of SB low T_g latex-based coating layers. It can be observed that, similarly to HC90-based coatings, there are areas showing very small voids. This shows how the particles of SB film-forming latex likely deform during the drying process, leading to areas of close packing of the structure. In the case of the thicker coating layer (Figure 5.32), the freedom of rearrangement of the particles leads to a tighter structure, in this case probably due to throat closure by the binder extrusion rather than by flocculation (and blockage) as was the case for starch-containing colours. The porosity decreases from 14.25 % for the thin (rod 2) coating layer to 12.76 % for the thicker (rod3) coating layer.
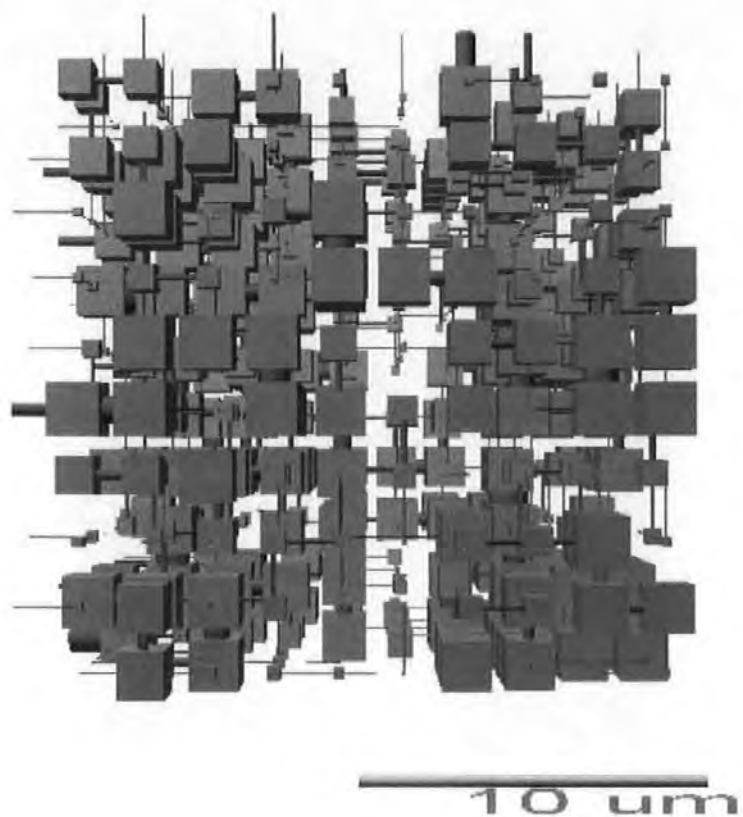
Figure 5.32 - Modelled structure of an HC60 + 25 w/w% styrene-butadiene low T_g latex coating applied with rod 2.
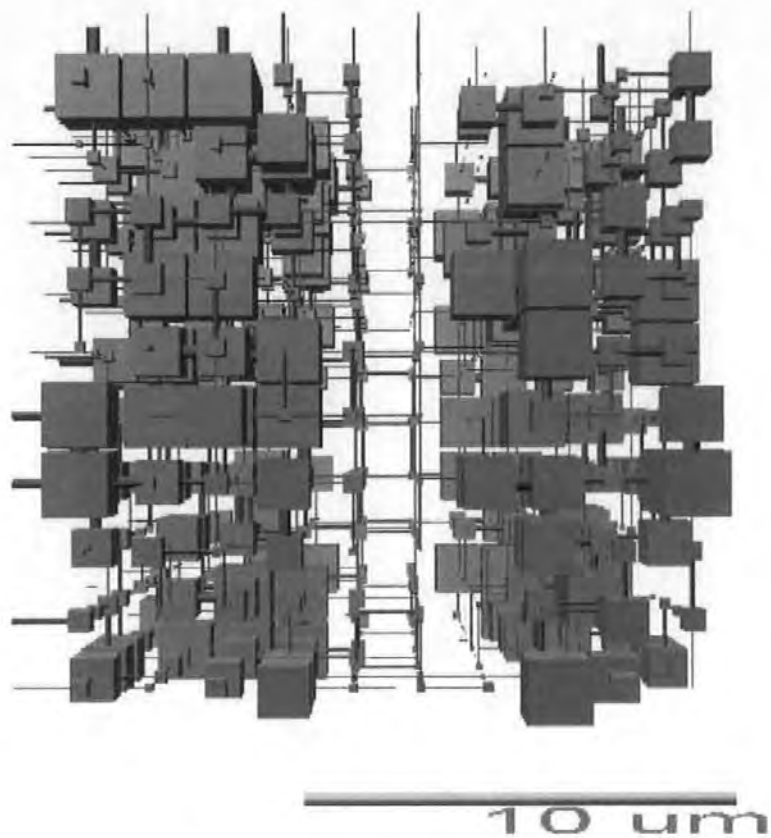
Figure 5.33 - Modelled structure of an HC60 + 25 w/w% styrene-butadiene low T_g latex coating applied with rod 3.
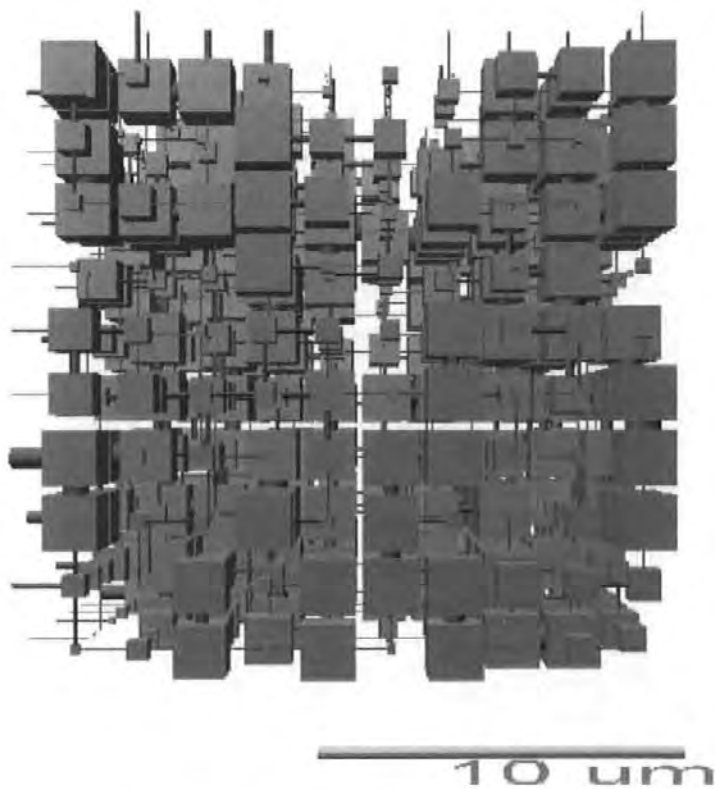
Figure 5.34 - Modelled structure of an HC60 + 25 w/w% styrene-butadiene high T_g latex coating applied with rod 2.

The use of high T_g latex in the coating formulation (Figure 5.34 to Figure 5.37) gives rise to more uniform structures, with larger voids. This shows, once more, that hard high T_g latex particles do not allow such a large deformation of the coating layer under the action of the shrinkage forces.
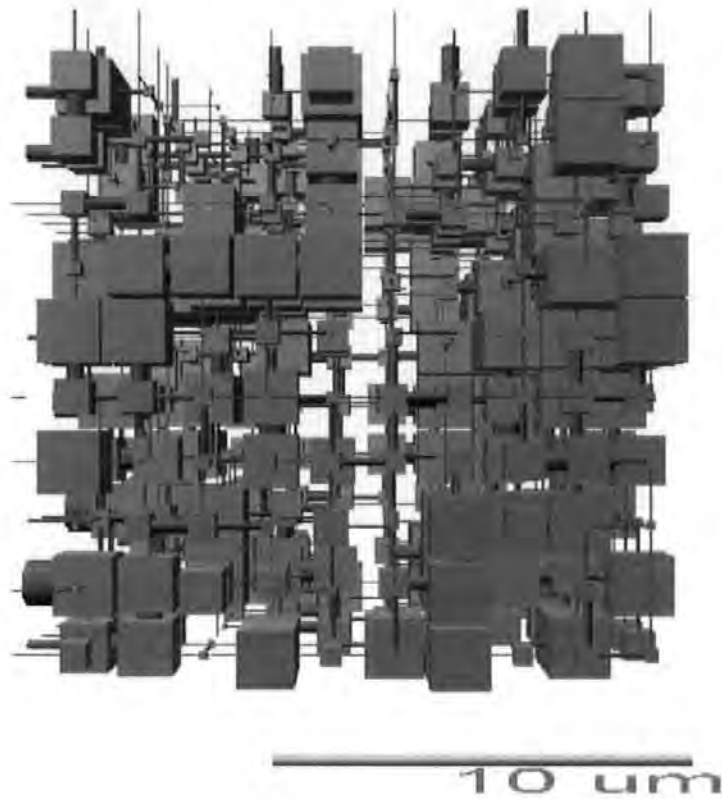
Figure 5.35 - Modelled structure of an HC60 + 25 w/w% styrene-butadiene high T_g latex coating applied with rod 3.

Figure 5.38 shows the difference in pore sizes and throat diameters for cm^3 of coating layers based on HC60 with 25 w/w% acrylic high T_g latex. The two distributions are similar, but the lower value of connectivity observed in the case of the thicker coating layer (rod 3) shows the higher degree of packing of the structure.
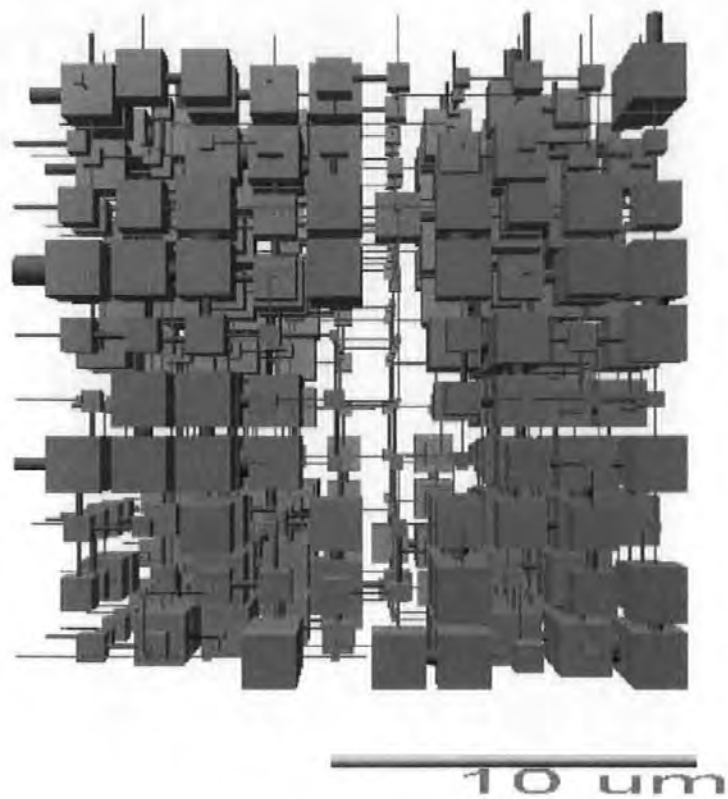
Figure 5.36 - Modelled structure of an HC60 + 25 w/w% acrylic high T_g latex coating applied with rod 2.
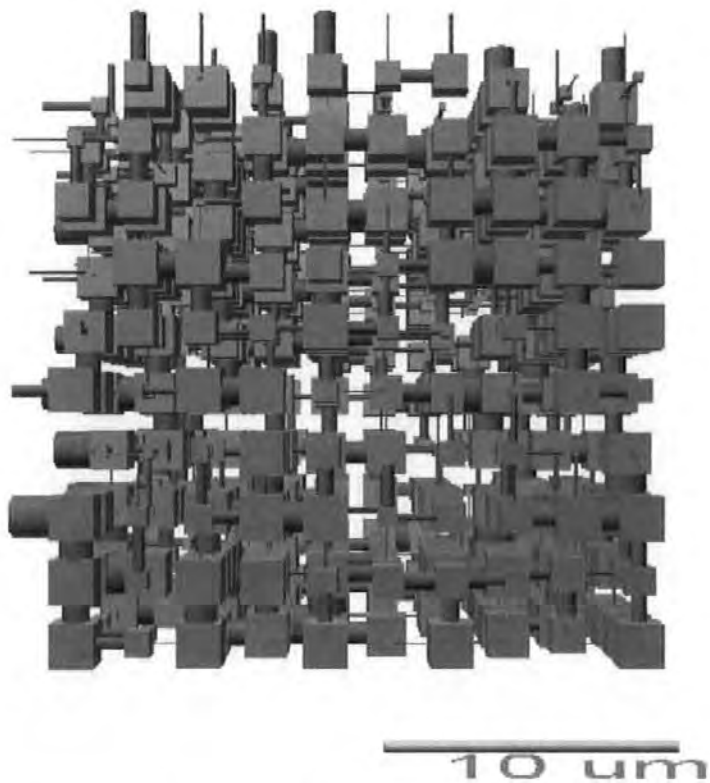
Figure 5.37 - Modelled structure of an HC60 + 25 w/w% acrylic high T_g latex coating applied with rod 3.
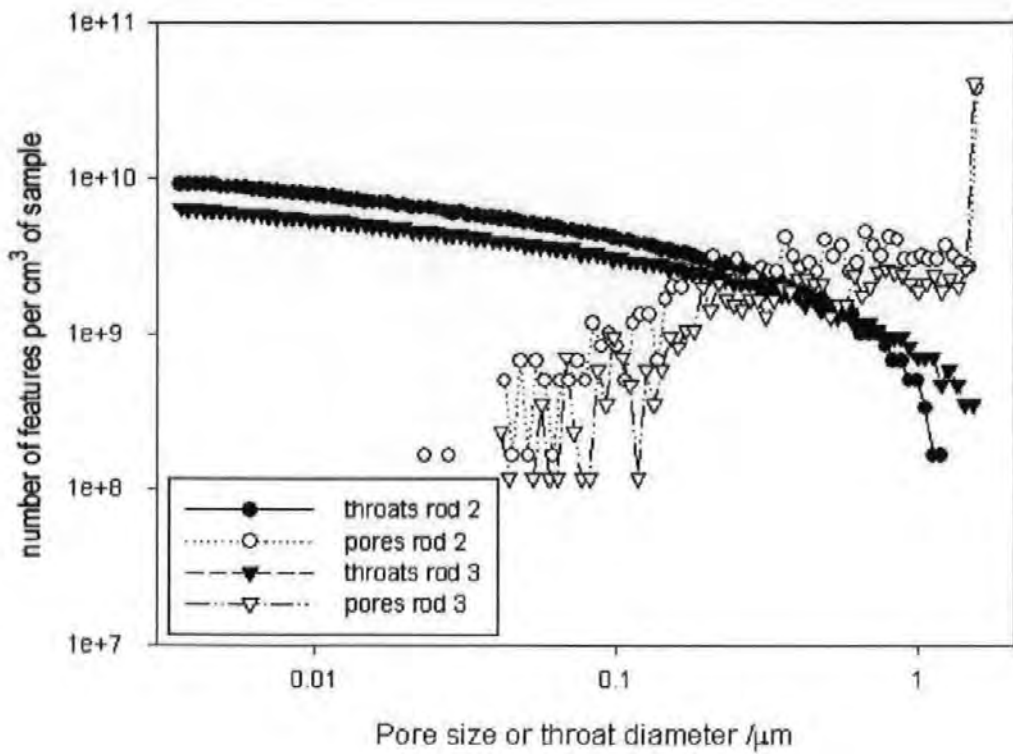
Figure 5.38 - Pore and throat size distribution in a cm^3 of HC60 + 25 w/w% acrylic high T_g latex coatings.
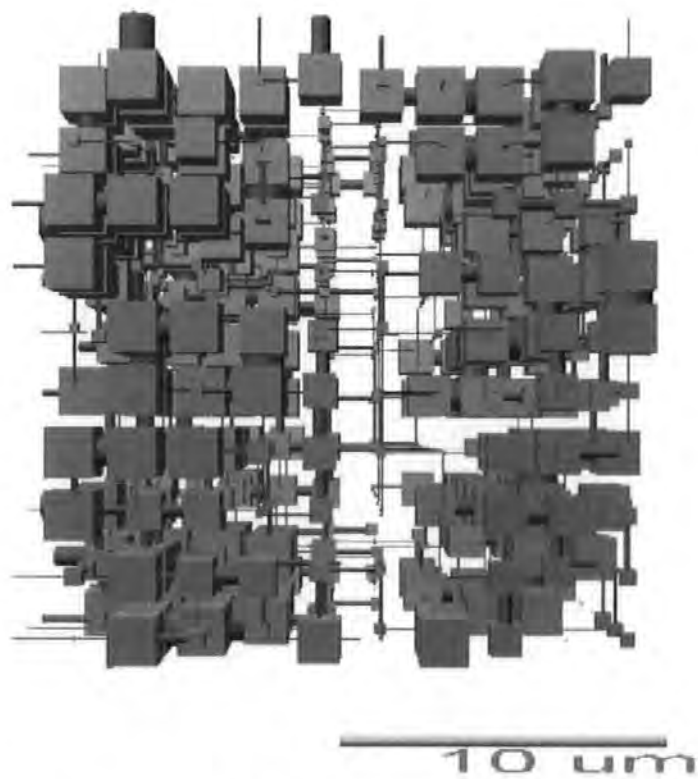
Figure 5.39 - Modelled structure of an HC60 + 25 w/w% starch coating applied with rod 2.
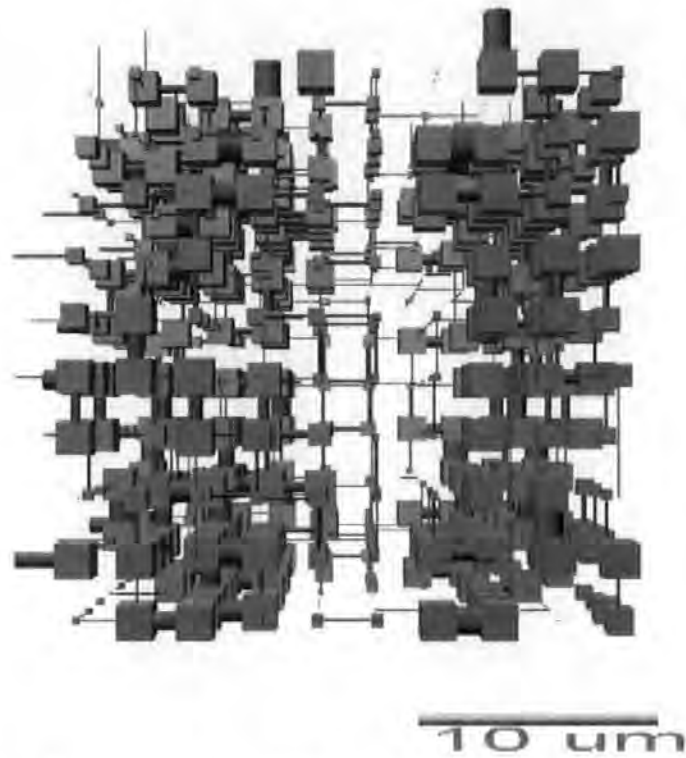
Figure 5.40 - Modelled structure of an HC60 + 25 w/w% starch coating applied with rod 3.

Figure 5.39 and Figure 5.40 show the modelled structures of dry coating layers prepared with HC60 and 25 w/w% starch. As previously observed for HC90-based coating layers, the use of starch in the coating formulation causes a partial flocculation and pore blockage of the pigment particles. This is confirmed by the presence of areas of close packing of the structures, with very small voids, and the presence of large solid elements. When the coating layer is thicker, these large solid skeletal elements have more freedom to rearrange upon drying, and this leads to a closer packing of the particles, with even smaller voids, as shown in Figure 5.40. This is confirmed by lower values of porosity and connectivity of the modelled structure, when compared with that of the thinner coating layer (Figure 5.39).

Table 5-5 shows the results of the Pore-Cor modelling on samples prepared with HC60 and 10 w/w% binder.

Table 5-5 - Simulation parameters resulting from the modelling of coating colours prepared with HC60 and 10 w/w% binder.

Sample	Experimental and simulated porosity / %	Simulated connectivity	Simulated correlation level	Simulated throat skew	Simulated pore skew	Figure number
SB low T_g latex rod 2	21.75	3.81	0.32	1.48	1.73	5.41
SB low T_g latex rod 3	18.67	5.74	0.27	1.59	3.43	5.42
SB high T_g latex rod 2	30.77	2.97	0.18	1.18	2.56	5.43
SB high T_g latex rod 3	25.74	5.80	0.21	1.62	4.91	5.44
Acrylic high T_g latex rod 2	26.09	3.40	0.33	1.15	3.23	5.45
Acrylic high T_g latex rod 3	24.76	3.16	0.32	1.00	4.66	5.46
Starch rod 2	17.36	3.35	0.42	0.70	2.96	5.47
Starch rod 3	15.70	5.26	0.22	0.48	4.18	5.48

Figure 5.41 and Figure 5.42 show the three-dimensional structures generated by Pore-Cor in the case of coating layers based on HC60 and 10 w/w% SB low T_g latex. These resulting structures are similar to those produced by Pore-Cor with the higher level of latex. The central areas of small voids show the effect of the soft latex particles, deforming under the action of the capillary forces and allowing the formation of a closely packed structure.

181
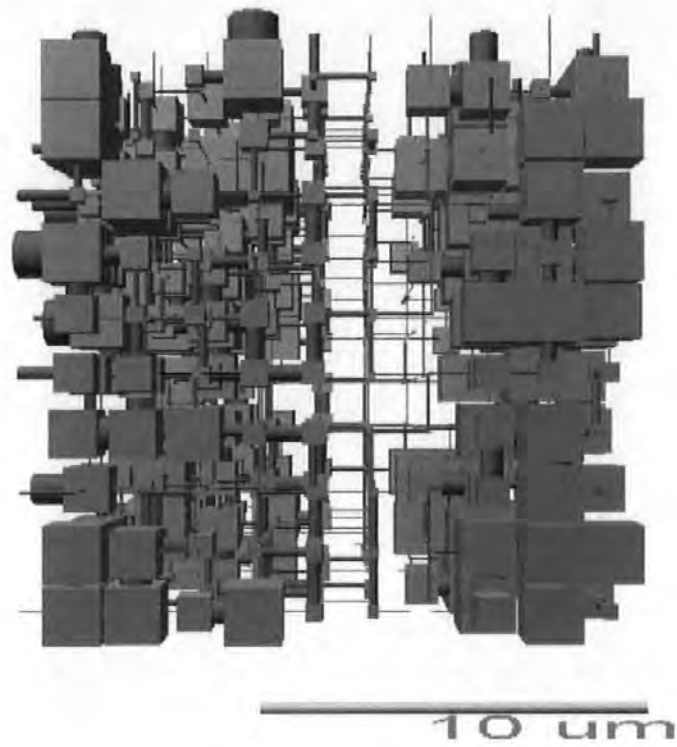
Figure 5.41 - Modelled structure of an HC60 + 10 w/w% styrene-butadiene low T_g latex coating applied with rod 2.
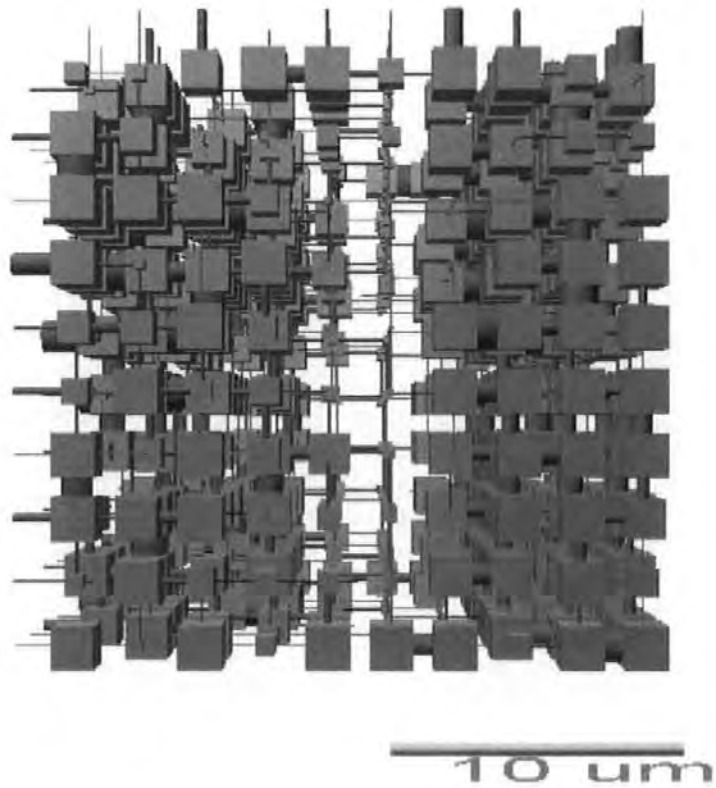
Figure 5.42 - Modelled structure of an HC60 + 10 w/w% styrene-butadiene low T_g latex coating applied with rod 3.
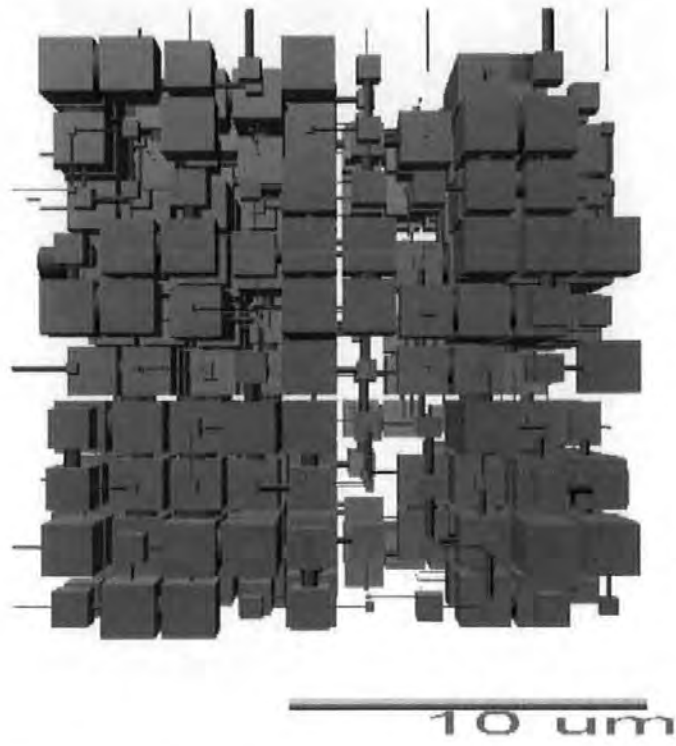
Figure 5.43 - Modelled structure of an HC60 + 10 w/w% styrene-butadiene high T_g latex coating applied with rod 2.
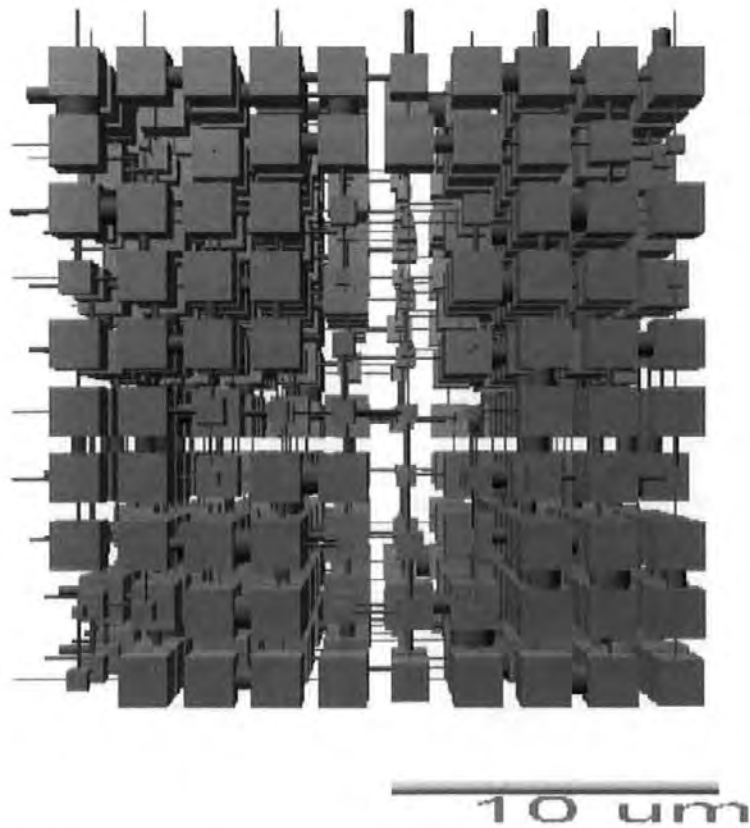
Figure 5.44 - Modelled structure of an HC60 + 10 w/w% styrene-butadiene high T_g latex coating applied with rod 3.

10 um
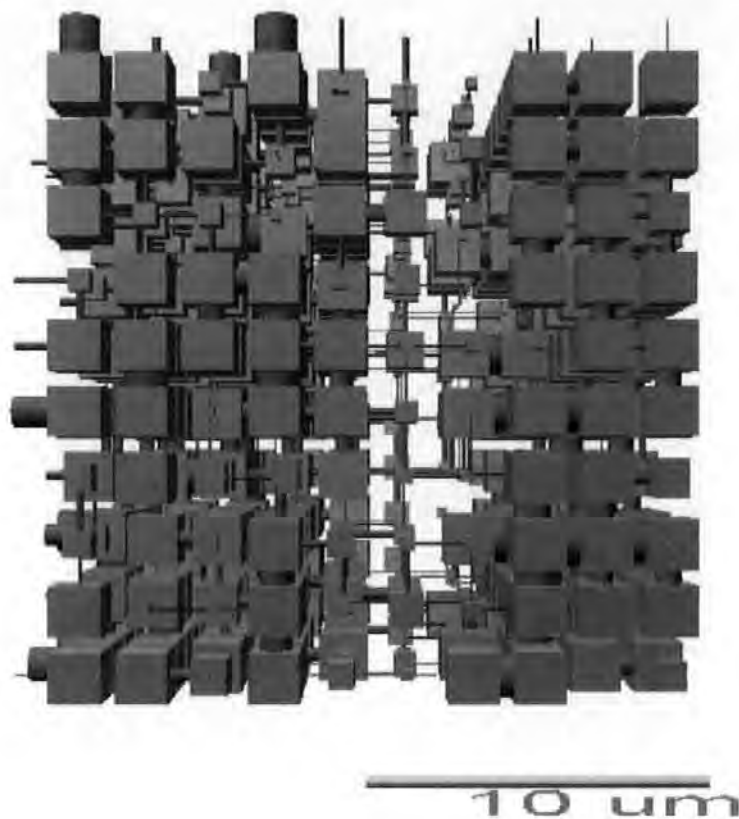
Figure 5.45 - Modelled structure of an HC60 + 10 w/w% acrylic high T_g latex coating applied with rod 2.

Once more the use of high glass transition temperature latex, which remains a hard sphere and does not film-form in the experimental conditions, is represented by the Pore-Cor model as having uniform structures with large pores (Figure 5.43 to Figure 5.46). When the coating layer is applied with rod 3, the particles are free to rearrange and lead to a slightly more closely packed structure, as shown by lower values of porosity.

Finally, the use of 10 w/w% starch in the colour formulation, gives rise again to uniform and more closely packed structures, with small void features and larger solid elements, confirming the hypothesis of a starch-induced flocculation (Figure 5.47 and Figure 5.48) and soluble binder blocking pores. Figure 5.49 shows that the thicker coating layer has a large number of very small throats when compared with the thinner coating layer. Also the value of porosity of the thicker layer is lower than the thin one.

184
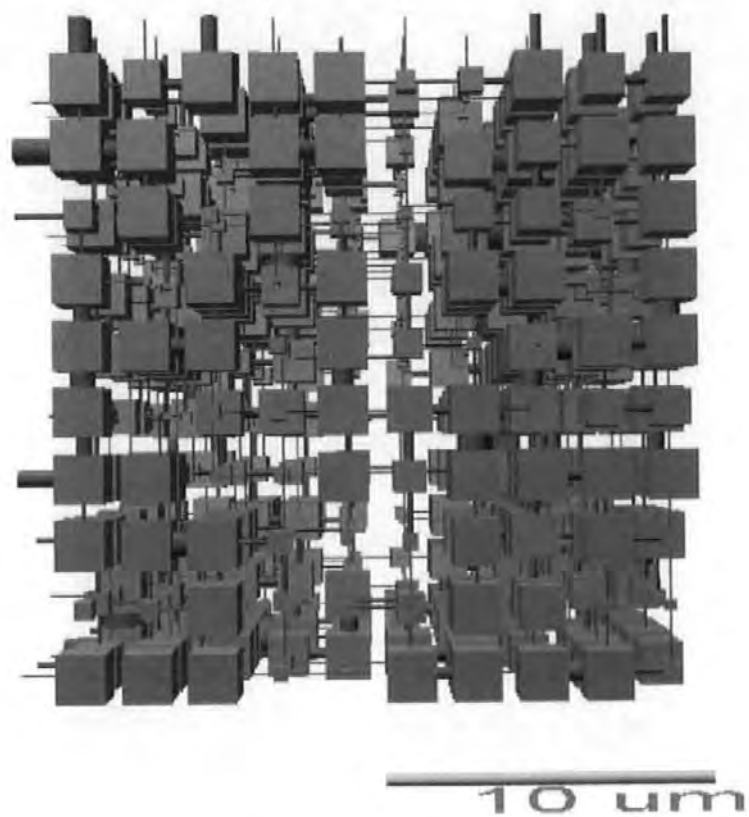
Figure 5.46 - Modelled structure of an HC60 + 10 w/w% acrylic high T_g latex coating applied with rod 3.
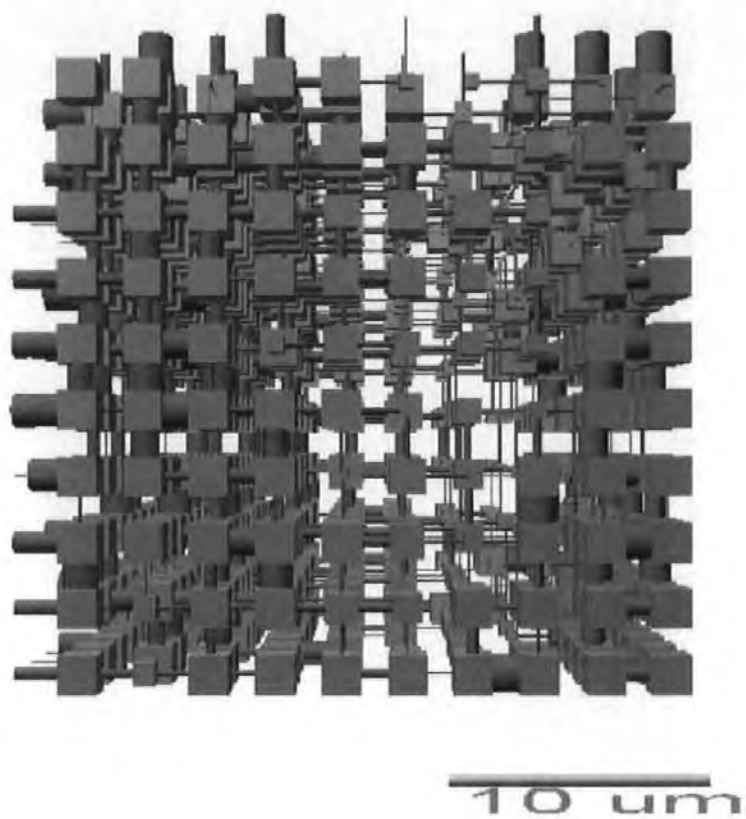
Figure 5.47 - Modelled structure of an HC60 + 10 w/w% starch coating applied with rod 2.
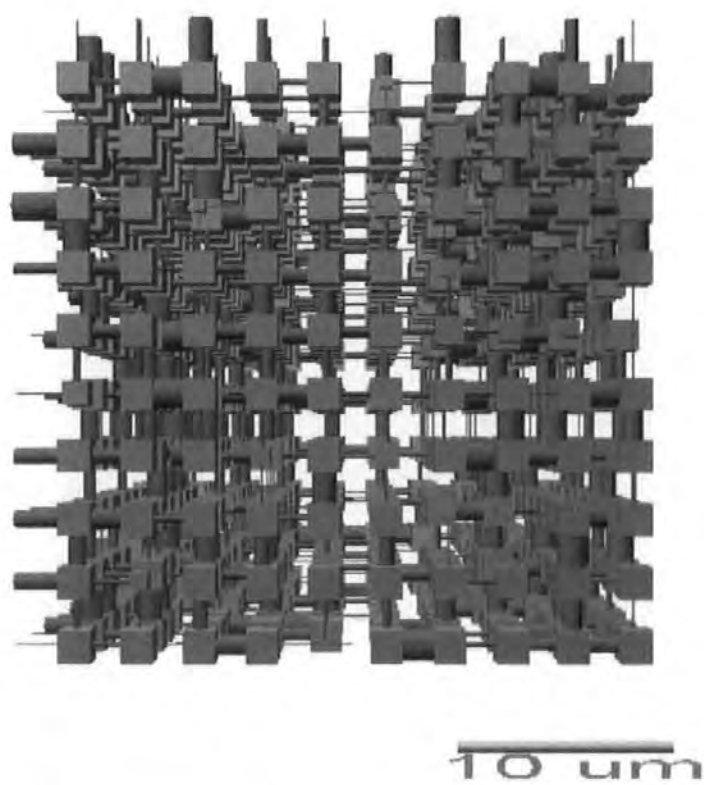
Figure 5.48 - Modelled structure of an HC60 + 10 w/w% starch coating applied with rod 3.
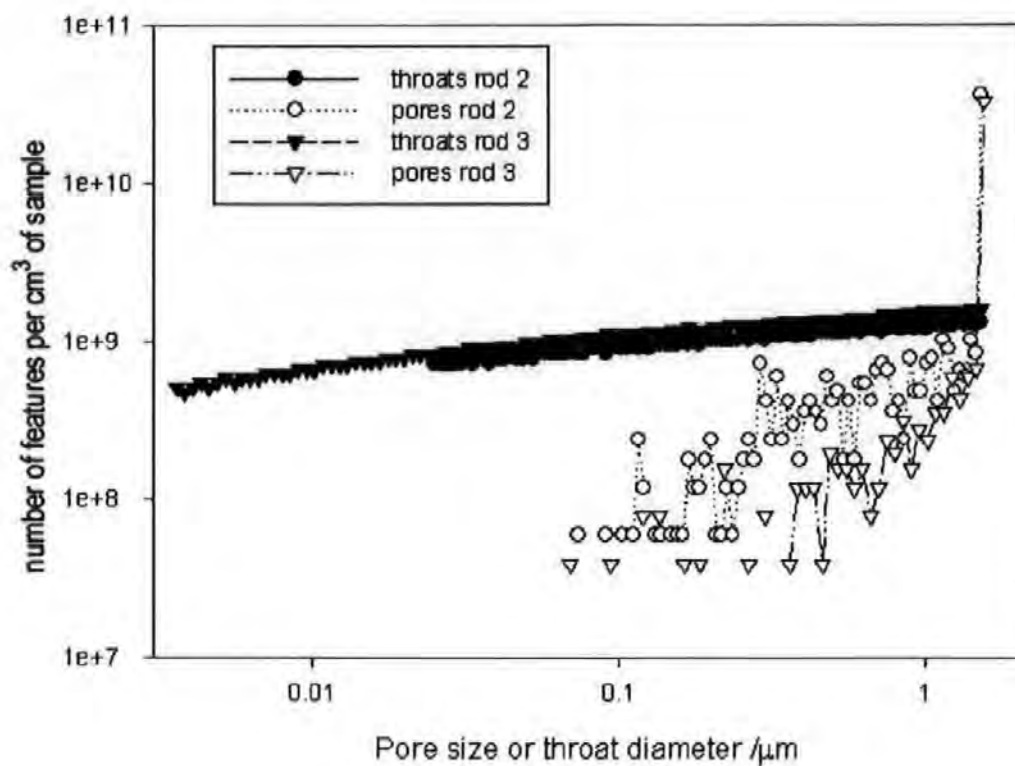
Figure 5.49 - Pore and throat size distribution in a cm^3 of HC60 + 10 w/w% starch coatings.

6 MODELLING THE REPRESENTATIVE PARTICLE SIZE DISTRIBUTION OF THE SKELETAL MATERIAL WITHIN POROUS MEDIA (Laudone *et al.*, 2005)

6.1 Introduction

When studying the structure of a porous medium, it is often of interest to know the effective sizes of the particles, or skeletal elements, which make up the solid matrix. The measurement of particle size distribution for an unconsolidated powder is relatively easy to carry out (section 1.8.5), for example by sedimentation. However, such measurement is much more complicated for a consolidated phase, as in the case of cement, filters, catalyst substrates or paper coating layers. In a geological study, information about the particles might assist, say, in determining the degree of cementation, such as that of a reservoir sandstone. In the preparation of a sinter or powder compact, it might allow the relative effects of pressure and temperature to be assessed, and hence the optimal process parameters required to achieve a desired structure.

A standard method of estimating the sizes of constituent particles is to study an electron micrograph such as that shown in Figure 6.1.
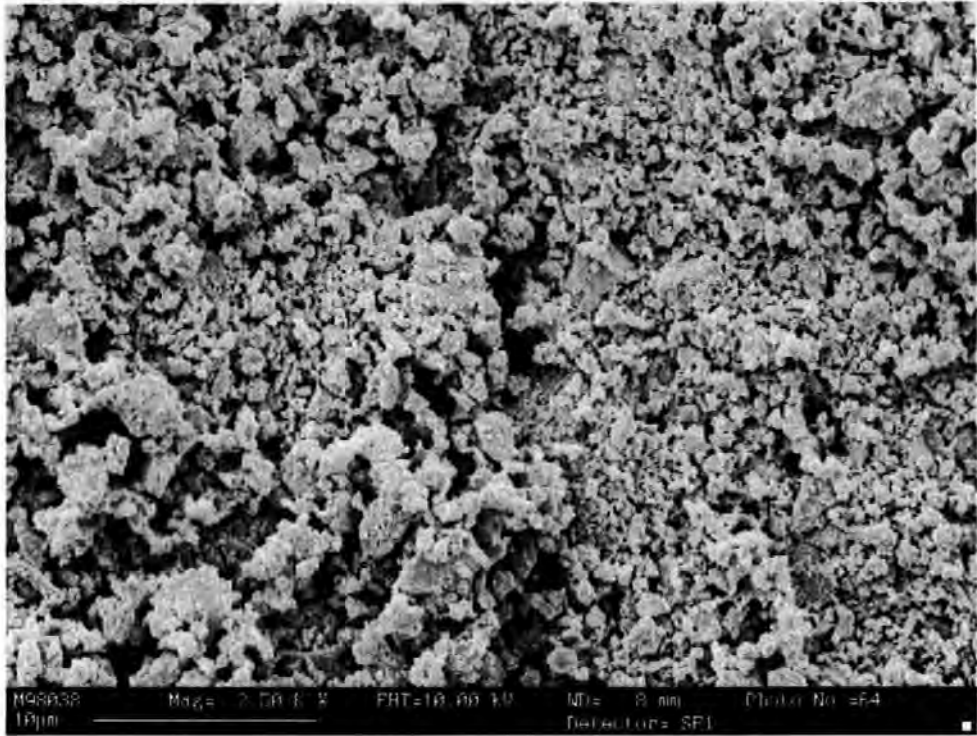
Figure 6.1 - Electron micrograph of a compressed calcium carbonate tablet: HC60-57.6 MPa.

It can be seen in the micrograph that some particles are almost discrete, and so their sizes can be readily estimated – in the present case diameters from around 0.2 μm up to around 5 μm. However, other particles are agglomerated or on top of other particles, so that estimation of their size, or that of the aggregates, is very difficult. Standard image analysis does not assist, because it requires the image colours/grey levels to be converted into a binary distribution representing either the solid or the pore space, and, in so doing, many visual depth clues are lost. The higher the degree of cementation, sintering or compaction of the matrix, the greater the problem of estimation.

An alternative approach is to study the flow and pressure characteristics a fluid passing through the matrix (permeability), or the pressure related intrusion or extrusion, and infer from the relationship between applied pressure or suction the sizes of the "particles" or features that are obstructing or attracting the fluid. In an early paper, Haynes discussed the behaviour of

189

water in soil (Haines, 1927). However, as he noted, water wets with advance wetting fronts which jump forward from particle to particle – the so-called Haines' jump. Estimation of the sizes of the particles beneath the wetting fronts is therefore impossible. Non-wetting fluids, such as mercury, percolate more predictably and therefore provide a more reliable estimate. Smaller particles contact other small particles with a greater degree of curvature at their point of contact, relative to large particles, so the connecting voids between them can be thought of as wider. Thus intrusion of mercury at low applied pressures can be associated with small particles, and intrusion at higher applied pressures with larger particles. This is the approach of Mayer and Stowe (Mayer and Stowe, 1965). The spherical particle packing was defined in terms of a single packing angle, σ, calculated from the porosity of the sample (Figure 6.2).
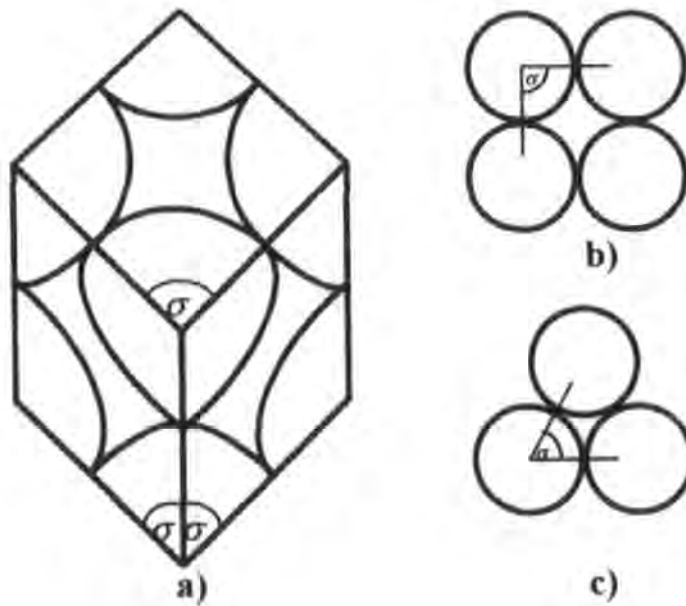
Figure 6.2 - Illustration of packing angle, σ, in an array of uniform spheres and examples of (b) square and (c) triangular openings formed by packing angles of 60° and 90° respectively.

The packing having identifiable access openings varies in shape from square, for the most porous packing (highest values of σ) to triangular for the closer packed structures. Mayer and Stowe gave a relationship that relates porosity, surface free energy of mercury and breakthrough pressure to a single particle diameter, characteristic of all the particles in the

190

packing. Current mercury porosimetry software, for example (Micromeritics, 1996) distributed with their Autopore mercury intrusion porosimeters, extends this procedure, applying it to every point on the mercury intrusion curve rather than a single breakthrough pressure. Effectively, this represents the porous material as being composed of spherical shells of regularly packed uniform spheres, with the smallest on the outside and the largest in the middle, as shown in Figure 6.3. However, their approach only applies to sorted arrangements of perfect spheres such as that shown in the figure, and is counter-intuitive with respect to the overall pore sizes.
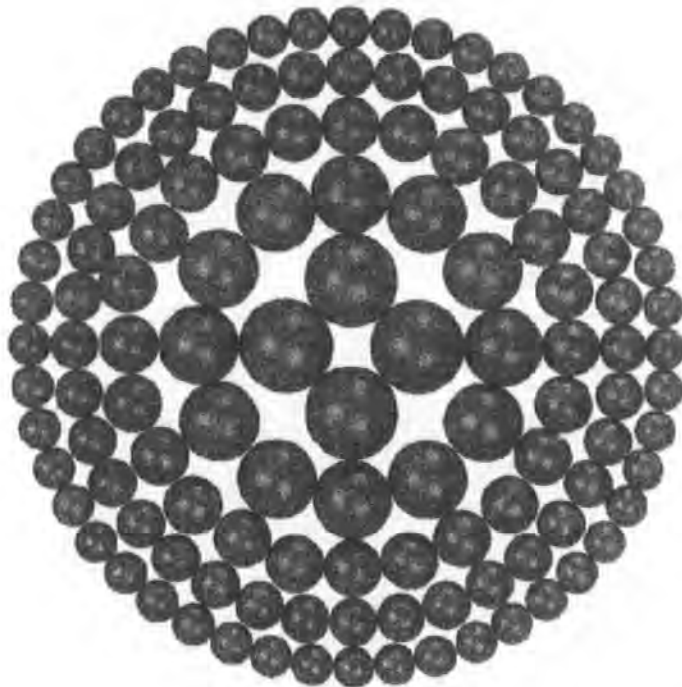
Figure 6.3 - A cross-section view through a solid as represented by the Mayer and Stowe method of estimating the particle size distributions.

The packing angle is assumed constant throughout the sample. At successively higher pressures, mercury breakthrough occurs through progressively smaller voids between packings of progressively larger spheres, until the material becomes saturated. However, this approach assumes that every channel is made up from two or more spherical particles of equal size

touching each other, and so breaks down for samples formed from particles over a range of shapes and sizes.

6.2 Representative particle size distribution in Pore Cor

Our interest in the estimation of the representative particle size distribution originates from hypothesis 6 of this work (see section 1.4). It was supposed that it is possible to extrapolate the FCC structure of a paper coating backwards in solids concentration from the known SCC dry structure, by increasing the porosity of the system with the same skeletal element particle size distribution within the network void model generated by Pore-Cor.

The Pore-Cor Research Suite package, before this work was carried out, contained reliable algorithms for only two very crude calculations of the representative solid skeletal elements associated with the space between eight cubical pores. The first is the hard sphere approximation (Figure 6.4).
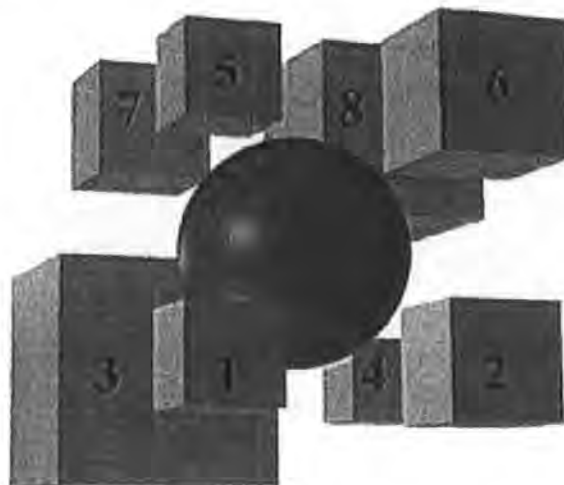
Figure 6.4 - Hard sphere diameter, D_h, is the minimum diagonal distance between pairs of pores.

The *hard sphere diameter* D_h, as the minimum diagonal distance between opposite pores surrounding the primary position:

$$D_h = \sqrt{3}\left(S - \frac{C_I}{2} - \frac{C_{II}}{2}\right),$$

Eq. 6.1

where C_I and C_{II} are the side lengths of the two diagonally opposed pores giving the smallest values for D_h and S is the pore-row spacing.

The second is the soft sphere model which represents somewhat better the volume of the skeletal element. If each skeletal element is assumed to be spherical and infinitely compressible, it could be deformed into a shape that fully occupies the solid phase space between eight pores. If this deformed sphere was allowed to return to a spherical shape with the same volume, then the diameter of this sphere would be given by:

$$D_c = 2\sqrt[3]{\frac{3\left[S^3 - \left(\frac{1}{8}\sum_{k=1}^{8}C_k^3 + \frac{1}{4}\sum_{k=1}^{12}\pi r_k^2 L\right)\right]}{4\pi}},$$

Eq. 6.2

where D_c is the diameter of the compressible sphere, C is the side length of the cubic pores and r is the radius of the cylindrical throats.

A novel and more sophisticated calculation for the spherical element associated with the solid phase space between eight pores in a Pore-Cor unit cell is now presented below, and involves the growth of the element within the confines of the eight-pore boundaries. This algorithm was previously developed by Mathews (Mathews *et al.*, 1999) but, in this work, it has been re-coded for much improved reliability, included in the main Pore-Cor Research Suite and optimised for speed and accuracy. A virtual reality representation of the skeletal solid elements within the Pore-Cor unit cell has also been added.

6.3 Growth of the skeletal elements (Mathews *et al.*, 1999)

In Figure 6.5, we consider a cubic array of eight neighbouring cubic pores. Such an arrangement is shown in Figure 6.6(a). The throats are omitted for clarity in Figure 6.6, and are also ignored in the calculation.
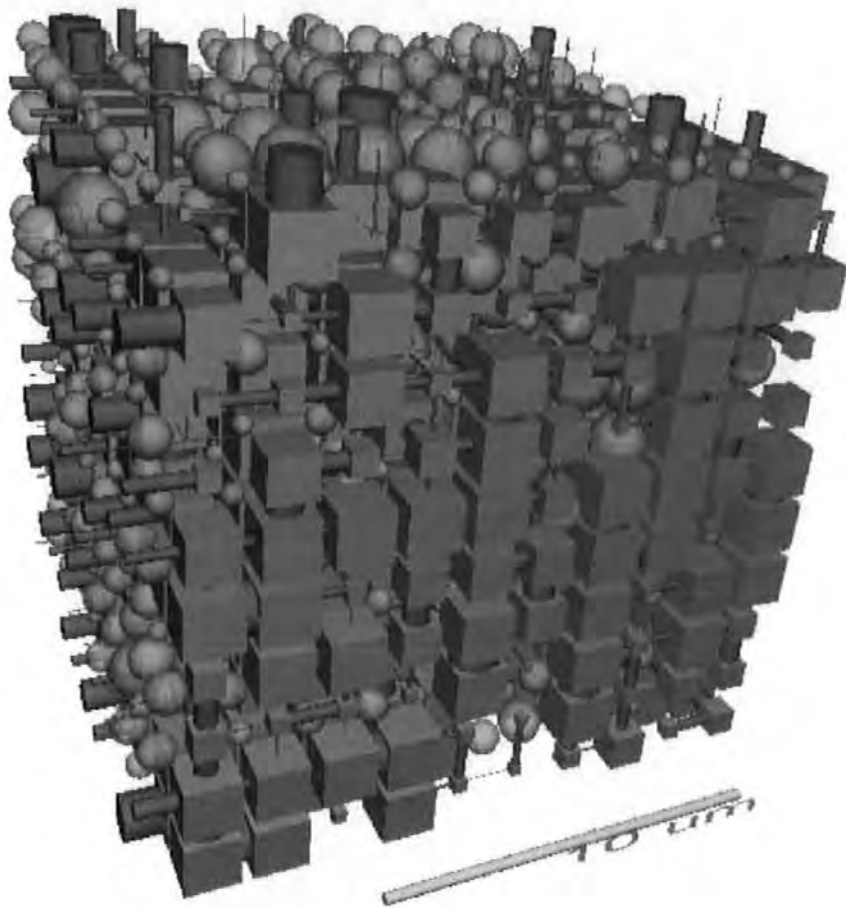
Figure 6.5 - Simulated void network and skeletal elements for HC60 compressed under a pressure of 57.6 MPa

The 'primary position' of the skeletal element is taken as being at the centre of a cube defined by the centres of the eight adjacent pores.
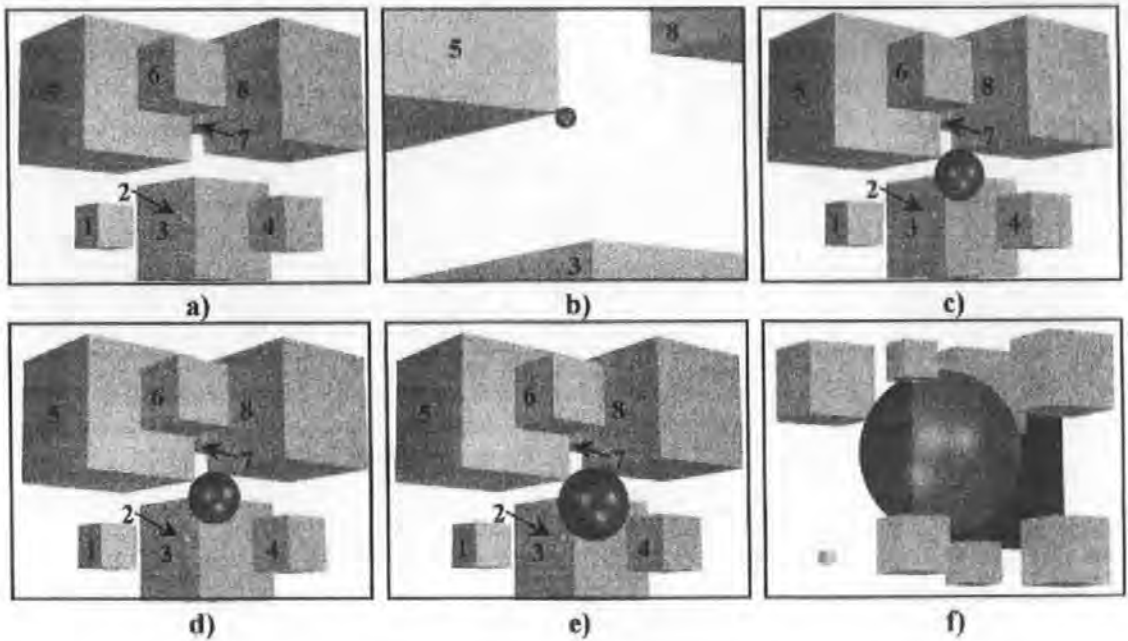
Figure 6.6 - Illustration of the algorithm used for the calculation of the particle size. a) the 8 pores defining the skeletal element space, b) the initial skeletal element particle centred on the primary position grows and finds a first contact point, c) the centre of the sphere moves away from the first contact point and the sphere finds a second contact point, d) and e) the growth of the sphere continues until the 4 contact points are found, or f) until the sphere touches the outer cube formed by the centres of the 8 pores.

The algorithm first measures the distance between the primary position and the closest corner of any of the eight cubic pores. It forms a sphere of this radius centred at the primary position. This sphere therefore has one contact point.

If q is a three-dimensional vector defining the primary position, Q, and c_1 is the vector defining the position of the first contact point, C_1, then the vector u

$$u = (1+\lambda)q - \lambda c_1$$

Eq. 6.3

defines the position, U, of a point lying in the line through Q and C_1. By incrementing λ, it is possible to adjust u until the distance D_1, between U and C_1, is equal to the distance D_2, between U and one of the remaining seven inner-facing corners of the pores. This sets the second contact point, C_2, with position vector c_2. If the second contact point is the corner of the pore opposite to the first contact point, the calculation is stopped, as the skeletal element

195

cannot grow further without invading the volume of the first two touching pores. If not co-linear, the three points, Q, C_1 and C_2, define a plane. It is possible to move the centre of the sphere away from the found position of U in the plane defined by the three points, perpendicular to the line between C_1 and C_2. The position, V, of the centre of the sphere is defined by:

$$v = (1+\mu)u - \frac{\mu}{2}(c_1 + c_2)$$

Eq. 6.4

The parameter μ can be incremented until a third contact point, c_3 is found, equidistant from the sphere centre to C_1 and C_2. The diameter of the sphere has incremented to D_3.

To find the fourth contact point, C_4, with position vector, c_4, the centre of the sphere is moved along the line

$$w = v + v\hat{n}$$

Eq. 6.5

where $\hat{n}$ is the unit vector normal to the plane through C_1, C_2 and C_3, given as:

$$\hat{n} = \frac{(c_3 - c_2) \times (c_2 - c_1)}{|c_3 - c_2||c_2 - c_1|}.$$

Eq. 6.6

The parameter v is increased until the spherical skeletal element makes its fourth contact point, which is equidistant from the centre of the sphere to C_1, C_2 and C_3. Its diameter is then D_4.

The diameter of the growing sphere can never exceed the pore-row spacing, S, Figure 6.6 (f). If all the diameters of all such spheres throughout the structure reached this limit, $D_u = S$, the resulting representation of the skeletal elements would be a cubic close-packed array of mono-sized spheres. In a continuous solid structure the maximum percentage of the volume of solid phase which can be represented by the cubic close-packing of spheres is $\pi/6$, corresponding to 52.4 % of the solid phase.

196

In most cases, $D_4 > D_3 > D_2 \approx D_h$, but for some unusual pore configurations, when the largest pores are all to one side of the primary position, it follows $D_4 < D_h$ (Figure 6.7).
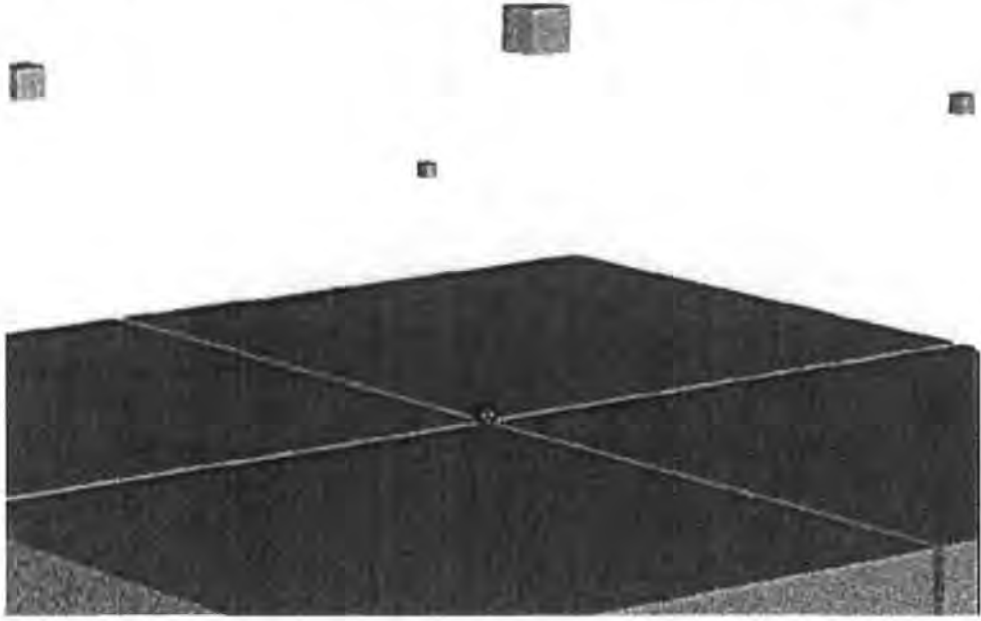
Figure 6.7 - A pore configuration that would result in $D_4 < D_h$.

Overall, the diameter was initially chosen as the maximum of D_h, D_4, D_3, and D_2. Then the resulting value was compared with D_u, and the minimum of these two values chosen to prevent possible overlap with an adjacent skeletal element.

Intuitively, one would expect the size distribution of the skeletal elements to descend asymptotically to zero at minimum and maximum size. In fact, the simulated size distribution can show peaks at each end. At the larger end, no size can be greater than D_u. So, as porosity $\Phi \rightarrow 0$, all $D \rightarrow D_u$, as mentioned above, causing a peak at maximum size. Conversely, to match structures with large porosities, the pores are packed together as closely as possible, leaving a minimum space between them of 0.001 d_{max}, where d_{max} is the size of the largest pore. Therefore as $\Phi \rightarrow \infty$, $D \rightarrow 0.001\ d_{max}$, causing a peak at minimum size. Also, high values of the pore skew parameter will tend to cause $D \rightarrow 0.001\ d_{max}$, and so, in the modelling, the value of this pore skew parameter is kept as low as possible.

197
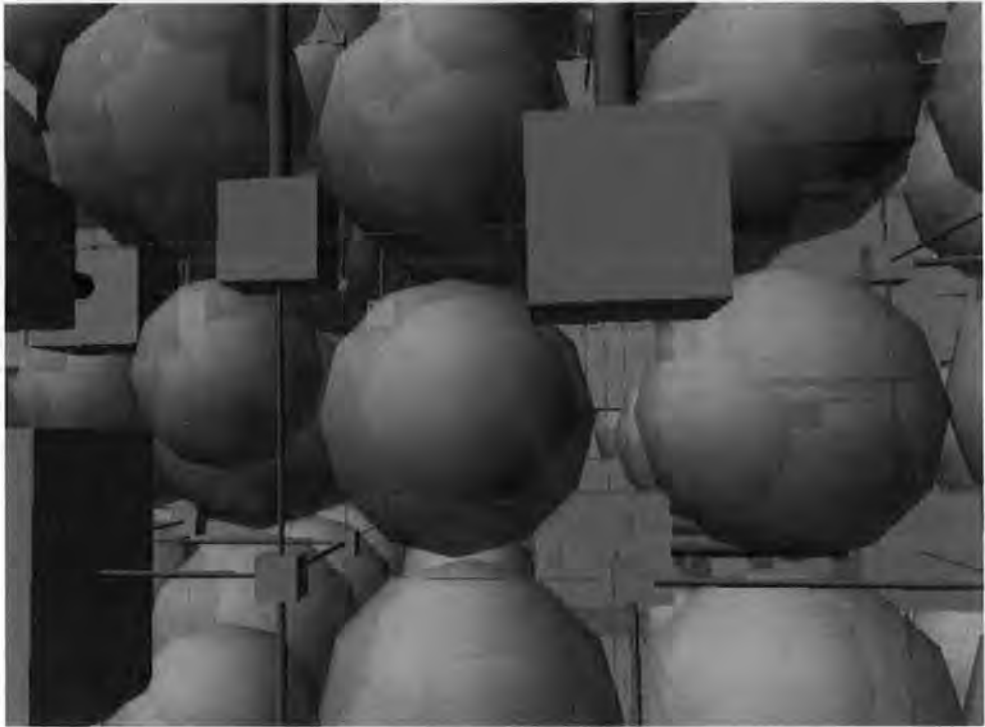
Figure 6.8 - Pore Cor unit cell with particles - detail

6.4 Experimental

6.4.1 Samples

In order to justify the assumptions in the model and to see how it matched a real structure, two different samples of Redhill sand, grades 30 and 65, each of known particle size, supplied by Sibelco (formerly Hepworth) Minerals and Chemicals Ltd, Redhill, Surrey, UK, were analysed by mercury intrusion porosimetry. The particle sizes were measured by the manufacturer using 11 sieves, giving 12 size ranges or 'bins'. To investigate the effect of the high pressure mercury intrusion on the packing of the samples, each sand sample was analysed ten times under the same experimental conditions. A more detailed validation of this algorithm for unconsolidated sand and Ballotini glass beads can be found in Mathews *et al.* (1999).

Also a series of calcium carbonate tablets were prepared following the method of (Schoelkopf *et al.*, 2000) using two different natural $CaCO_3$ powders from the same limestone source as

used in the rest of the experimental work, (Orgon, France, Omya AG), HC60 and HC90, having, as previously described, respectively, 60 w/w% and 90 w/w% of particles with diameter < 2 µm, as measured by sedimentation using a Sedigraph, 5100 instrument (Micromeritics, USA).

The tablets were formed by applying a compression force onto a 60 g sample of the dry powder mineral pigments, acting over a circular cross sectional area of 17.35 cm^2, using an hydraulic press. Seven different pressures were used covering the range 57.6 MPa to 259.4 MPa for HC60, and two pressures, 144.1 MPa and 201.7 MPa, for HC90. The resulting tablets had measurably different porosities, as shown in section 6.5.2.

6.4.2 Mercury porosimetry on sand and CaCO₃ tablets

The sand and CaCO₃ tablets were analysed by mercury intrusion porosimetry using an Autopore III instrument, by Micromeritics, USA, as previously described for the coatings.

The sand particles were assumed to be incompressible. For the CaCO₃ tablets, the results of the mercury intrusion porosimetry measurements were corrected for sample compression by applying the equation of Gane *et al.* (Gane *et al.*, 1995), incorporated into the software Pore-Comp (section 2.1.1), once again as described earlier for the coating samples.

6.5 Results

6.5.1 Sand

Figure 6.9 and Table 6-1 show the results of mercury intrusion porosimetry on the two types of sand. Only three of the ten runs on each are shown, namely the minimum (Run 1), intermediate (Run 2), and maximum intrusion (Run 3). It can be seen that the volume of

mercury intruded, and hence the effective porosity of the packed particles, differs substantially due to different particle packing in each run.
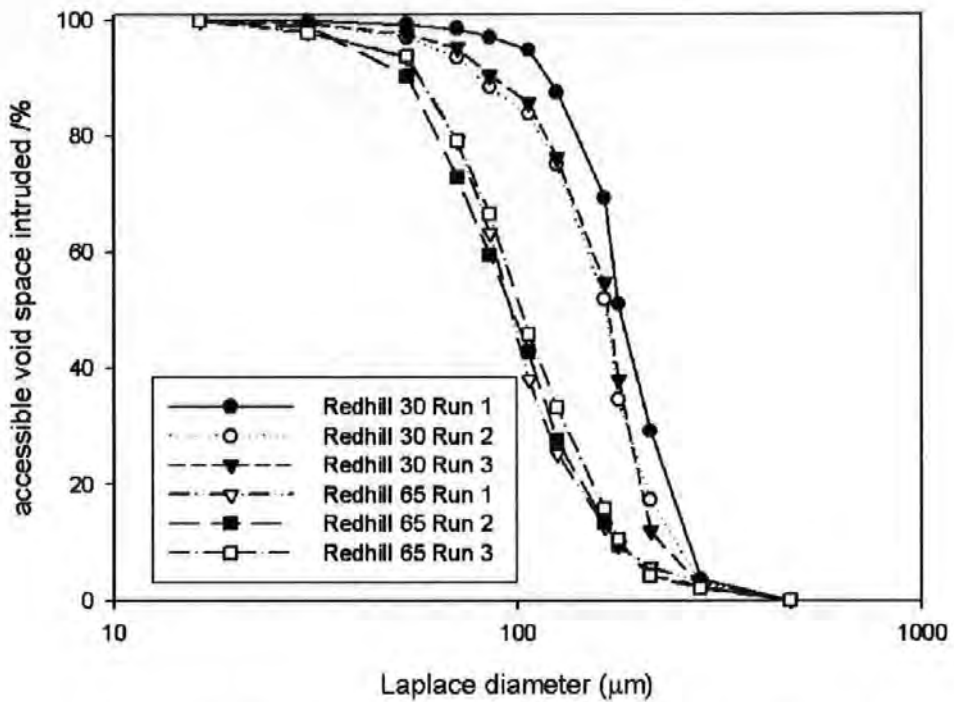
Figure 6.9 - Mercury intrusion porosimetry for Redhill sand samples.

Table 6-1 - Volume % porosity for Redhill sand samples.

Sample :	Redhill 30	Redhill 30	Redhill 30	Redhill 65	Redhill 65	Redhill 65
Run :	1	2	3	1	2	3
Porosity/%	34.9	40.7	41.9	39.6	44.4	45.6

200
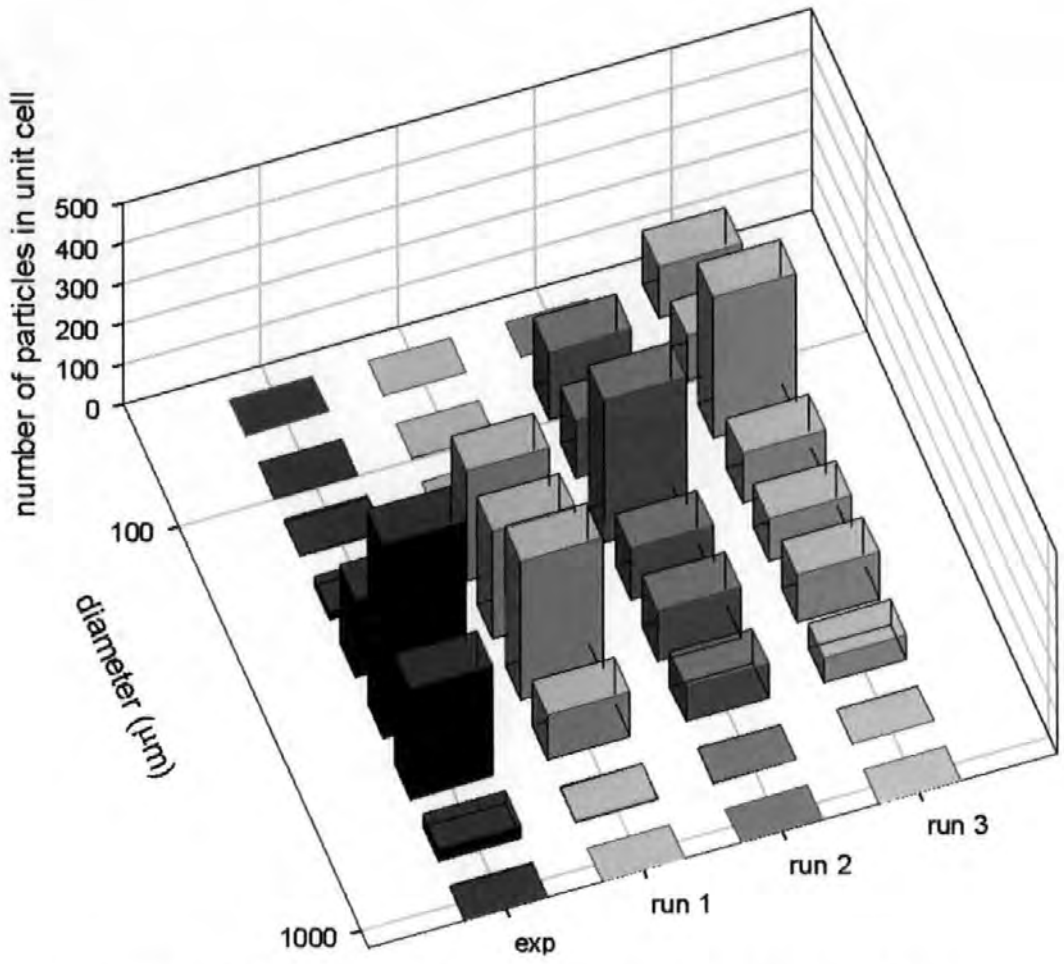
Figure 6.10 - Experimental and simulated size distributions for Redhill 30 sand.
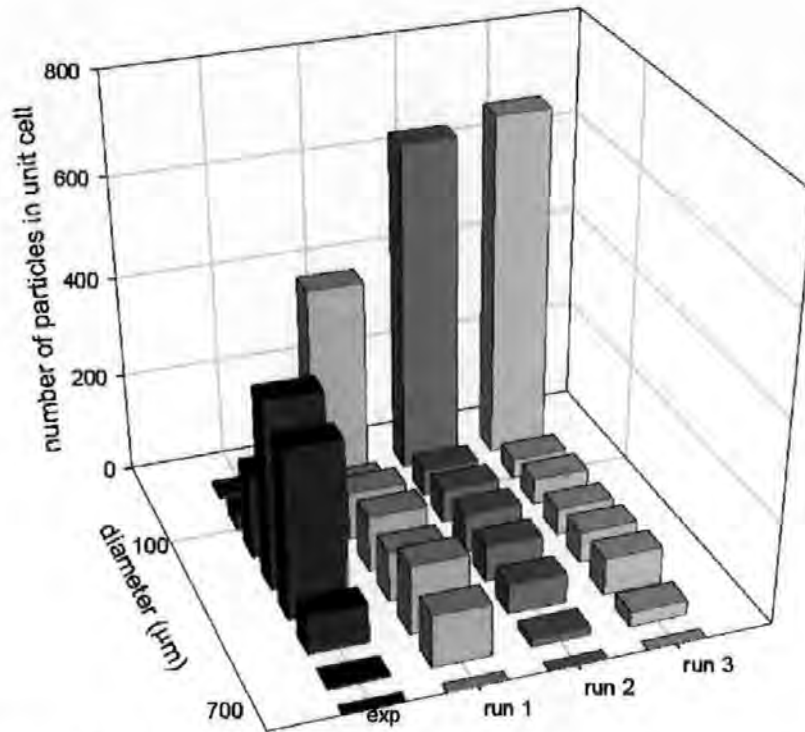
Figure 6.11 - Experimental and simulated size distributions for Redhill 65. The peaks in the size range are due to artefacts, as discussed in the text.

Figure 6.10 and Figure 6.11 show the experimental particle sizes of the Redhill 30 and 65 sand, respectively, plotted as histograms on a logarithmic size axis. Also shown are the skeletal element size distributions generated from the first stochastic realisation of the simulated networks fitted to each of the six mercury intrusion curves shown in Figure 6.9, and shown selectively from the minimum, medium and highest porosity samples, run 1, run 2 and run 3 respectively. The skeletal elements represent between 8 % and 11 % of the actual solid phase of the sand. Runs 2 and 3 for each sample have a higher porosity, so must be more loosely packed. To simulate this higher porosity, the network model tends to either bulk up the pores with the pore skew parameter and/or pack the pores as close together as possible. This gives rise to a peak at minimum size in Figure 6.11, as explained above.

A statistical test is required to assess the similarity of the experimental and simulated results. As the distributions are skewed, because of truncation and/or artefacts at the top and bottom of

202

each distribution, the Mann-Whitney non-parametric test has been used (Dancey and Reidy, 2002). The two-tailed asymptotic significance P is derived from the ranks of the absolute values of the differences between the two variables, and treats top and bottom peaks of the size distribution more appropriately than a test based on variance alone. For the test, the simulated skeletal elements were grouped into the same size bins as the experimental results. The statistical tests were performed using SPSS (Statistical Package for Social Sciences, a product of SPSS Inc.) for Windows v.10.

Table 6-2 - Sand: values of the Mann-Whitney statistic P for pairwise comparison of random sampling of the binned size distributions of the experimental measurements and simulated skeletal elements.

Pairs of samples compared	Redhill 30	Redhill 65
Exp and Run1	0.089	0.175
Exp and Run3	0.000	0.000
Exp and Run2	0.000	0.000
Run1 and Run3	0.000	0.000
Run1 and Run2	0.000	0.000
Run2 and Run3	0.000	0.283

It can be seen that for both Redhill 30 and Redhill 65, the experimental particle sizes are the same ($P > 0.05$) as the sizes of the skeletal elements for the corresponding Run 1 – i.e. the run with the closest optimal particle packing. All other comparisons are different ($P < 0.05$) except Redhill 65 Run 2 and Run 3, which of course itself does not relate to experiment.

Figure 6.12 shows particle distributions corresponding to different stochastic realisations of the structures. All are identical ($P > 0.05$).
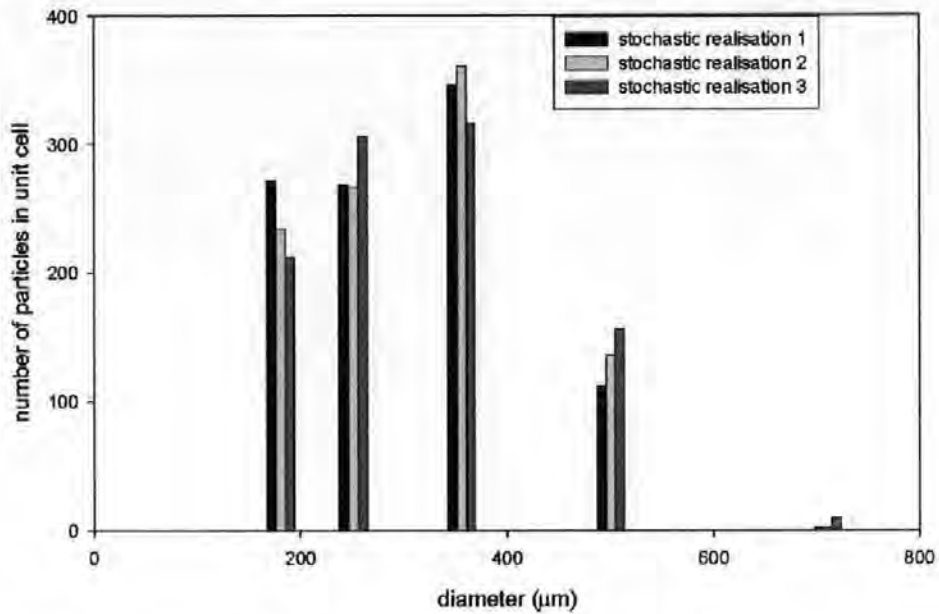
Figure 6.12 - Simulation of Redhill 30 sand based on run 1 mercury porosimetry intrusion curve.

6.5.2 Calcium carbonate

Figure 6.13 and Table 6-3 show the results of the mercury intrusion porosimetry on the calcium carbonate tablets. It is important to recognise that in the case CaCO₃ tablets, the application of the mercury pressure did not lead to irreproducible results, as had been the case for the coarser sand samples, i.e. the pressure of compression in forming the tablets was enough to define an externally un-repackable structure as pressure was applied to the mercury. This means that the skeletal element size distributions should always represent the skeleton well, i.e. behave like the data seen for the minimum effective porosity possible for the sand.

Two anomalies can be observed. The porosity is expected to decrease for increasing tablet formation pressures, but, in Table 6.3, it can be observed that the HC60 144.1 MPa tablet does not follow this trend. The Laplace diameter, corresponding to the mercury intrusion pressure, is expected to decrease with increasing tablet formation pressures. In the case the HC60 86.5

204

MPa tablet the Laplace diameters, at which mercury intrusion is measured, are much smaller than those measured for tablets created applying higher formation pressures.
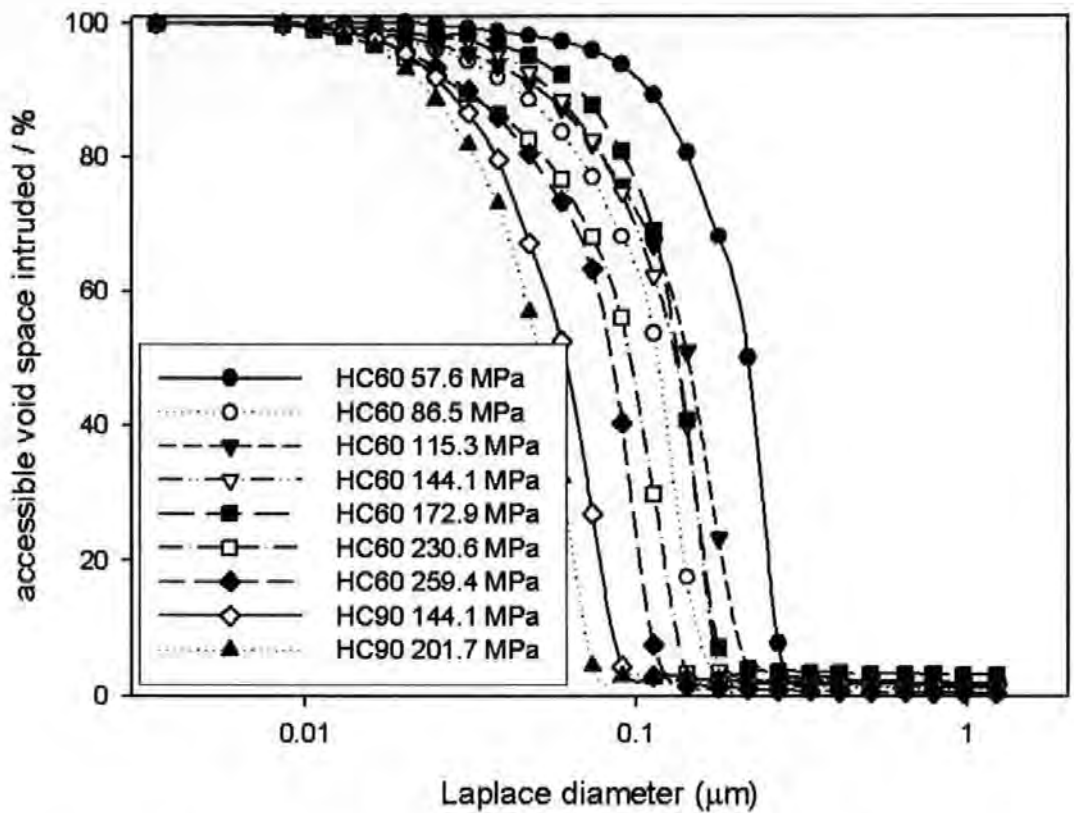
Figure 6.13 - Mercury intrusion porosimetry for HC60 and HC90 tablets.

Table 6-3 - Volume % porosity for HC60 and HC90 tablets.

Sample : Compression	HC60	HC60	HC60	HC60	HC60	HC60	HC60	HC90	HC90
/MPa :	57.6	86.5	115.3	144.1	172.9	230.6	259.4	144.1	201.7
Porosity/%	28.7	26.8	24.3	28.0	22.1	21.7	19.3	26.8	23.8

Figure 6.14 represents the size distributions of the skeletal elements, modelled using the mercury intrusion curves for the HC60 tablets prepared under different pressures. The skeletal elements for all the HC60 and HC90 simulations ranged from 20 % to 32 % of the actual total solid phase – a higher percentage than for sand, because of the lower porosity of these samples

205

and therefore ability of the network model to represent a larger fraction of the solid phase volume.

All the size distributions were different from the experimental distribution and they were all different from each other (Table 6.4). Figure 6.15 shows the average size of the simulated particles, which increase as the formation pressure of the tablets increases.

Thus the model implies that the lowest pressure (57.6 MPa) generates skeletal elements of entirely different sizes to the constituent particles. It also shows an increased aggregation of skeletal elements from 57.6 MPa to 259.4 MPa. This effect can be confirmed by visual comparison of the simulated unit cells in Figure 6.5 (page 194) and Figure 6.17 (page 211).

A visual comparison between the sizes of the aggregated particles of HC60 at 57.6 MPa shown in the electron micrograph, Figure 6.1, and the skeletal elements generated by the simulation algorithm, Figure 6.14, confirms a realistic match.
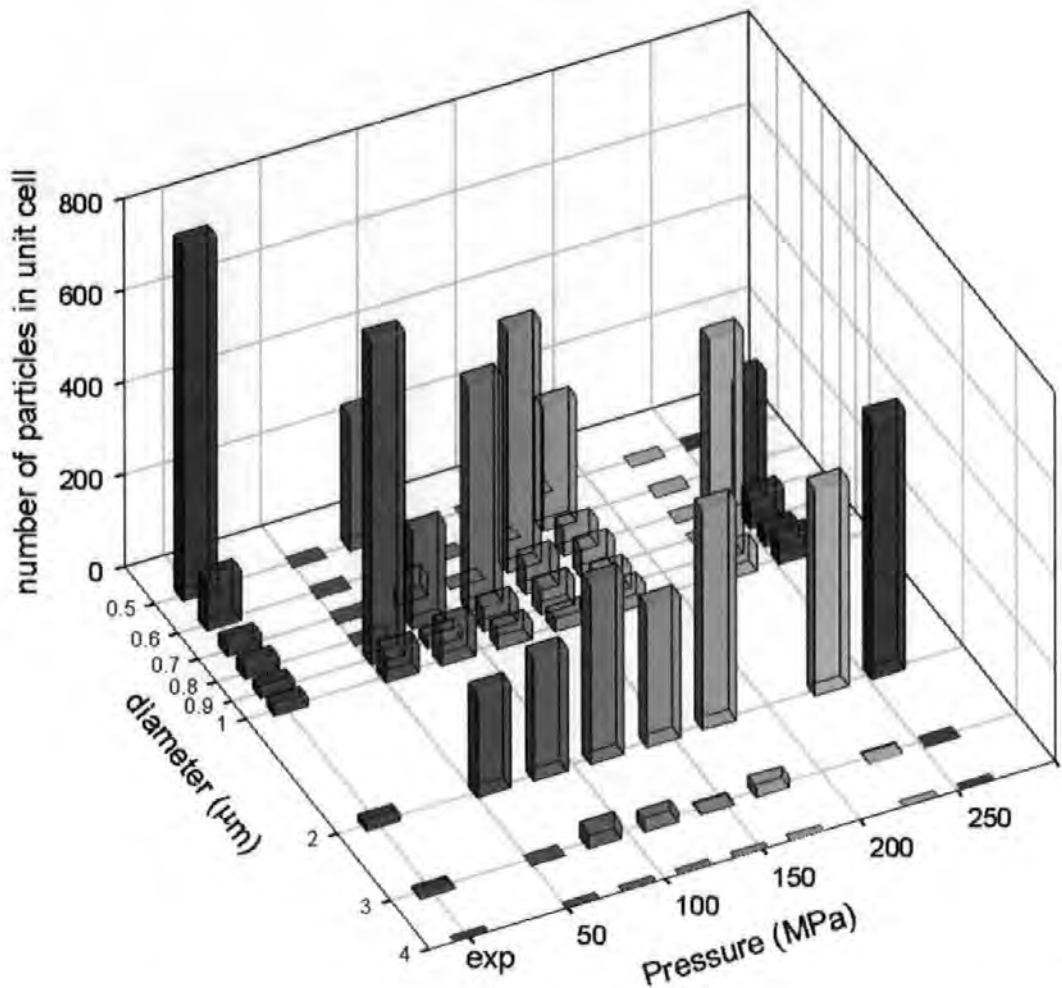
Figure 6.14 - Particle size distribution for HC60 powder measured experimentally (exp), and skeletal element size distributions derived from the modelling of tablets of the powder compacted under pressures in the range 57.6 MPa to 259.4 MPa.

Table 6-4 - HC samples: non-zero values of the Mann-Whitney statistic P, as for Table 6-2. All other combinations gave P equal to zero.

Pairs of samples compared	P
HC60 115.3 MPa and 172.9 MPa	0.016
HC90 144.1 MPa and 230.6 MPa	0.008
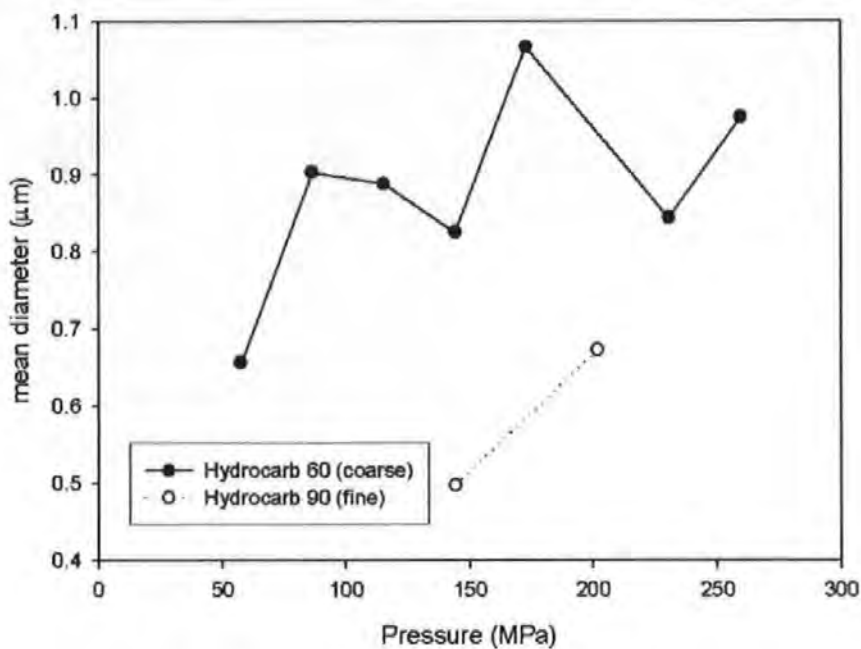
Figure 6.15 - Mean diameters of the skeletal elements for HC60 and HC90.
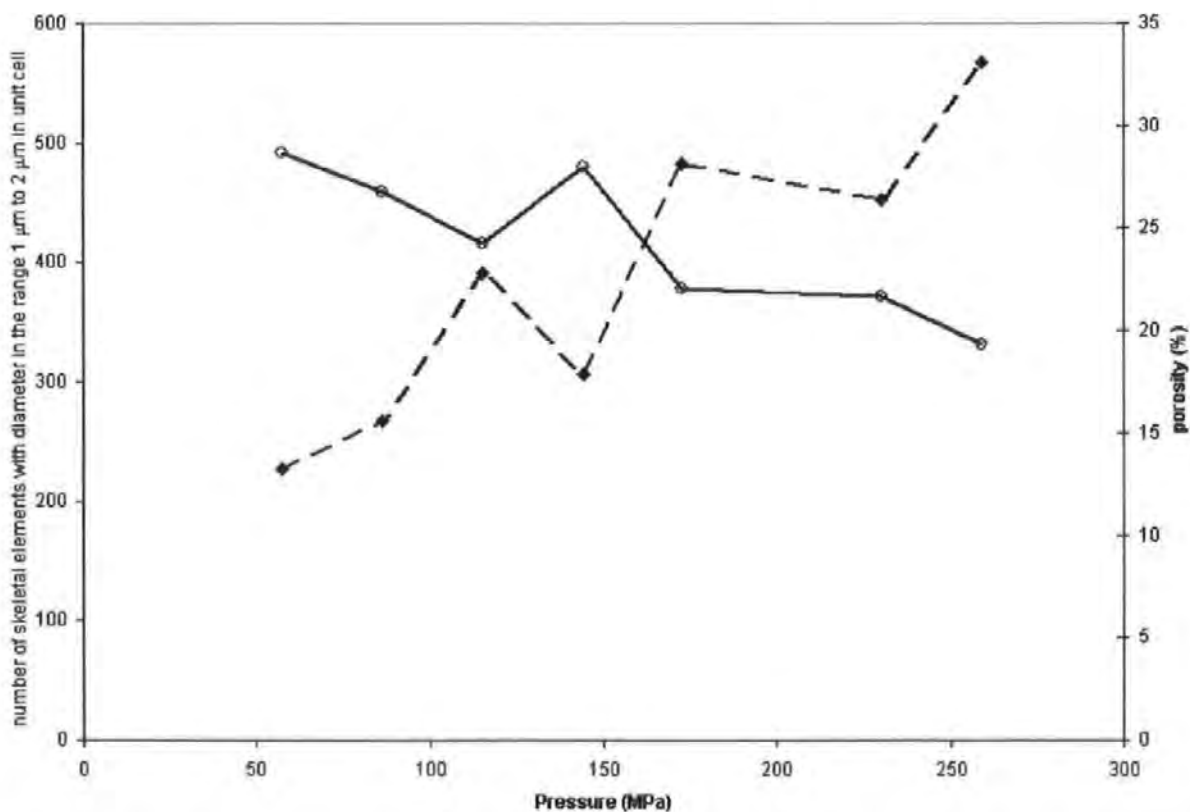
Figure 6.16 - Number of skeletal elements with a diameter in the range 1 μm to 2 μm in unit cell (dashed line) and porosity % (continuous line) for the HC60 tablets.

208

Figure 6.16 shows the number of skeletal elements in the simulated unit cells of HC60 tablets having a diameter in the range from 1 μm to 2 μm. This size range is free from artefacts at maximum and minimum size, described earlier, so is a reliable indicator of particle aggregation. A much clearer trend can be observed, with an increase in number of relatively large skeletal elements in tablets created by applying a higher pressure. The only large deviation from such a trend is observed in the case of HC60 144.1 MPa tablet, which is also the one presenting an anomaly in the value of measured porosity.

The findings shown in Figure 6.15 are important in respect to the design of coating structures formed under differing finishing/compression conditions (gloss calendering, for example) using pigments of known particle size distribution. In the studies of Gane *et al.* (Gane *et al.*, 1999), it was seen that absorption depth of a liquid into compressed tablets varied strongly according to the compression applied in forming the tablets. Especially in the case of HC60, it was noted that the level of unfilled pores rose as porosity increased, reaching a maximum and then suddenly declining. There is clear indication here too, in respect to skeletal element size, of a change in structure parameters, in that the mean effective skeletal element size drops dramatically at the highest porosity point (lowest compression). This may be taken as an indication that the action of compression is to form a structure of aggregates within the looser preliminary matrix structure, i.e. a highly compressed structure occurring in regions within a more loosely formed structure. These two structure types combining could well lead to a differentiated absorption dynamic such that the larger pores tend to remain unfilled during absorption, i.e. preferential absorption defined by the higher capillarity of the aggregate structures. The finer pores, on the other hand, have a higher resistance to flow and thus lower permeability. The higher the compression, the more the overall structure unifies into the new more compressed material.

209

Given the logarithmic nature of the Pore-Cor pore size distribution, providing greater number occurrence of fine pores (in linear space), the average value of the skeletal elements is going to be weighted inversely, i.e. strongly toward the larger aggregate size. Hence, the skeletal element size distribution is going to be relatively insensitive to subtle changes in the finer elements, and so the observed insensitivity to this assumed uniforming step in the compressed structure at higher pressures. Nonetheless, the change between fine elements and compressed "cemented" or "annealed" aggregates is striking and corresponds with the observed change in absorption dynamic.

In Figure 6.14 it can also be observed that the size distributions of the skeletal elements show a large number of the largest elements. This is an artefact due to the geometrical structure of the Pore-Cor unit cell, which limits the size of the skeletal element to that of the pore-row spacing.
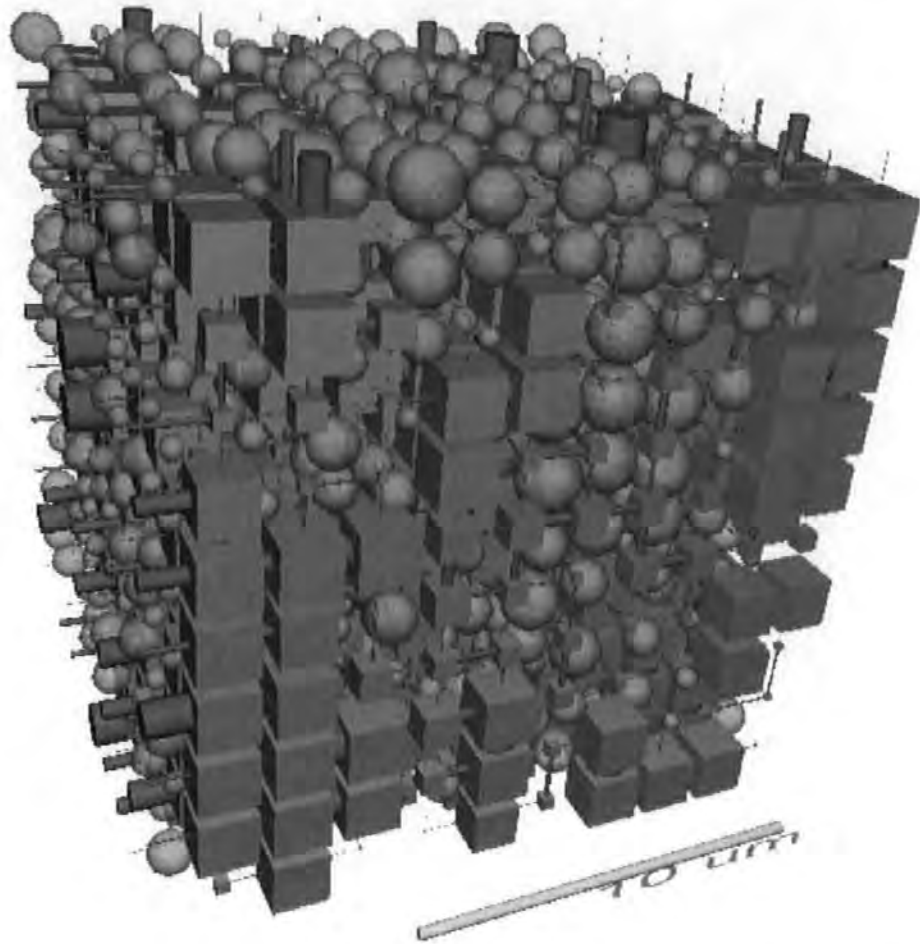
Figure 6.17 - As for Figure 6.5, but compressed under a pressure of 86.5 MPa

Figure 6.18 shows a comparison between the size distributions of the skeletal elements of HC90 under different pressing forces, and the experimental powder. Once again, there is no similarity ($P < 0.05$) between the sizes of the experimental particles and the skeletal elements, and an increase in pressing force changes the distribution ($P = 0$) while increasing the mean size by 36 %. If we once again refer to Gane *et al.* (Gane *et al.*, 1999), we note that they illustrate the filling of finer pore structures during liquid imbibition, such as those derived from fine GCC (HC90), as being more continuous, with lower levels of unfilled pores.
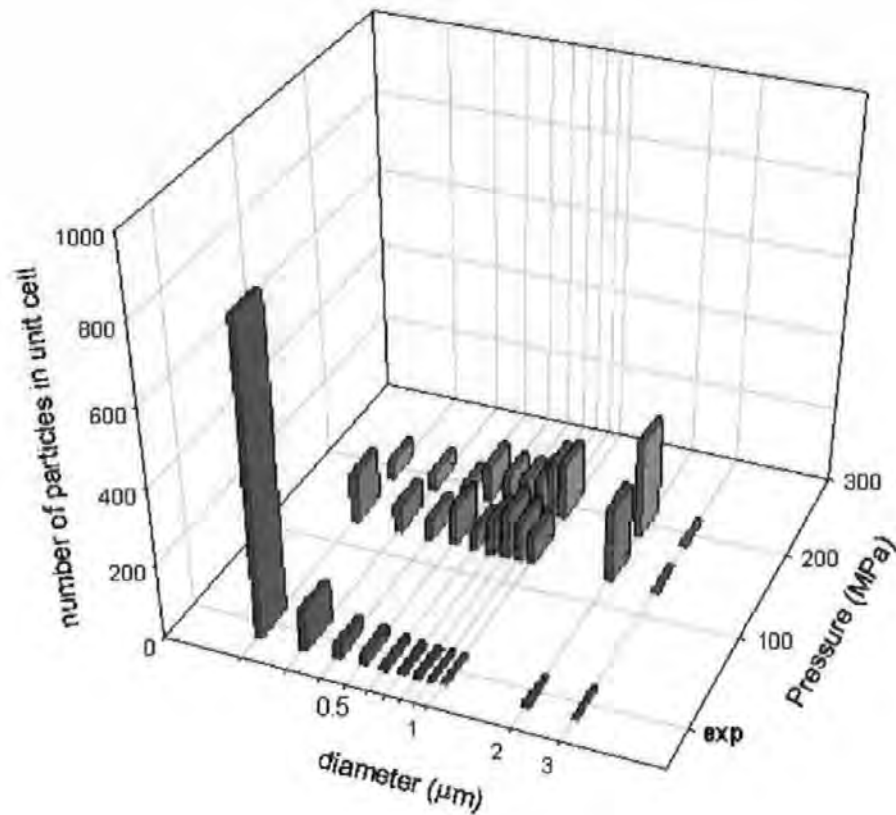
Figure 6.18 - Comparison of the experimental powder particle size distribution of HC90 and the skeletal element size distribution in tablets formed under different pressing forces.

6.6 Conclusions

An algorithm for the calculation of the effective skeletal element size distribution within a network model, previously developed and validated by Mathews *et al.* (1999), has been optimised for speed and accuracy. It has been developed to include a calculation of the solid phase represented by the skeletal elements and a virtual reality representation of the structures. The algorithm correctly simulated skeletal elements of the correct size distribution for two different sand samples, but only for those samples that happened to pack optimally under the applied mercury pressure in the mercury porosimeter.

For two different samples of compressed calcium carbonate, the simulation demonstrates that on pressing at the minimum pressure (57.6 MPa or 144.1 MPa), the skeletal elements differ

212

from the constituent particle sizes, as expected. It also shows a trend of increasing size as the pressing force is increased. For the coarser carbonate (HC60), this increase in average skeletal element size is strongly affected by the experimental mercury intrusion porosimetry. The increase of skeletal elements size between a formation pressure of 57.6 MPa and 86.5 MPa is larger than expected, and this is due to an anomalous trend in the mercury intrusion pressure for the HC60 86.5 MPa tablet. Also the reduction in average skeletal element size for the HC60 144.1 MPa tablet can be explained by taking into account the anomalously high value of porosity measured for this tablet. For the finer carbonate (HC90), the mean size of the skeletal elements increases by 36 % as the pressure is increased from 144.1 MPa to 201.7 MPa, Table 6-4.

The number of skeletal elements in a unit cell with diameter in the range 1 μm to 2 μm increases monotonically with pressure, Figure 12, except for one sample with an anomalous porosity.

The derivation of representative particle or skeletal element sizes from mercury intrusion is an indirect way of measuring them, and cannot compete with direct methods where available. It can also yield distributions with peaks at minimum and/or maximum size. These can be artefacts introduced by the model in an attempt to achieve very high or low porosities, but may also reveal the effects of incomplete consolidation.

This algorithm is now to be applied to the paper coating layers under study for shrinkage in this work, in order to estimate their representative solid skeletal element size and size distribution. The results of these calculations are presented in Chapter 7.

7 MODELLING THE SIZE DISTRIBUTION OF SKELETAL ELEMENTS IN PIGMENT TABLETS AND PAPER COATING

7.1 Introduction

The skeletal element size distribution algorithm, which has been previously described (Chapter 6) and validated for unconsolidated sand samples and consolidated calcium carbonate pigment tablets, has been used to simulate the size distribution of the elements that make up the solid phase of preformed tablets of calcium carbonate and latex, and paper coating layers.

The void structures generated by Pore-Cor for different paper coating layers have been already presented and analysed in detail in Chapter 5. It is important to point out that the main aim of the Pore-Cor software package is to model the void space of the porous samples, as explained in section 5.1. In order to match the porosity of the samples, the distribution of pores within the modelled structure is changed by means of a modelling parameter, the pore-skew. The skeletal element size distributions can show artefacts (extremely large or small elements) due to the use of the pore-skew modelling parameter, as explained in section 6.3. These artefacts cannot be completely removed from the Pore-Cor model, but they can be, to an extent, suppressed by controlling the values of pore-skew. The resulting trends of the sizes of the skeletal elements should therefore give a useful approximation to the effective particle size distribution within the porous material, consisting of the single particles of the pigment and/or agglomerates of particles, themselves acting as a single large skeletal element. This assumption was validated in Chapter 6, and is utilised in this chapter for the samples described below.

7.2 Experimental

Calcium carbonate tablets were prepared using two different natural $CaCO_3$ powders from the same limestone source, produced by Omya AG and named HC60 and HC90, having 60 w/w% and 90 w/w% of particles with diameter < 2 µm, respectively, as previously described in chapter 3. A low glass transition temperature ($T_g = 5$ °C) acrylic latex, namely Acronal S360D (BASF, Germany), was added to the system, at 5 w/w% on a dry basis, to act as a binder. The tablets were dried for 3 hours under a pressure of 15 bar (Ridgway *et al.*, 2004). The tablets were analysed by mercury intrusion porosimetry and the results were corrected for compressibility of the sample, as previously explained in section 2.1.1.

The paper coatings studied with the skeletal element algorithm were the same as used in the bending strip experiments (section 3.4) and which were modelled in Chapter 5.

7.3 Results

7.3.1 CaCO₃ and latex tablets

The tablets, analysed by mercury intrusion porosimetry, showed, after correction for compressibility, the values of porosity of 22.4 % for the HC90-based and 20.7 % for HC60-based ones, respectively.

Figure 7.1 and Figure 7.2 show the skeletal element distributions corresponding to different stochastic realisations of the structures. It can be seen, qualitatively, that the results are similar for different stochastic realisations.
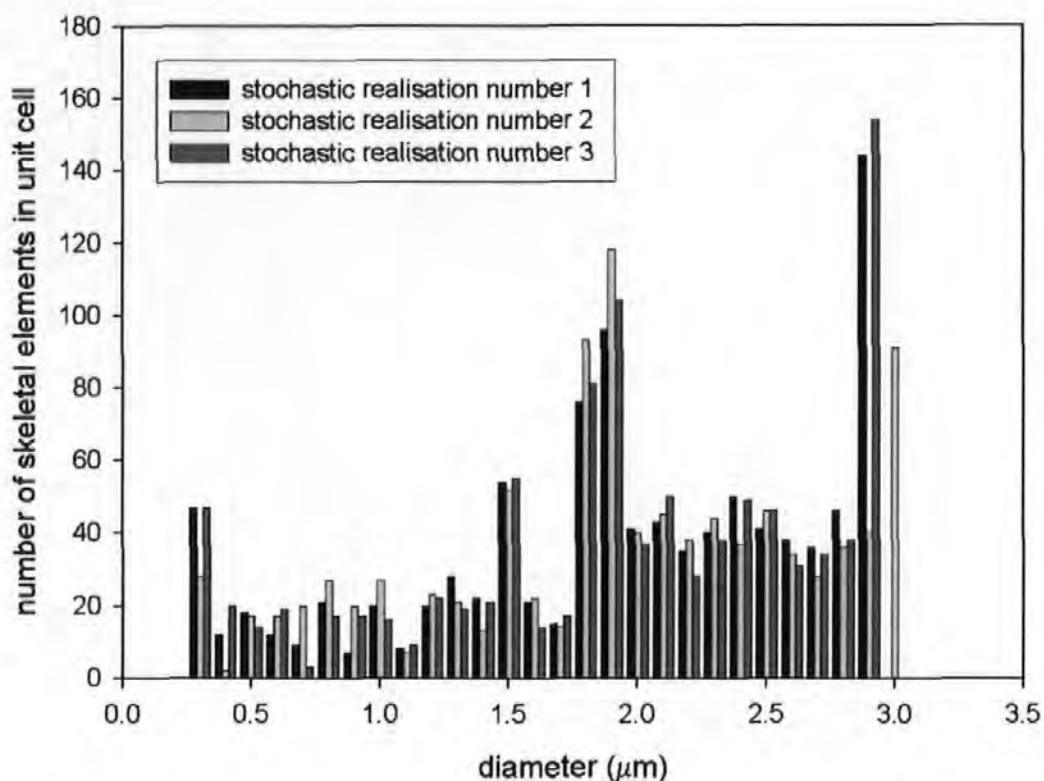
Figure 7.1 - Skeletal element size distribution in a tablet of HC60 + acrylic low T_g latex.
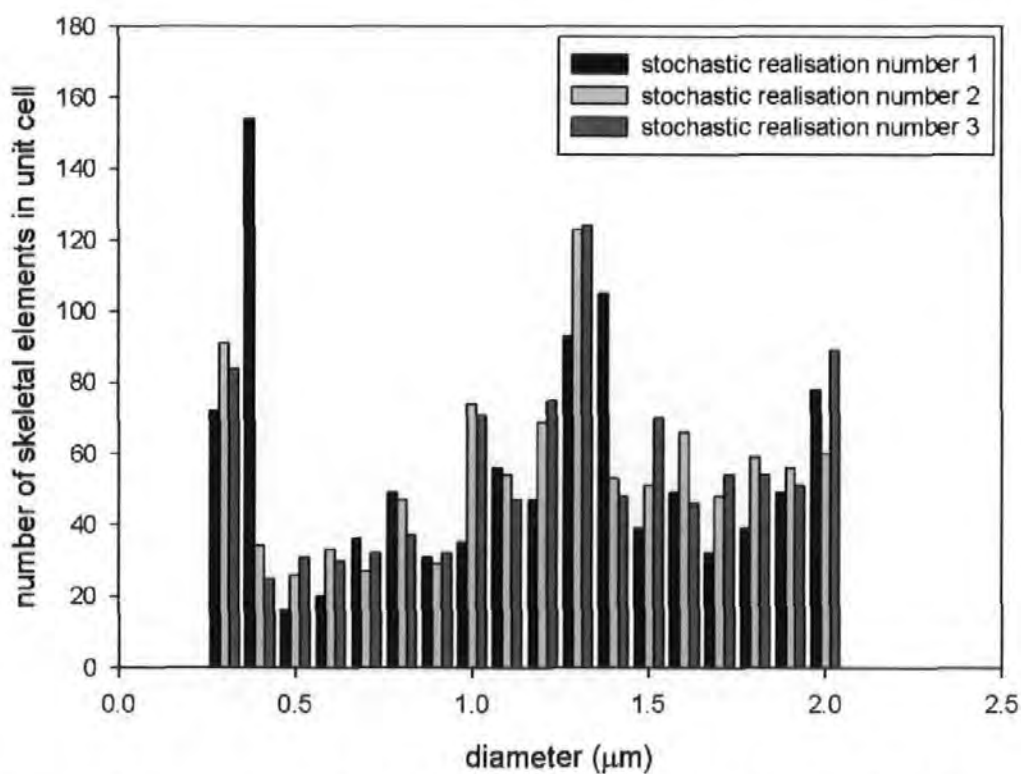
Figure 7.2 - Skeletal element size distribution in a tablet of HC90 + acrylic low T_g latex tablet

The results for three different stochastic realisations were also compared using the Mann-Whitney non-parametric test, section 6.5.1. As before a value of P greater than 0.05 indicates that the distributions are similar, while a value of P smaller than 0.05 indicates that the differences between the distributions are statistically significant.

Table 7-1 - Values of the Mann-Whitney statistic P for pairwise comparison of simulated skeletal elements corresponding to three different stochastic realisations on $CaCO_3$ – latex tablets.

Pairs of stochastic realisation numbers	HC60 + latex tablet	HC90 + latex tablet
1 - 2	0.79	0.057
1 - 3	0.45	0.045
2 - 3	0.96	0.054

From the histograms of the skeletal element distributions and from Table 7-1 it can be observed that the results of simulations corresponding to different stochastic realisations are identical in the case of HC60-based tablets ($P \gg 0.05$) and statistically similar for HC90-based tablets ($P \approx 0.05$).

By comparing the results of the simulations on the two different tablets it can be observed that, as expected, the skeletal elements generated by the simulation algorithm for the HC60 – based tablet are larger than those generated for the HC90 – based one. A statistical comparison between these distributions confirms that the difference is significant ($P = 0$).

As previously explained in section 6.3, in a continuous solid structure the maximum percentage of the volume of solid phase which can be represented by the cubic close-packing of spheres is 52.4 %. In the case of the calcium carbonate and latex tablets, the skeletal elements generated by the algorithm represent 28.5 % of the total solid phase volume of the samples.

7.3.2 Paper coating layers

The skeletal element size distributions for different paper coating layers were also generated with the algorithm described and validated in chapter 6. For each paper coating formulation, different stochastic realisations have been generated and, as a consequence, different size distributions. These have also been compared by the Mann-Whitney statistic test and all showed a value of P larger than 0.05. This means that, as for the tablets, the different stochastic realisations of the structures give skeletal element size distributions that are statistically equal to each other. Hence, the results presented below show only the size distribution for one stochastic realisation for each coating colour formulation. The results of statistical tests on the skeletal element size distributions of different coating colour formulations can be taken as yielding $P = 0$, unless otherwise stated.

The three-dimensional representations of Pore Cor unit cells are shown in Figure 7.3 and Figure 7.4. They represent the void space and the skeletal elements, as modelled by the software, of an HC90 with styrene-butadiene low T_g latex and HC90 with starch coating layers.

The skeletal elements generated by the algorithm used here, in the case of the different paper coating layers, represent between 30 to 41 % in volume of the total solid phase of the samples.
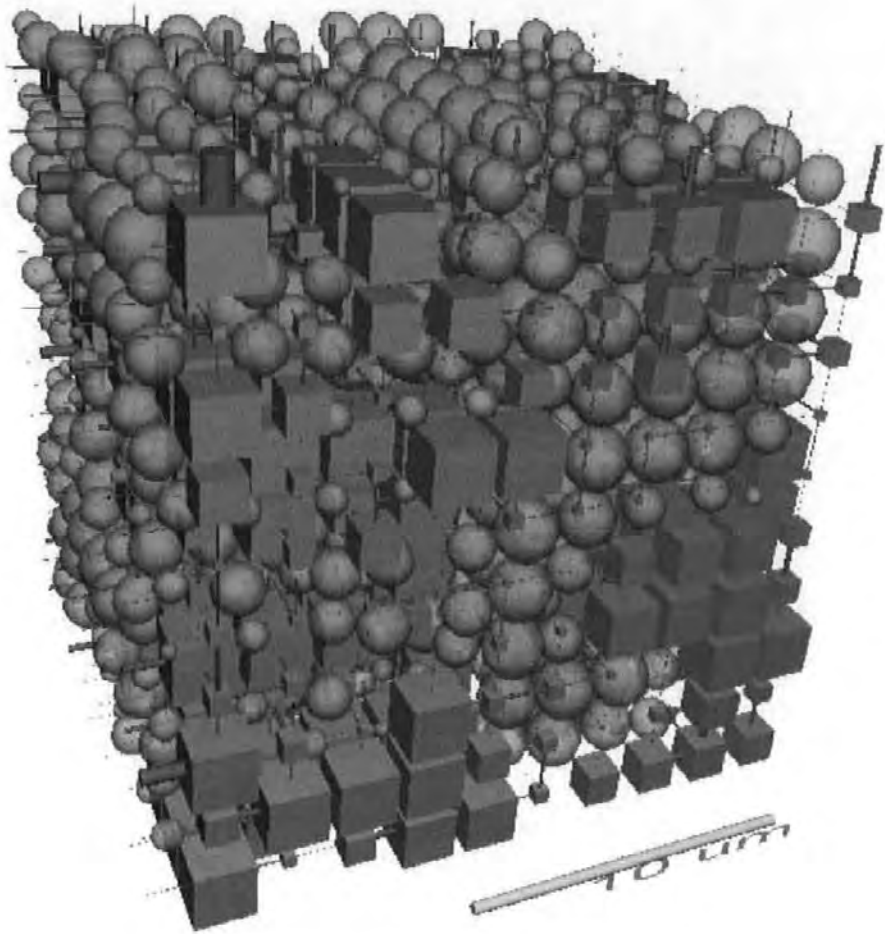
Figure 7.3 - Three-dimensional representation of a Pore-Cor unit cell with skeletal elements generated between the pores for a low coat weight sample of HC90 + 25 w/w% styrene-butadiene low T_g latex. The distribution of the skeletal elements for this sample can be found in Figure 7.7.
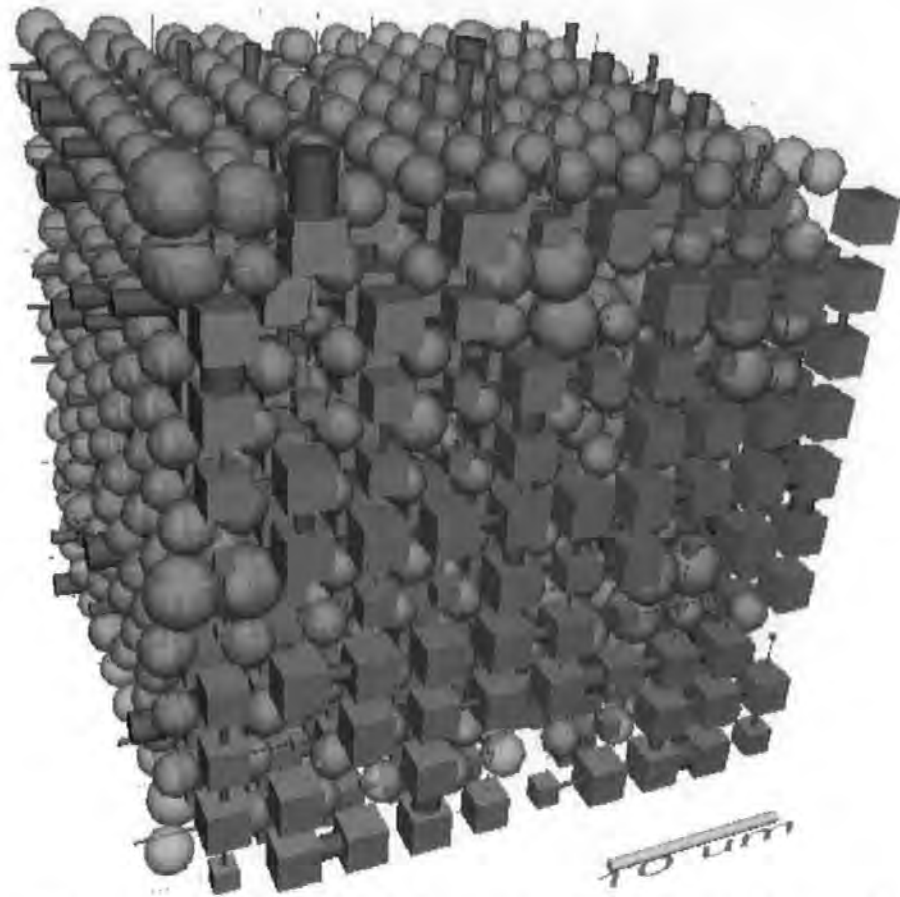
Figure 7.4 - Three-dimensional representation of a Pore-Cor unit cell with skeletal elements for an HC90 + 25 w/w% starch low coat weight sample. The distribution of the skeletal elements for this sample can be found in Figure 7.11. Note that the scale bar is shorter than that in Figure 7.3 and, therefore, the skeletal elements are larger.

Figure 7.5 and Figure 7.6 show the results of the skeletal element size distribution calculation for the paper coating layers based on calcium carbonate and, respectively, 25 w/w% and 10 w/w% of high T_g acrylic latex. All the skeletal element size distributions in this section are presented as minimum (○), maximum (▼) and average (●) diameter of skeletal element. It appears from a comparison between Figure 7.5 and Figure 7.6 that, as expected, the skeletal elements for the HC60-based coating layers are larger than those in an HC90-based coating layer, and this difference is statistically significant as the values of P, the Mann-Whitney pair-wise comparison statistics, are zero in every case. Figure 7.5 and Figure 7.6 also show that the thickness of the coating layer affects significantly the skeletal element size distribution, with thicker coating layers showing larger skeletal elements. This observation arises from the noted

220

decrease in porosity as coating thickness increases, the porosity loss being partly compensated for in the model by larger skeletal elements. It also appears that the amount of non–filming acrylic binder in the coating colour formulations does not cause an increase in skeletal element size. In the case of coarse calcium carbonate (Figure 7.6), the size distribution for 10 w/w% and 25 w/w% of binder in a thick coating layer is identical ($P = 0.062$).
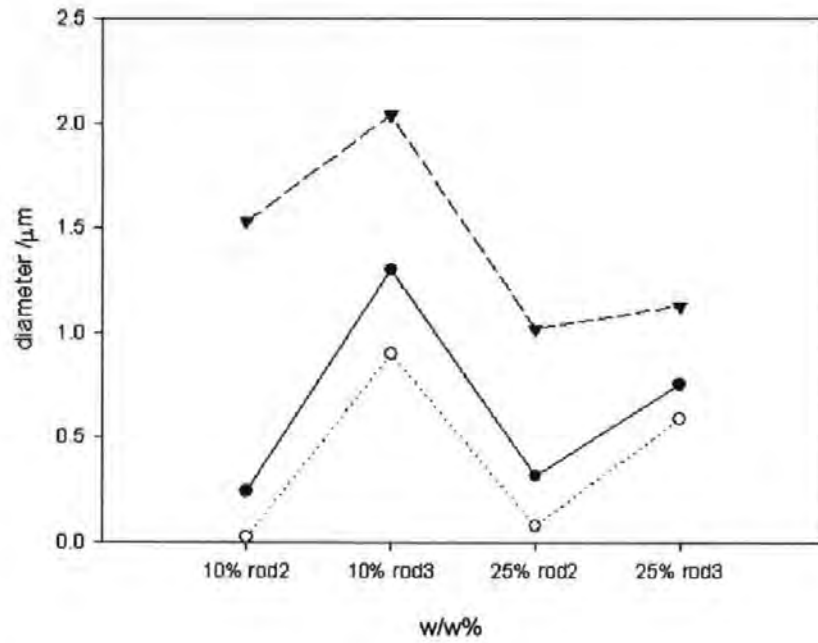
Figure 7.5 - Skeletal element size distribution for an HC90 and acrylic high T_g latex coating layer. Minimum (○), maximum (▼) and average (●) diameter of skeletal element.
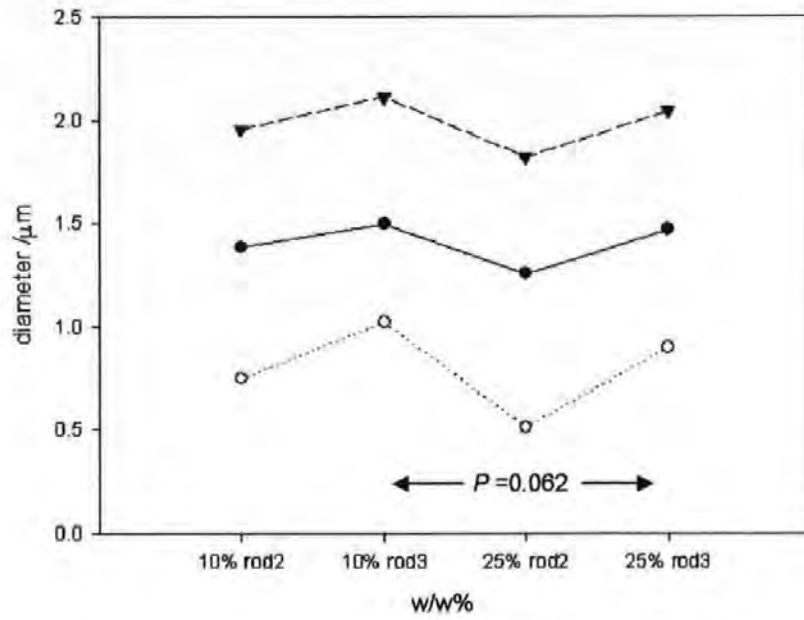
Figure 7.6 - Skeletal element size distribution for an HC60 and acrylic high T_g latex coating layer. Minimum (○), maximum (▼) and average (●) diameter of skeletal element.

The same trends can be observed in Figure 7.7 and Figure 7.8, where composition of the paper coating layers is similar, but the high T_g latex has a different chemical formulation.
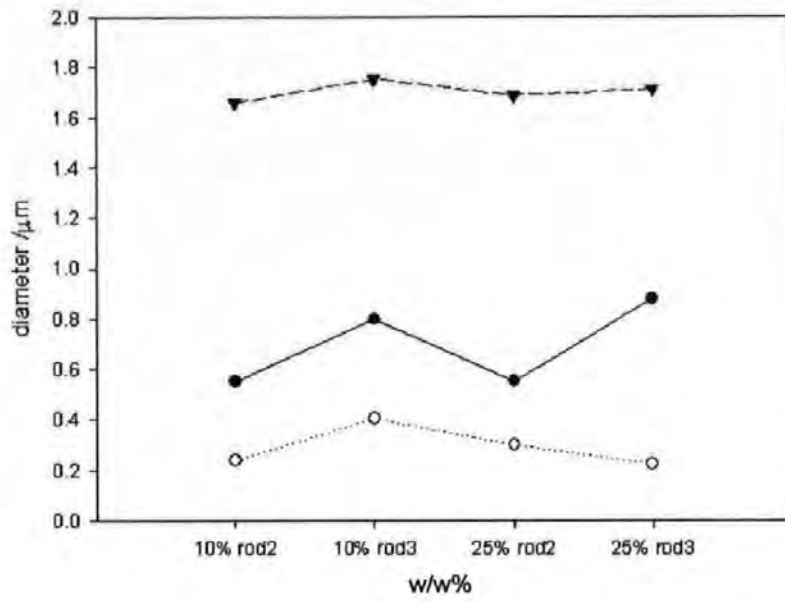
Figure 7.7 - Skeletal element size distribution for an HC90 and SB high T_g latex coating layer. Minimum (○), maximum (▼) and average (●) diameter of skeletal element.
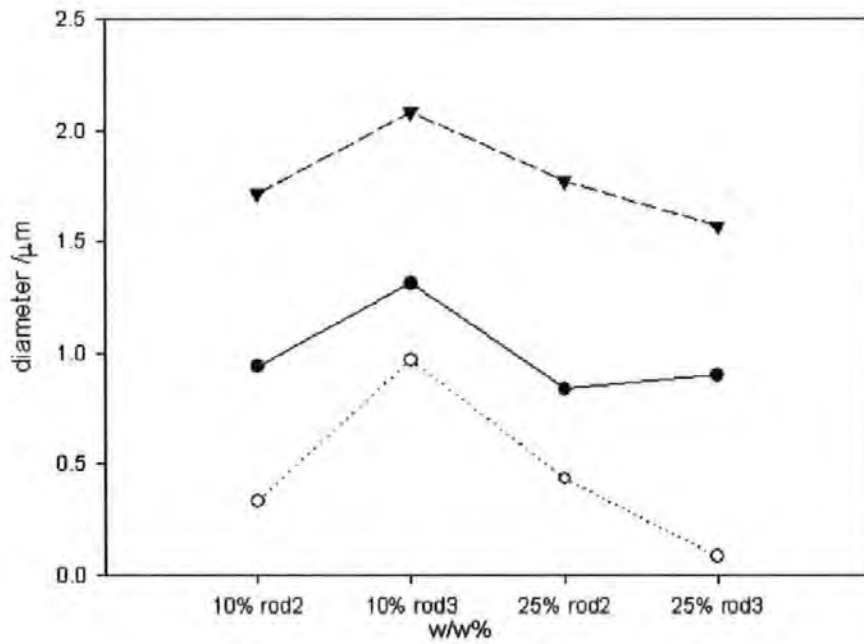
Figure 7.8 - Skeletal element size distribution for an HC60 and SB high T_g latex coating layer. Minimum (○), maximum (▼) and average (●) diameter of skeletal element.
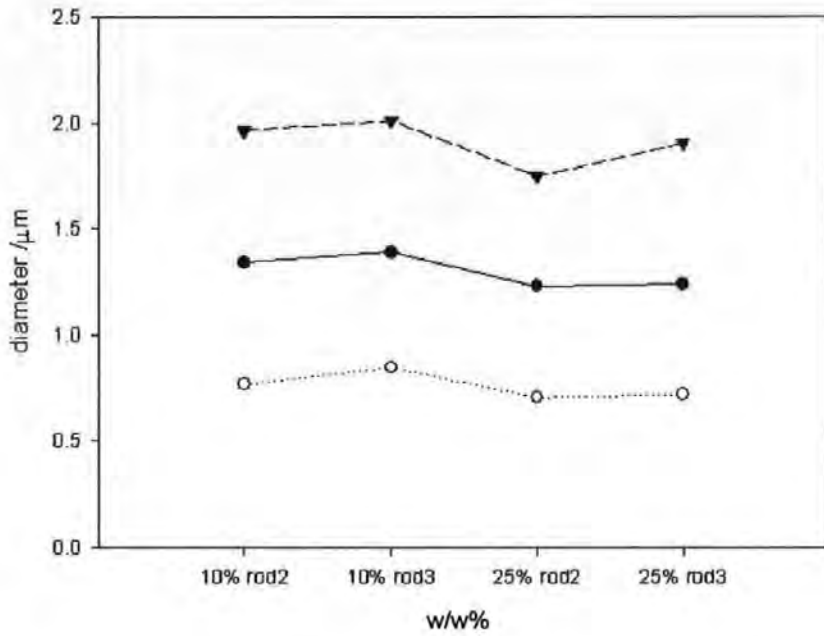
Figure 7.9 - Skeletal element size distribution for an HC90 and SB low T_g latex coating layer. Minimum (○), maximum (▼) and average (●) diameter of skeletal element.
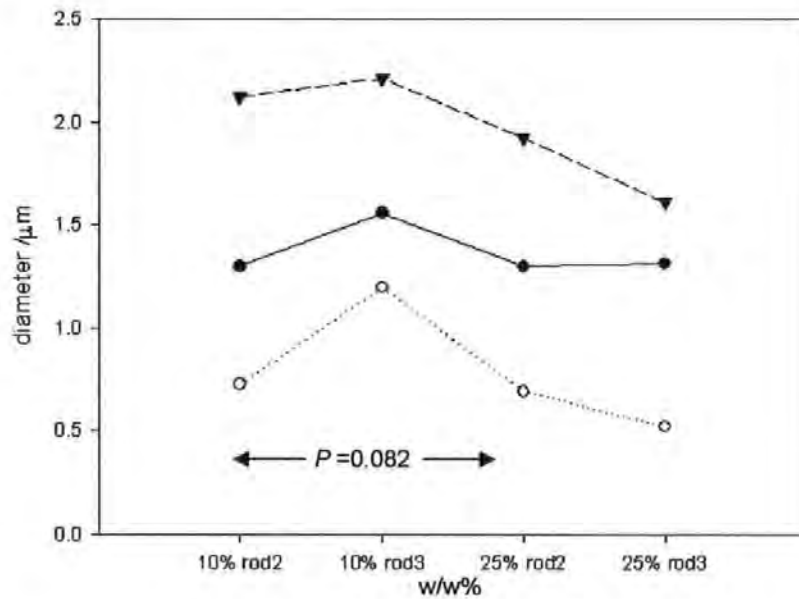
Figure 7.10 - Skeletal element size distribution for an HC60 and SB low T_g latex coating layer. Minimum (○), maximum (▼) and average (●) diameter of skeletal element.

Figure 7.9 and Figure 7.10 show the results of the size distribution calculations for paper coating layers prepared using calcium carbonate and a styrene-butadiene low T_g latex. The filming of the latex affects the size distribution of the skeletal elements: Figures 7.9 and 7.10 show larger skeletal elements both in the minimum and maximum size range when compared to high T_g latices (Figures 7.5 to 7.8). The use of a coarser pigment leads to a larger skeletal elements and an increasing amount of applied coating colour also leads to larger skeletal elements.

The amount of low T_g binder does not seem to affect the size of the skeletal elements in the case of the HC60, and, with a thin coating layer, the two distributions are statistically very similar ($P = 0.082$). This suggests that the coating is constrained in its shrinkage behaviour due to the larger pigment particle size.

The last case presented in this study is that of coating colour formulations based on calcium carbonate and starch. It is well known (Järnström *et al.*, 1995a; Husband, 1998) that starch adsorbs on the surface of clay mineral pigments, causing bridging flocculation. In the case of calcium carbonate the starch adsorption is not so clearly defined and documented. Rather, an osmotic effect caused by size exclusion results in depletion flocculation (Tadros, 1978). This effect can be observed also in the results presented in Figure 7.11 and Figure 7.12. The sizes of the skeletal elements are larger than in the case of latex-based coating colours. The starch also serves to exclude fine pores from the model, as shown in sections 5.5 and 5.6. Given the high shrinkage of starch-containing colour, the tight packing of the skeletal elements is to be expected.
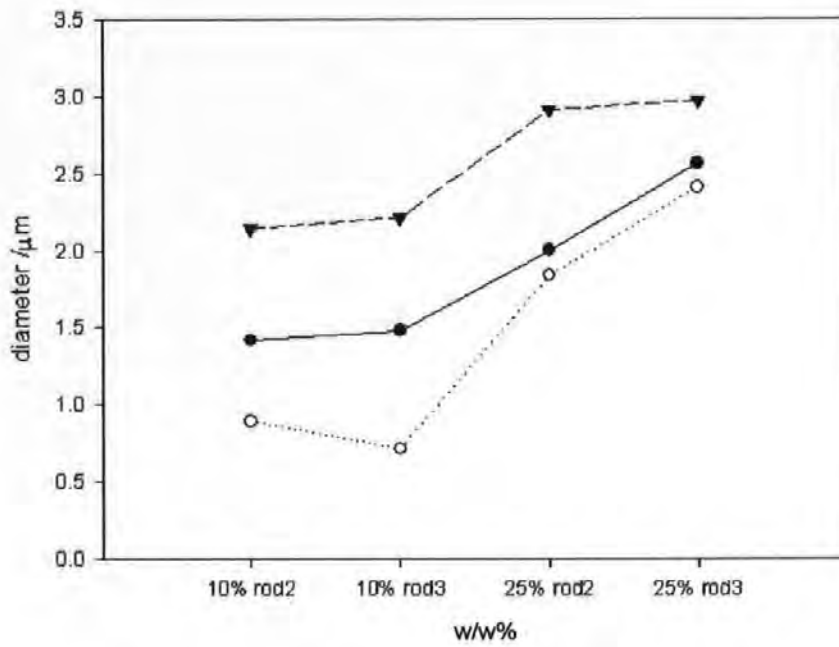
Figure 7.11 - Skeletal element size distribution for an HC90 and starch coating layer. Minimum(○), maximum (▼) and average (●) diameter of skeletal element.
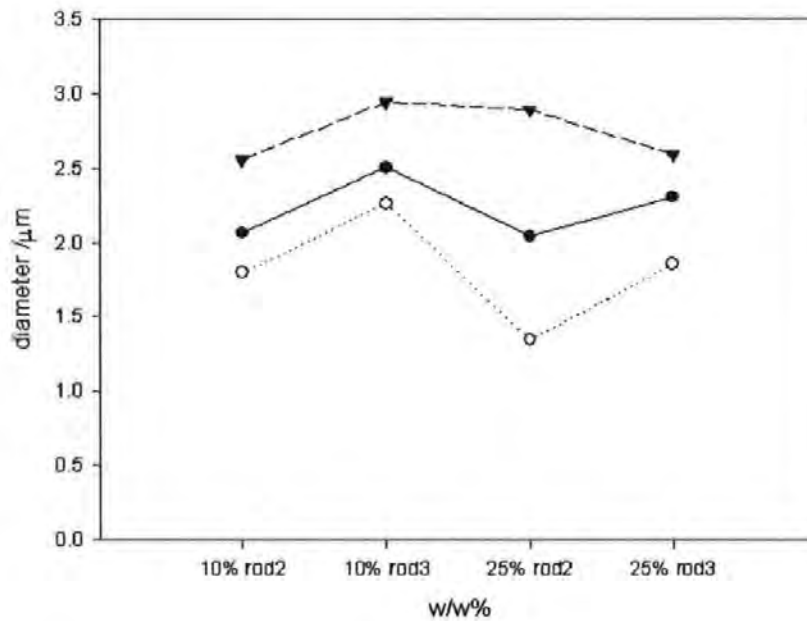
Figure 7.12 - Skeletal element size distribution for an HC60 and starch coating layer. Minimum(○), maximum (▼) and average (●) diameter of skeletal element.

Once more, the effect of coating weight can be observed, with increasingly large skeletal elements for thicker coating layers, reflecting, as discussed before, the greater freedom for consolidation and reduction of porosity.

7.4 Conclusions

The results of the simulations on tablets of calcium carbonate plus latex showed larger skeletal elements for coarser mineral pigment, as expected.

Different paper coating formulations have been studied in comparison. The results show that when high T_g latex is used as binding agent, the size of the skeletal element is smaller than in any other case. This supports the fact that the latex particles do not film-form during drying under the experimental conditions, and stay as hard spheres. This is also supported indirectly by the observation that different amounts of high T_g latex lead to very similar skeletal element distributions (Figure 7.6). On the other hand, low T_g latex particles either film-form upon drying, or become extruded or intruded into the porous structure under the forces experienced during drying. These processes give rise to expectedly larger skeletal elements, and effectively block off access to smaller pores. The use of starch as binder in our coating colour formulation reflects the partial flocculation of the pigment particles together with strong film forming, generating low porosity structures with very large skeletal elements.

The observed increase in sizes of skeletal elements with the thickness of the coating layer can be explained by taking into account the freedom of rearrangement of the particles of pigment and binder upon drying of the coating layer. As the coating layer dries, the particles of binder and pigment will rearrange. When a higher weight, thicker coating layer is applied on the substrate, the particles have more space available for rearrangement. They are no longer being

constrained in the vertical direction by the presence of the large particles, which in the case of lower coating weights are themselves as big as the coating layer itself. This freedom of rearrangement will result in a highly packed structure, as shown by lower values of porosity, with a larger number of ultra-fine features, pores and throats. The simple geometric representation of the void space and of the solid phase of the porous material, used by the network simulation software, cannot take into account such ultra-fine void features and, therefore, the final results show larger solid elements.

In section 4.4.2 an hypothesis has been formulated, that the particle-particle interactions in the coating colour, which result in an elastic response of the colour to internal stress, will strongly affect the structure of the coating at the FCC, when the immobilisation of the wet colour begins. Also it was hypothesised that as the drying process continues, the final dry structure at the SCC and the skeletal element size distribution will be affected too. It is expected that coating colours, based on similar pigments and showing similar viscoelastic properties, will also develop similar skeletal element size distributions. The modelled skeletal elements for HC60 and HC90, respectively, with different high T_g latices show similar sizes (Figure 7.5 to Figure 7.8) and, as shown in Figure 4.23 to Figure 4.26, similar viscoelastic behaviour, with very low interaction between pigment and binder particles. This strongly supports the hypothesis previously formulated.

The correlation between the sizes of the skeletal elements in the final dry structure and the viscoelastic properties in the wet colour appears even clearer in the case of low T_g latex-based formulations. Figure 4.26 shows that the interactions between HC60 and low T_g latex are slightly stronger than in the case if high T_g latex and, as a consequence, the skeletal elements shown in Figure 7.10 are only slightly larger than in the cases shown in Figure 7.6 and

Figure 7.8. Figure 4.28, on the other hand, shows that the interaction between the finer HC90 carbonate and the low T_g latex particles are far larger than those observed for high T_g latex. This, as expected, results in skeletal elements on average far larger for the HC90 with low T_g latex-containing colour than those modelled for HC90 with high T_g latex (Figures 7.5 and 7.7).

The hypothesis of a correlation between the rheological properties of the wet colours and the final dry structure of the coating layers holds in the case of carbonate and starch coating colours too. As discussed in section 4.4.2, the elastic modulus G' for the starch-based coating colour extends far as a function of the applied shear stress (Figure 4.29 and Figure 4.30), showing strong long range interaction between the different components of the wet colour. A consequence of these strong interactions is the formation of larger skeletal elements, as shown in Figure 7.11 and Figure 7.12.

It is important to take this relationship between particle-particle interaction in the wet phase and the size of the skeletal elements in the dry structure of the coating layer into account. It suggests that the packing of the structure upon drying, resulting in the dry structure at the SCC, is strongly affected by the rheology of the system. The structure of the coating colour at the FCC is also, therefore, a direct consequence of the rheology of the system, in particular the viscoelastic interactions.

All these findings support the previously hypothesised mechanism of the drying process and the influence of binder-pigment interactions and coating thickness on the final properties of a dry coating layer.

The skeletal element size distributions have been used in combination with the water-loss data of the samples upon drying to model the void network structure of a drying coating layer at the FCC using the modelled SCC (dry) structure as a starting point. These calculations will be presented in Chapter 8.

8 MODELLING THE SHRINKAGE IN PAPER COATING

8.1 Introduction

The experimental measurements and modelling simulations that were presented in the previous chapter of this thesis represent a novel approach to the study of the drying process of a paper coating layer. The measurement of the shrinkage forces (Chapter 3), the study of the strength and nature of the interactions between binder and pigment (Chapter 4), and the modelling of the void space and the effective skeletal elements distributions in the dry coating layer (Chapters 5 and 7) form components of the analysis necessary to understand the processes involved. This multi-component description is not yet complete, but the jigsaw pieces obtained during this research project represent important and precise parts of the whole picture. Thanks to these pieces, it is possible to draw conclusions on the whole process and describe a model of the drying process of a pigmented paper coating layer, based on a proposed stick-slip mechanism.

8.2 Stick-slip mechanism

The shrinkage forces, measured in Chapter 3, develop continuously while the evaporative drying of the coating colour proceeds. However, the analysis of the particle-particle interaction within the coating colour suggests that this continuous development of forces between the FCC and the SCC is only the averaged effect of a discrete stick-slip process, in which the accommodation of the shrinkage generating forces is partly accomplished as the structure itself consolidates against the particle-particle friction forces.
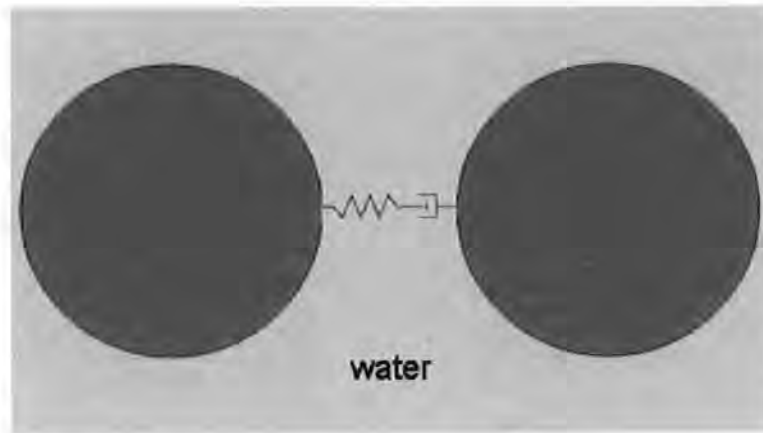
Figure 8.1 - Before the FCC the interactions between the particles (dark grey) can be represented by a viscoelastic model (Maxwell spring and dashpot).

Before the FCC the interactions between the particles can be represented by a viscoelastic model (Figure 8.1) and studied via rheological measurements (Chapter 4). When the FCC has been reached and surface capillaries begin to form, the stress builds in the system. This causes the system to distort. Then the system collapses until the next structure meniscus forms. This continues until the SCC is reached. Such behaviour cannot be defined as a continuous process as it depends on the particle boundary properties and the phenomena of particle packing. The discontinuity inherent in the mechanism suggests that a stick-slip model can be used as a representation via the following analogy. Two particles (pigment and/or binder) are drawn together by the capillary force, but in order to make them move towards each other, the capillary force must overcome the action of a resistance force derived from the surrounding structure matrix, similar to the friction the particles would experience if they were standing on a solid plane (Figures 8.2 to 8.4 where the planar contact represents the surrounding matrix).
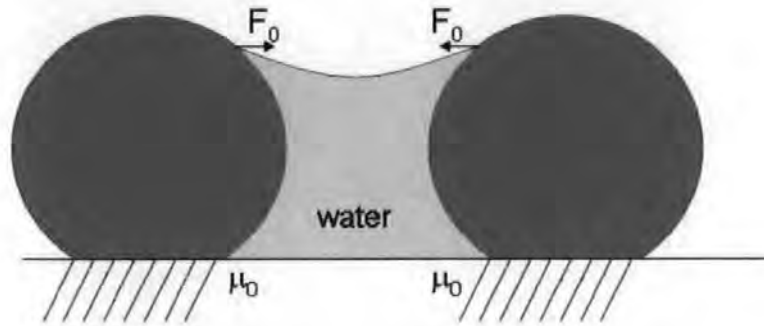
Figure 8.2 - Contribution of the resistance force to the stick-slip process, occurring between FCC and SCC. When the capillaries appear on the surface of the coating layer, the capillary forces do not cause motion of the particles immediately, as a resistance force, represented as friction, has to be overcome (stick).
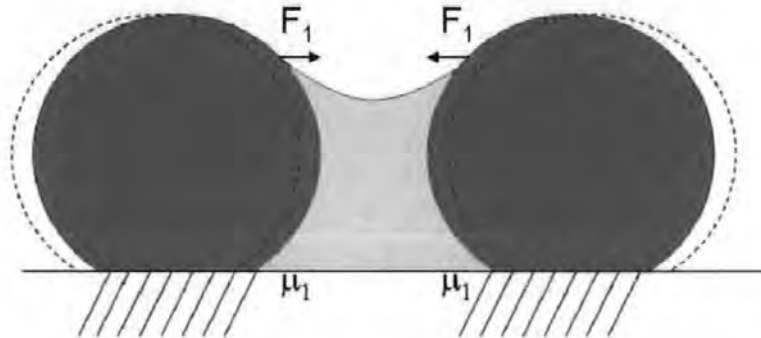
Figure 8.3 - As the water evaporates, the capillary force increases and overcomes the action of the resistance force, causing the flow of the particles (slip). The resistance force also increases as the water evaporates ($\mu_1 > \mu_0$).
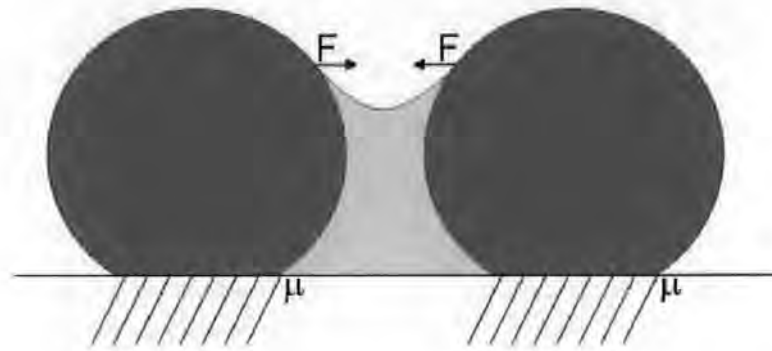
Figure 8.4 - The resistance forces cause the particles to stick once again ($\mu > \mu_1$), until the capillary forces overcome their action. This process continues until the system reaches the SCC.

In Figure 8.2 to 8.4, μ_0, μ_1 and μ represent the action of the resistance force in the stick-slip mechanism and $\mu_0 < \mu_1 < \mu$.

An indication of the tendency of the system to resist this collapse is given by the elastic interactions, G', between the particles in the coating colour. These have been presented in section 4.5 for the coating colour initially applied to the substrate. Obviously the interactions between particles while the shrinkage is occurring (between the FCC and the SCC) will be greater than the values of G' measured for the coating colour before it reaches the FCC. However, the different viscoelastic trends shown by the various coating formulations reflect their predicted behaviours between FCC and SCC and support the idea of a stick-slip mechanism. Accordingly, in the stick-slip model there is an energy barrier and, once exceeded, the system snaps into the new energy minimum. The hard latices in their respective coating colours rapidly build a large G' at low stress and then G' rapidly collapses as stress increases, as shown in Figures 4.23 to 4.26. The soft low T_g latex (Figures 4.27 and 4.28) and the starch (Figures 4.29 and 4.30), on the other hand, build the G' such that the drying system

234

stores energy during a large distortion of the structure. The stress effectively reflects the work done on the elastic structure, and it is seen that G' exists right through to large stress values. Only at even larger distortions, does the system slowly begin to collapse.

This explains why the systems experience different bending moments during drying. The hard high T_g latex system starts to support the meniscus but then quickly crumbles, whereas the soft low T_g latex and starch systems continue to support the meniscus structure while it distorts the layer.

The hard sphere high T_g latex-based system does indeed shrink to some extent in volume terms, but the yield is in the z direction and at low shrinkage forces, similar to a powder settling. The soft low T_g latex-based systems retain their structures and distort so that the shrinkage forces are manifest over long range throughout the matrix structure in the in-plane xy directions. This difference in short- to long-range action is the key that explains the different shrinkage forces for hard and soft (filming) latices.

As already discussed in section 7.5, the sizes of the skeletal elements within the modelled paper coating reflect the dependence of the structure on the short or long range action of the shrinkage forces. When low T_g latices or starch are used as binders, the shrinkage forces are allowed to act for longer because the structure is held in place, while it distorts, by the elastic interactions within the components of the coating. This results in structures with lower values of porosity and larger solid skeletal elements. When high T_g latex is used in the coating formulation, the shrinkage forces cause the structure to collapse, as the elastic interactions between the coating components are weak. As a consequence, smaller skeletal elements within a loosely packed structure with high values of porosity can be observed.

Another point supporting the stick-slip mechanism described above is that the maximum stress, shown in Chapter 3, especially for latex-based coating formulations, is not generally related to coat weight. This suggests that the stress can only have been produced within the surface of the coating, or only within a layer less than or equal to the minimal coating thickness tested. This coating thickness is equal to or less than the coarsest particle at lightest weight and so the phenomenon must be restricted to the surface layer equal to or less than the particle size. The menisci can reach deeper inside the structure, but clearly this is limited, at the maximum stress or SCC, to the surface of the coating only. This means that coating deforms maintaining the menisci at the surface for as long as the structure can deform.

After the SCC concentration has been reached the particles touch each other and no further movement is possible (Figure 8.5). The high T_g latex particles do not film form and the structure does not hold the shrinkage stress, while the low T_g latex particles do film form and they partially retain the shrinkage stress.

film of binder
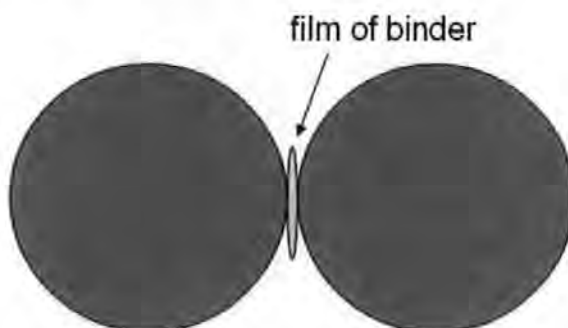
Figure 8.5 - Beyond the SCC the particles in the system are touching. In order to draw the particles closer together, an external force must overcome the bulk modulus of the sample, as happens in the mercury intrusion porosimeter at high pressures (section 2.1.1)

8.3 Modelling the coating structures immediately after the FCC

As previously explained in section 7.2, the particle-particle interactions in the coating colour affect strongly the size of the skeletal elements in the drying coating colour at the FCC and, as a consequence, at the SCC, when the immobilisation of the coating layer is complete. By

236

taking into consideration, in the case of hard high T_g latex, that the latex particles are not film-forming in the drying conditions it is possible to make the assumption that the skeletal elements modelled on the dry coating colour are the same as those which make up the drying coating colour immediately after the FCC has been reached. The dynamic formation of capillaries on the surface of the coating colour cannot be represented by Pore-Cor, which has the capabilities to represent only snapshots of the drying system.

Pore-Cor structures of the drying coating colour immediately after the FCC cannot be created directly as there are no mercury intrusion porosimetry data available from this state. However, by creating a structure having the same skeletal elements distribution as measurably occurs at SCC, together with a higher value of porosity to account for the water lost upon evaporation, it is possible to create a model structure of the coating colour approximating to that after the FCC and consequently at any intermediate step between the FCC and SCC. For example, the dry structure of an HC90 + 25 w/w% of acrylic high T_g latex with low coating weight has a dry porosity of 37.7 % in volume. This would also be the value of porosity of the structure at the SCC if all the water were to be removed. The SCC void structure and the skeletal elements simulated with Pore-Cor can be observed in Figure 8.6.
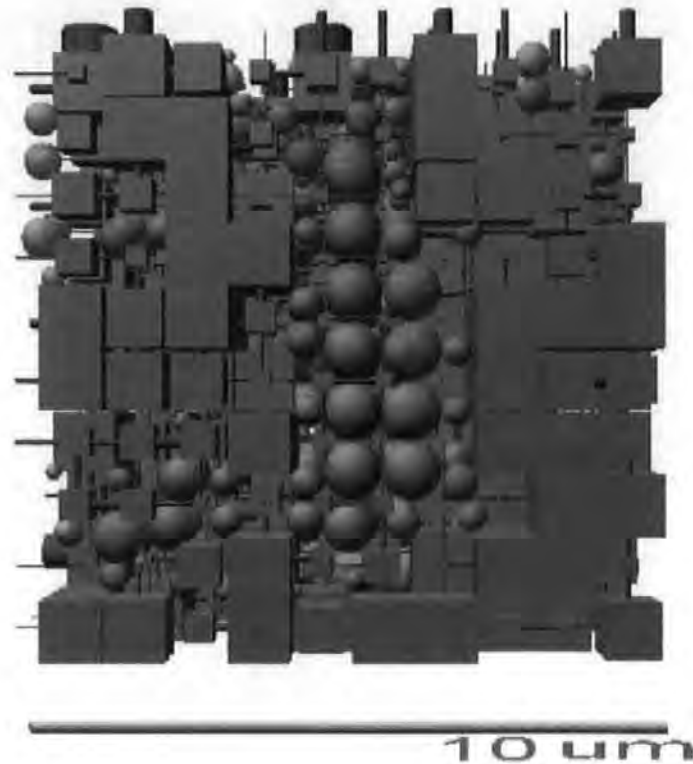
Figure 8.6 - Structure of HC90 + 25 w/w% acrylic high T_g latex layer with low coating weight at the SCC. The porosity of this structure is 37.7 %.

The same coating immediately after the FCC has a porosity of 67.0 % in volume, which includes the volume occupied by the water lost by evaporation between the beginning and the end of the shrinkage process. An intermediate structure, with porosity value halfway between the porosity values of FCC and SCC, and called the intermediate critical concentration ICC, has been generated. In Figure 8.7 the ICC structure with porosity of 52.4 % can be observed, while Figure 8.8 shows the structure of the coating immediately after the FCC, when the shrinkage phenomenon begins, as if no water were present in the system. The structures of the drying coating colour after the FCC and at the ICC had skeletal element size distribution as close as possible to the SCC structure, as shown in Figure 8.9.
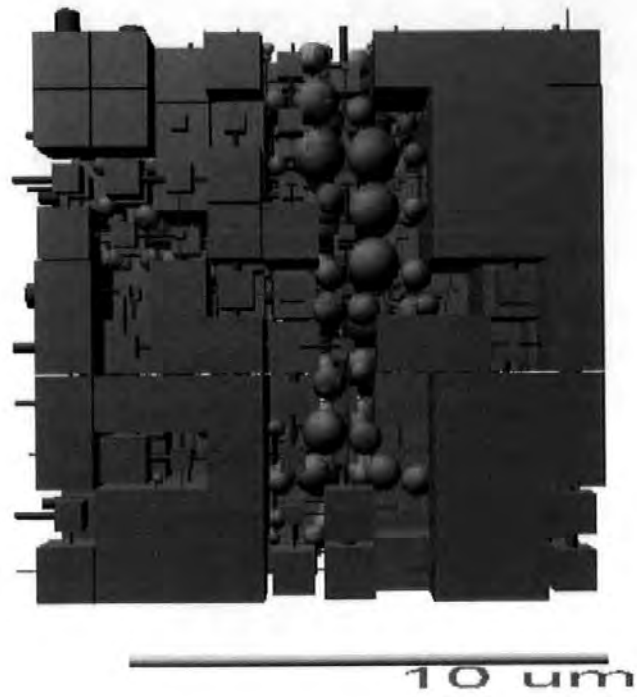
Figure 8.7 - Structure of HC90 + 25 w/w% acrylic high T_g latex layer with low coating weight. Intermediate step with 52.4 % porosity.
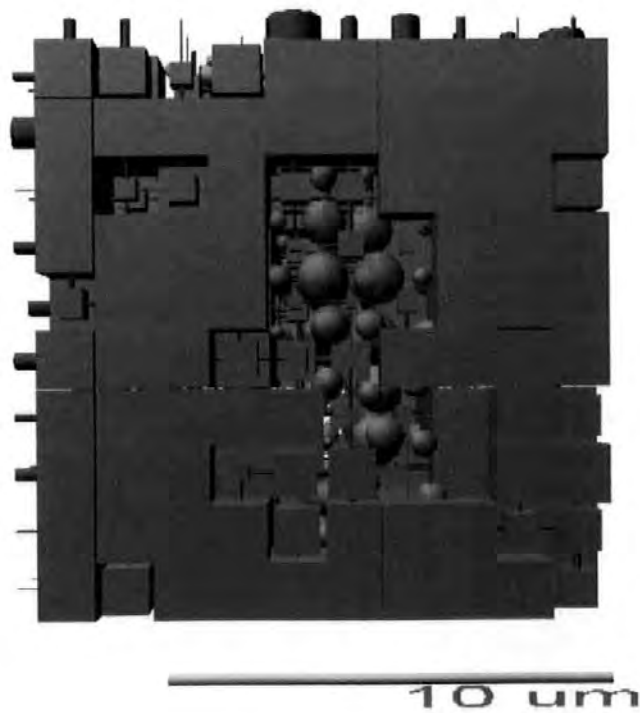
Figure 8.8 - Structure of HC90 + 25 w/w% acrylic high T_g latex layer with low coating weight at the FCC. The porosity of this structure is 67.0 %.
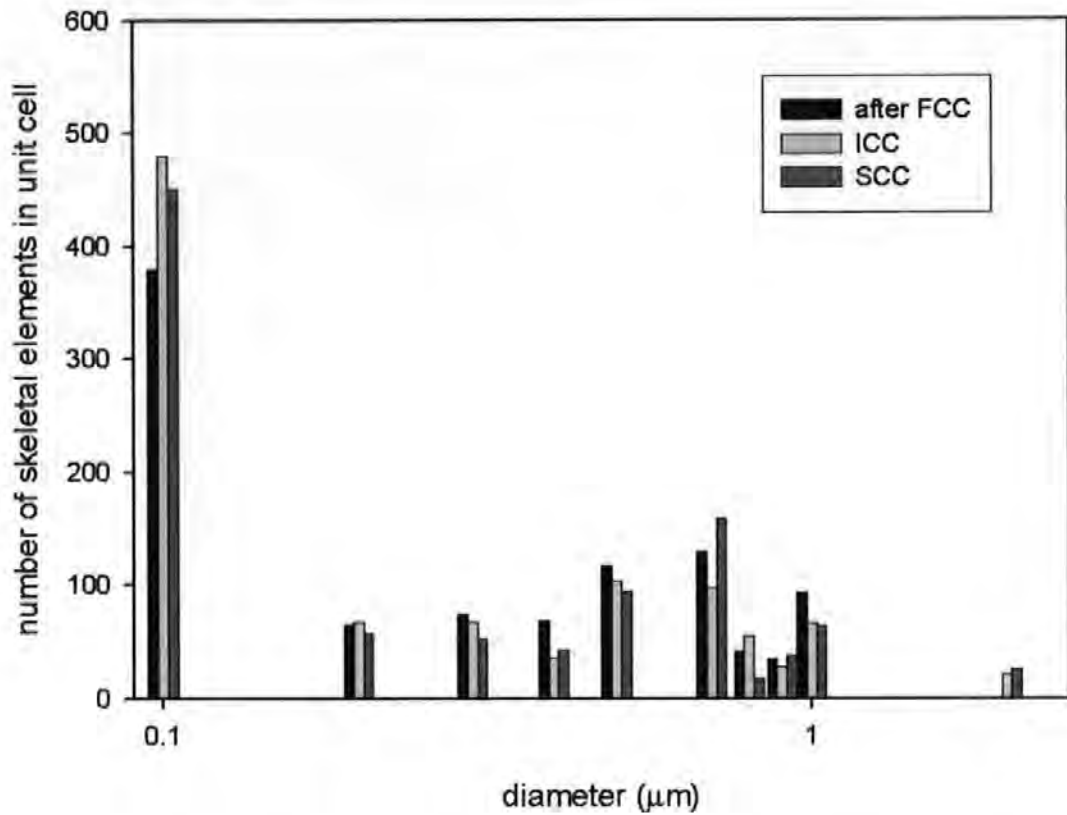
Figure 8.9 – Skeletal elements for the structures presented in Figures 8.6 to 8.8.

It can be observed by comparing the scale-bars in Figures 8.6 to 8.8 that, as expected, as we go backwards from the dry coating layer (SCC) to the beginning of the shrinkage process (immediately after the FCC) the size of the unit cell increases and the unit cell shows larger voids, while the skeletal elements within this void space remain constant. Using this argumentation, it is possible to recreate a realistic model structure for the coating layer at the FCC, despite the lack of mercury porosimetry data. This structure then allows the calculation of the capillary forces acting on the surface of the coating layer between FCC and SCC.

The same procedure was repeated for an HC60 + 25 w/w% of acrylic high T_g latex, HC90 + 25 w/w% of SB low T_g latex and HC60 + 25 w/w% of SB low T_g latex, and the results are presented in Table 8-1.

Table 8-1 - Volume % porosity for HC + latex samples (with low coating weight) immediately after the FCC, at the ICC and at the SCC.

Drying stage / Sample	Immediately after FCC	ICC	SCC
HC90 + 25 w/w% of acrylic high T_g latex	67	52.4	37.7
HC60 + 25 w/w% of acrylic high T_g latex	53.1	35.6	19.8
HC90 + 25 w/w% of SB low T_g latex	46.9	37	15.5
HC60 + 25 w/w% of SB low T_g latex	63.2	38.7	14.2

8.4 Capillary forces acting between FCC and SCC and comparison with experimental measurements.

When the coating layer dries between FCC and SCC, surface capillaries appear, and, as a consequence, capillary forces develop on the surface of the coating colour. The appearance of capillaries deeper in the porous network occurs only after the SCC, when further shrinkage cannot take place. Therefore, the calculation of capillary forces in the simulated porous network must be limited to the first layer of throats in the xy plane of the simulated Pore-Cor unit cells. The calculation of the horizontal component (x direction) of the capillary force in a cylindrical capillary of radius R according to the Laplace equation $F = 4\pi R \gamma \sin\theta$ (section 1.8.2) leads to an inconsistency in the results. If the contact angle approximates to 0, as in the case of water on most similar solid materials, this would lead to a vanishingly low value for the horizontal component of the capillary force. This is obviously not in agreement with experimental observations. The problem arises due to the lack of information about the actual orientation of the surface pore and its internal wall orientation, and the meniscus shape which is assumed spherical in the Laplace equation. In order to resolve such an inconsistency without taking into consideration more complicated equations for the calculation of the capillary pressure, the vertical components of the capillary forces were calculated in the first layer of

horizontal throats (y direction) by using $F = 4\pi R \gamma \cos\theta$ and the results were normalised to include the number of throats in the x direction (Figure 8.10).
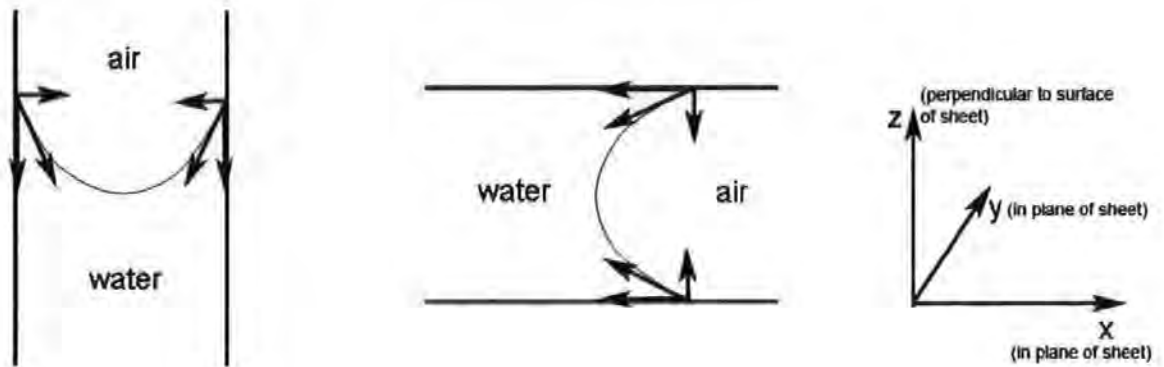
Figure 8.10 - Vertical and horizontal cylindrical throats and the capillary force components.

The resultant force was then normalised for the total coated surface (xy plane) of the Synteape sample, in order to make a comparison with the experimentally measured forces. The results were also normalised for the total capillary surface, i.e. the area contribution from the open capillary entrance cross-section diameters was calculated and the resultant force was divided by the total capillary cross-sectional area. The results for such a calculation on pigmented coating colour samples with acrylic high T_g and SB low T_g latex are shown in Figure 8.11 together with the results of the experimental measurements of the shrinkage forces presented in Chapter 3.

In Figure 8.11 the experimentally measured shrinkage forces measured immediately after the FCC has been reached are not represented, as the FCC represents a discontinuity in the drying process. A more detailed explanation will follow in section 8.5.
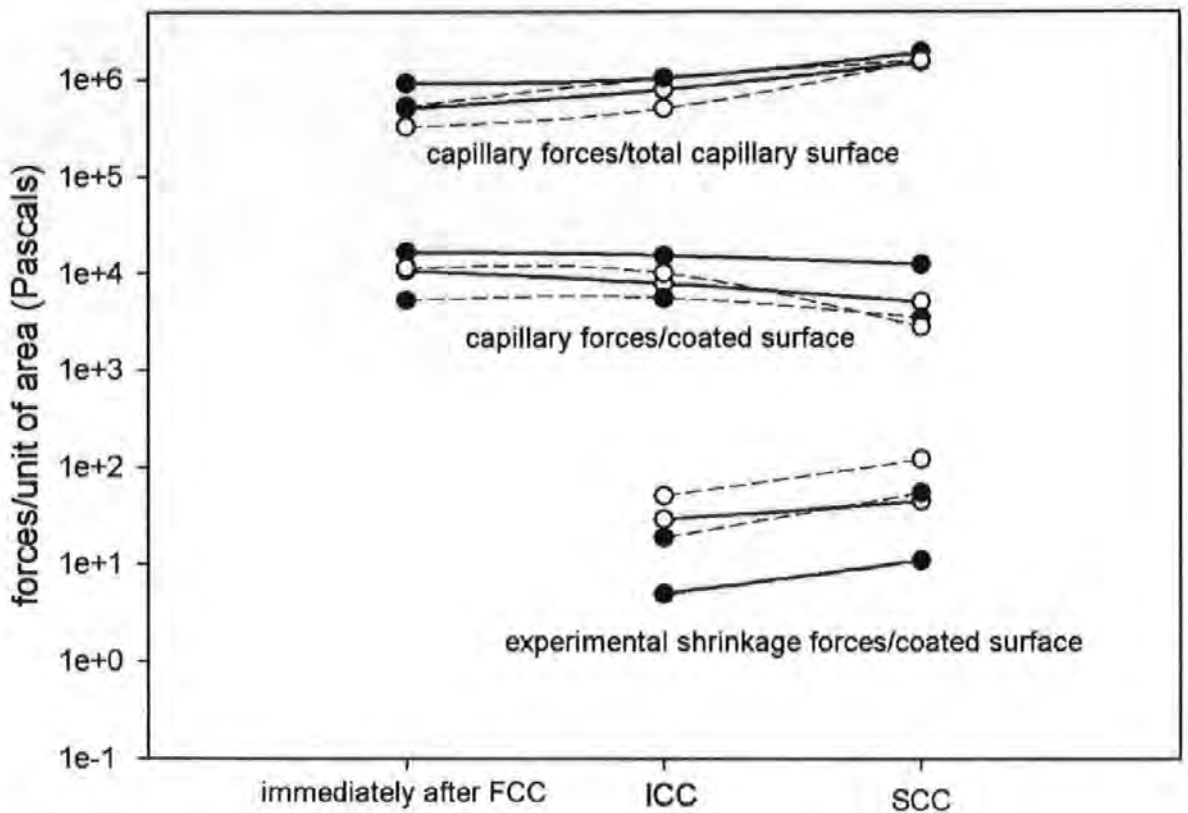
Figure 8.11 - Capillary forces per unit area of coated surface, capillary forces per unit area of capillary surface and shrinkage forces per unit area of coated surface. HC60 (empty circle) and HC90 (full circle) with acrylic high T_g latex (full line) and SB low T_g latex (dashed line), respectively.

The modelled capillary forces are two to three orders of magnitude larger than the experimentally measured shrinkage forces. This can be explained by the stick-slip mechanism suggested in section 8.2. While the capillary forces per unit area of surface are large, the resulting shrinkage forces are smaller, supporting the idea that the observed shrinkage of the structure is only the average effect of a stick-slip phenomenon.

It is interesting to observe that, for all the samples modelled with this technique, the capillary forces per unit area of total capillary surface increase while the coating dries. This is expected, as the capillaries get smaller upon drying. On the other hand, the capillary forces per unit area of coated surface decrease upon drying. As the simulated coating layer dries between FCC and SCC, the simulated unit cell gets smaller. For the force per unit area of coated surface to get

243

smaller, the reduction in total surface capillary radius must be larger than the reduction in unit cell surface. This could be seen, from the experimental point of view for the real drying coating layer, as a reduction in the number of active throats taking part in the shrinkage process. This would result in a reduction of the total capillary force per unit of coated surface. This reduction in capillary forces per unit of coated area also supports the suggested stick-slip mechanism. While these capillary forces get smaller upon drying, the resulting shrinkage increases and reaches its maximum at the SCC. This suggests that the resistance force, which was previously compared to a friction force, increases upon drying. Intuitively the forces opposing the motion of particles would certainly increase as the coating dries; the solid content of the suspension increases and the extent of the binder-pigment and pigment-pigment interactions gets stronger.

Figure 8.11 and the experimental measurements presented in Chapter 3 show that the low T_g latex-based coating colours show higher values of shrinkage forces acting upon drying. However, the modelled capillary forces are larger in the case of high T_g latex-based coating formulations. This suggests the stick-slip phenomenon is largely responsible for the resulting shrinkage of the structure. In Chapter 4 it was observed that the particle-particle interactions within a low T_g latex-based coating colour are far larger than those in a high T_g latex-based one. In high T_g latex-based coating formulations the particles have more freedom to move and the resistance forces are small. This allows the capillary forces to act on a shorter time and spatial scale, as the forces causing the particles to "stick" are smaller. When low T_g latex is used in the coating formulations, the interactions between the components of the coating colour are larger and, as a consequence, they cause the capillaries to be supported for longer and the resulting capillary forces to stay in place and act on a longer and larger scale. These

observations support the idea that the shrinkage process in drying paper coating layer takes place with a stick-slip mechanism.

8.5 Discussion

A full quantitative analysis of the results of this model of the shrinkage process is not possible, as there are no data available for the resistance force (or friction force) that causes the capillary forces to yield to shrinkage only if a certain energetic barrier is overcome. The estimation of such a resistance force, which dynamically changes as the coating dries, is possible only by modelling the interaction between particles within the high-solid content drying coating colour. Such a model should take into account elastic and viscous interaction between the particles of binder, the pigment and the evaporating liquid medium. Mechanical friction between the particles should also be taken into consideration. The development of such a model goes beyond the scope of this thesis, as it would represent a wide and complex research project in its own right, and it will be left for future research. However, it is possible to infer important information, supporting the suggested stick-slip mechanism, by the observation of the experimentally measured shrinkage forces, the modelled capillary forces at the SCC and the mercury intrusion data for these samples.

The modelled capillary forces per unit area of coated surface (xy plane) can be converted into capillary forces per cross sectional area of the coating layer (yz plane). This makes it possible to compare these modelled forces and the highest pressure at which mercury is intruding the samples without causing compression of the samples itself. By taking into consideration that $\cos 5 \sim -\cos 140$, where $5°$ and $140°$ being respectively the contact angles of water and mercury, it would be expected that the maximum mercury intrusion pressure had a value of the same order but opposite sign to the capillary forces at the SCC.

Table 8.2 shows the values of the maximum pressure of mercury intruding the void space of the sample and the capillary forces per cross sectional area of the sample at the SCC.

Table 8-2 - Maximum Hg intrusion pressure, capillary forces per cross sectional area at the SCC and measured shrinkage forces.

	HC90+acrylic high T_g latex	HC60+acrylic high T_g latex	HC90+SB low T_g latex	HC60+SB low T_g latex
Maximum Hg intrusion pressure (MPa)	112	72	90	90
Capillary force per unit cross-sectional area of coating at SCC (MPa)	111	45.6	31.3	25.7
Maximum experimental shrinkage force per unit area of coated surface (Pa)	11	45	55	121

It can be observed in Table 8.2 that the values of maximum mercury intrusion pressure and capillary force per cross sectional area match for the HC90 and acrylic high T_g latex sample. This is also the sample that shows the lowest value of measured shrinkage force. For all the other samples the maximum intrusion pressure is higher than the capillary forces per cross sectional area of the sample, and, the larger the difference between the two values, the higher the value of measured shrinkage forces. These observations lead to the conclusion that, when the interactions between the particles within the coating colour are weaker, as in the case of HC with high T_g latex, the system behaviour can be described with a hard-sphere model, where the particles have more freedom of movement and the stick-slip mechanism plays a minor role. Given that the bulk modulus of the system is elastically linear, the same forces are

246

experienced by the sample when pulling in (shrinkage during water loss) and when pushing out (mercury intrusion) of the pore. In this case the stopping point for the shrinkage, when the SCC has been reached, is represented by the mechanical bulk modulus of the sample. This is what is observed in the case of HC90 with acrylic high T_g latex, where the forces causing the particles to stick are too weak to hold the structure and the capillaries in place, while the structure is distorting. This yields small measured shrinkage forces.

When the interactions between the particles are stronger, the stopping point of the shrinkage forces is not the bulk modulus of the sample, but a sticking force, which is the difference between the maximum intrusion pressure and capillary force at the SCC. When the value of this sticking force is higher the drying system yields higher values of measured shrinkage forces, as the structure does not crumble and rearrange continuously while distorting, but the capillaries are supported for longer and cause larger shrinkage in the xy plane.

Another interesting observation is that higher shrinkage forces and greater influence of the stick-slip mechanism can be observed for HC60-based samples. In Chapter 4 it was observed that HC90-based samples, containing finer carbonate particles, showed stronger particle-particle interactions in the wet phase. This discrepancy between the rheological data and the stick-slip model of the drying process suggests that, as the coating dries, the packing of the latex particles within the network formed by the carbonate particles plays an important role. HC60-based coating can pack the latex particles more efficiently and this results in an increased stick-slip effect within the coating layer.
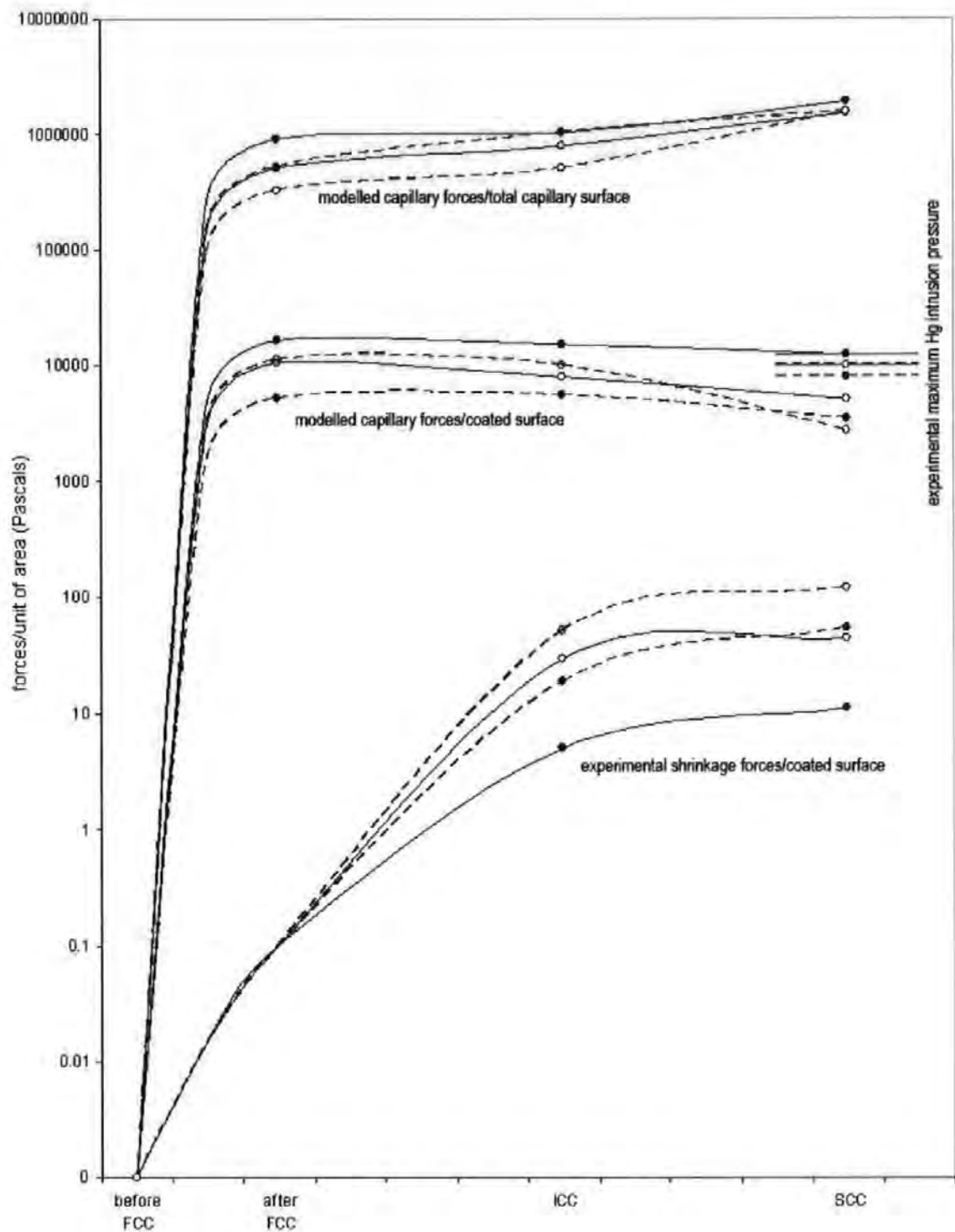
Figure 8.12 – Modelled capillary forces per unit area of coated surface, modelled capillary forces per unit area of capillary surface and experimental shrinkage forces per unit area of coated surface. HC60 (empty circle) and HC90 (full circle) with acrylic high T_g latex (full line) and SB low T_g latex (dashed line). The isolated points at the SCC represent the experimental maximum Hg intrusion porosimetry pressure normalised for the unit area of coated surface.

Figure 8.12 shows the modelled capillary forces, the experimentally measured shrinkage forces and the maximum mercury intrusion point normalised to unit area of coated surface. This graph shows how the capillary forces and the resulting shrinkage forces develop at the FCC, which represents a point of discontinuity for the drying process.

For the HC90 with acrylic high T_g latex sample, Figure 8.12 (full circle full line), the stick-slip mechanism does not take place and the system behaves according to a hard-sphere model. The stopping point for the shrinkage is represented by the mechanical resistance to compression of the coating layer (bulk modulus). As shown in Figure 8.12, this is the same as the maximum intrusion pressure of mercury before the mercury starts to compress the sample. In all other cases the difference between the capillary forces at the SCC and the maximum mercury intrusion pressures suggests, once more, the presence of a sticking or resistance force present during shrinkage. This resistance force at the SCC is the stopping point of the drying process when the stick-slip mechanism takes place and the sticking forces equals the capillary-induced shrinkage force.

9 OVERVIEW

The aim of this final chapter is to give a brief overview of the whole research project, in the context of the hypotheses stated in section 1.4. The hypotheses were subdivided into three sub-categories according to the process, experimentation and modelling. As shown in section 1.4, these hypotheses are not directly observable and not fully accepted in the research literature to date.

Process

1. shrinkage occurs between the first critical concentration (FCC) and second critical concentration (SCC), as defined in section 1.4, and the extent of shrinkage is linked to the extent of structural difference between FCC and SCC;

2. the shrinkage of a coating colour upon drying is not caused by a shrinkage of the emulsion polymer or soluble binder(s) commonly used, but is a meniscus driven phenomenon;

3. capillaries, and, as a consequence, meniscus forces, appear on the surface of a drying paper coating layer because the dynamic rearrangement of the forming pigmented network, to compensate for the water loss, is a process that requires initiation by the meniscus forces;

4. the work required to progress the rearrangement process is due to the component interactive resistance forces within the drying coating colour, which oppose the free rearrangement of the particles, related to the various particulate and chemical species in the slurry;

Experiment

5. since the forces acting during shrinkage cause a coated paper formulation on an elastically flexible substrate to curl up, a quantitative measure of the degree of curl can be used to give a quantitative measure of the shrinkage forces;

250

6. the shrinkage process can be realistically modelled by Pore-Cor by extrapolating backwards, in respect to drying process time, from the known SCC by increasing the porosity of the system while maintaining the same skeletal element particle size distribution;

7. the driving forces acting in the modelled process are the same as in the experimental process.

9.1 Work carried out

As stated in section 1.4, no direct experimental method is available to study the drying process from the point of view of the interaction between the particles after the FCC. Therefore the hypotheses were tested by a combination of experimentation and modelling, and inferences derived from these.

During this research project a novel experimental technique (section 2.3) was developed, able to monitor the bending of a strip of an elastic substrate coated with different coating colour formulations. Also the weight loss of the samples upon drying was measured. By applying equations derived from the study of Beam Theory (section 2.3.1), it was possible to calculate the value of the force acting on the surface of the drying coating colour that caused the elastic material to bend. This made it possible to probe hypothesis 5. The results agreed with those of Wedin *et al.* (Wedin *et al.*, 2004), giving support for the reliability of the method. However, there is no other type of experimental method with which to check the results, so their accuracy must be inferred from their self-consistency and explicable trends.

The shrinkage stress measurements showed how starch-based coating colours shrink more than latex-based ones and how high T_g latex-based coating colours do not retain the stress

developed upon drying and during shrinkage, while starch- and low T_g latex-based ones do retain it, at least partially. Also the influence of the amount of binder in the coating formulation and coating thickness was shown, in that exceeding the critical pigment volume concentration was not a controlling parameter when emulsion or soluble binders were used.

The mercury intrusion porosimetry results presented in section 3.1 give an indication of the different void space structure of the dry coating layers. These experimental results were also used to create simulated void network structures, using the Pore-Cor software. The analysis of this simulation of the dry coating layer structure is presented in Chapter 5 and it shows a very close correlation between the final dry structure of the paper coating and the extent of the shrinkage measured experimentally. The coating colours developing higher values of stress upon drying (section 3.4) are the ones which present a tighter packing of the final dry structure, with lower values of porosity and smaller voids. On the other hand, although the starting point of the drying process is similar, in terms of pigment-binder ratio, for all the coating colour formulation analysed, the FCC structures are not, however, similar, due to differences in low shear viscosity in respect to suspected elastic interactions. This indirectly proves that the extent of shrinkage is linked to the extent of structural difference between FCC and SCC (hypothesis 1).

The experimental study of the shrinkage of the different components of a coating colour and complete coating colour formulations containing different binders (section 3.4) proved that the shrinkage of a coating layer upon drying is not due to the shrinkage of the binder, but it is driven by the capillary forces developing within the drying coating colour as the water evaporates (hypothesis 2). Hypothesis 2 is proven by the fact that shrinkage can be observed when calcium carbonate only, with no binder, is used, and that the shrinkage force is not

252

maintained in this pigment-only case once the water has been completely removed. Furthermore, confirming the lack of binder shrinkage per se, when the elastic substrate strips were coated with binders only, with no pigment, they showed less shrinkage than for pigment on its own. When full coating colour formulations were used, the amount of shrinkage, however, was strongly affected by the binder used in the formulation in combination with the pigment. Starch-based coating colours showed the larger amount of shrinkage, while high T_g latex-based ones showed the smallest. The shrinkage was retained, at the end of the experiments, only by those coatings based on film-forming polymers (low T_g latex and starch) at the temperature used for drying.

The study of the rheological viscoelastic properties of the coating colours presented in Chapter 4 showed that the interactions between the different species in a coating colour correlate with the final structure of the coating layer. The interactions between the binder and the pigment are weak in the case of high T_g latex, while low T_g latex and starch show stronger interactions. Also, the low T_g latex- and starch-based coating colours show higher values of shrinkage stress upon drying and a tighter dry void structure. These observations led to the suggestion that the drying process involving high shrinkage follows a stick-slip mechanism, as opposed to a hard-sphere model. This stick-slip mechanism (section 8.2) involves the evolution of a resistance force, which represents an energetic barrier that the capillary forces on the surface of the coating colour have to overcome in order to cause the flow and rearrangement of the structure as the drying proceeds from FCC to SCC. The resistance force supports the menisci formed on the surface of the drying coating layer and allows them to act to cause shrinkage in the xy plane of the coating layer. When the resistance force is weaker, the menisci are not held in place and this causes the structure to shrink mainly in the z direction. This resistance force is related to the extent of the interactions between the pigment and the binder within the drying

coating layer and can therefore be inferred from the study of the rheology of the coating colour. Also the packing of the binder particles within the network of pigment particles plays an important role, as explained in section 8.5.

A full elucidation of the resistance force and its effect on the stick-slip mechanism is not possible within the currently available method. However, by applying symmetry of capillary pressure between essentially non-wetting and wetting liquids, a study of the values of maximum pressure of mercury intruding the structure in comparison with the modelled capillary forces acting at the SCC made it possible to gain an understanding of how the stick-slip process reaches its final point of equilibrium. It was shown that when the maximum mercury intrusion pressure and the simulated capillary stress at the SCC are similar, as in the case of HC90 with acrylic high T_g latex, the system behaves according to a hard-sphere model, and the final point of the shrinkage process is represented by the mechanical bulk modulus of the system. In such cases, the capillary forces yield small shrinkages in the xy plane. When the system follows the stick-slip model, the capillary stresses at the SCC are smaller than the maximum mercury intrusion point. This discrepancy between the maximum intrusion pressure and the capillary forces indicated the existence of a resistance force within the drying system. The larger the difference between the maximum mercury intrusion pressure and the capillary forces at the SCC, the larger the yield of the capillary forces to shrinkage in the xy plane. This combination of experimental and modelling techniques confirmed the validity of hypotheses 3 and 4, where hypothesis 3 tries to explain what drives the 'slip', and hypothesis 4 is the existence of 'stick'.

Pore-Cor was used in Chapter 5 to model the void space of the porous coating layers. The simulated unit cells, in the case of high T_g latex-based coating layers, showed uniform

structures. Starch-based ones showed a higher level of correlation, confirming the hypothesis of starch-induced flocculation.

In Chapter 6 a new algorithm was developed, able to calculate the size of the largest spherical elements that could be fitted between the pores of the Pore-Cor unit cell. These spherical elements are a representation of the effective particle size distribution of the porous material, modelled by Pore-Cor, and termed the skeletal element size distribution. The algorithm was validated on unconsolidated sand samples and consolidated calcium carbonate tablets, showing values close to the experimental particle size distribution for the sand sample, and giving logical trends for the $CaCO_3$ tablets. The same algorithm was then used on the modelled structures of the dry coating colour layer (Chapter 7). This made it possible to obtain information about the size of the skeletal elements in the coating at the SCC, when the particles cannot move any more. As expected, the coating based on starch showed the largest skeletal elements, due to starch-induced flocculation of the particles. The smallest skeletal elements were shown with the high T_g latex-based coating layers.

Using the modelled skeletal elements, representative of the solid phase of the coating colour at the SCC, it was possible to generate modelled structures representative of the drying coating colour. This was achieved by creating Pore-Cor structures having the skeletal element size distribution determined at SCC, but given higher values of porosity, which accounted for the water lost during the drying process. The FCC structure and an intermediate concentration structure, with porosity value halfway between the porosity at FCC and at SCC, were modelled, as shown in section 8.3.

The modelled structures representative of the different steps of the drying coating colour between FCC and SCC were then used to calculate the capillary forces acting on the surface of the coating (section 8.4). It was subsequently shown, in section 8.5, that the values of these modelled capillary forces are in good agreement with the maximum mercury intrusion pressure for the sample showing the smallest amount of shrinkage. This suggests that the modelling was realistic (hypothesis 6). The differences observed between the maximum mercury intrusion pressure and the capillary forces in the cases of low T_g latex-based coating layers, which also showed a large measured shrinkage in the xy plane, supported the idea of the stick-slip model previously described (section 8.5). This confirmed the validity of hypothesis 7 and achieved the main aim of this research project, which was to measure and model the evaporative drying of a paper coating layer, and explain the processes involved.

This research project does not have direct environmental applications. However, by reaching a deeper understanding of the processes involved in the drying of a paper coating layer and of the role played by the different species in the coating formulations, its conclusions could be used in the development of more environmentally friendly coating formulations, involving the use of natural binders but without their detrimental effects on the final product.

9.2 Future work

As explained in section 8.5, the model developed in this research project can only be validated indirectly by comparing experimental and modelling data representative of the SCC structures, and experimental and modelling data of the coating formulation wet-phase. A full quantitative modelling analysis of the stick-slip model proposed for the drying mechanism cannot be, at this point, achieved because of the lack of information on the interaction between the particles in these high solid content drying systems. Future research could focus on the development of

a model describing the particle-particle and particle-fluid phase interactions, so that the resistance forces causing the stick-slip phenomenon to occur could be quantified.

Also the influence of the absorption of water by the base paper on the drying process, as in a real paper coating system, could be studied by developing an experimental device, which could simulate such behaviour, and by extending the existing model to take account of it.

APPENDIX

Fortran 90 code of the skeletal elements size distribution algorithm (not to be reproduced or used without the author's permission).

```
! ***************************************************************
! skeletal elements size distribution 2
!    Last change: GML  12 Sep 2003    9:56 am

subroutine partsize2()
REAL smallreal
REAL A , Cu , X , Y , Z , distanceUC1 , mindist , distdiff , distanceVC1 , distanceVC2 , distdiff1 , distdiff2

REAL XP,YP,ZP
INTEGER L,k,j
DIMENSION Cu(8) , X(50) , Y(50) , Z(50) , dummy2(3)
DIMENSION CUX(1000),CUY(1000),CUZ(1000)
INTEGER touchingcube , firsttouchingcube
REAL XC1 , YC1 , ZC1   !C1 = first contact point
REAL XU , YU , ZU , XV , YV , ZV ,D1(1000),D2(1000),D3(1000),minccd(1000),RH(1000)
REAL lambda , step , mu
INTEGER flag, flag2
!REAL XN,YN,ZN
REAL XC2 , YC2 , ZC2  !C2 = second contact point
!REAL XC3 , YC3 , ZC3  !C3 = third contact point
REAL  xpartposn,ypartposn ,zpartposn   ! absolute position of centre of particle
REAL porerow, sidelength(1111),dummy(100),maxdiameter(1000), maxradius(1000) , ccda(1000) ,ccdb(1000),ccdc(1000) ,ccdd(1000)
CHARACTER*45 particlecomment
CHARACTER dummychar,dummychar2
REAL dummyused, aspec, totvol
COMMON/porepositions/cux,cuy,cuz
COMMON/pi_value/pi
common/unitcelldata/dummy2,aspec  !note todo 8/1/04 - feed in pore row spacing A(1) etc through this common statement
!open unitcell.csv and get side length of the 1000 pores and the pore row spacing

print *,'in partsize2 dummy2(1)=',dummy2(1),'aspec=',aspec
open (23,file='datafiles\unitcell.csv',status='unknown')


read (23,*) dummychar

do L=1,1000
  READ(23,*) dummy(1), dummy(2),dummy(3),dummy(4),sidelength(L), dummy(5),dummy(6),dummy(7),dummy(8),dummy(9),dummy(10),&
  &dummy(11),dummy(12),dummy(13),dummy(14),dummy(15),dummy(16),dummy(17),dummy(18),dummy(20),dummy(21),dummy(22),&
  &dummy(23),dummy(24),dummy(25),dummy(26),dummy(27),dummy(28),dummy(29),dummy(30),dummy(31),dummy(32),dummy(33),&
  &dummy(34),dummy(35),dummy(36),dummy(37),dummy(38),dummy(39),dummy(40),dummy(41),dummy(42),dummy(43),dummy(44),&
  &dummy(45),dummy(46),dummy(47),dummy(48),dummy(49),dummy(50),dummy(51),dummy(52),dummy(53),dummy(54),porerow,dummy(55),&
  &dummy(56)
  end do
  close (23)

dummychar=dummychar2
dummychar2=dummychar
dummyused = 0
do j=1,100
dummy(j)=dummyused
dummyused=dummy(j)
end do


do j=1,111
sidelength(j+1000)=sidelength(j)   ! side length of pores
end do

smallreal = 1e-20

OPEN (3,FILE='datafiles\partposn.csv',STATUS='unknown')
OPEN (4,FILE='datafiles\particle.wrl',STATUS='unknown')

! CALCULATE POSITIONS OF CUBE CENTRES
A=porerow
do k=1,1000   ! k is particle number

X(1)=0
Y(1)=0
Z(1)=0
X(2)=X(1)+A
Y(2)=Y(1)
Z(2)=Z(1)
X(3)=X(1)
Y(3)=Y(1)+A
```

```
Z(3)=Z(1)
X(4)=X(1)+A
Y(4)=Y(1)+A
Z(4)=Z(1)
X(5)=X(1)
Y(5)=Y(1)
Z(5)=Z(1)+A
X(6)=X(1)+A
Y(6)=Y(1)
Z(6)=Z(1)+A
X(7)=X(1)
Y(7)=Y(1)+A
Z(7)=Z(1)+A
X(8)=X(1)+A
Y(8)=Y(1)+A
Z(8)=Z(1)+A

100 CONTINUE


Cu(1)=sidelength(k)
Cu(2)=sidelength(k+1)
Cu(3)=sidelength(k+10)
Cu(4)=sidelength(k+11)
Cu(5)=sidelength(k+100)
Cu(6)=sidelength(k+101)
Cu(7)=sidelength(k+110)
Cu(8)=sidelength(k+111)

!CALCULATE POSITIONS OF INNER CUBE CORNERS
X(10)=X(1)+(0.5*Cu(1))
Y(10)=Y(1)+(0.5*Cu(1))
Z(10)=Z(1)+(0.5*Cu(1))
X(11)=X(2)-(0.5*Cu(2))
Y(11)=Y(2)+(0.5*Cu(2))
Z(11)=Z(2)+(0.5*Cu(2))
X(12)=X(3)+(0.5*Cu(3))
Y(12)=Y(3)-(0.5*Cu(3))
Z(12)=Z(3)+(0.5*Cu(3))
X(13)=X(4)-(0.5*Cu(4))
Y(13)=Y(4)-(0.5*Cu(4))
Z(13)=Z(4)+(0.5*Cu(4))
X(14)=X(5)+(0.5*Cu(5))
Y(14)=Y(5)+(0.5*Cu(5))
Z(14)=Z(5)-(0.5*Cu(5))
X(15)=X(6)-(0.5*Cu(6))
Y(15)=Y(6)+(0.5*Cu(6))
Z(15)=Z(6)-(0.5*Cu(6))
X(16)=X(7)+(0.5*Cu(7))
Y(16)=Y(7)-(0.5*Cu(7))
Z(16)=Z(7)-(0.5*Cu(7))
X(17)=X(8)-(0.5*Cu(8))
Y(17)=Y(8)-(0.5*Cu(8))
Z(17)=Z(8)-(0.5*Cu(8))



!!!!!!!!!!!!!!!!!!!!!!!!!!!!!!!!!!!!!!!!!!!!!!!!!!!!!!!!!!!!!!!
!    hard sphere diameter    !!!!!!!!!!!!!!!!!!!!!!!!!!!!!!!!!!!!!!!
!!!!!!!!!!!!!!!!!!!!!!!!!!!!!!!!!!!!!!!!!!!!!!!!!!!!!!!!!!!!!!!

!  Calculate corner-to-corner distances for 'Steel ball' radius
!  Cu is changed to a 2-d array, however the geometry calculations are not correct

     ccda(k) = (A-Cu(1)-Cu(8))*((3)**0.5)
     ccdb(k) = (A-Cu(2)-Cu(7))*((3)**0.5)
     ccdc(k) = (A-Cu(3)-Cu(6))*((3)**0.5)
     ccdd(k) = (A-Cu(4)-Cu(5))*((3)**0.5)
     minccd(k) = MIN(ccda(l),ccdb(l),ccdc(l),ccdd(l),A)
!Modified by adding A to list above by GPM amd GML 7/1/04 - prevents hard spheres bigger diameter than pore-row spacing



RH(k)=(minccd(k)/2)

if (k.eq.2) then
WRITE(3,*) 'hard sphere for particle 2:',ccda(k),ccdb(k),ccdc(k),ccdd(k),A,minccd(k)
end if

!coordinates of the primary position  - i.e the central point in space between the centres of the eight pores
XP=X(1)+(0.5*A)
YP=Y(1)+(0.5*A)
ZP=Z(1)+(0.5*A)
```

259

```fortran
touchingcube = 1 ! three dummy values to be over-written
mindist = 1.000
flag2 = 1

!calculate distance of the primary position to the closest cube corner
call calcdist(XP,YP,ZP,A,Cu,X,Y,Z,touchingcube,mindist,flag2)
! if value of flag2 returned by calcdist = 0 the has touched corner, if flag2 = 1 then has touched side or edge
if (k.eq.2) then
WRITE(3,*) 'after call to calcdist,',XP,',',YP,',',ZP,',',A,',',Cu,',',X,',',Y,',',Z,',',touchingcube,',',mindist,',',flag2
end if
XC1 = X(touchingcube+9)
YC1 = Y(touchingcube+9)
ZC1 = Z(touchingcube+9)

! specify positions for virtual reality
xpartposn = XP + CUX(k)
ypartposn = YP + CUY(k)
zpartposn = ZP + CUZ(k)

firsttouchingcube = touchingcube
D1(k)=mindist      ! radius when sphere touches first corner
if (k.eq.2) then
WRITE(3,*) 'D1(2),',D1(k)
end if
if (flag2.eq.0) then   !%%%%%% has touched corner so OK to caculate second contact point

!second contact point
!step=porerow/200

! if pore row spacing was greater than 200 step increment would be bigger than 1 -> WRONG...hence
!if (step.ge.1) then
 step = 0.01  ! works generally OK with step=0.1, but sometimes small overlaps
! print *,'step=',step
!end if

flag=0
flag2=0
lambda=step
do WHILE(flag.eq.0)
if (flag2.eq.0) then


XU= ((1+lambda)*XP) - (lambda*XC1)
YU= ((1+lambda)*YP) - (lambda*YC1)
ZU= ((1+lambda)*ZP) - (lambda*ZC1)

!calculate distance of U from C1
distanceUC1=((((XU-XC1)**2)+((YU-YC1)**2)+((ZU-ZC1)**2))**0.5)
!calculate closest corner to U (not C1)
call calcdist(XU,YU,ZU,A,Cu,X,Y,Z,touchingcube,mindist,flag2)
!D2temp(k)=mindist

distdiff= mindist-distanceUC1
if (ABS(distdiff).le.0.001) then
 flag=1
end if

if (ABS(X(touchingcube+9)-XC1).lt.smallreal) then

          if(ABS(Y(touchingcube+9)-YC1).lt.smallreal) then

                    IF(ABS(Z(touchingcube+9)-ZC1).lt.smallreal)then

                    flag = 0
                    end if
          endif
endif

!check if new closer corner is opposite to first closest corner: if it is, set flag = 2 to stop calculation later
if (firsttouchingcube.eq.1) then
     if (touchingcube.eq.8) then
     flag=2
     end if
end if
if (firsttouchingcube.eq.2) then
     if (touchingcube.eq.7) then
     flag=2
     end if
end if
if (firsttouchingcube.eq.3) then
     if (touchingcube.eq.6) then
     flag=2
     end if
end if
if (firsttouchingcube.eq.4) then
     if (touchingcube.eq.5) then
```

260

```fortran
            flag=2
            end if
      end if
      if (firsttouchingcube.eq.5) then
            if (touchingcube.eq.4) then
            flag=2
            end if
      end if
      if (firsttouchingcube.eq.6) then
            if (touchingcube.eq.3) then
            flag=2
            end if
      end if
      if (firsttouchingcube.eq.7) then
            if (touchingcube.eq.2) then
            flag=2

            end if
      end if
      if (firsttouchingcube.eq.8) then
            if (touchingcube.eq.1) then
            flag=2
            end if
      end if
      lambda=lambda+step


      else if (flag2.eq.1) then
            flag=1
      endif
!check if sphere is touching sides of outer cube. If it is , then set flag = 1 to stop calculation later
      if ((XU+mindist).GT.(A)) then
            flag=1
      end if
      if ((YU+mindist).GT.(A)) then
            flag=1
      end if
      if ((ZU+mindist).GT.(A)) then
            flag=1
      end if
      if ((XU-mindist).lt.0) then
            flag=1
      end if
      if ((YU-mindist).lt.0) then
            flag=1
      end if
      if ((ZU-mindist).lt.0) then
            flag=1
      end if
      if (flag.eq.1) THEN
      particlecomment="stopped at outer cube after 1st point"! added to designate particles in Virtual Reality
      END if

      end do

      ! specify positions for virtual reality
      xpartposn = XU + CUX(k)
      ypartposn = YU + CUY(k)
      zpartposn = ZU + CUZ(k)

      D2(k)=mindist

      XC2 = X(touchingcube+9)
      YC2 = Y(touchingcube+9)
      ZC2 = Z(touchingcube+9)
      ENDIF !%%%%%%%%%

      if (flag.eq.2) then ! first two contact points are opposite corners so stop

      if (k.eq.2) then ! debug print
        write (3,*) '2nd point for particle',k,'mindist,xc2,yc2,zc2',mindist,',',xc2,',',yc2,',',zc2
      end if


      ELSEIF (flag.ne.2)  then  ! first two contact points are not opposite so maybe OK to find third contact point
      if (flag2.eq.0) THEN !&&&&&& still not touching any edges or sides of pores, so OK to find third contact point

      flag=0
      mu=0
      do WHILE(flag.eq.0)
      if (flag2.eq.0) then
      XV = ((1+mu)*XU)-((mu*0.5)*(XC1+XC2))
      YV = ((1+mu)*YU)-((mu*0.5)*(YC1+YC2))
      ZV = ((1+mu)*ZU)-((mu*0.5)*(ZC1+ZC2))
      distanceVC1=((((XV-XC1)**2)+((YV-YC1)**2)+((ZV-ZC1)**2))**0.5)
      distanceVC2=((((XV-XC2)**2)+((YV-YC2)**2)+((ZV-ZC2)**2))**0.5)
```

261

```fortran
call calcdist(XV,YV,ZV,A,Cu,X,Y,Z,touchingcube,mindist,flag2)
!D3temp(k)=mindist
if (k.eq.2) then
WRITE(3,*) 'mindist,',mindist
end if
distdiff1= mindist-distanceVC1
distdiff2= mindist-distanceVC2
if (ABS(distdiff1).le.0.001) then
 if (ABS(distdiff2).le.0.001) then
 flag=1
 endif
endif
if (ABS(X(touchingcube+9)-XC1).lt.smallreal) then

        if(ABS(Y(touchingcube+9)-YC1).lt.smallreal) then

                if(ABS(Z(touchingcube+9)-ZC1).lt.smallreal)then

                flag = 0
                end if

        endif
endif
 if (ABS(X(touchingcube+9)-XC2).lt.smallreal) then

        if(ABS(Y(touchingcube+9)-YC2).lt.smallreal) then

                if(ABS(Z(touchingcube+9)-ZC2).lt.smallreal)then

                flag = 0
                end if

        endif
endif
mu=mu+step
if (k.eq.2) then
WRITE(3,*) 'mu,',mu
end if
else if (flag2.eq.1) then
     flag=1
   endif

!check if sphere is touching sides of outer cube and stop calculation if it is
if ((XV+mindist).GT.(A)) then
    flag=1
end if
if ((YV+mindist).GT.(A)) then
    flag=1
end if
if ((ZV+mindist).GT.(A)) then
    flag=1
end if
if ((XV-mindist).lt.0) then
    flag=1
end if
if ((YV-mindist).lt.0) then
    flag=1
end if
if ((ZV-mindist).lt.0) then
    flag=1
end if
if (flag.eq.1) THEN
particlecomment="stopped at outer cube after 2nd point"! added to try and designate particles
 if (k.eq.2) then
  WRITE(3,*) 'flag,XV,YV,ZV',flag,XV,YV,ZV
 end if
end if


end do

! XC3 = X(touchingcube+9)       these lines not used
! YC3 = Y(touchingcube+9)
! ZC3 = Z(touchingcube+9)

! calculate absolute posiion of centre of particle for Virtual Reality
 xpartposn = XV + CUX(k)
 ypartposn = YV + CUY(k)
 zpartposn = ZV + CUZ(k)

D3(k)=mindist
ENDIF !&&&&&&
endif

! D1(k) is first contact point diameter
! D2(k) is second contact point diameter - if 2nd contact point is found
! D3(k) is third contact point diameter - if 3rd contact point is found
```

262

```
! D2temp(k) is second contact point diameter - during loop - even if no 2nd contact point found
! D3temp(k) is third contact point diameter - during loop - even if no 3rd contact point found
maxradius(k)= MAX(D1(k),D2(k),D3(k),RH(k))
maxradius(k)= MIN(maxradius(k),A/2)

if (abs(maxradius(k)-rh(k)).lt.smallreal) then
! we have chosen the hard sphere diameter as being the biggest, so centre the particle on the primary position
!XV = xp
!YV = yp
!ZV = zp
particlecomment="hardsphere"
!PRINT *, "hardsphere"
end if

! GPM and GML 7/1/04 :
! check that the particle hasn't got a diameter larger than the pore row spacing
! because it has tried to fit its diameter across the diagonal of the available space
maxdiameter(k)=2*maxradius(k)
IF ((abs(maxradius(k)-D3(k)).lt.smallreal).AND.(flag2.eq.0)) THEN
particlecomment="3 contact points" !if the sphere has three contact points label it as such
END IF


WRITE (3,*) k,',',xpartposn,',',zpartposn,',',ypartposn,',',maxdiameter(k),',',XV,',',ZV,',',YV
WRITE (3,*) k,',',D1(k),',',D2(k),',',D3(k),',',RH(k)

! IF (particlecomment.eq."stopped at outer cube after 2nd point") THEN !This is used as a diagnostic tool and should not remain
WRITE (4,*) 'Particle { particleposition',   xpartposn/a*10 , zpartposn*10/(a*aspec),ypartposn/a*10 ,&
&'particleradius', maxdiameter(k)/a*5,'particlecomment "particle ',k,', diameter',maxdiameter(k),' microns, ',&
&particlecomment,' " particlecolor   1.00  0.50  1.00 }'
! END IF  !This is used as a diagnostic tool and should not remain

particlecomment=""

!PRINT *,k/10,'%completed'
END do ! end of main k loop
close (3)  ! close particle posn output file
close (4)  ! close particle VRML data output file

!write to file
OPEN (3,FILE='datafiles\partdist.csv',STATUS='replace')

totvol= 0 ! total volume of particles
do k=1,1000
 WRITE (3,*) (maxdiameter(k))
 totvol=totvol + pi*maxdiameter(k)**3/6
end do
 WRITE (3,*) 'total vol,',totvol
 close (3)


return
END subroutine partsize2

!!!!!!!!!!!!!!!!!!!!!!!!!!!!!!!!!!!!!!!!!!!!!!!!!!!!!!!!!!!!!!!!!!!!!!!!!!!!!!!!!!!!!!!!!!!!!!!!!!!!
! CALCULATE SHORTEST DISTANCE FROM point TO CUBE.
! FIRST CALCULATE HOW MANY OF (X-Cu), (Y-Cu), (Z-Cu) ARE POSITIVE.

subroutine calcdist(XA,YA,ZA,SUBA,CuSIDE,SUBX,SUBY,SUBZ,subtouchingcube,submindist,subflag)

INTEGER TOTPOS1 , TOTPOS2 , TOTPOS3 , TOTPOS4 , TOTPOS5 , TOTPOS6 , TOTPOS7 , TOTPOS8 , J ,subtouchingcube,subflag
REAL SUM1 , SUM2 , SUM3 , SUM4 , SUM5 , SUM6 , SUM7 , SUM8 , AUXX , AUXY , AUXZ , DIST . SUBA , XA , YA . ZA , cornerdist
DIMENSION AUXDIFFX(8) , AUXDIFFY(8) , AUXDIFFZ(8)
DIMENSION AUXX(10) , AUXY(10) , AUXZ(10) , DIST(8)
DIMENSION CuSIDE(8) , SUBX(50) , SUBY(50) , SUBZ(50),cornerdist(8)
REAL submindist, smallreal

smallreal=1e-20
! FOR CUBE 1
        TOTPOS1=0
        SUM1=0
    AUXDIFFX(1)=XA-(0.5*CuSIDE(1))
        AUXDIFFY(1)=YA-(0.5*CuSIDE(1))
        AUXDIFFZ(1)=ZA-(0.5*CuSIDE(1))
        IF(AUXDIFFX(1).GT.0) THEN
                TOTPOS1=TOTPOS1+1
                SUM1=SUM1+AUXDIFFX(1)**2
        END IF
        IF(AUXDIFFY(1).GT.0) THEN
                TOTPOS1=TOTPOS1+1
                SUM1=SUM1+AUXDIFFY(1)**2
        END IF
        IF(AUXDIFFZ(1).GT.0) THEN
                TOTPOS1=TOTPOS1+1
                SUM1=SUM1+AUXDIFFZ(1)**2
        ENDIF
```

263

```
! CUBE 2

AUXX(1) = SUBA-XA
TOTPOS2 = 0
SUM2 = 0
AUXDIFFX(2)=AUXX(1)-(0.5*CuSIDE(2))
AUXDIFFY(2)=YA-(0.5*CuSIDE(2))
AUXDIFFZ(2)=ZA-(0.5*CuSIDE(2))
            IF(AUXDIFFX(2).GT.0) THEN
                    TOTPOS2=TOTPOS2+1
                    SUM2=SUM2+AUXDIFFX(2)**2
            END IF
            IF(AUXDIFFY(2).GT.0) THEN
                    TOTPOS2 =TOTPOS2+1
                    SUM2=SUM2+AUXDIFFY(2)**2
            END IF
            IF(AUXDIFFZ(2).GT.0) THEN
                    TOTPOS2 =TOTPOS2 +1
                    SUM2=SUM2+AUXDIFFZ(2)**2
            ENDIF

! CUBE 3
AUXY(1)=SUBA-YA
TOTPOS3=0
SUM3=0
AUXDIFFX(3)=XA-(0.5*CuSIDE(3))
AUXDIFFY(3)=AUXY(1)-(0.5*CuSIDE(3))
AUXDIFFZ(3)=ZA-(0.5*CuSIDE(3))
            IF(AUXDIFFX(3).GT.0) THEN
                    TOTPOS3=TOTPOS3+1
                    SUM3=SUM3+AUXDIFFX(3)**2
            END IF
            IF(AUXDIFFY(3).GT.0) THEN
            TOTPOS3=TOTPOS3+1
            SUM3=SUM3+AUXDIFFY(3)**2
            END IF
            IF(AUXDIFFZ(3).GT.0) THEN
                    TOTPOS3=TOTPOS3+1
                    SUM3=SUM3+AUXDIFFZ(3)**2
            ENDIF

! CUBE 4
AUXY(2)=SUBA-YA
AUXX(2)=SUBA-XA
TOTPOS4=0
SUM4=0
AUXDIFFX(4)=AUXX(2)-(0.5*CuSIDE(4))
AUXDIFFY(4)=AUXY(2)-(0.5*CuSIDE(4))
AUXDIFFZ(4)=ZA-(0.5*CuSIDE(4))
            IF(AUXDIFFX(4).GT.0) THEN
                    TOTPOS4 =TOTPOS4+1
                    SUM4=SUM4+AUXDIFFX(4)**2
            END IF
            IF(AUXDIFFY(4).GT.0) THEN
                    TOTPOS4=TOTPOS4+1
                    SUM4=SUM4+AUXDIFFY(4)**2
            END IF
            IF(AUXDIFFZ(4).GT.0) THEN
                    TOTPOS4 =TOTPOS4+1
                    SUM4=SUM4+AUXDIFFZ(4)**2
            ENDIF

! CUBE 5
AUXZ(1)=SUBA-ZA
TOTPOS5=0
SUM5=0
AUXDIFFX(5)=XA-(0.5*CuSIDE(5))
AUXDIFFY(5)=YA-(0.5*CuSIDE(5))
AUXDIFFZ(5)=AUXZ(1)-(0.5*CuSIDE(5))
            IF(AUXDIFFX(5).GT.0) THEN
                    TOTPOS5=TOTPOS5+1
                    SUM5=SUM5+AUXDIFFX(5)**2
            END IF
            IF(AUXDIFFY(5).GT.0) THEN
                    TOTPOS5=TOTPOS5+1
                    SUM5=SUM5+AUXDIFFY(5)**2
            END IF
            IF(AUXDIFFZ(5).GT.0) THEN
                    TOTPOS5=TOTPOS5+1
                    SUM5=SUM5+AUXDIFFZ(5)**2
            ENDIF

! CUBE 6
AUXX(3)=SUBA-XA
AUXZ(2)=SUBA-ZA
TOTPOS6=0
```

```
SUM6=0
AUXDIFFX(6)=AUXX(3)-(0.5*CuSIDE(6))
AUXDIFFY(6)=YA-(0.5*CuSIDE(6))
AUXDIFFZ(6)=AUXZ(2)-(0.5*CuSIDE(6))
            IF(AUXDIFFX(6).GT.0) THEN
                        TOTPOS6=TOTPOS6+1
                        SUM6=SUM6+AUXDIFFX(6)**2
            END IF
            IF(AUXDIFFY(6).GT.0) THEN
                        TOTPOS6=TOTPOS6+1
                        SUM6=SUM6+AUXDIFFY(6)**2
            END IF
            IF(AUXDIFFZ(6).GT.0) THEN
                        TOTPOS6=TOTPOS6+1
                        SUM6=SUM6+AUXDIFFZ(6)**2
            ENDIF

! CUBE 7
AUXY(3)=SUBA-YA
AUXZ(3)=SUBA-ZA
TOTPOS7=0
SUM7=0
AUXDIFFX(7)=XA-(0.5*CuSIDE(7))
AUXDIFFY(7)=AUXY(3)-(0.5*CuSIDE(7))
AUXDIFFZ(7)=AUXZ(3)-(0.5*CuSIDE(7))
            IF(AUXDIFFX(7).GT.0) THEN
                        TOTPOS7=TOTPOS7+1
                        SUM7=SUM7+AUXDIFFX(7)**2
            END IF
            IF(AUXDIFFY(7).GT.0) THEN
                        TOTPOS7=TOTPOS7+1
                        SUM7=SUM7+AUXDIFFY(7)**2
            END IF
            IF(AUXDIFFZ(7).GT.0) THEN
                        TOTPOS7=TOTPOS7+1
                        SUM7=SUM7+AUXDIFFZ(7)**2
            ENDIF

! CUBE 8
AUXX(4)=SUBA-XA
AUXY(4)=SUBA-YA
AUXZ(4)=SUBA-ZA
TOTPOS8=0
SUM8=0
AUXDIFFX(8)=AUXX(4)-(0.5*CuSIDE(8))
AUXDIFFY(8)=AUXY(4)-(0.5*CuSIDE(8))
AUXDIFFZ(8)=AUXZ(4)-(0.5*CuSIDE(8))
            IF(AUXDIFFX(8).GT.0) THEN
                        TOTPOS8=TOTPOS8+1
                        SUM8=SUM8+AUXDIFFX(8)**2
            END IF
            IF(AUXDIFFY(8).GT.0) THEN
                        TOTPOS8=TOTPOS8+1
                        SUM8=SUM8+AUXDIFFY(8)**2
            END IF
            IF(AUXDIFFZ(8).GT.0) THEN
                        TOTPOS8=TOTPOS8+1
                        SUM8=SUM8+AUXDIFFZ(8)**2
            ENDIF
cornerdist(1)=100000
cornerdist(2)=100000
cornerdist(3)=100000
cornerdist(4)=100000
cornerdist(5)=100000
cornerdist(6)=100000
cornerdist(7)=100000
cornerdist(8)=100000

subflag=0

! CALCULATE SHORTEST DISTANCES FROM STARTING POINT
DIST(1)=SUM1**0.5
IF(TOTPOS1.EQ.1) THEN
            !PRINT *,'Cube 1:Shortest distance (to a side) is ',DIST(1)
        subflag=1
ELSE IF(TOTPOS1.EQ.2) THEN
            !PRINT *,'Cube 1:Shortest distance (to an edge) is ',DIST(1)
        subflag=1
ELSE IF(TOTPOS1.EQ.3) THEN
            !PRINT *,'Cube 1:Shortest distance (to a corner) is ',DIST(1)
        cornerdist(1)=DIST(1)
ENDIF

DIST(2)=SUM2**0.5
IF(TOTPOS2.EQ.1) THEN
    !        PRINT *,'Cube 2:Shortest distance (to a side) is ',DIST(2)
```

265

```
            subflag=1
      ELSE IF(TOTPOS2.EQ.2) THEN
      !        PRINT *,'Cube 2:Shortest distance (to an edge) is ',DIST(2)
            subflag=1
      ELSE IF(TOTPOS2.EQ.3) THEN
      !        PRINT *,'Cube 2:Shortest distance (to a corner) is ',DIST(2)
            cornerdist(2)=DIST(2)
      ENDIF

            DIST(3) =SUM3**0.5
      IF(TOTPOS3.EQ.1) THEN
            !PRINT *,'Cube 3:Shortest distance (to a side) is ',DIST(3)
            subflag=1
      ELSE IF(TOTPOS3.EQ.2) THEN
      !        PRINT *,'Cube 3:Shortest distance (to an edge) is ',DIST(3)
            subflag=1
      ELSE IF(TOTPOS3.EQ.3) THEN
      !        PRINT *,'Cube 3:Shortest distance (to a corner) is ',DIST(3)
            cornerdist(3)=DIST(3)
      ENDIF

            DIST(4)=SUM4**0.5
      IF(TOTPOS4.EQ.1) THEN
      !        PRINT *,'Cube 4:Shortest distance (to a side) is ',DIST(4)
            subflag=1
      ELSE IF(TOTPOS4.EQ.2) THEN
      !        PRINT *,'Cube 4:Shortest distance (to an edge) is ',DIST(4)
            subflag=1
      ELSE IF(TOTPOS4.EQ.3) THEN
      !        PRINT *,'Cube 4:Shortest distance (to a corner) is ',DIST(4)
            cornerdist(4)=DIST(4)
      ENDIF

            DIST(5)=SUM5**0.5
      IF(TOTPOS5.EQ.1) THEN
      !PRINT *,'Cube 5:Shortest  distance (to a side) is ',DIST(5)
      subflag=1
      ELSE IF(TOTPOS5.EQ.2) THEN
      !PRINT *,'Cube 5:Shortest  distance (to an edge) is ',DIST(5)
      subflag=1
      ELSE IF(TOTPOS5.EQ.3) THEN
      !PRINT *,'Cube 5:Shortest distance (to a corner) is ',DIST(5)
      cornerdist(5)=DIST(5)
      ENDIF

            DIST(6)=SUM6**0.5
      IF(TOTPOS6.EQ.1) THEN
      !PRINT *,'Cube 6:Shortest distance (to a side) is ',DIST(6)
      subflag=1
      ELSE IF(TOTPOS6.EQ.2) THEN
      !PRINT *,'Cube 6:Shortest distance (to an edge) is ',DIST(6)
      subflag=1
      ELSE IF(TOTPOS6.EQ.3) THEN
      !PRINT *,'Cube 6:Shortest distance (to a corner) is ',DIST(6)
      cornerdist(6)=DIST(6)
      ENDIF

            DIST(7)=SUM7**0.5
      IF(TOTPOS7.EQ.1) THEN
      !PRINT *,'Cube 7:Shortest distance (to a side) is ',DIST(7)
      subflag=1
      ELSE IF(TOTPOS7.EQ.2) THEN
      !PRINT *,'Cube 7:Shortest distance (to an edge) is ',DIST(7)
      subflag=1
      ELSE IF(TOTPOS7.EQ.3) THEN
      !PRINT *,'Cube 7:Shortest distance (to a corner) is ',DIST(7)
      cornerdist(7)=DIST(7)
      ENDIF

            DIST(8)=SUM8**0.5
      IF(TOTPOS8.EQ.1) THEN
      !        PRINT *,'Cube 8:Shortest distance (to a side) is ',DIST(8)
            subflag=1
      ELSE IF(TOTPOS8.EQ.2) THEN
      !        PRINT *,'Cube 8:Shortest distance (to an edge) is ',DIST(8)
            subflag=1
      ELSE IF(TOTPOS8.EQ.3) THEN
            !PRINT *,'Cube 8:Shortest distance (to a corner) is ',DIST(8)
            cornerdist(8)=DIST(8)
      ENDIF


      submindist=MIN(cornerdist(1),cornerdist(2),cornerdist(3),cornerdist(4),cornerdist(5),cornerdist(6),cornerdist(7),cornerdist(8))


      DO 400, J=1,8
```

```
         if (ABS(cornerdist(J)-submindist).lt.smallreal) then
         subtouchingcube = J
         end if
400 CONTINUE

!PRINT *, subtouchingcube
!PRINT *,'Minimum distance from', XA, YA, ZA, 'to a cube corner is ', submindist


RETURN
END subroutine calcdist
```

REFERENCES

Adamson, A.W. (1990) *Physical Chemistry of Surfaces*, A. Wyley Interscience Publication, New York.

Allen, T. (1981) *Particle Size Measurement*. Chapman and Hall Ltd., London, England.

Backfolk, K., Grankvist, T., and Triantafillopolous, N. (2003) Slip Rheology of Coating Colors Containing Calcium Carbonate Pigments with Narrow Particles Size Distributions, *2003 Tappi Advanced Coating Fundamentals Symposium*, Tappi Press.

Bernada, P. and Bruneau, D. (1996) *Tappi Journal* **79**: pp 130-143.

Bernada, P. and Bruneau, D. (1997) *Drying Technology* **15**: pp 2061-2087.

Bodurtha, P., Matthews, G.P., Kettle, J.P., Lohmander, S., and James, P.W. (2001) The influence of structural anisotropy on fluid permeation in porous media, *2001 Advanced Coating Fundamentals Symposium*, San Diego, Tappi Press.

Bodurtha, P. (2003) Novel techniques for investigating the permeation properties of environmentally friendly paper coatings: The influence of structural anisotropy on fluid permeation in porous media, *PhD Thesis*, University of Plymouth.

Bodurtha, P., Matthews, G. P., Kettle, J. P. and Roy I. M.., (2005) *Journal of Colloid and Interface Science* **283**: pp 171-189.

Bosanquet, C.H. (1923) *Philosophical Magazine, Series 6* **45**: pp 525-531.

Bousfield, D.W. (1993) Rheology-Structure Relationship through Particle Motion Modeling. *1993 Tappi Advanced Coating Fundamentals Symposium*, Atlanta, Tappi Press.

Dancey, C.P. and Reidy, J. (2002) *Statistics Without Maths for Psychology*. Prentice Hall.

Einstein, A. (1906) *Annelen der Physik* **19**: pp 289-306.

Einstein, A. (1911) *Annelen der Physik* **34**: pp 591-592.

Faure, J.P., Rabot, Y., Vidal F. and Pouyet, J. (1991) *Revue A T I P* **45**: pp 227-230.

Frenner, R.T. (2003), *Mechanics of Solids*: pp 314-388, Blackwell Scientific Publications.

Gane, P.A.C. (1997) Relaxation-induced dilatancy in separable visco-elastic suspensions: proposing a novel rheological phenomenon, *1997 Tappi Advanced Coating Fundamentals Symposium*, Atlanta, Tappi Press.

Gane, P.A.C., Kettle, J.P., Matthews, G.P. and Ridgway, C.J. (1995) *Industrial and Engineering Chemistry Research* **35**: pp 1753-1764.

Gane, P.A.C., Matthews, G.P., and Schoelkopf, J. (2000) Coating Imbibition Rate Studies of Offset Inks: A Novel Determination of Ink-on-Paper Viscosity and Solids Concentration using the Ink Tack Force-Time Integral, *2000 TAPPI International Printing & Graphic Arts Conference*, Tappi Press.

Gane, P.A.C., Schoelkopf, J., Spielmann, D.C, Matthews, G.P., and Ridgway, C.J. (1999) Observing fluid transport into porous coating structures: some novel findings, *1999 Tappi Advanced Coating Fundamentals Symposium*, Atlanta, Tappi Press.

Gao, C. (1997) *Applied Physics Letters* **71**: pp 1801-1803.

Gao, C., Dai P., Homola, A. and Weiss, J. (1998) *Journal of Tribology-ASME* **120**: pp 358-368.

Gaydos, J. (1996) *Colloids and Surfaces A-Physicochemical and Engineering Aspects* **114**: pp 1-22.

Groves, R. and Lanham, A. (1991) *Paper Technology* **32**: pp 28-34.

Groves, R., Matthews, G.P., Heap, J., McInnes, M.D., Penson, J.E., and Ridgway, C.J. (2001) Binder Migration in Paper Coatings - A New Perspective, *12th Fundamental Research Symposium, The Science of Papermaking*, Oxford.

Haines, W.B. (1927) *Journal of Agricultural Science* **17**: pp 264-290.

Hirasaki, G.J. and Yang, S.Y. (2002) Dynamic contact line with disjoining pressure, large capillary numbers, large angles and pre-wetted, precursor, or entrained films, Contact Angle, Wettability and Adhesion Vol. 2 (Mittal, K.L. ed.), VSP.

Husband, J. C. (1997) A Comparison of the Interactions of Various Starch Derivatives and Sodium Carboxymethyl Cellulose with Kaolin and Paper Coating Latex Suspensions, *PhD Thesis*, University of Manchester-Institute of Science and Technology.

Husband, J.C. (1998) *Colloids and Surfaces* **A131**: pp 145-159.

Husband, J.C. (2000) *Nordic Pulp and Paper Research Journal* **15**: pp 382-386.

Järnström, L., Lason, L. and Rigdahl, M. (1995a) *Colloids and Surfaces A-Physicochemical and Engineering Aspects* **104**: pp 191-205.

Järnström, L., Lason, L., Rigdahl, M. and Eriksson, U. (1995b) *Colloids and Surfaces A-Physicochemical and Engineering Aspects* **104**: pp 207-216.

Jennings, B.R. and Parslow, K. (1988) *Proceedings of the Royal Society of London Series A-Mathematical Physical and Engineering Sciences*, **419**: pp 137.

Johnson, A., Roy, I.M., Matthews, G.P. and Patel, D. (2003) *European Journal of Soil Science* **54**: pp 477-489.

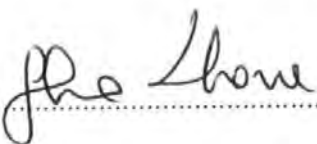Johnson, R.W., Abrams, L., Maynard R. and Amick, T.J. (1999) *Tappi Journal* **82**: pp 239-251.

Kettle, J.P. and Matthews, G.P. (1993) Computer Modelling of the Pore Structure and Permeability of Pigmented Coatings, *1993 Advanced Coating Fundamentals Symposium*, Atlanta, Tappi Press.

Knackstedt, M.A., Sheppard, A., Pinczewski, W.V., Sok, R., Hyde, S.T., Senden, T., and Ramsden, S. (2000) Meso-scale Physics-disordered Materials, University web site: http://www.rsphysse.anu.edu.au/appmaths/disord.html, The Australian National University.

Laudone, G.M., Matthews, G.P. and Gane, P.A.C (2004) *Industrial and Engineering Chemistry Research* **43**: pp 712-719.

Laudone, G.M, Matthews, G.P., Gane, P.A.C., Matthews, A.G., Ridgway, C.J., Schoelkopf, J. and Huggett, S. (2005) *Powder Technology*, submitted for publication.

Laurindo, J.B. and Prat, M. (1996) *Chemical Engineering Science* **51**: pp 5171-5185.

Laurindo, J.B. and Prat, M. (1998a) *Drying Technology* **16**: pp 1769-1787.

Laurindo, J.B. and Prat, M. (1998b) *Chemical Engineering Science* **53**: pp 2257-+.

Lodge, A.S. (1964) *Elastic Liquids - An Introductory Vector Treatment of Finite-Strain Polymer Rheology*. Academic Press, London.

Lohmander, S. (2000a) *Nordic Pulp and Paper Research Journal* **15**: pp 221-230.

Lohmander, S. (2000b) *Nordic Pulp and Paper Research Journal* **15**: pp 300-305.

Lucassen, J. (1992) *Colloids and Surfaces* **65**: pp 131-137.

Mathews, T.J., Matthews G.P. and Huggett S. (1999) *Powder Technology* **104**: pp 169-179.

Matthews, G.P. (2000) Computer modelling of fluid interactions in porous coatings and paper, *International Paper and Coating Chemistry Symposium*, Stockholm.

Matthews, G.P., Moss, A.K., Spearing, M.C. and Voland, F. (1993) *Powder Technology* **76**: pp 95-107.

Mayer, R.P. and Stowe, R.A. (1965) *Journal of Colloid Science* **20**: pp 893-911.

Micromeritics (1996) Mercury Porosimetry Particle Size Distribution Template, Application Note [79], Micromeritics.

Moreau, S. (1994) Structure des couches pigmentaires-Etude de leur sechage, *PhD Thesis*, Institute National Polytechnique de Grenoble.

Muguruma, Y., Tanaka, T. and Tsuji, Y. (2000) *Powder Technology* **109**: pp 49-57.

Niskanen, K.J., Rasi, M., Aaltosalmi U., Timonen, J., and Jataja.M. (1999) Permeability of Paper: Experiments and Numerical Simulations, *1999 Tappi International Paper Physics Conference*, Tappi Press.

Ostrowicki, A. and Ramthun, J. (1999) *Wochenblatt fur Papierfabrikation* **6**: pp 338-393.

Pan, S.X., Davis, H.T. and Scriven, L.E. (1995) *Tappi Journal* **78**: pp 127-143.

Peat, D.M.W., Matthews, G.P., Worsfold, P.J. and Jarvis, S.C. (2000) *European Journal of Soil Science* **51**: pp 65-79.

Perera, D. (1995) Stress Phenomena in Organic Coatings, in *Paint and Coating Testing Manual* (Koleske JV ed.) pp 585-599.

Persson, T., Järnström, L., and Rigdahl, M. (1995) Effect of method of preparation of coating colours on the rheological behaviour and properties of coating layers and coated papers, *1995 Tappi Coating Fundamentals Symposium*, Tappi Press.

Ridgway, C.J. and Gane, P.A.C. (2002) *Colloids and Surfaces A-Physicochemical and Engineering Aspects* **206**: pp 217-239.

Ridgway, C.J. and Gane, P.A.C. (2003) *Nordic Pulp & Paper Research Journal* **18**: pp 24-31.

Ridgway, C.J., Gane, P.A.C. and Schoelkopf, J. (2002) *Journal of Colloid and Interface Science* **252**: pp 373-382.

Ridgway, C.J., Gane, P.A.C. and Schoelkopf J. (2004) *Colloids and Surfaces A-Physicochemical and Engineering Aspects* **236**: pp 91-102.

Ridgway, C.J., Ridgway, K. and Matthews, G.P. (1997) *Journal of Pharmacy and Pharmacology* **49**: pp 377-383.

Ridgway, C.J., Schoelkopf, J., Matthews, G.P., Gane, P.A.C. and James, P.W. (2001) *Journal of Colloid and Interface Science* **239**: pp 417-431.

Roper, J.A. and Attal, J.F. (1993) *Tappi Journal* **76**.

Scheidegger, A.E. (1974) *The Physics of Flow Through Porous Media*. University of Toronto Press, Toronto.

Schoelkopf, J. (2002) Observation and modelling of fluid transport into porous paper coating structures, *PhD Thesis*, University of Plymouth.

Schoelkopf, J., Gane, P.A.C., and Ridgway, C.J. (2003) Pigment coating permeability: measurement and correlation with wetting front penetration, *2003 Tappi 8th Advanced Coating Fundamentals Symposium*, Chicago, Tappi Press.

Schoelkopf, J., Gane, P.A.C., Ridgway, C.J. and Matthews, G.P. (2001) *Nordic Pulp and Paper Research Journal* **15**: pp 422-430.

Schoelkopf, J., Gane, P.A.C., Ridgway, C.J. and Matthews, G.P. (2002) *Colloids and Surfaces A-Physicochemical and Engineering Aspects* **206**: pp 445-454.

Schoelkopf, J., Ridgway, C.J., Gane, P.A.C., Matthews, G.P. and Spielmann D.C. (2000) *Journal of Colloid and Interface Science* **227**: pp 119-131.

Spearing, M.C. (1991) The Measurement and Modelling of the Pore-Level Network Properties of Sandstones, *PhD Thesis*, Polytechnic South West.

Tadros, T.F. (1978) *J Colloid Interface Sci* **64**: pp 36.

Tappi (2000) Bending Stiffness (Four Point Method), *Tappi Test Methods*, Tappi Press.

Toivakka, M. and Eklund, D. (1995) Prediction of suspension rheology through particle motion simulation. *1995 Tappi Coating Fundamentals Symposium*, 161-176. Atlanta, TAPPI Press.

Toivakka, M. and Nyfors, K. (2000) Pore Space Characterization of Coating Layers. *2000 Tappi Coating Conference*, Washington DC, Tappi Press

Triantafillopolous, N. (1996) *Paper Coating Viscoelasticity - And Its Significance to Blade Coating*, Tappi Press, Atlanta.

Triantafillopolous, N. and Grankvist, T. (1994) *Paperi ja Puu - Paper and Timber* **76**: pp 663-667.

Watanabe, J. and Lepoutre, P. (1982) *Journal of Applied Polymer Science* **27**: pp 4207-4219.

Webb, P.A. and Orr, C. (1997) *Analytical Methods in Fine Particle Technology*, Micromeritics, Norcross,GA.

Wedin, P., Martinez, C.J., Lewis, J.A., Daicic, J. and Bergstrom, L. (2004) *Journal of Colloid and Interface Science* **272**: pp 1-9.

Willembacher, N., Hanciogullaru, H. and Wagner, H.G. (1997) *Chemical Engineering Technology* **20**: pp 557-563.

Willet, C.D., Adams, M.J., Johnston, S.A. and Seville, J.P.K. (2000) *Langmuir* **16**: pp 9396-9405.

Xiang, Y. and Bousfield, D. (2001) Effect of Coat Weight and Drying condition on Coating Structure and Ink-Setting. *2001 Advanced Coating Fundamentals*, San Diego, California, Tappi Press.

Yan, Y.D., Burns, J.L., Jameson, G.J. and Biggs, S. (2000) *Chemical Engineering Journal* **80**: pp 23-30.

Zhang, B. and Nakajima, A. (1999) *Journal of Colloid and Interface Science* **211**: pp 114-121.

Copyright statement

This copy of the thesis has been supplied on condition that anyone who consults it is understood to recognise that its copyright rests with its author and that no quotation from the thesis and no information derived from it may be published without the author's prior written consent.

i